UNIVERSIDAD NACIONAL AUTÓNOMA DE MÉXICO
PROGRAMA DE POSGRADO EN ASTROFÍSICA

Instituto de Astronomía

COLAPSO Y ACRECIÓN EN NÚCLEOS ESTELARES CON ROTACIÓN

TESIS

PARA OPTAR POR EL GRADO DE
DOCTOR EN CIENCIAS (ASTROFÍSICA)

PRESENTA
ALDO ALBERTO BATTA MÁRQUEZ

TUTORES O TUTOR
DR. WILLIAM HENRY LEE ALARDIN, INSTITUTO DE ASTRONOMIA

MÉXICO, D. F. ABRIL 2014

A mi familia
(perro y gatos incluidos)

Agradecimientos

Quisiera agradecer antes que nada a Eva, por ser mi mejor amiga y mi compañera, por acompañarme a lo largo de esta aventura, por ayudarme a encontrarle solución a problemas que encontré en el camino y sobre todo por ayudarme a despejar mi mente del trabajo, espero haberte ayudado de la misma forma durante este tiempo y que continuemos así por mucho tiempo. También quiero agradecer a mi mamá y mi hermano Alex, quienes siempre han estado ahí para mi y que sé que seguirán apoyándome durante el resto de mi vida. Gracias a mi papá y a mis hermanos Brenda y Diego que además de darme su apoyo, me brindan momentos alegres cada que los veo.

No puedo dejar de agradecerle a William (el jefe) por todo el apoyo que me dio durante la maestría y el doctorado, asegurándose de que me preparara de la mejor manera posible para lo que viene después. A pesar de estar sumamente ocupado como director del instituto, siempre encontró tiempo para platicar y ayudarme con mi proyecto. Espero poder utilizar todo lo que invirtió en mi para convertirme en un investigador y docente tan dedicado como él. También quisiera agradecer al grupo de Nucleares (Raga, Esquivel, Pablo, Ary y Claudio) que también formó parte de mi formación y que me brindó momentos divertidos durante el posgrado. Espero seguir en contacto con ustedes y que el próximo grupo de trabajo en el que me encuentre sea al menos la mitad de divertido y amable.

También quiero agradecer aquí a los sinodales de mi tesis Dr. William Lee, Dr. Alex Raga, Dra. Gloria Koenigsberger, Dr. Fabio De Colle y Dr. Erick Nagel. Las pláticas que tuve con ustedes (aún cuando algunas fueron por correo electrónico) fueron de mucha ayuda para mejorar este trabajo y espero que ésta no sea la última vez que cruzamos nuestros caminos en la vida académica ni en la personal.

De igual forma quiero agradecer a mi segunda familia, que me ha acompañado desde hace años; Daniel, Sergio, Abel, Silvia, Claudia, Mau (y los que me falten). Gracias por compartir conmigo los momentos importantes en sus vidas, espero que sigamos así. Por último pero no por ello menos importantes, quiero agradecer a los amigos que he hecho en mi paso por el célebre IA-CU. Gracias chamos (Roberto, Rodrigo, Alejandra, Paco, Claudio, Jonn y demás) por formar parte de esa segunda familia, la cual me ha brindado muy gratos momentos durante mi paso por el doctorado. Espero no me falte alguien más, pero si es así no se molesten, moléstense si no los invito a la fiesta de celebración.

Beso y abrazo para todos.

Contents

Resumen

A lo largo de este resumen, se mostrarán los principales objetivos y resultados obtenidos durante la realización de este proyecto de doctorado. Para lograr hacerlo suficientemente corto, se omitieron algunos detalles sobre el trabajo que hubo detrás de esta tesis. Sin embargo, toda la información pertinente se encuentra contenida en los demás capítulos de la tesis, en donde se muestra a detalle el proceso de obtención de los resultados mostrados aquí.

Comenzaremos con una breve y concisa introducción al problema que este proyecto intenta atacar, seguida de los principales requerimientos y procedimientos que se siguieron para obtener los resultados. Finalmente se presentarán los resultados más importantes, seguidos de las conclusiones e implicaciones.

Introducción

Los destellos de rayos gamma (GRB) son eventos en los que se observan flujos intensos de radiación cuyo máximo en la distribución de energía se encuentra en la banda de rayos γ (Fig. 1). La duración de estos destellos va desde fracciones de segundo a varias decenas de minutos y su luminosidad isotrópica está entre los $10^{49} - 10^{52}$ ergs/s. Estas luminosidades hacen que los GRB sean los objetos más luminosos observados hasta el momento. Sin embargo hay evidencia que indica que la radiación de estos eventos está altamente dirigida a lo largo de un cono con apertura de unos cuantos grados (Frail et al., 2001; Panaitescu & Meszaros, 1999; Sari et al., 1999), lo cual indica que la energía liberada por los mismos se encuentra alrededor de los 10^{51} ergs, comparable con la energía liberada en una explosión de supernova.

Las altas energías y la variabilidad observada en escalas de milisegundos (Fig 2), sugieren la presencia de un objeto compacto en el mecanismo de producción de estos eventos. Hasta el momento, a pesar de la falta de evidencia directa, se cree que los GRBs son el resultado de intensos eventos de acreción hipercrítica en objetos compactos como estrellas de neutrones (NS por sus siglas en inglés) o agujeros negros (BH por sus siglas en inglés) en donde se libera energía violentamente, generando a su vez la radiación electromagnética observada (ver Piran, 2004; Nakar, 2007; Lee & Ramirez-Ruiz, 2007; Gehrels et al., 2009 para revisiones detalladas).

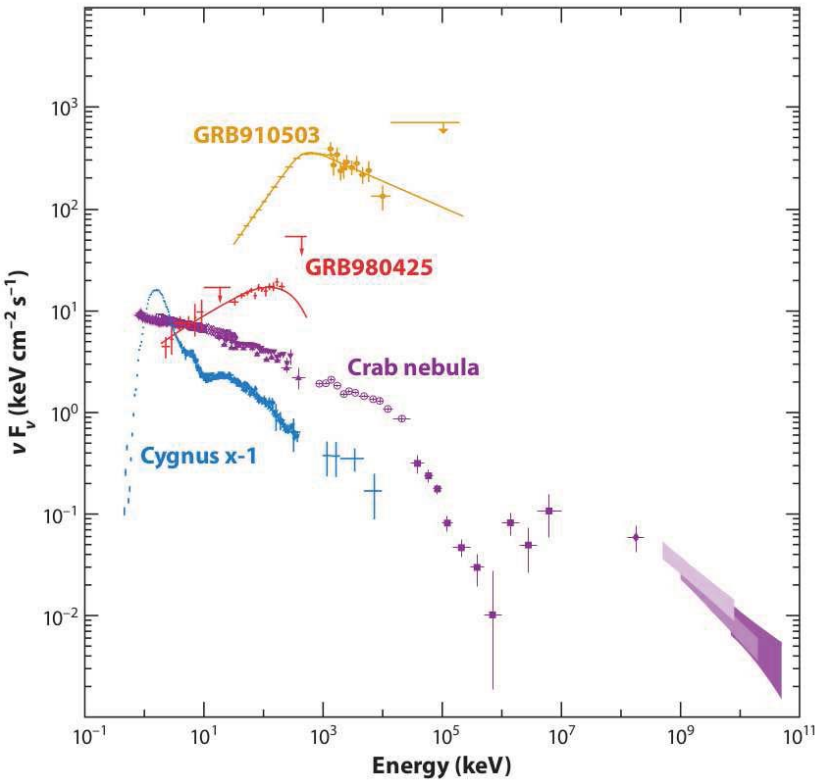

Figure 1: Distribución espectral de energía de dos GRBs (Kaneko et al., 2007, 2008) junto con el pulsar de la nebulosa de cangrejo (Kuiper et al., 2001) y el candidato a agujero negro (BH) galáctico Cygnus X-1 (McConnell et al., 2002). Los espectros de los GRBs son todos distintos entre ellos. Figura tomada de Gehrels et al. (2009).

Estos GRBs generalmente son seguidos de intensas emisiones con longitudes de onda que van desde rayos X hasta el radio. Es gracias a esta post luminiscen-

cia que se pueden identificar lineas de absorción o emisión que permiten calcular la distancia al punto de origen del evento (van Paradijs et al., 2000). Se ha encontrado que los destellos de corta duración (menor a 1 segundo) se producen generalmente a $z \lesssim 1$ mientras que los destellos de larga duración se producen a $z \simeq 1 - 5$ o mayor y compiten con los cuásares como los objetos más lejanos observados (Berger, 2011). En la mayoría de los casos, las galaxias asociadas a la formación de destellos de rayos gamma cortos (sGRB por sus siglas en inglés) tienen características diferentes a las asociadas a destellos de rayos gamma largos (lGRB por sus siglas en inglés) (Gehrels et al., 2009).

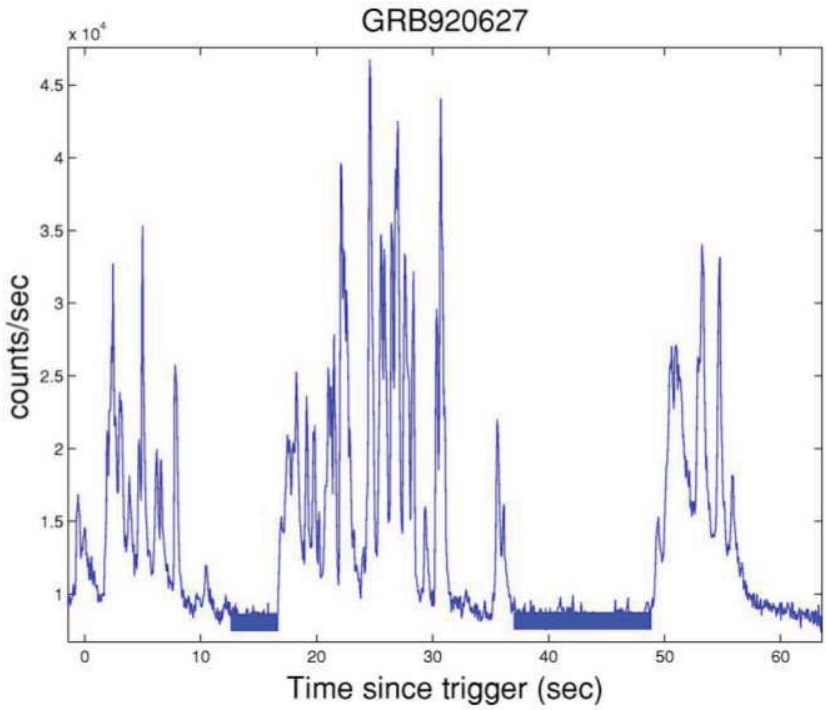

Figure 2: Curva de luz del GRB 920627. Se puede notar la variabilidad con distintas escalas de tiempo δt (dada por el ancho de los picos), que va de fracciones de segundo a varios segundos. Imagen tomada de Piran (2004).

Los sGRB están distribuidos de forma aleatoria en su galaxia anfitrión, la cual generalmente contiene una alta población de estrellas viejas (Lee & Ramirez-Ruiz, 2007; Berger, 2011). Por su parte, los lGRB se producen en galaxias con intensa formación estelar (encontradas generalmente a $Z > 1$) y en ocasiones los lGRB pueden ser asociados a observaciones de supernovas (SN) sin líneas de

hidrógeno (tipo Ib o Ic) que ocurren en la misma galaxia y que se detectan unos días después del destello cuando la intensidad de su post luminiscencia baja lo suficiente. La observación del destello de rayos gamma GRB980425 (nombrado así por el año, mes y día en el que ocurrió) en conjunción con la inusual supernova SN1998bw (Galama et al., 1998) fue el primero de este tipo de asociaciones entre lGRB y SN. Estas observaciones proporcionan evidencia fuerte de que la producción de lGRB está asociada con la muerte de estrellas masivas (Fruchter et al., 2006; Levesque et al., 2014). Las revisiones hechas por Woosley & Bloom (2006) y Hjorth & Bloom (2012) muestra la evidencia encontrada hasta el momento, que apoya la conexión entre los lGRBs y las SNs tipo Ic a bajo corrimiento al rojo z.

A pesar de que no todas las características observacionales se pueden explicar con un solo modelo teórico, existe un consenso en que los GRBs son producidos cuando la energía cinética de un flujo relativista es disipada (modelo de la bola de fuego; Piran, 2004; Gehrels et al., 2009). En este escenario, el GRB es producido por disipación dentro del mismo flujo relativista, mientras que la post luminiscencia es producida por choques externos de este flujo relativista con material circundante que pudo provenir de la estrella masiva y/o del medio interestelar. Este modelo de la bola de fuego está basado en una serie de requerimientos mínimos que se necesitan para formar un GRB:

- Material moviéndose a velocidades relativistas: Prácticamente todos los modelos de GRBs involucran el movimiento de material relativista con factores de Lorentz $\Gamma > 100$. Además de basarse en argumentos teóricos, se tienen pruebas observacionales directas de este argumento, como el centelleo de la emisión en radio (Goodman, 1997) y la auto absorción de baja frecuencia (Katz & Piran, 1997), que proveen un estimado de la expansión de la región donde se produce la post luminiscencia, la cual puede explicarse solamente con una expansión relativista. El movimiento relativista también implica que los fotones observados son menos energéticos en el marco de referencia en el que fueron emitidos. A pesar de que todos los modelos de sGRB invocan movimiento de material relativista, ninguno explica de manera convincente cómo éste es producido. Tampoco hay consenso en si se trata de un flujo relativista de bariones con alta energía cinética o si es un flujo dominado por campos magnéticos, o una combinación de ambos.

- Disipación: La energía de este flujo relativista es disipada para proporcionar energía para generar el GRB y la post luminiscencia. La disipación sucede a través de choques en los cuales el material transforma parte de su energía cinética en energía interna que puede luego ser radiada. Sari & Piran (1997)

mostraron que solamente los choques que ocurren dentro del mismo flujo relativista cuando material con alta velocidad alcanza un cascarón con una velocidad menor, pueden producir la variabilidad observada en la fase de GRB[1] ($dt \ll T$, donde T es la duración del destello). Existe un acuerdo general en que la post luminiscencia es producida por choques externos del material relativista con materia circundante.

- Radiación sincrotrón: Una vez que se tiene disipación de energía del flujo relativista,la mayoría de los modelos de GRBs utiliza la emisión sincrotrón de electrones relativistas acelerados dentro de los choques, para explicar la radiación observada tanto para el GRB como su post luminiscencia. Otra alternativa es la emisión sincrotrón auto Compton (Ghisellini & Celotti, 1999; Waxman, 1997) o dispersión Compton inverso de luz externa (Brainerd, 1994; Shemi, 1994; Shaviv & Dar, 1995; Lazzati et al., 2004).

- Chorros colimados de material (jets): La aparición de quiebres (cambios de pendiente) acromáticos en muchas de las curvas de post luminiscencia es interpretada como el producto de la disminución del factor de Lorentz del material relativista. A medida que Γ disminuye, la colimación disminuye hasta abarcar la totalidad del jet relativista con ángulo de apertura θ_0. Cuando $\Gamma < 1/\theta_0$, la colimación debida al movimiento relativista se vuelve menor y la radiación se emite de manera más isotrópica y lejos de la línea de visión, disminuyendo así la cantidad de radiación observada. De igual manera, un jet relativista se expande hacia los lados cuando el material del jet alcanza $\Gamma < 1/\theta_0$, lo cual también reduce el flujo observado (Panaitescu & Meszaros, 1999; Rhoads, 1999; Sari et al., 1999). Otra interpretación considera que existe una estructura universal para estos chorros colimados y que la orientación en la observación genera las diferencias observadas (Lipunov et al., 1999; Rossi et al., 2002; Zhang & Meszaros, 2002). Todos estos escenarios implican energías totales menores a la isotrópica y una mayor tasa de ocurrencia de estos eventos (que no observamos debido a que no están dirigidos hacia nosotros).

- Un objeto compacto: Si damos por sentado que el GRB se produce debido a la disipación de energía de un jet de material relativista altamente colimado que presenta rompimientos en la curva de luz en el óptico, la energía total liberada es de $\sim 10^{51}$ ergs (Frail et al., 2001; Panaitescu & Kumar, 2001). Esta energía es similar a la liberada en una SN, en donde se tiene formación de

[1]La densidad del medio es tan baja que los choques entre partículas son poco probables. Por lo tanto, en lugar de colisiones entre las partículas, las colisiones se dan entre éstas y los campos magnéticos y las ondas de plasma.

un objeto compacto (NS o BH). Además, no existe otra fuente conocida que sea capaz de producir tanta energía en tan corto tiempo. El proceso requiere la disipación de la energía producida por $0.1\ M_{\odot}$ en la vecindad del objeto compacto en una escala de tiempo relativamente corta, lo cual sugiere un proceso violento que podría indicar el nacimiento del mismo objeto compacto. La escala de tiempo más corta mostrada en la variabilidad del GRB (de unos cuantos milisegundos) nos da una estimación del tamaño de la región en donde ocurren los procesos responsables de las variaciones (~ 300 km). Y la acreción en un objeto compacto parece el mejor candidato para explicar el tamaño de la región y la variabilidad observada. La evidencia más reciente de que un objeto compacto está relacionado con la producción de sGRB proviene de la asociación observacional de la post luminiscencia de algunos lGRB con el espectro de una SN (Galama et al., 1998; Woosley & Bloom, 2006). Esto, combinado con la asociación de observaciones de lGRB con galaxias con alta producción de estrellas indica que al menos una población de sGRB está relacionada con la muerte de estrellas masivas (Fruchter et al., 2006; Levesque et al., 2014), en donde podrían formarse NSs o BHs.

En este trabajo estaremos enfocados al estudio del motor central que proporciona la energía ($\gtrsim 10^{51}$ erg) que será utilizada para producir el chorro de material relativista, que a su vez disipará su energía cinética para producir el GRB. Para este motor central existen varios modelos, que pueden dividirse en dos grandes grupos: aquellos capaces de lograr producción de energía durante un largo periodo de tiempo (capaces de explicar los lGRB) y los que producen energía durante periodos cortos (sGRB). En cuanto a los sGRB, se cree que son producidos durante eventos violentos que ocurren en la últimas etapas de evolución de una fracción pequeña de estrellas. Eventos como la fusión de estrellas de neutrones binarias (Goodman, 1986; Paczynski, 1986), fusión de un sistema BH-NS (Lee & Kluzniak, 1995; Janka et al., 1999), y algunos otros escenarios para la formación de sGRB son discutidos en el artículo de revisión de Lee & Ramirez-Ruiz (2007), junto con las características más importantes de los sGRB.

Por otra parte, dada la aparente relación de los lGRB con la muerte de estrellas masivas (que puede ser confirmada para ~ 10 objetos), los modelos más aceptados para explicar la formación de lGRB se basan en el violento colapso de una estrella Pre Supernova (PreSN). En tal escenario el núcleo de hierro de la estrella colapsa en una proto estrella de neutrones (pEN) con rápida rotación y tal vez un intenso campo magnético, que podría volverse el motor central del GRB o bien, colapsar en un BH cuya acreción de material producirá la enorme cantidad de energía necesaria para producir el destello. En caso de que se forme una pEN

con rápida rotación e intenso campo magnético, la presencia del campo magnético en la estrella con rotación diferencial induce la inestabilidad magneto rotacional (MRI) (Balbus & Hawley, 1998), que amplifica el campo magnético de manera exponencial produciendo flujos bipolares que podrían resultar en luminosidades de $\sim 10^{52}$ ergs, la explosión de la estrella como SN o un GRB (Akiyama et al., 2003; Williams, 2005; Metzger et al., 2011). Mientras que si la pEN acreta suficiente materia durante su formación, ésta colapsará directamente en un BH y tendremos el escenario del Colapsar propuesto por Woosley (1993) donde el núcleo de la estrella colapsa casi directamente en un BH, alrededor del cual las capas externas de la estrella formarán un disco de acreción que será calentado y acretado durante la escala de tiempo dinámica $t_{\rm dyn}$ que le tomará a la estrella de masa M_s y radio R_s colapsar:

$$t_{\rm dyn} \sim \sqrt{\frac{R_s^3}{2GM_s}} \sim 1100 \left(\frac{R_s}{R_\odot}\right)^3 \left(\frac{M_s}{M_\odot}\right)^{-1} \text{ s} \qquad (1)$$

Este escenario nos proporciona un motor capaz de producir una gran cantidad de energía durante largos periodos de tiempo, y las variaciones en la producción de esta energía podrían verse reflejadas en la producción del chorro y del GRB. El tiempo que dure la producción de energía del colapsar dependerá directamente de la estructura de la estrella PreSN que lo formó (perfil de densidad, rotación, masa y radio) así como de otros mecanismos físicos que son capaces de alterar la caída del material (procesos de enfriamiento o calentamiento, campos magnéticos).

El modelo del Colapsar

Existen dos variantes principales para este modelo; en una de ellas se forma una proto-estrella de neutrones (pNS por su ssiglas en inglés) antes de formarse un BH a partir del núcleo. La intensa acreción de material en la pNS induce su colapso en un BH luego de unos cuantos segundos. En el segundo escenario el núcleo colapsa directamente en un BH sin pasar por una etapa de pNS. Existen varios trabajos que estudian la posibilidad de la formación directa de un BH a partir del colapso de una de estas estrellas PreSN. Recientemente Dessart et al. (2012) realizaron simulaciones en 1D incluyendo relatividad general (RG) y una aproximación para el escape y absorción de neutrinos producidos, en donde encontraron que la mayoría de las estrellas PreSN producidas por Woosley & Heger (2006) (llamadas desde ahora WH06), fallaban en formar un BH directamente de su núcleo de Fe. En su lugar,

estas estrellas formaron pNSs de rápida rotación, capaces de sufrir una inestabilidad magneto hidrodinámica (Balbus & Hawley, 1991; Hawley & Balbus, 1991), la cual evitaría la caída de material sobre la pNS, evitando así su colapso en un BH. Sin embargo, existen otros trabajos en simulaciones en 2D y RG (Mizuno et al., 2004a,b; Sekiguchi & Shibata, 2007, 2011) donde se obtiene la formación directa de un BH a partir del colapso de distintos núcleos. Las ecuaciones de estado (EoS por sus siglas en inglés) y micro física incluida en estas simulaciones parece ser de importancia en el destino final del núcleo, pero la incertidumbre más grande sigue en las propiedades de la estrella PreSN a punto de colapsar, tal como su tasa de rotación, masa y radio, los cuales sólo podrán obtenerse a partir de mejorar los modelos de evolución estelar.

Al momento, los modelos estelares más utilizados para describir la estructura de estrellas PreSN que podrían generar un lGRB son aquellos realizados por WH06, en los cuales estudian la evolución de estrellas rotando rápidamente hasta el punto en que se llega a su fase PreSN. El destino de estas estrellas depende en gran medida de la historia de pérdida de masa (en la cual hay mucha incertidumbre), su rotación (la cual es tratada de manera aproximada en los modelos 1D) y de la presencia de campos magnéticos (sobre los cuales se sabe poco). La pérdida de masa es un ingrediente indispensable para obtener un Colapsar, ya que de esta forma se puede garantizar que la estrella no contenga envolvente de H (lo cual concuerda con las observaciones de sGRB asociados a SNs) y además hace más fácil que un chorro de material relativista sea capaz de atravesar la estrella, salir de ella y aún así tener suficiente energía cinética ($\Gamma > 100$) para producir el GRB y su postluminisencia. Entre los mecanismos que pueden ayudar a perder la envolvente de H de una de estas estrellas se encuentran la interacción con otra estrella en un sistema binario, o a través de intensos vientos estelares. Sin embargo, la pérdida de masa puede alterar otro ingrediente indispensable para este escenario, la rotación. En caso de que se pierda demasiada masa por vientos estelares, el momento angular de toda la estrella disminuirá considerablemente (por conservación de momento angular), lo cual frenará la rotación de la estrella, indispensable para la formación de un disco de acreción alrededor del BH. La interacción con una estrella compañera en un sistema binario puede resultar en pérdida o ganancia de momento angular, dependiendo principalmente del periodo orbital y el tiempo que pasa en secuencia principal (SP) la estrella de mayor masa (de Mink et al., 2013).

El momento angular de la estrella es crucial para la producción de un GRB (Lee & Ramirez-Ruiz, 2006). Al formarse un disco de acreción Kepleriano cerca del BH, la temperatura del material será suficientemente alta para que los neutrinos se vuelvan la principal fuente de enfriamiento, al igual que en el contexto de una supernova señalado por Chevalier (1989) y Houck & Chevalier (1991). Este eficiente

enfriamiento por neutrinos permite que la acreción proceda a tasas extremadamente altas liberando una enorme cantidad de energía. La energía producida por la emisión de neutrinos podría ser suficiente para generar el GRB, pero también la extracción de energía rotacional del BH mediante el mecanismo de Blandford-Znajek (Blandford & Znajek, 1977) podría generar suficiente energía para producir el GRB. La combinación de ambos mecanismos tampoco debe descartarse. En el caso de neutrinos, si el momento angular de la estrella es demasiado grande, el disco se formará demasiado lejos del BH, lo cual resultará en un disco más frío, que emite menos neutrinos, mientras que una estrella con muy poco momento angular caerá casi radialmente en vez de formar un disco y la producción de neutrinos también se verá reducida debido a que el material está siendo acretado muy rápidamente, arrastrando consigo los neutrinos que podrían ser emitidos.

MacFadyen & Woosley (1999) fueron los primeros en realizar una simulación numérica detallada de un colapsar, en la cual se calculó la energía producida por neutrinos, y se exploró la propagación de un jet relativista través de la estrella para distintas eficiencias de conversión de la energía previamente producida (Zhang et al., 2003; MacFadyen et al., 2001). Uno de los resultados que obtuvieron fue la expulsión de la envolvente estelar en una especie de hypernova. Sin embargo sus simulaciones no consideraban relatividad especial, necesaria para modelar los flujos relativistas construidos con la energía obtenida del Colapsar ni la nucleosíntesis que es de suma importancia en las explosiones de supernova. Luego de este estudio se han realizado muchos otros en 2D, suponiendo simetría azimutal (e.g., Proga et al., 2003; Fujimoto et al., 2006; Nagataki et al., 2007; Nagataki, 2009; Lopez-Camara et al., 2009, 2010; Sekiguchi & Shibata, 2011). Sin embargo, ha habido pocos estudios en 3D, que podrían mostrar la potencial importancia de la auto-gravedad del material de la estrella y las inestabilidades que podrían formarse al considerar tres dimensiones. El primer estudio en considerar esto fue el de Rockefeller et al. (2006) en el cual se estudió el colapso de estrellas de población III de $60\ M_{\odot}$ con rotación. Ellos encontraron la formación de inestabilidades en el disco, manifestadas principalmente como ondas espirales, las cuales contribuían al transporte de momento angular en el disco. Más recientemente Taylor et al. (2011) consideraron un progenitor de WH06 con rotación rápida formado por la fusión de 2 estrellas de He. Ellos también encontraron la formación de inestabilidades en el disco y obtuvieron luminosidades de neutrinos $L_{\nu} \gtrsim 10^{51}$ erg s^{-1}, suficientemente grandes para producir un GRB. Hay que notar que en todos estos modelos, el BH permanece fijo en el origen de la configuración originalmente esférica y la caída de material de la envolvente se remplaza por una inyección de masa aproximada a la tasa esperada de caída de la estrella. Esta suposición es correcta siempre y cuando la masa del disco y las estructuras formadas sea despreciable en comparación con

la del BH (el cual podría no ser el caso), o si las capas que caen no presentan fuertes asimetrías en su distribución de masa.

En este trabajo nos enfocamos en estudiar cómo la auto-gravedad en combinación con un enfriamiento eficiente (en este caso los neutrinos), podrían afectar la evolución y estructura del disco de acreción en el contexto del modelo del Colapsar. En lugar de hacer uso de una ecuación de estado muy compleja, quisimos estudiar soluciones genéricas con un enfriamiento simplificado que reprodujera las eficiencias de enfriamiento esperadas en un Colapsar. En particular ponemos especial atención a la comparación entre las escalas de tiempo de enfriamiento y las dinámicas, a fin de observar el efecto que tienen en la formación de estructura y en la evolución del flujo de acreción y pérdida de energía. En la siguiente sección daremos un resumen de las condiciones iniciales utilizadas en nuestro estudio, así como de la física que incluimos en nuestras simulaciones.

Condiciones Iniciales y Consideraciones Físicas

Para construir las condiciones iniciales necesarias para el modelo de Colapsar, decidimos construir estrellas politrópicas ($P = K\rho^{\gamma}$; $\gamma = 1+1/n = 5/3$) en equilibrio hidrostático a partir de la ecuación de Lane-Emden (ver Shapiro & Teukolsky, 1983):

$$\frac{1}{\xi^2}\frac{d}{d\xi}\left(\xi^2\frac{d\theta}{d\xi}\right) + \theta^n = 0$$

$$\text{donde,} \qquad \xi = rA = r\left(\frac{4\pi G\rho_c^2}{(n+1)P_c}\right)^{1/2} = r\left(\frac{4\pi G}{(n+1)K\rho_c^{1/n-1}}\right)^{1/2} \qquad (2)$$

$$\text{y} \qquad \rho = \rho_c\theta^n$$

Dado el índice politrópico $n = 3/2$, la densidad central de la estrella $\rho_c = 2.53{\times}10^9$ g cm^{-3} y su masa M_s, los demás parámetros como la constante politrópica K y el radio de la estrella R_s quedan definidos y la ecuación (2) puede resolverse para obtener los perfiles radiales de densidad, presión y energía interna (ρ, P y u respectivamente) de la estrella. De esta forma se obtuvo una estrella politrópica de $4.5\ M_\odot$ en equilibrio hidrostático y sin rotación cuyas propiedades se muestran en la tabla 1. La densidad central de esta estrella corresponde a la densidad central del núcleo de Fe del modelo de estrella PreSN 16TB de Woosley & Heger

(2006). Las propiedades de la estrella en 1D fueron mapeadas mediante un método Monte Carlo, en una distribución esférica de partículas en 3D cuya distribución de masa obedece la distribución de masa original en 1D. Sin embargo, al momento de construir la distribución 3D, se sustituyeron las 2 $M_\odot$ más internas de la estrella por una sola partícula de la misma masa localizada en el centro de la distribución esférica. Esta partícula representará al BH. De esta forma nuestra configuración inicial consiste en un BH de 2 $M_\odot$ situado en el origen, rodeado de un cascarón esférico de masa $M_{\rm env} = 2.5\ M_\odot$ que se extiende desde $r_{\rm int}$ hasta R_s (ver tabla 1).

Parámetro del sistema	valor
M_s	$4.5\ M_\odot$
$M_{\rm env}$	$2.5\ M_\odot$
R_s	1715.7 km
$r_{\rm int}$	844.69 km
$t_{\rm dyn} = \sqrt{R^3/GM_s}$	0.0919 s

Table 1: Parámetros principales de la envolvente politrópica ($M_{\rm env}, R_s, r_{\rm int}$) y del sistema ($t_{\rm dyn}$,$M_s$).

Al construir la distribución en 3D, se añadió rotación de cuerpo rígido a la envolvente utilizando una velocidad angular de $\Omega_0 = 8.33\ {\rm s}^{-1}$. Se tuvo especial cuidado de que esta velocidad angular proporcionara la mayor cantidad de materia posible en el disco de acreción. Para esto definimos Ω_0 en términos de radio de circularización final r_c al que se encontraría el material de la envolvente en una órbita kepleriana alrededor del BH. Una estimación de la relación entre Ω_0 y r_c puede obtenerse al asumir un potencial Newtoniano para el BH y que la presión de gas no contribuye considerablemente en la dinámica alrededor del BH, así como la conservación de momento angular inicial en la posición inicial de la envolvente $r_i = (R_i^2 + z^2)^{1/2}$, donde R_i es el radio en coordenadas cilíndricas en el plano XY y Z_i es la posición original en Z. De esta forma r_c puede expresarse como:

$$r_c = \Omega_0^2 R_i^4 / GM(r_i), \tag{3}$$

donde $M(r_i)$ es la masa contenida al interior de r_i. Para este calculo se asumió simetría esférica, lo cual implica una sobre estimación de r_c. La figura 3 muestra un mapa de color del radio de circularización en el plano meridional (R_i, Z_i) para tres distintas velocidades angulares ($\Omega_0 = 8.33, 6.0, 3.5\ {\rm s}^{-1}$). Entre más azul sea la región, más cerca del BH caerá. El material que se encuentre en los polos del eje de rotación caerá prácticamente en caída libre y será acretado por el BH. Podemos

ver que con la velocidad angular utilizada en la simulaciones tenemos un disco de acreción que se extiende desde $0.001 \lesssim R/R_s \lesssim 1$. Debido a que supusimos simetría esférica, el radio de circularización que se obtendría al intercambiar las $2M_\odot$ más internas por el BH será el mismo que considerando la masa contenida al interior $M(r_i)$.

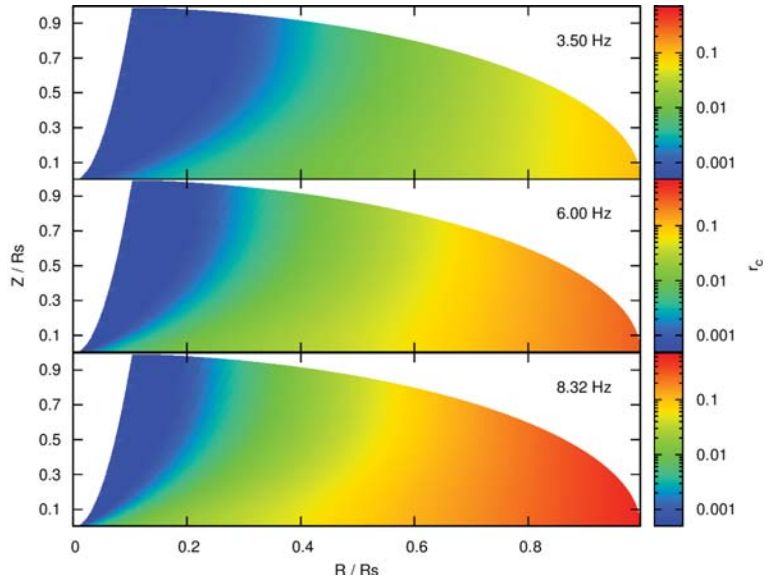

Figure 3: Radio de circularización r_c para la estrella politrópica de $4.5\ M_\odot$ como función del radio cilíndrico R/R_s (en el eje X y Z/R_s (en el eje Y) para tres diferentes velocidades angulares ($\Omega_0 = 8.32,\ 6.0,\ 3.5\ \mathrm{s}^{-1}$ de abajo para arriba). Para la construcción de este diagrama se adopta una distribución esférica de masa $M(r_i)$.

La velocidad angular $\Omega_0 = 8.33\ \mathrm{s}^{-1}$ corresponde a un radio de circularización para el material en r_{int} de $r_c = 7.49\ r_{\mathrm{acc}}$, donde r_{acc} es el radio de acreción que se definirá más adelante. De esta forma, dado que r_c está sobre estimado, garantizamos que se formará un disco de acreción que se extenderá de $7.5\ r_{\mathrm{acc}} \lesssim R < 1.0\ R_s$ y como vemos en la figura 3, habrá una gran cantidad de material de la envolvente que no caerá directamente al BH. De igual forma se compararon las velocidades de rotación obtenidas para $\Omega_0 = 8.33\,\mathrm{s}^{-1}$ con la velocidad de rompimiento V_{break} de la estrella de $4.5\ M_\odot$, es decir, la velocidad de rotación a la cual la estrella deja de estar ligada por gravedad. La figura 4 muestra una estimación de la velocidad de rompimiento normalizada (línea roja) en función del radio de la estrella junto con la velocidad de rotación ecuatorial para distintos radios de circularización $r_c \propto \Omega_0^2$. Vemos que nuestra elección de r_c nos asegura que la estrella no está girando suficientemente rápido como para destruirse debido

a la rotación.

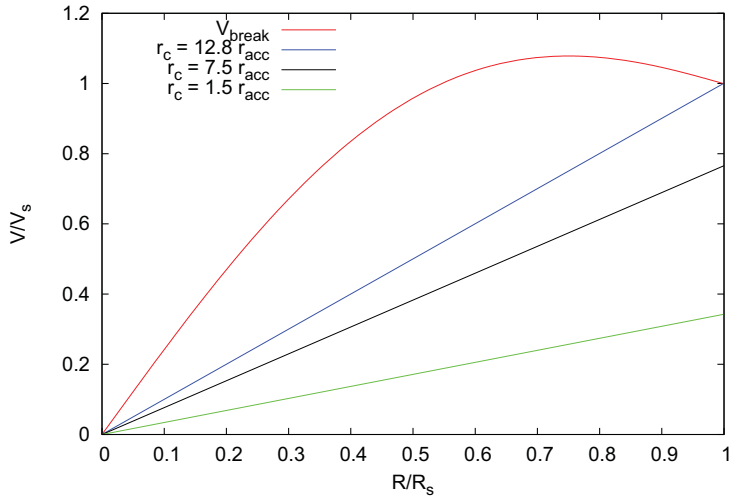

Figure 4: Velocidades de rotación en el plano ecuatorial para rotación de cuerpo rígido con radios de circularización ($r_c \propto \Omega_0^2$) 12.8 $r_{\rm acc}$ (línea azul), 7.5 $r_{\rm acc}$ (línea negra) y 1.5 $r_{\rm acc}$ (línea verde). En la gráfica también se muestra la velocidad de rompimiento $V_{\rm break}$ como función del radio de la estrella politrópica de 4.5 $M_\odot$ (línea roja).

A partir de esta configuración inicial, se estudió el colapso y acreción de las envolventes politrópicas de 2.5 $M_\odot$ en el BH de 2 $M_\odot$ localizado y fijado en el centro de la distribución inicialmente esférica. Las simulaciones fueron realizadas en el código GADGET-2 (Springel, 2005; Springel et al., 2001) cuyo tratamiento para la hidrodinámica (el cual utilizaremos) está basado en Smooth Particle Hydrodynamics (SPH) y las interacciones gravitacionales de N cuerpos es calculada mediante una estructura de árbol (como la utilizada por Hernquist & Katz (1989) en su código TREESPH) y distintos criterios de apertura de nodos que son tratados en detalle en el Capítulo 2. A continuación hablaremos un poco de los procesos físicos que tuvieron que incluirse a GADGET-2 para poder estudiar nuestro sistema en el contexto del Colapsar.

Física del Agujero Negro

En relatividad general (RG), un agujero negro sin rotación (Schwarzschild, 1916) de masa $M_{\rm BH}$ implica la definición del radio gravitacional $r_g = 2GM_{\rm BH}/c^2$. Este radio representa al horizonte de eventos y por lo tanto no puede haber observadores estáticos dentro de $r < r_g$. Al estudiar el movimiento de una partícula de prueba

en órbitas circulares alrededor de un BH de Schwarzschild se obtiene una relación entre el momento angular L y la distancia r de la partícula al BH, a partir de la cual se obtiene la posición de la órbita circular estable más cercana al BH $r_{\rm isco} = 3\ r_g$. A $r > 3\ r_g$ pueden existir órbitas circulares estables para partículas en un disco de acreción, mientras que a $r < 3\ r_g$ todas son inestables y terminan cayendo al BH. En nuestra simulación consideraremos la posición de esta última órbita circular estable como nuestro radio de acreción $r_{\rm acc} = 3\ r_g$ de forma que todo el material a $r < r_{\rm acc} = r_{\rm isco}$ será considerado como acretado por el BH y sus propiedades (como masa momento, momento angular, etc.) serán transferidas al BH.

Nuestra simulación considera al BH como una partícula de $2\ M_\odot$ fija en el origen de la distribución esférica. Sin embargo, para estudiar la dinámica del disco de acreción alrededor del BH, el potencial gravitacional Newtoniano no proporciona una buena aproximación a la dinámica que se tendría si se resolviera el problema utilizando RG. Puesto que resolver el problema de la dinámica de un disco de acreción autogravitante y masa considerable alrededor del BH puede volverse increíblemente costoso computacionalmente, decidimos aproximar la dinámica del material alrededor del BH, utilizando un potencial pseudo-Newtoniano capaz de reproducir algunas de las propiedades dinámicas más importantes que se obtendrían en relatividad general (RG).

El potencial utilizado es el de Paczynski-Wiita (Paczynski & Wiita, 1980), que reproduce de forma exacta la posición de la última órbita circular estable y de la órbita marginalmente estable ($r_{\rm isco} = 3\ r_g$ y $r_{\rm mb} = 2\ r_g$ respectivamente) de un BH de Schwarzschild.

$$\Phi_{\rm PW} = -\frac{GM_{\rm BH}}{r - r_g} \tag{4}$$

Este potencial también reproduce con mayor precisión que el potencial Newtoniano, la forma de la distribución de momento angular Kepleriano $L(r) = \left(r^3 d\phi/dr\right)^{1/2}$ obtenida para una partícula de prueba orbitando alrededor de un BH de Schwarzschild (ver figura 5). La desviación de la distribución en RG se traducirá en tasas de acreción un tanto diferentes, sin embargo se tiene un acuerdo mucho mejor que considerando el potencia Newtoniano.

Una vez que una partícula de gas es acretada, su masa es removida y transferida al BH. Esto cambia las propiedades del BH luego de un tiempo de integración dt en el cual se habrá acretado una masa $M_{\rm acc}$ a una tasa $M_{\rm acc}/dt$. Esto modifica r_g y a su vez el radio de acreción $r_{\rm acc}$ y el potencial $\Phi_{\rm PW}(r)$. A fin de garantizar que el potencial PW y la rutina encargada de la acreción del gas en el BH funcionaran

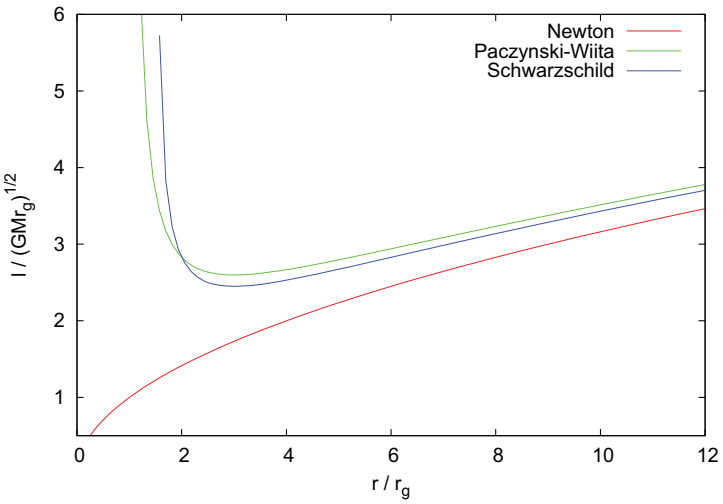

Figure 5: Distribución Kepleriana de momento angular para una partícula de prueba en órbita circular en un potencial Newtoniano (línea roja), un potencial de Paczynski-Wiita (línea verde) y un agujero negro de Schwarzschild (línea azul).

correctamente, se realizaron varias pruebas del colapso y acreción de estas envolventes politrópicas a fin de asegurar conservación de masa y momento durante el proceso. Mas detalles sobre estas pruebas pueden verse en el capítulo 2.

Termodinámica y Enfriamiento

El código GADGET-2 incluye una ecuación de estado de gas ideal, en términos de una función entrópica $A(s) \equiv P/\rho^{\gamma}$. Donde $\gamma = 5/3$ es el índice adiabático. Por lo tanto, tuvimos que incluir una rutina que se encargara del enfriamiento del gas para poder explorar su importancia en la evolución del disco de acreción. Sin esta rutina, el sistema sólo podrá perder energía (interna, cinética o potencial) cuando las partículas de gas son acretadas por el BH. A pesar de que este escenario no se daría en el contexto de un Colapsar, en donde se espera que haya una importante pérdida de energía por producción de neutrinos, decidimos estudiarlo a fin de determinar la importancia del enfriamiento en la formación de estructura en el disco de acreción.

El estudiar el colapso adiabático nos dará información sobre la formación de inestabilidades en una envolvente donde el mecanismo de enfriamiento por neutrinos es altamente ineficiente. De igual forma un colapso isotermo, nos proporcionará información sobre la formación de estructura en un disco de acreción con

un mecanismo de enfriamiento altamente eficiente, el cual mantiene la temperatura de la envolvente constante. En este último escenario, las pérdidas de energía son inmediatas, y la envolvente habrá perdido una gran cantidad de energía antes de formar el disco de acreción, lo cual podría resultar en un escenario no muy parecido al esperado en un Colapsar. Para estudiar el colapso isotermo de la envolvente se tomó $\gamma \simeq 1$ en la EoS.

Con el fin de explorar el efecto de diferentes eficiencias en el mecanismo de enfriamiento (neutrinos), exploramos la transición de un colapso adiabático ($\gamma = 5/3$) sin enfriamiento a uno isotermo ($\gamma \simeq 1$) en nuestras envolventes politrópicas. Para esto tomamos $\gamma = 5/3$, e incluimos un mecanismo sencillo de enfriamiento basado en una escala de tiempo de enfriamiento $t_{\rm cool}$ que se mantiene constante durante la simulación. Esta escala de tiempo depende de la escala de tiempo dinámica del disco de acreción $t_{\rm disk}$

$$t_{\rm cool} = \beta t_{\rm disk}\ , \qquad \frac{du_i}{dt} = -\frac{u_i}{t_{\rm cool}}. \tag{5}$$

Este mecanismo de enfriamiento está determinado por la energía interna del material u_i y el parámetro de eficiencia β, el cual determina cuantas veces el material orbita el BH antes de enfriarse considerablemente. Para $\beta \gg 1$ el gas completa varias orbitas alrededor del BH antes de enfriarse, y el colapso del material y la dinámica del disco será muy parecido al caso adiabático. Mientras que para $\beta \ll 1$ el material se enfriará antes de completar una órbita alrededor del BH y el colapso y evolución del disco se parecerán más al caso isotermo, en donde la envolvente cae casi en caída libre (excepto por la rotación) hacia el BH. Sin compresión o expansión del material, el único cambio que debería sufrir la energía interna de la envolvente sería el cambio dado por la ecuación (5) y el enfriamiento sería exponencial.

La escala de tiempo dinámico del disco $t_{\rm disk}$ puede ser estimada de la velocidad angular inicial utilizada para las simulaciones ($t_{\rm disk} \sim 1/\Omega_0 \sim 0.12$ s). Luego de la formación del disco, la velocidad angular del material será muy cercana a la kepleriana y Ω_0 no representará la velocidad angular de toda la envolvente, pero esta estimación nos dará una idea del tiempo que tardará en enfriarse el material más cercano al BH.

Enfriamiento por Neutrinos

Con el fin de obtener resultados en el contexto del modelo del Colapsar, estudiamos las condiciones en que podría tenerse formación de inestabilidades en el disco de

acreción con la presencia de un mecanismo de enfriamiento tan eficiente como el de producción de neutrinos por aniquilación y/o captura de pares en nucleones libres, que son los procesos más importantes para producción de neutrinos en un disco de acreción en esas condiciones. Para esto exploramos los casos en que nuestro tiempo de enfriamiento $t_{\rm cool}$ es igual a la escala de tiempo de enfriamiento por neutrinos t_ν que se espera tener en el material. Por lo que se estimó el rango de tiempo en que se encuentra t_ν para las temperaturas y densidades esperadas en el Colapsar. La escala de tiempo de enfriamiento por neutrinos puede ser calculada a partir de la tasa de pérdida de energía por neutrinos q_ν y la energía interna del material u, de tal forma que $t_\nu = u_{\rm V}/q_\nu$.

Una primera aproximación a la tasa de pérdida de energía por neutrinos fue propuesta en el trabajo de Narayan et al. (2001), en donde estudian distintos escenarios de acreción en un objeto compacto (BH) en el contexto de producción de GRBs. Para una temperatura T dada y densidad ρ, la tasa de enfriamiento por neutrinos por unidad de volumen estará dada por (Narayan et al., 2001):

$$q_\nu \simeq 5 \times 10^{33} T_{11}^9 + 9.0 \times 10^{23} \rho T_{11}^6 \text{ ergs cm}^{-3} \text{ s}^{-1}, \tag{6}$$

donde el primer término del lado derecho de la ecuación proviene de la aniquilación de pares y el segundo de la captura de pares en nucleones libres (estimado para un gas completamente fotodesintegrado con fracción de masa de nucleones libres es $X_{\rm nuc} = 1$). Ambos términos dependen sensiblemente de la temperatura $T_{11} = T/10^{11}$ K, por lo que se requieren altas temperaturas $T \gtrsim 10^{10}$ K, para que el enfriamiento se vuelva relevante.

Ahora nos falta estimar la temperatura a la cual se encontrará el material al llegar a la barrera centrífuga en r_c en donde es calentado y chocado. Para esto estimaremos la velocidad de caída libre del material $v_{\rm ff}$ considerando que la presión no afecta la dinámica de la caída, que no tenemos rotación y que al llegar a r_c el material transformará toda su energía cinética en energía térmica. Esto nos dará un límite superior $T_{\rm up}$ para la temperatura a la cual se encontrará el material en r_c en función de su posición inicial r_i. Para el radio de circularización utilizado en nuestras simulaciones, $r_c = 7.5\, r_{\rm acc}$, se puede encontrar que $T_{\rm up}$ toma valores entre 10^{10} K $\lesssim T \lesssim 10^{11}$ K. Por lo que asumiremos que el material adquiere temperaturas 10^{10} K $\lesssim T \lesssim 10^{11}$ K cerca del BH. Por otra parte la densidad promedio de la estrella politrópica es $\bar{\rho} \sim 10^9$ g cm^{-3}. Esto implica que luego de colapsar en el BH, el volumen en que esté contenido el material será al menos 10 veces menor, esto implica que el material podrá alcanzar densidades al menos 10 veces mayores, dependiendo de la presión local y la eficiencia del mecanismo de enfriamiento. Por lo que consideraremos densidades comparables con las consideradas por Narayan et al. (2001), 10^{10} g cm$^{-3} \lesssim \rho \lesssim 10^{12}$ g cm^{-3}.

Ahora, para calcular la escala de tiempo de enfriamiento por neutrinos necesitamos estimar la energía interna por unidad de volumen $u_{\rm V}$ del material, de forma que $t_\nu = u_{\rm V}/q_\nu$. En el material tendremos tres contribuciones principales. La primera proviene del gas ideal compuesto de partículas α y nucleones libres obtenidos de la fotodesintegración del material. La segunda contribución será la de la radiación que se encontrará atrapada dentro del material debido a las altas densidades que se tienen en regiones donde se tiene enfriamiento por neutrinos. Por último, habrá una contribución de electrones y positrones relativistas con degeneración arbitraria. Para obtener una aproximación de $u_{\rm V}$ consideraremos que los pares electrón-positrón son altamente relativistas y no están degenerados, con lo cual podemos escribir la energía interna por unidad de volumen $u_{\rm V}$ como:

$$u_{\rm V} = \frac{3}{2}\frac{kT\rho}{\mu m_p} + \frac{11}{4}aT^4, \tag{7}$$

donde el primer término corresponde al gas ideal, y el segundo a radiación y electrones-positrones relativistas combinados.

A partir de (6) y (7) y considerando densidades entre $\rho \simeq 10^{10} - 10^{12}$ g cm^{-3} y temperaturas del orden de $T \simeq 10^{10} - 10^{11}$ K, podemos estimar la escala de tiempo de enfriamiento por neutrinos que se espera en r_c como se muestra en la figura 6. Esto indica que la escala de tiempo t_ν se encontrará entre $\sim 10^{-4}$ y unos cuantos segundos, dependiendo principalmente de la temperatura del sistema (la cual determina la energía interna). En la tabla 2 se muestran los distintos tiempos de enfriamiento $t_{\rm cool}$ utilizados en nuestras simulaciones, que se encuentran dentro del rango de tiempos característicos de enfriamiento por neutrinos que encontramos en la figura 6.

Con el fin de tener una idea de la precisión de las simulaciones, se realizaron varias pruebas de convergencia del colapso y acreción de estas envolventes politrópicas en el BH, usando 50,000, 500,000 y 5,000,000 de partículas de SPH de igual masa. Luego de varias pruebas, encontramos que las simulaciones con más de 500 000 partículas de SPH no mostraban diferencias importantes en la tasa de acreción obtenida o en las propiedades generales del disco de acreción, por lo que todas las simulaciones se realizaron con este número de partículas. Aún más, dado que los datos completos de la simulación se podían guardar en archivos de tamaño $\lesssim 30$ MB, fuimos capaces de obtener una muy buena resolución de tiempo entre cada archivo de datos $\sim 1/20 t_{\rm dyn}$ la cual fue de utilidad para estudiar la aparición de inestabilidades en el disco. Los capítulos 2 y 3 muestran con mayor detalle algunas de las pruebas realizadas al código para asegurar su buen funcionamiento.

Dada la naturaleza de nuestro trabajo, es de gran importancia asegurar que la resolución de partículas en el disco de acreción sea suficientemente grande como

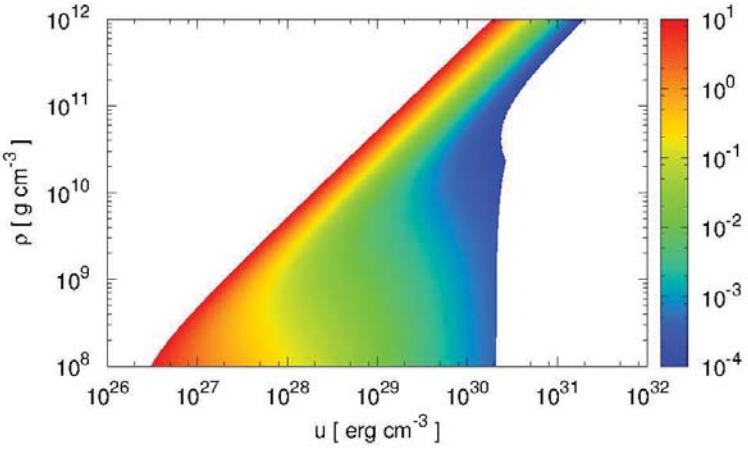

Figure 6: Escala de tiempo de enfriamiento por neutrinos t_ν esperada para material compuesto de gas ideal ($\mu = 1/2$) con contribuciones térmicas de pares electrón-positrón relativistas y presión de radiación (ecuación 7).

para resolver la formación de estructura espiral o grumos. Como fue mostrado por Bate & Burkert (1997), para tener una buena representación de la fragmentación en una simulación de SPH, la masa de Jeans del disco debe ser mayor que la masa mínima resoluble en las simulación $M_{\rm min}$ dada por:

$$M_{\rm min} = 2M_{\rm tot}(N_{\rm neigh}/N_{\rm tot}), \tag{8}$$

donde $M_{\rm tot}$, $N_{\rm tot}$ y $N_{\rm neigh}$ son la masa total, el número total de partículas y el número de vecinos de SPH respectivamente. Para todas nuestras simulaciones encontramos que en todo momento, la masa de Jeans M_J a radios $R < 0.9R_p$ eran al menos un orden de magnitud menor que la masa de resolución de la simulación. Mientras que para $R > 0.9R_p$ esta condición no siempre se cumplía. Por lo tanto es seguro decir, que para $R \lesssim 0.9R_p$, donde más del 90% de la masa del disco se encuentra contenida, se tiene resolución suficiente para observar formación de estructura.

Resultados y Discusión

Primero discutiremos las características generales del flujo de acreción obtenido para las distintas simulaciones, tal como la tasa de acreción $\dot{M} = dM/dt$, y la

Modelo	Eficiencia de enfriamiento β	$t_{\rm cool}$	$t_{\rm cool}/t_{\rm dyn}$
β13.4	10.27	1.2319 s	13.4
β2.68	2.054	0.24639 s	2.68
β1.34	1.027	0.12319 s	1.34
β0.67	0.513	0.061595 s	0.67
β0.134	0.1027	0.012319 s	0.134
β0.067	0.0513	0.0061595 s	0.067

Table 2: Tiempos de enfriamiento $t_{\rm cool}$ y parámetros de eficiencia β usados en las simulaciones. Los tiempos de enfriamiento se encuentran dentro de los valores esperados para el tiempo de enfriamiento por neutrinos obtenido en la figura 6. Los modelos son nombrados conforme al factor $t_{\rm cool}/t_{\rm dyn}$ de cada uno de ellos.

tasa total de pérdida de energía $L_c = \sum du_i/dt$, definida por la energía interna de las partículas de SPH y el tiempo de enfriamiento $t_{\rm cool}$ mostrado en la tabla 2. Estas cantidades nos darán información sobre cambios generales en el comportamiento del sistema debidos a las distintas eficiencias de enfriamiento. Más adelante analizaremos casos particulares para buscar una relación entre el comportamiento de estas cantidades y las propiedades específicas del disco, así como con la escala de tiempo de enfriamiento.

Tasas de acreción y masa del Agujero Negro

Puesto que la envolvente politrópica se encuentra inicialmente a una distancia $r_{\rm int} \sim R_s/2$ del BH, la acreción no comenzará hasta que el material en $r_{\rm int}$ caiga al radio de acreción del BH de 2 $M_\odot$ en $r_{\rm acc} = 3\ r_g \simeq 17$ km. El tiempo que le tomará a la envolvente llegar a ese punto se verá afectado por la presión de gas, que en caso de ser despreciable, se traduciría en un tiempo de caída libre $t_{\rm fall} \sim t_{\rm dyn}/2$. En realidad, la presión de gas acelerará la caída del material haciendo que $t_{\rm fall} \lesssim t_{\rm dyn}/2$.

La figura 7 muestra la tasa de acreción en función del tiempo para los distintos modelos explorados. En todos ellos, la acreción comienza en tiempos entre $0.02\,{\rm s} \lesssim t \lesssim 0.05\,{\rm s}$ dependiendo de la eficiencia de enfriamiento. Entre más eficiente es el enfriamiento mayor es el valor de $t_{\rm fall}$ y el de la tasa de acreción alcanzada al inicio del colapso. En el panel de abajo de la figura 7 se muestran los modelos con enfriamiento lento (β13.4, β2.68 & β1.34) con mayor parecido al modelo adiabático (línea roja). Mientras que en el panel superior se muestran

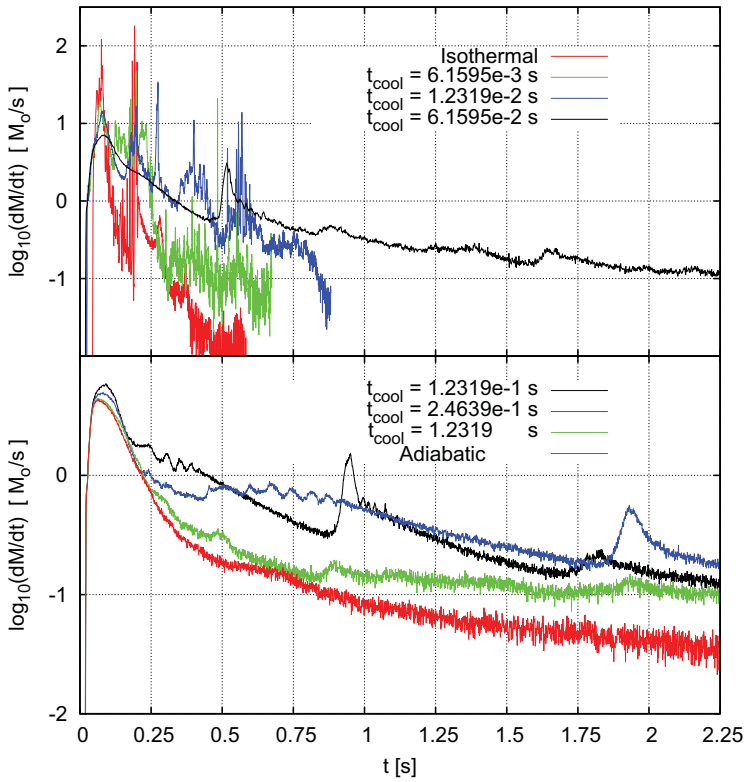

Figure 7: Tasa de acreción del BH (en masas solares por segundo) obtenida en las distintas simulaciones. En el panel superior se muestran las envolventes con tiempo de enfriamiento $t_{\rm cool}$ más pequeño ($\beta 0.067, \beta 0.134, \beta 0.67$, líneas verde, azul y negra respectivamente), con similitudes con el modelo isotermo (línea roja), mientras que el panel inferior muestra las envolventes cuyo enfriamiento es más lento y muestran mayor parecido con el modelo adiabático ($\beta 13.4, \beta 2.68, \beta 1.34$, líneas verde, azul y negra respectivamente).

los modelos con enfriamiento más rápido que más se parecen al modelo isotermo ($\beta 0.67$, $\beta 0.134$ & $\beta 0.067$). Se puede notar que los modelos con enfriamiento más eficiente muestran una mayor cantidad de variaciones en dM/dt y de mayor intensidad que modelos con menor eficiencia en el enfriamiento. Las simulaciones de modelos con tiempo de enfriamiento muy pequeño tuvieron que ser terminadas a tiempos más cortos debido a la demanda computacional impuesta por el paso de tiempo cada vez más corto requerido en las etapas finales. Nos aseguramos de que en la simulación nunca se llegara a energías internas demasiado bajas imponiendo un límite inferior a la temperatura del sistema para que se aplicara el mecanismo de enfriamiento ($T > 1000$ K).

Todos los modelos muestran un máximo en la tasa de acreción alrededor de $t \lesssim 0.1$ s debido a la acreción del material de los polos de rotación de la envolvente (como se mostró en la figura 3). A medida que el material alcanza el BH, se forma un choque que se propaga hacia afuera. Si el enfriamiento es poco eficiente, tendremos una evolución adiabática para este choque, el cual frenará la caída de material y prevendrá que parte de éste llegue al BH. Mientras que para un enfriamiento suficientemente eficiente, el material chocado (con alta temperatura y energía interna) perderá energía, lo cual ralentizará el choque y la caída de material será frenada en menor proporción que en el caso adiabático. Esto se traduce en tasas de acreción mayores que se observan como el máximo cerca de $t \sim 0.1$ s en la figura 7.

Si el choque es suficientemente fuerte para ralentizar la caída de material, la tasa de acreción se verá disminuida considerablemente. Esto junto con el agotamiento de material con poco momento angular se reflejará en una disminución en la tasa de acreción mostrada en tiempos 0.1 s $\lesssim t \lesssim 0.25$ s en la figura 7. Esto no parece aplicarse por completo a los modelos con enfriamiento más eficiente ($\beta 0.134$, $\beta 0.067$ y βIso) que muestran intensas variaciones en dM/dt luego de $t \simeq 0.1$ s, alcanzando valores superiores a los obtenidos durante el colapso del material con poco momento angular. Una vez que el choque pasa a través de toda la envolvente, el material se asentará en un disco de acreción alrededor del BH, cuya altura en el eje Z decrecerá al aumentar la eficiencia de enfriamiento. A partir de este momento, el material del disco podrá caer en el BH si hay transporte de momento angular. Esto puede observarse en la figura 7 para tiempos mayores que $t \sim 0.3$ s en donde la tasa de acreción ha disminuido cerca de un orden de magnitud respecto al máximo inicial.

Las variaciones intensas en dM/dt tienen que deberse a cambios en la manera en que el momento angular es transportado en el material. En particular, el modelo $\beta 0.134$ (línea azul del panel superior de la figura 7) muestra varios picos en dM/dt en tiempos $t \sim 0.2, 0.3,$ y 0.4 s. Esto sugiere la presencia de algún patrón cuasi periódico presente en la acreción del modelo $\beta 0.134$, lo cual estudiaremos más adelante en nuestro trabajo.

Eficiencia de enfriamiento y pérdida de energía

Los modelos con el enfriamiento dado por la ecuación (5) perderán energía en cada paso de tiempo a una tasa $du_i/dt = -u_i/t_{\text{cool}}$. Esta tasa de enfriamiento depende de la energía interna u_i en la posición (r, ϕ, z). Por lo tanto la pérdida de energía no será uniforme en el tiempo ni el espacio. Y si consideramos la contribución de

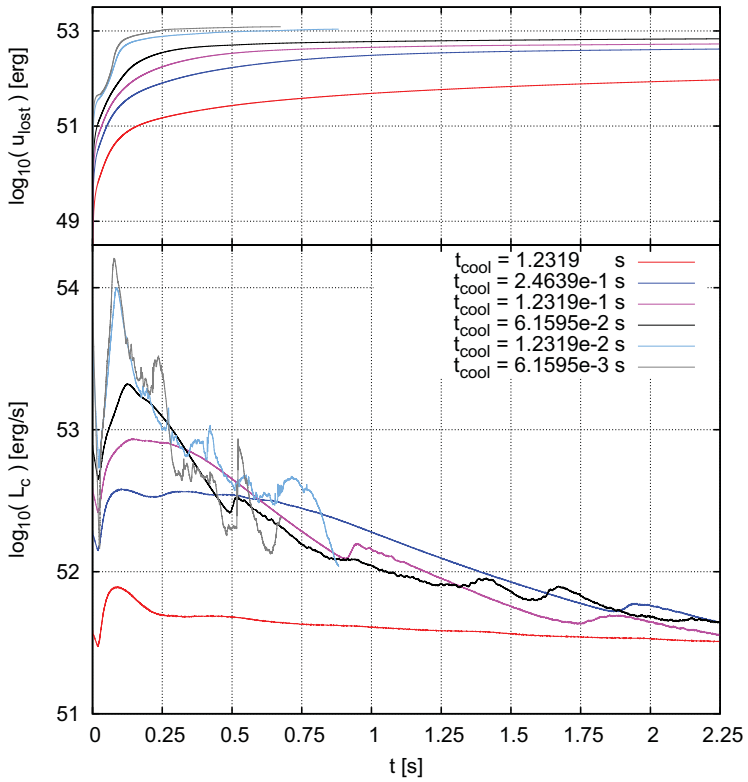

Figure 8: Tasa de pérdida de energía L_c (panel inferior) en erg/s para los modelos $\beta 13.4$ (línea roja), $\beta 2.68$ (línea azul), $\beta 1.34$ (línea rosa), $\beta 0.67$ (línea negra), $\beta 0.134$ (línea azul claro) y $\beta 0.067$ (línea gris). En el panel superior se muestra la evolución de la pérdida integrada de energía del sistema $u_{\rm lost}$.

cada partícula de SPH, podemos obtener la tasa de pérdida de energía total $L_c = \sum_j (-du_j/dt)_j$ a cada tiempo t. Nótese que L_c es positiva, lo cual nos permite asociar la tasa de pérdida de energía, con la luminosidad de neutrinos L_ν que se tendría en un disco de acreción con tiempo característico de enfriamiento $t_\nu = t_{\rm cool}$. El panel inferior de la figura 8 muestra las tasas de pérdida de energía L_c (que equivalen a la luminosidad de neutrinos esperada) para los distintos tiempos de enfriamiento utilizados en nuestras simulaciones. El máximo valor de L_c se obtiene para el modelo con enfriamiento más eficiente ($t_{\rm cool}$ más pequeño), llegando hasta $L_c \sim 10^{54}$ erg s^{-1} $= 1000$ foe s^{-1} [2]. La energía total perdida por el enfriamiento $u_{\rm lost} = \int L_c \, dt$ se muestra en el panel superior de la figura 8, cuyo máximo valor

[2] 1 foe $= 10^{51}$ erg, indica el orden de magnitud de la energía"fifty one ergs" por sus siglas en inglés

de $u_{\rm lost} \sim 10^{53}$ erg se alcanza por el modelo $\beta 0.067$ en un tiempo $t \lesssim 0.7$ s.

A medida que incrementa la eficiencia de enfriamiento, las variaciones en L_c se vuelven más intensas y frecuentes. Al comparar las figuras 7 y 8, podemos ver que la mayoría de las variaciones intensas mostradas en dM/dt coinciden en tiempo con las variaciones intensas en L_c. Y puesto que un rápido incremento en L_c es posible solamente cuando se tiene un importante aumento en la energía interna ($du/dt = -u/t_{\rm cool}$), debe haber ocurrido algún proceso que cause un aumento en u. Ya que las variaciones mostradas tanto en $\dot{M}$ como L_c aparecen al incrementar la eficiencia de enfriamiento, parece lógico asumir que la formación de estructura en el disco de acreción está produciendo estos cambios. Por lo tanto nos dedicamos a estudiar en detalle la morfología del disco para los modelos que mostraban incrementos intensos en estas cantidades, a fin de buscar la formación de estructuras, como brazos espirales.

Basados en las tasas de pérdida de energía obtenidas para nuestros distintos modelos y la suposición de que el enfriamiento por neutrinos tendrá una escala de tiempo característica t_ν dentro de los valores de $t_{\rm cool}$ que utilizamos, podemos esperar que al utilizar un enfriamiento más realista de neutrinos obtengamos luminosidades L_ν entre $1 \lesssim L_c \lesssim 2000$ foe s^{-1} (dependiendo de la temperatura y densidad local). En un modelo más realista, el enfriamiento eficiente por neutrinos estará restringido a las zonas más calientes y densas del disco (cerca del BH), y este mecanismo no será eficiente durante el colapso inicial de la envolvente, cuando el material aún no se acerca demasiado al BH. Esto podría afectar considerablemente las tasas de pérdida de energía al inicio de la simulación. Por otra parte, este trabajo no está considerando la posibilidad de que los neutrinos emitidos sean dispersados por el material con muy alta densidad ($\rho \gtrsim 10^{12}$ g cm^{-3}) donde la opacidad debida a partículas α se vuelve importante para los neutrinos (Shapiro & Teukolsky, 1983). Al considerar este efecto la luminosidad por neutrinos disminuiría y es probable que se evite que el material se enfríe de manera eficiente en estas regiones.

Escalas de tiempo características

Para cada modelo, se realizaron transformadas de Fourier a la evolución temporal de $\dot{M}$, L_c y la componente radial de momento en coordenadas cilíndricas P_r a fin de obtener información sobre frecuencias o escalas de tiempo características presentes en cada una de estas cantidades. Cualquier escala de tiempo característica se verá reflejada como un pico en la amplitud de la transformada de Fourier $|F(\nu)|^2$. Las figuras 9 y 10 muestran las transformadas de Fourier de L_c (línea roja), $\dot{M}$

(línea azul) y P_r (línea negra) para todos los modelos explorados en este trabajo (excepto L_c para los casos adiabático e isotermo) como función del inverso de la frecuencia $t = 1/\nu$ (en segundos).

Se puede observar de estas figuras que existe una transición en los picos en $|F(\nu)|^2$ que aparecen en $\dot{M}$ y L_c en los tiempos $t \simeq 0.2$ y 0.05 s a medida que se aumenta la eficiencia de enfriamiento. El pico en $t \simeq 0.05$ s comienza a desaparecer en la transformada de L_c a partir del modelo $\beta 2.68$. La transformada de L_c muestra picos menos intensos a escalas de tiempo entre ~ 0.02 s y ~ 0.001 s.

Al analizar la transformada de Fourier de P_r se puede notar que al incrementar la eficiencia de enfriamiento aparecen picos cada vez más grandes a tiempos característicos más pequeños. Esto indica que el disco de acreción podría tener una frecuencia de oscilación radial, la cual podría inducir la formación de inestabilidades en el mismo. En general, si analizamos las figuras 9 y 10 podemos ver que al aumentar la eficiencia de enfriamiento se incrementan el número de picos que aparecen a frecuencias más grandes (a tiempos característicos menores) en las transformadas de Fourier. Esto coincide con el aumento en la cantidad de variaciones intensas en $\dot{M}$ y L_c que se observa al aumentar la eficiencia de enfriamiento. También se puede ver que los modelos con el enfriamiento más eficiente son los únicos en mostrar variaciones intensas en escalas de tiempo más cortas que 10 milisegundos, y como se dijo en la sección anterior, estas variaciones parecen deberse a la formación de inestabilidades en el disco.

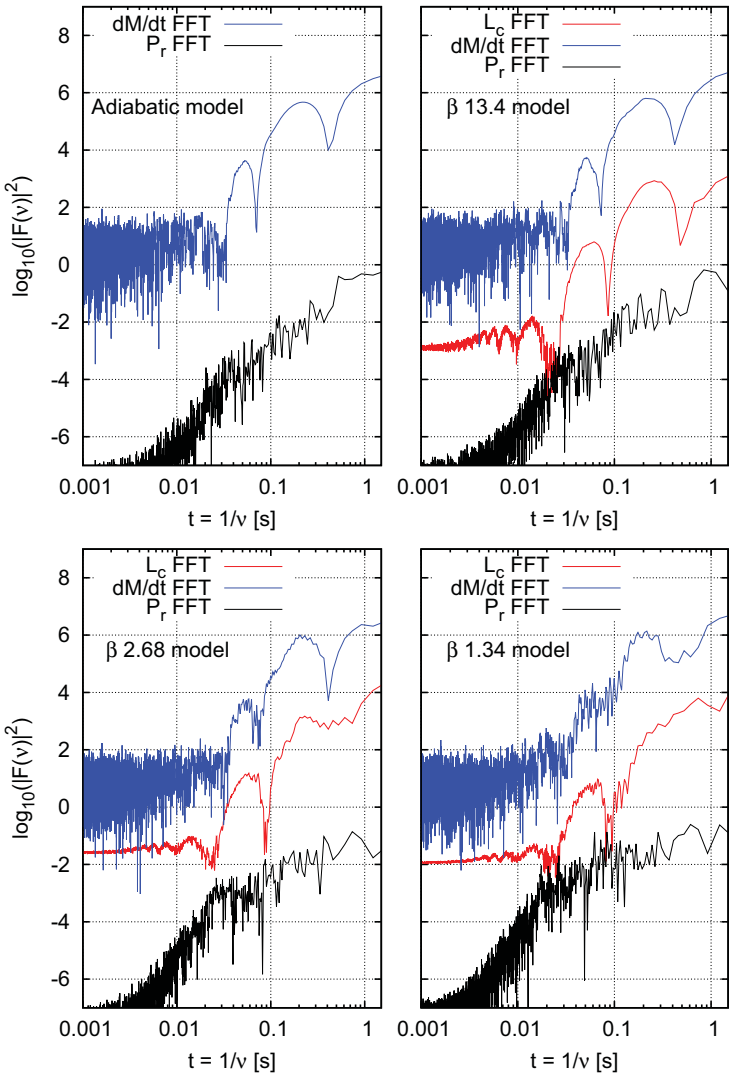

Figure 9: Amplitud normalizada de la transformada de Fourier $|F(\nu)|^2$ de la tasa de acreción $\dot{M}$ (línea azul), la tasa de pérdida de energía L_c (línea roja) y de la componente radial de momento lineal P_r (línea negra) en función del inverso de la frecuencia $1/\nu$ (en segundos), para los modelos adiabático, $\beta 13.4$, $\beta 2.68$ y $\beta 1.34$ (sólo se muestra la transformada de L_c para modelos con enfriamiento). El espectro obtenido para la tasa de acreción $\dot{M}$ muestra picos de frecuencias características a tiempos $t = 1/\nu \simeq 0.2$ y 0.05 s que también aparecen en el espectro de L_c. Al aumentar la eficiencia de enfriamiento se altera la posición e intensidad de estos picos y el modelo $\beta 1.34$ presenta un pico adicional en el espectro de P_r en $t \simeq 0.02$ s.

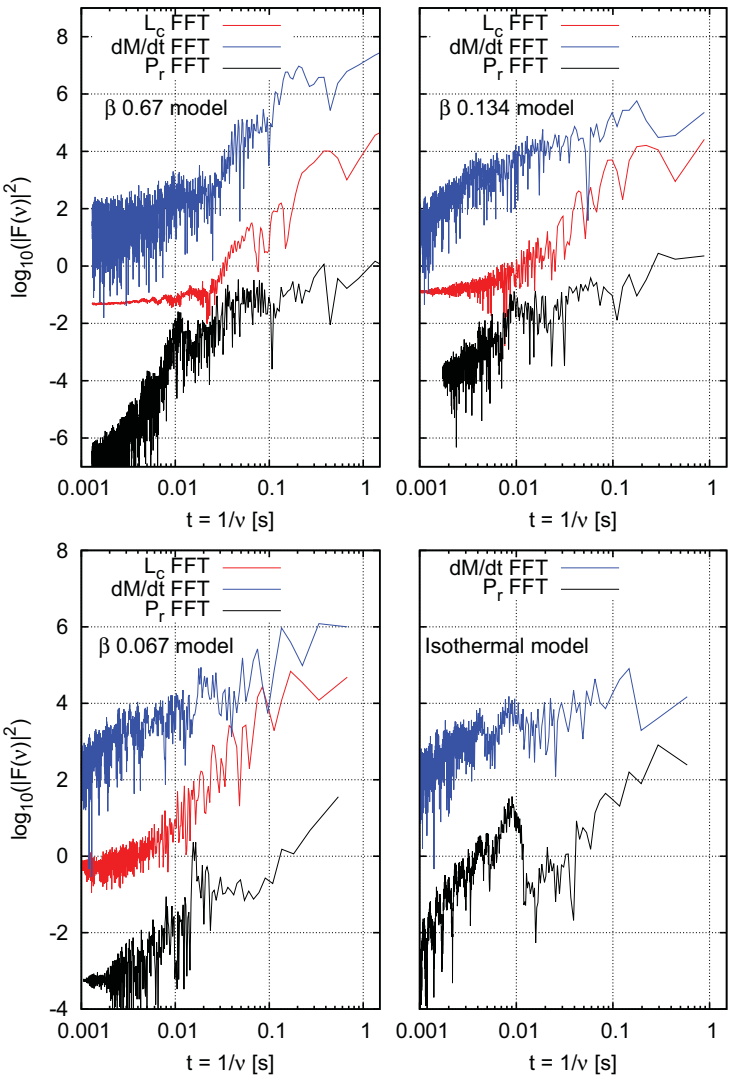

Figure 10: Amplitud normalizada de la transformada de Fourier $|F(\nu)|^2$ de la tasa de acreción $\dot{M}$ (línea azul), la tasa de pérdida de energía L_c (línea roja) y de la componente radial de momento lineal P_r (línea negra) en función del inverso de la frecuencia $1/\nu$ (en segundos), para los modelos $\beta 0.67$, $\beta 0.134$, $\beta 0.067$ e isotermo. Un enfriamiento más eficiente aumenta el número de picos intensos a altas frecuencias (escalas de tiempo más cortas). La presencia de intensos picos en P_r sugiere que el disco de acreción está oscilando.

Formación de estructuras en el disco

Para comprobar si la formación de estructuras en el disco de acreción es la responsable de las rápidas e intensas variaciones observadas en $\dot{M}$ y L_c, debemos buscar evidencia de la aparición de inestabilidades en el disco. En caso de que dichas inestabilidades se manifiesten como estructura espiral, podemos utilizar el método utilizado por Zurek & Benz (1986) para buscar la formación de inestabilidades no axisimétricas. Éste método consiste en realizar una transformada de Fourier a la distribución azimutal de masa $\Phi_M = \int \left[\int \rho(\phi, r, z)dz\right] r\, dr$ al tiempo t, definiendo la amplitud del modo m como:

$$C_m = \frac{1}{2\pi}\int_0^{2\pi} e^{im\phi}\Phi_M d\phi. \tag{9}$$

La magnitud de cada modo $|C_m|^2$ nos dará información acerca de la presencia de estructuras con sobre densidad que se repitan cada $2\pi/m$ radianes en el disco. Por lo tanto, la intensidad relativa $|c_m|^2 = |C_m|^2/|C_0|^2$ nos dará información sobre la intensidad (cantidad de masa) de m brazos espirales comparada con la masa integrada del disco C_0 al tiempo t. Al graficar la evolución en el tiempo de estos modos de Fourier podremos asociar incrementos importantes en su intensidad con eventos de formación de brazos espirales.

La figura 11 muestra la evolución en el tiempo de la intensidad de los modos $|c_m|^2$ ($m = 1, 2, 3, 4$), para los modelos $\beta 2.68$ (líneas rojas) y $\beta 1.34$ (líneas azules). Se puede ver que en ambos modelos, el modo $m = 2$ es el que alcanza el valor más alto durante todo el intervalo de tiempo ($|c_2|^2 \gtrsim 10^{-2}$). El máximo en el modo ($|c_2|^2$ coincide con el tiempo en que se observan los incrementos intensos en L_c y dM/dt mostrados en la figura 12. De hecho, el modo $m = 2$ comienza a incrementar antes de que las variaciones en la tasa de acreción y de pérdida de energía comiencen. Esto nos indica que el crecimiento de este modo $m = 2$ parece estar produciendo los incrementos en L_c y dM/dt. Para confirmar si en realidad se observan 2 brazos espirales en los tiempos donde $|c_m|^2 \gtrsim 10^{-2}$ podemos graficar un mapa de la densidad superficial $\sigma(r, \phi)$ integrada a lo largo del eje de rotación. La figura 13 nos muestra mapas de la densidad superficial del disco de acreción $\Sigma(r, \phi) = \int \rho(r, \phi, z)dz$ para los modelos $\beta 2.68$ (panel izquierdo) y $\beta 1.34$ (panel derecho) en los tiempos en que el modo $m = 2$ de cada una de estas simulaciones alcanza su máximo ($|c_m|^2 \gtrsim 10^{-2}$ en $t = 1.9$ s y 0.91 s respectivamente).

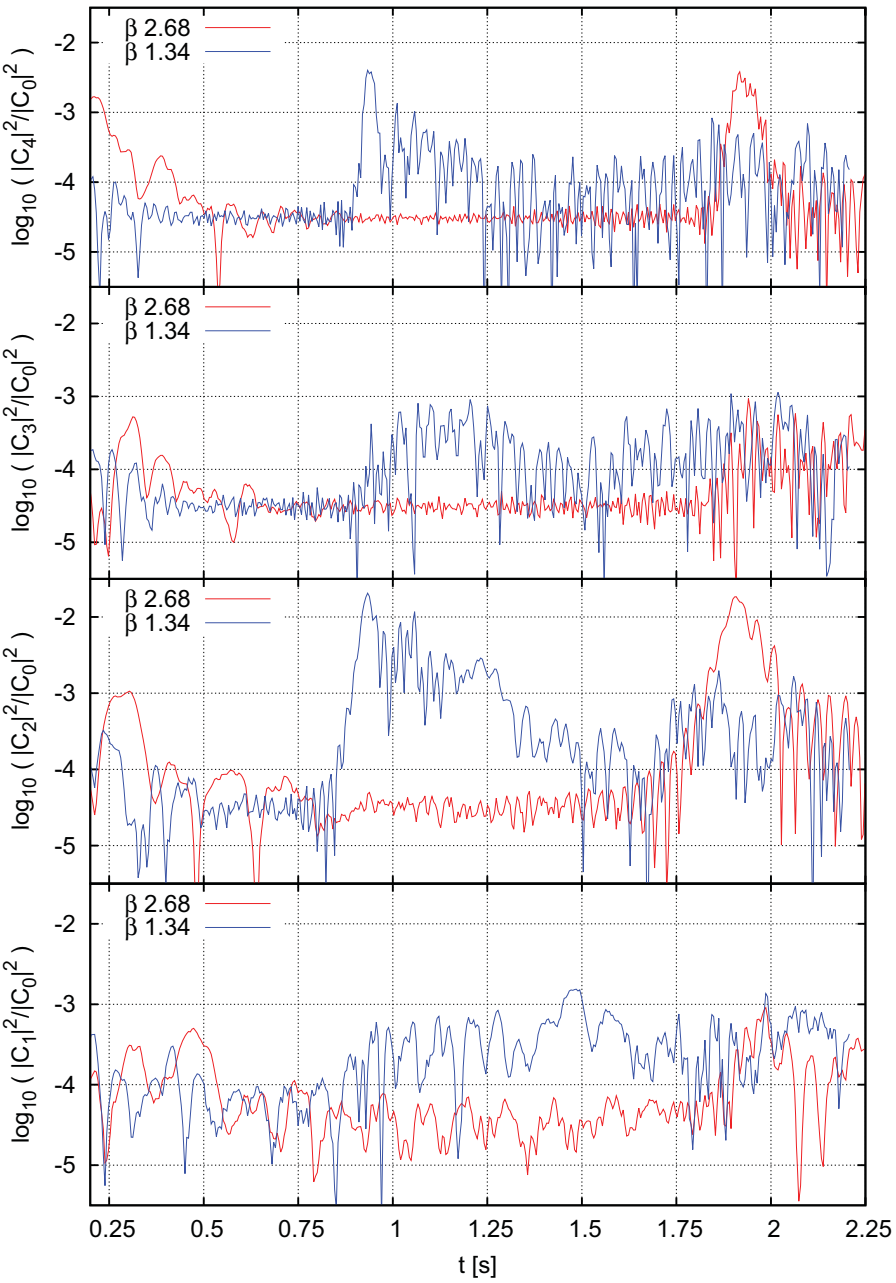

Figure 11: Evolución de la magnitud $|c_m|^2$ ($m = 1, 2, 3$ y 4) de la transformada de Fourier de la distribución de masa azimutal Φ_M de los modelos $\beta 2.68$ (líneas rojas) y $\beta 1.34$ (líneas azules). Ambos modelos presentan un aumento importante en el modo $m = 2$ en $t = 0.8$ y 1.75 s respectivamente, cuyo máximo se alcanza en ~ 0.9 y 1.9 s, volviéndose el modo más intenso por al menos un orden de magnitud.

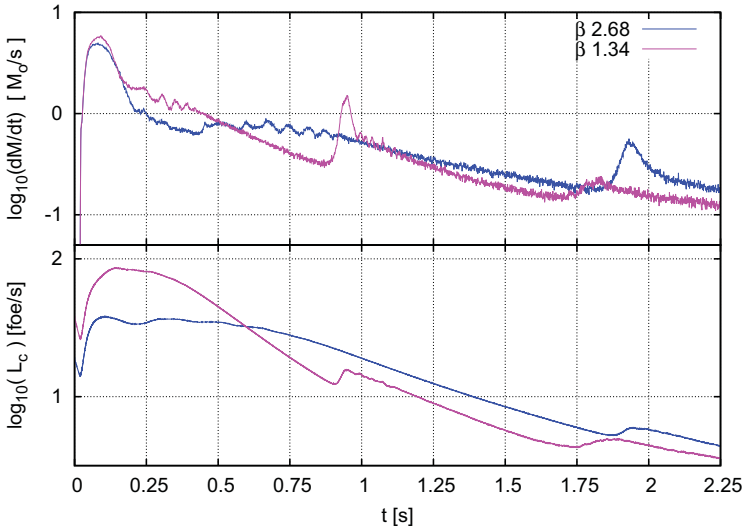

Figure 12: Evolución de las tasas de acreción de masa (panel superior) y de pérdida de energía (panel inferior) de los modelos $\beta 2.6$ (líneas azules) y $\beta 1.34$ (líneas rosas). El modelo $\beta 2.68$ tiene el parámetro de enfriamiento β más grande que presenta un incremento importante en $\dot{M}$ y L_c después de haberse formado el disco de acreción. El tiempo en el cual ocurre esta intensa variación en $\dot{M}$ y L_c disminuye con el tiempo de enfriamiento $t_{\rm cool}$.

Al aumentar la eficiencia de enfriamiento se obtienen variaciones más intensas y a tiempos más tempranos en la intensidad de los modos de Fourier $|c_m|^2$. Esto indica que se tiene formación de estructura a etapas más tempranas de la formación del disco de acreción y que además parecen ser más intensas (más masivas) comparadas con la masa total del disco. La figura 14 muestra la evolución de la intensidad $|c_m|^2$ de los modos $m = 1, 2, 3, 4$ para los modelos $\beta 0.67$ (izquierda) y $\beta 0.134$ (derecha). En el modelo $\beta 0.67$ aún puede identificarse con relativa facilidad el primer evento de formación de estructura en $t \simeq 0.5$ s que provoca la intensa variación en la tasa de acreción y de pérdida de energía mostrada en la figura 15. Sin embargo, para el modelo $\beta 0.134$ el escenario es un tanto diferente, y esto se debe a que la envolvente se enfrió demasiado antes de caer en el BH, por lo que la formación de estructura se dio tan pronto como se formó el disco de acreción. A pesar de esto hay un evento de formación de estructura en el modelo $\beta 0.134$ que se observa en todos los modos explorados y que puede asociarse con el fuerte incremento en dM/dt y L_c observado en $t \simeq 0.52$ s.

En la figura 16 se pueden observar mapas de la densidad superficial al tiempo $t = 0.52$ s para los modelos $\beta 0.67$ y $\beta 0.134$. En este tiempo es cuando se observa en ambos modelos un incremento en algunos de los modos de Fourier $|c_m|^2$ que puede asociarse a incrementos en dM/dt y L_c mostrados en la figura 15. Un resul-

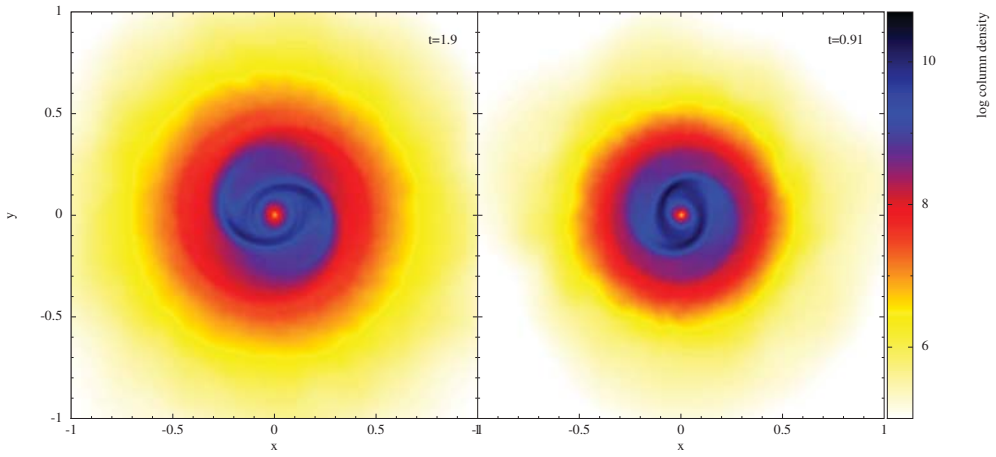

Figure 13: Densidad superficial del disco de acreción en g/cm^{-3} para los modelos $\beta 2.68$ (izquierda) y $\beta 1.34$ (derecha) en los tiempos en que sus modos $m = 2$ alcanzan $|c_m|^2 \gtrsim 10^{-2}$. Es fácil indentificar la presencia de dos brazos espirales alrededor del BH situado en el centro de la distribución.

tado importante de nuestras simulaciones es que al incrementar la eficiencia de enfriamiento, el disco de acreción, además de formar inestabilidades no axisimétricas es capaz de fragmentarse en grumos altamente densos y compactos. Estos grumos comienzan a observarse en el modelo $\beta 0.67$ luego de $\sim$ 1 s. El tiempo en que comienza la fragmentación depende de la eficiencia de enfriamiento, a mayor eficiencia, el disco se fragmenta con mayor rapidez luego de la formación del disco. Tal es el caso de los modelos $\beta 0.134$ y $\beta 0.067$ que presentan fragmentación justo desde el inicio de la formación del disco en $t \simeq 0.2$ s.

El fenómeno de fragmentación en un disco de acreción no es nuevo. Trabajos como el de Gammie (2001) y Rice et al. (2003) comenzaron el estudio de la fragmentación de discos con un enfriamiento como el que presentamos en la ecuación (5). En sus trabajos encontraron la existencia de un valor crítico para el parámetro de enfriamiento $\beta_{\text{crit}} \gtrsim 3$ para el cual, discos con $\beta < \beta_{\text{crit}}$ presentan fragmentación. Trabajos más recientes han encontrado una dependencia del valor de β_{crit} con la resolución de la simulación (Meru & Bate, 2011, 2012; Lodato & Clarke, 2011) y la implementación del enfriamiento en las ecuaciones de SPH (Rice et al., 2012). Sin embargo, en ninguno de estos trabajos se ha tratado de aplicar este tipo de enfriamiento a un escenario como el del Colapsar. El que no hayamos encontrado fragmentación para $\beta \gtrsim 1.34$ en nuestros discos de acreción masivos ($M_{\text{disk}} \gtrsim 1 M_{\odot}$), concuerda con el resultado obtenido por Rice et al (2003), en donde se observó que el valor crítico β_{crit} parece disminuir a medida que la masa del disco aumenta.

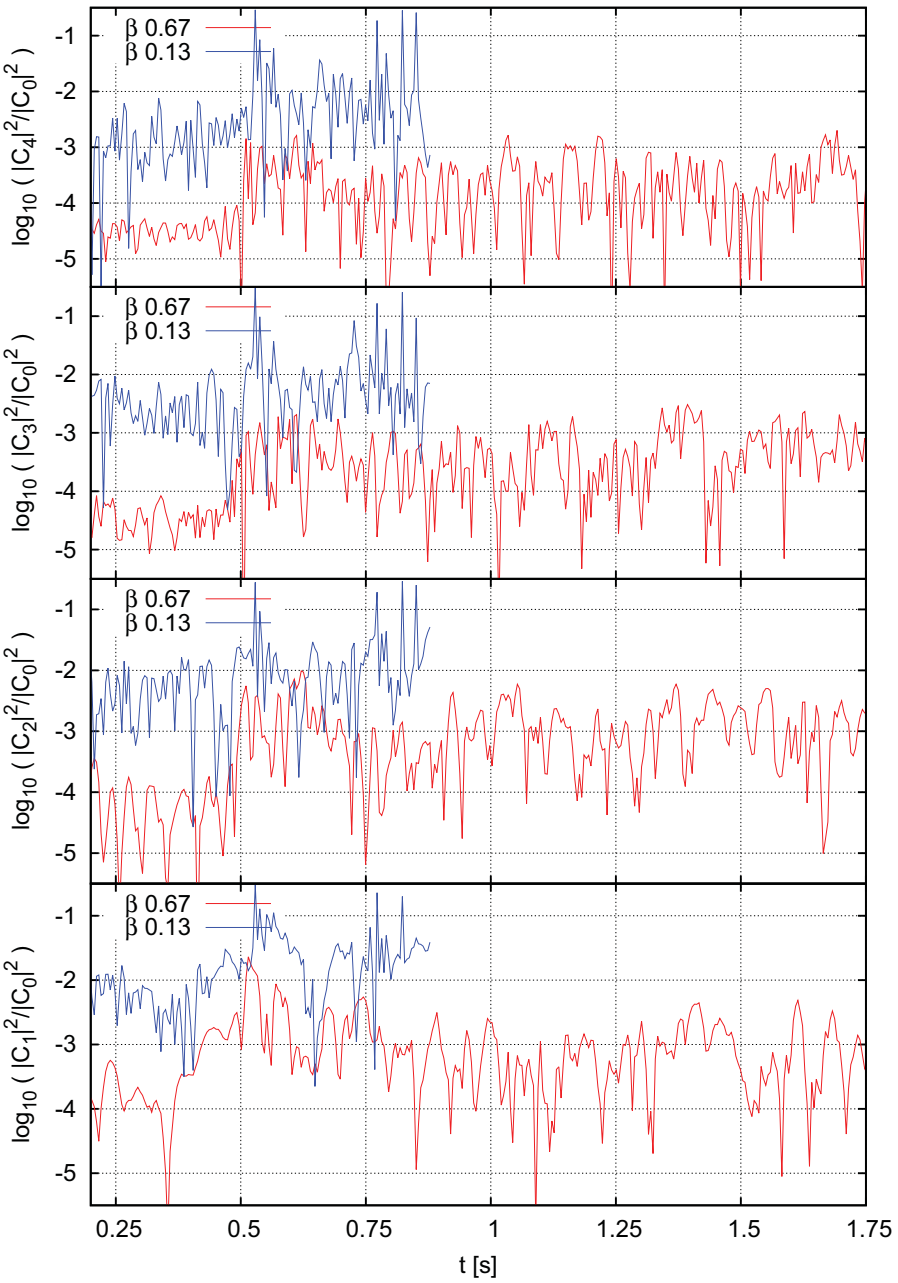

Figure 14: Evolución de la magnitud $|c_m|^2$ ($m = 1, 2, 3$ y 4) de la transformada de Fourier de la distribución de masa azimutal Φ_M de los modelos $\beta 0.67$ y $\beta 0.134$. El modelo $\beta 0.67$ muestra modos con valores $\lesssim 10^{-3}$ antes de $t \simeq 0.5$ s cuando el modo $m = 1$ crece hasta volverse el más importante. En cambio, el modelo $\beta 0.13$ tiene modos con valores mayores a 10^{-3} desde $t = 0.25$ s cuando el disco de acreción está recién formado. Todos los modos del modelo $\beta 0.134$ crecen considerablemente en $t \simeq 0.52$ s.

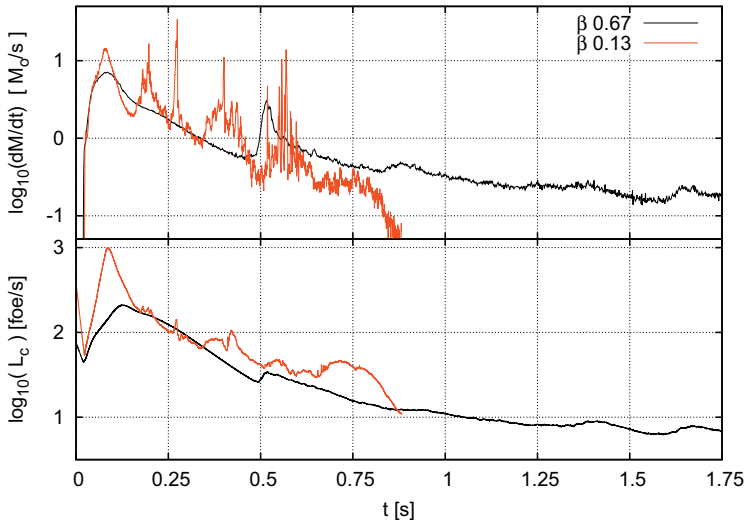

Figure 15: Evolución de las tasas de acreción de masa (panel superior) y de pérdida de energía (panel inferior) de los modelos $\beta 0.67$ (líneas negras) y $\beta 0.13$ (líneas anaranjadas). El aumento en L_c y dM/dt mostrado en el modelo $\beta 0.67$ en $t \simeq 0.5$ s, coincide con el máximo en el modo $m = 1$ de Fourier de la figura 14.

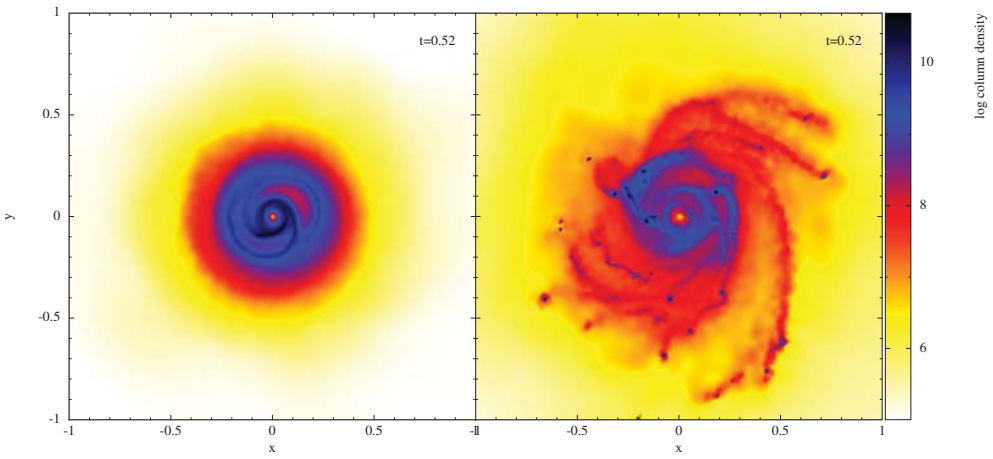

Figure 16: Densidad superficial del disco de acreción en g/cm^{-3} para los modelos $\beta 0.67$ (izquierda) y $\beta 0.134$ (derecha) $t = 0.52$ s cuando ambos muestran intensos crecimientos en uno o más de sus modos de Fourier. El modelo $\beta 0.134$ muestra intensa fragmentación del disco que comienza desde $t \sim 0.2$ s.

En el capítulo 3 se muestra un estudio más detallado de la formación de estructura de los modelos $\beta 2.68$, $\beta 1.34$, $\beta 0.67$, $\beta 0.134$ y $\beta 0.067$ que muestran variaciones intensas en dM/dt y L_c. El proceso que se siguió fue el mismo que se

mostró en este resumen pero en lugar de utilizar mapas de densidad se utilizaron mapas del parámetro de Toomre (Toomre, 1964) dado por:

$$Q_T = \frac{\kappa c_s}{\pi G \Sigma} \tag{10}$$

donde, $\kappa = (\partial W/\partial r)^{1/2}$ es la frecuencia epicíclica del movimiento de material en el disco[3], obtenida a partir de perturbaciones a primer orden en el potencial efectivo $W(r) = \phi(r) + l^2/2r^2$, $\Sigma(r, \phi)$ es la densidad superficial, c_s es la velocidad del sonido local y l es el momento angular. Al evaluar el parámetro de Toomre a lo largo del disco Q_T se pudieron distinguir las zonas de alta densidad y baja presión (velocidad del sonido) en donde el material se vuelve inestable gravitacionalmente.

Conclusiones

Se realizó un estudio exhaustivo del colapso de envolventes de $2.5\ M_\odot$ en un BH de $2\ M_\odot$ en el escenario del Colapsar, mediante simulaciones hidrodinámicas en 3D (SPH) que incluyen una ecuación de estado simplificada en la que el gas ideal domina sobre las demás componentes (radiación y un gas caliente de $e^{\pm}$). También incluimos una prescripción simplificada de enfriamiento basada en las tasas de emisión de neutrinos que se esperan a las densidades y temperaturas en el Colapsar, con los cuales pudimos explorar escenarios que iban desde el adiabático al isotermo, con el fin de identificar y caracterizar la morfología y la variación en la estructura inducida en el disco de acreción, resultado de la pérdida de energía por neutrinos. Con estas consideraciones, que discutiremos más adelante, encontramos características globales que probablemente estarían presentes en el colapso de núcleos estelares, las cuales pueden ser relevantes para determinar la dinámica y producción de energía que da lugar a la producción de GRBs cosmológicos a partir de la muerte de estrellas masivas.

A continuación resumimos los resultados más importantes:

• El parámetro más importante que determina la liberación de energía en el colapso de un núcleo estelar en el contexto del Colapsar es la tasa de rotación. Si es demasiado lenta, el núcleo colapsará esencialmente en caída libre y será acretado por el BH, liberando poca de la energía que tiene disponible (similar a un flujo de acreción de Bondi). Si la rotación es demasiado rápida, se formará un

[3]La frecuencia epicíclica indica la frecuencia característica de oscilación del disco cuando el potencial al que está sujeto es sometido a una perturbación lineal. Este análisis indica que el disco tendrá un movimiento tipo oscilador armónico caracterizado por la frecuencia epicíclica κ.

disco de acreción demasiado alejado del BH y el enfriamiento por neutrinos no será eficiente (esto debido a la alta sensibilidad del enfriamiento por neutrinos a la temperatura). La combinación de colocar la barrera centrífuga de material tan cerca como sea posible del BH pero sin permitir que sea acretada, es realmente importante para tener un evento exitoso. En 2D, esto ha sido previamente caracterizado (Lee & Ramirez-Ruiz, 2006; Lopez-Camara et al., 2009, 2010) y es igual de importante en 3D. En este sentido, el modelar al agujero negro a través del potencial de Paczynski-Wiita, es el ingrediente más importante en cuanto a efectos gravitacionales se refiere, y aunque el considerar un BH con rotación alteraría cuantitativamente el resultado, no se alteraría cuantitativamente esta conclusión.

• Al aumentar la eficiencia de enfriamiento, se tiene formación de estructura más abundante e intensa que a su vez produce intensas variaciones en la tasa de acreción y de pérdida de energía. La duración e intensidad de las variaciones se relaciona con la intensidad y el tiempo de vida de las estructuras colapsadas, ya sea estructura espiral o grumos. Estructuras muy densas (con parámetros de Toomre $Q \ll 1$) y con modos de Fourier $|c_m|^2$ intensos contienen una cantidad considerable de gas dentro de regiones relativamente compactas y pueden por lo tanto ser acretadas rápidamente, conduciendo a grandes variaciones en dM/dt y L_c. La frecuencia de estas variaciones aumenta con la eficiencia de enfriamiento, como se observa en las transformadas de Fourier de la evolución de $\dot{M}$ y L_c en las figuras 9 y 10.

• Las estructuras espirales que se forman son transitorias en naturaleza, formándose y desapareciendo en unos cuantos periodos orbitales. La intensidad de los modos $m = 1, 2$ es generalmente la más alta para enfriamientos no tan eficientes, pero al aumentar la eficiencia de enfriamiento ($t_{cool} \ll t_{disk}$) todos los modos ($m = 1, 2, 3, 4$) pueden alcanzar intensidades similares.

• Además de inducir cambios en dM/dt y L_c, la estructura formada en el disco es capaz de romper la simetría en la interacción gravitacional entre el disco y el BH. Esto puede verse en la figura 10, donde se observa que la componente radial de momento lineal P_r desarrolla frecuencias características indicando oscilaciones en el disco. La frecuencia de estas oscilaciones aumenta con la eficiencia de enfriamiento. Tales oscilaciones en P_r son fácilmente observadas al observar por separado la evolución de las componentes del momento lineal P_x y P_y. Al forzar al BH a permanecer fijo en el centro de la distribución original no podemos concluir nada concreto de este efecto, pero claramente estas oscilaciones podrían tener consecuencias importantes en la dinámica del sistema, lo cual se discutirá más adelante.

• La pérdida de energía integrada de nuestros modelos va de 10^{51} a 10^{54} ergs. Esta energía representa solamente la energía que podría ser emitida por neutrinos. Por su parte, la energía de acreción integrada $E_{\rm acc} = \int \dot{M}c^2 dt$ va de 10^{54} a 3×10^{54} erg. Este par de resultados indican que la energía necesaria para producir un GRB está presente en el sistema. El cómo se produce el jet relativista y el GRB a partir de ella es un asunto diferente. Pero es claro que la variabilidad del jet producido dependerá del mecanismo que genera dichas variaciones en la producción de energía.

• La formación y destrucción de estructuras, en particular brazos espirales y grumos, no solo es transitoria sino recurrente de manera ordenada. Esto puede verse al observar la evolución temporal de dM/dt y L_c (Figs.7 y 8) en donde se muestra que al incrementar la eficiencia de enfriamiento, el intervalo entre episodios de incremento de estas cantidades se reduce. Debido a que el disco está perdiendo masa por la acreción, la intensidad de estos episodios suele ser menor (salvo en el caso de acreción de grumos).

• De acuerdo con nuestra implementación del enfriamiento, Ec. (5), la energía interna promedio por unidad de masa del disco de acreción $u_M = U/M_{\rm disk}$ está directamente relacionada con la tasa de pérdida de energía L_c mediante:

$$u_M = \frac{U}{M_{\rm disk}} = \frac{1}{M_{\rm disk}}\left(\sum_j u_{i,j}\right) = \frac{t_{\rm cool}L_c}{M_{\rm disk}}, \tag{11}$$

donde $u_{i,j}$ es la energía interna de la partícula j y $M_{\rm disk}$ es la masa del disco de acreción al tiempo t. Esto hace que u_M contenga información de la pérdida de energía y la tasa de acreción (que determina la masa restante del disco). La evolución de u_M como función del tiempo normalizado $t/t_{\rm cool}$, muestra algunas propiedades intrínsecas de nuestro escenario de enfriamiento.

La figura 17 muestra la evolución como función de $t/t_{\rm cool}$, de la energía interna promedio por unidad de masa normalizada a su valor inicial $u_M/u_{M,0}$ ($u_{M,0} = u_M(t=0)$) para todas las simulaciones que utilizaron nuestra implementación de enfriamiento. Todos los modelos muestran la disminución inicial en u_M debida al enfriamiento y al colapso de la envolvente (la cual se expande durante la caída), seguida de un intenso incremento debido al choque (que se aleja del BH) producido por el material caliente que alcanza su barrera centrífuga cerca del BH. Estos dos eventos se producen en tiempos $t \lesssim t_{dyn}$ y por lo tanto los modelos con $t_{\rm cool} \gtrsim t_{\rm dyn}$ comenzarán a acretar material y formarán un disco de acreción en tiempos $t \lesssim t_{\rm cool}$. Mientras que modelos con $t_{\rm cool} \ll t_{\rm dyn}$ formarán un disco de acreción hasta después de haber transcurrido varios tiempos de enfriamiento.

Estos últimos modelos son intrínsecamente diferentes y por lo tanto no se espera que tengan el mismo comportamiento general que el resto de los modelos. Sin embargo, los modelos con $t_{\rm cool} \gtrsim t_{\rm dyn}$ muestran un incremento en u_M a un tiempo $7.2 > t/t_{cool} > 8.2$, que corresponde al momento en que se tiene el primer evento de formación de estructura observado en los modelos $\beta 2.68$, $\beta 1.34$ y $\beta 0.67$. La excepción a esta regla es el modelo $\beta 13.4$, que no muestra ningún aumento significativo en u_M ni eventos de formación de estructura.

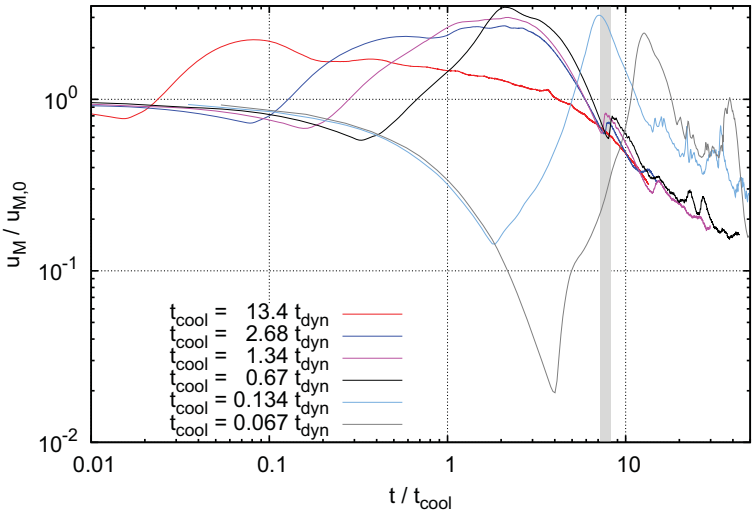

Figure 17: Energía interna total por unidad de masa u_M como función de $t/t_{\rm cool}$ para los distintos modelos de enfriamiento. La zona sombreada de color gris ($7.2 \leq t/t_{\rm cool} \leq 8.2$) abarca los tiempos en que los modelos con $t_{\rm cool} \gtrsim t_{\rm dyn}$ muestran el primer evento de formación de estructura en el disco, el cual se observa como un incremento en u_M a excepción del modelo $\beta 13.4$ (línea roja).

Esta excepción puede explicarse al considerar la velocidad del sonido mínima promediada azimutalmente $c_{s,\rm min} = \min(c_s(R), (0.05 < R/R_s < 1)$, a partir de la cual podemos estimar un límite superior al tiempo $t_{\rm pert} = R_s/c_{s,\rm min}$, que le tomaría a una perturbación en la presión el transmitir su información a través del disco de tamaño R_s. En particular, esta perturbación podría ser inducida por el mecanismo de enfriamiento. Entonces, si la escala de tiempo de enfriamiento es más chica que esta escala de tiempo de perturbación $t_{\rm pert}$, existe una región en el disco de acreción en donde cualquier disminución importante en la presión (producida por una reducción en la energía interna) podría no ser inmediatamente compensada por procesos hidrodinámicos antes de que el gas sufra un colapso. El modelo $\beta 13.4$ se encuentra en la situación opuesta, dado que en todo momento

se satisface que $t_{\rm cool} > 2\ t_{\rm pert}$ (como se ve en la figura 18) y por lo tanto no se espera que haya ningún evento de formación de estructura mientras la condición $t_{\rm cool}/t_{\rm pert} \lesssim 1$ no se satisfaga.

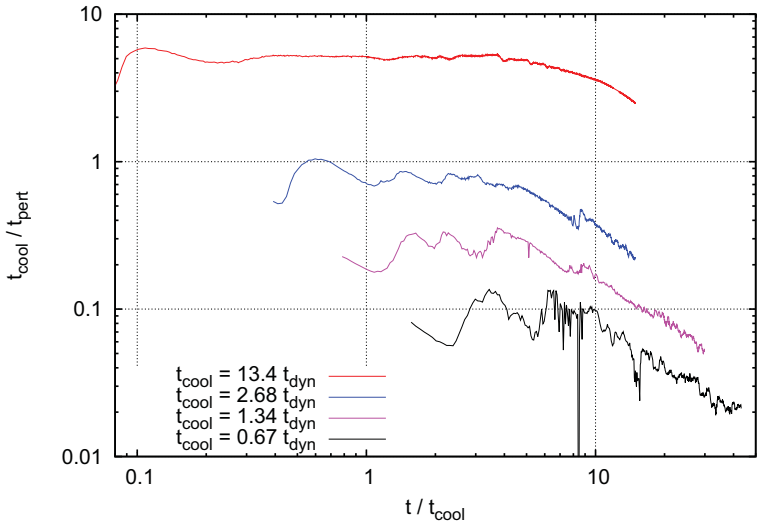

Figure 18: Evolución de la razón $t_{\rm cool}/t_{\rm pert}$ para los modelos β13.4, β2.68, β1.34 y β0.67. Los modelos con enfriamiento más eficiente tienen $t_{\rm cool}/t_{\rm pert} < 1$ y por lo tanto son capaces de desarrollar inestabilidades debidas a formación de estructura.

Sin duda hay lugar para mejorar el trabajo que aquí presentamos y a continuación discutiremos brevemente los puntos principales:

• En primer lugar, se requiere una implementación más detallada y exacta del enfriamiento de neutrinos y de la ecuación de estado para obtener resultados más realistas. En particular la fuerte dependencia de la pérdida de energía por neutrinos de la temperatura $T/10^{11}$ K, hace que hasta un pequeño gradiente de temperatura en el disco (que estará determinado por la rotación del material y la EoS) produzca una drástica disminución en la emisión de neutrinos lejos del BH. En nuestra implementación de enfriamiento, si bien la pérdida de energía depende proporcionalmente de la energía interna (y por lo tanto del gradiente de temperatura del disco), el tiempo de enfriamiento $t_{\rm cool}$ es el que determina si el enfriamiento será eficiente o no. Este es tal vez uno de los puntos que requiere mayor investigación a fin de obtener resultados más realistas para el modelo de Colapsar.

• Los resultados obtenidos indican que la interacción gravitacional entre el disco y el BH no siempre nos permitirá asumir que el último se encuentra inmóvil.

En cambio, éste oscilará con el disco como en un sistema binario. Esto tiene dos consecuencias importantes: primero, la tasa de acreción podría modificarse de alguna forma, ya que los grumos y estructuras espirales formadas no serían acretados y destruidos de la misma manera, y segundo, el lugar de la acreción y de potencial formación del jet que se producirá, se encontrará en movimiento continuo dentro del disco y la envolvente estelar, un análisis cuantitativo de este efecto es claramente necesario y podría tener consecuencias importantes, ya que se ha asumido comúnmente que la inyección de energía que produce el flujo relativista hacia el exterior de la estrella, se mantiene inmóvil en el centro de la estrella.

• Aunque el potencial PW captura las características más importantes de la Relatividad General en cuanto a la dinámica de la acreción, un tratamiento completamente relativista sería deseable. En particular, no sólo los efectos de un BH con rotación (de Kerr) sino del campo producido por el mismo flujo, el cual, como hemos visto es capaz de producir un jalón importante en el objeto central. También sería deseable seguir al menos de forma aproximada, la formación del BH a partir del colapso de la parte interna del núcleo. Esto podría resultar en una tasa de acreción más realista en las primeras etapas del colapso y podría alterar la distribución de masa del disco formado alrededor del BH.

• Finalmente, un tratamiento correcto de los neutrinos debería incluir los efectos del transporte de neutrinos y la inyección de energía que pueden tener en regiones de alta densidad ($\rho \gtrsim 10^{11}$ g cm^{-3}) debido a dispersión inelástica con nucleones libres y partículas α. Estos efectos podrían inhibir o limitar la formación de estructura en el disco, aún en el régimen de dispersión elástica.

La gran variedad de comportamientos vistos aquí, muestra que el realizar estudios en 2 dimensiones del colapso de núcleos estelares es insuficiente para explicar en su totalidad el comportamiento general y la variabilidad que podría tenerse en estos sistemas, aún cualitativamente. Puesto que sabemos que no todas las estrellas que colapsan producirán un GRB, es importante identificar cuales son las condiciones que llevan a su producción. Resultados preliminares en la interacción gravitacional del BH y el disco nos llevan a pensar que esto podría ser de importancia en el comportamiento y evolución de los discos de colapsares y será tema del trabajo a futuro.

Chapter 1

Introduction

Despite collapse and accretion of rotating material is a common phenomena in astrophysics, its complexity makes its study very difficult. It implies the formation of an accretion disk, whose structure, stability and evolution has important implications for topics such as Gamma-Ray bursts (GRBs), Young Stellar Objects and Active Galactic Nuclei. When extreme temperatures and densities are reached in such systems, complex cooling/heating processes take place and non-trivial equations of state (EOS) must be used (Lee et al., 2005). This makes hydrodynamics calculations difficult (and slow) and translates into a very reduced number of results derived from 3D models which include rotation effects, self-gravity and the instabilities that might come from them. These accretion processes are able to produce huge amounts of energy on short time scales.

The amount of energy that can be obtained from accretion directly depends on the size of the accreting object. This can be seen by estimating an upper limit for the available energy of the infalling matter, whose potential energy is completely transformed into heat which is radiated as photons or an energetic particle[1]. Thus, when infalling matter approaches the accreting object of radius R_*, the available potential energy per unit mass $\varepsilon_g \sim GM_*/R$ will increase as $R \to R_*$. This implies that the smaller the size of the accreting object, the higher the amount of energy that can be obtained. Therefore, assuming a steady accretion rate $\dot{m}$ onto a Schwarzschild black hole (Schwarzschild, 1916) with a gravitational radius

[1] By considering a 100% efficiency in the conversion of potential energy into heat and then radiation, we will obtain the maximum amount of energy available from accretion.

$R_* = r_g = 2GM_{\rm BH}/c^2 = 5.909 \times 10^5$ cm and mass $M_* = M_{\rm BH} = 2\ M_\odot$, the luminosity produced by accretion can be written as:

$$L_{\rm acc} = \frac{GM_{\rm BH}\dot{m}}{R_*} \sim 10^{54} \left(\frac{\dot{m}}{M_\odot\ {\rm s}^{-1}} \right)\ {\rm erg\ s}^{-1} \tag{1.1}$$

Therefore, for a given accreting object, the obtained luminosity would be determined by the accretion rate, which in turn depends on the efficiency with which material gets close to the black hole (BH). For this to happen, there must be a cooling mechanism able to convert the internal energy into radiation or emission of some energetic particle. Without any cooling mechanism, infalling material near the BH will become too hot and its pressure could halt the infall of more material, preventing the accretion and diminishing the accretion luminosity[2]. Thus, the more efficient the cooling process, the more material could reach the accreting region. This would raise the accretion rate and therefore, the produced luminosity. It is not clear that (1.1) holds for accretion onto a BH since R_* does not refer to a hard surface but to a region into which matter can enter and never escape. Part of the accretion energy could enter such region and will never be observed, therefore, such uncertainty is parametrized by a dimensionless quantity η, accounting for the efficiency of the accretion energy produced:

$$L_{\rm acc} = \eta \dot{m} c^2 \tag{1.2}$$

We can estimate an upper limit to this efficiency parameter η from equation (1.1), by considering R_* as the closest position to the BH where all radiation emitted can still escape the BH (when not emitted directly towards it). Certainly material getting to the event horizon $r_g = R_* = 2GM_{\rm BH}/c^2$ will not be able to emit much of its energy outwards, but by considering R_* as the position of the innermost stable circular orbit $r_{\rm isco} = 3\ r_g$ we can guarantee that most of the energy (radiation) emitted outwards could still escape the BH potential. Thus, the maximum luminosity that can be obtained from accretion of material falling at a rate $\dot{m}$ onto a BH is:

$$L_{\rm acc,max} \simeq \frac{GM_{\rm BH}\dot{m}}{3r_g} = \frac{GM_{\rm BH}\dot{m}}{GM_{\rm BH}/c^2} = \frac{\dot{m}c^2}{6} = 0.16\ \dot{m}c^2\ {\rm erg\ s}^{-1}. \tag{1.3}$$

[2]The duration of such scenario will depend on the characteristic time scale it takes the material to cool down (lose energy) and considerably decrease the pressure which prevents further material to be accreted.

Thus, it is safe to say that infalling material will transform its potential energy into heat and radiation with an efficiency not bigger than $\eta \sim 0.1$. So, in order to produce $\sim 10^{52}$ erg s^{-1} there should be an accretion rate greater than $\sim 10^{-1} M_\odot$ s^{-1}. Such accreting rates allow us to estimate the density near a 2 $M_\odot$ BH by considering that material is being accreted radially at a velocity $\sim c$, at a rate:

$$\dot{m} \sim 4\pi\rho R_*^2 c \qquad \Rightarrow \qquad \rho = \frac{\dot{m}}{4\pi R_*^2 c} \gtrsim 10^9 \text{ g cm}^{-3} \tag{1.4}$$

This implies that at such accretion rates, Thomson's optical depth is $\tau_{\rm T} \sim n^{1/3} R_* \sim 10^{16}$, and photons are incapable of escaping, making radiative cooling inefficient. In this case, if no other cooling mechanism is present, there is a limit on the luminosity that can be obtained from quasi-spherical accretion onto a BH given by the Eddington limit $L_{\rm Edd} = 4\pi G M c\, m_p/\sigma_{\rm T} = 1.3 \times 10^{38}$ erg s^{-1}. This limit is obtained by considering Thomson scattering, which results in an Eddington luminosity several orders of magnitude below the accretion luminosity from (1.1). But if we consider neutrino emission as the cooling mechanism taking away internal energy from the material, we have a cross section associated to neutrino interactions many orders of magnitude smaller than the one for photons. This translates into a higher Eddington limit, which allows higher accretion rates. For example, using the cross section for neutrino pair production ($\sigma_\nu \propto E_\nu^2$), the Eddington limit can be rewritten as:

$$L_{\text{Edd},\nu} = 8 \times 10^{53} \left(\frac{E_\nu}{50 \text{ MeV}}\right)^{-2} \left(\frac{M}{M_\odot}\right) \text{ erg s}^{-1}, \tag{1.5}$$

where M is the mass of the accreting object and E_ν the energy of the neutrinos. Assuming all mass is converted efficiently into neutrino energy, this luminosity has an associated accretion rate (Lee & Ramirez-Ruiz, 2007):

$$\dot{M}_{\text{Edd},\nu} = \frac{L_{\text{Edd},\nu}}{c^2} = 0.44 \left(\frac{M}{M_\odot}\right) \left(\frac{E_\nu}{50 \text{ MeV}}\right)^{-2} M_\odot \text{ s}^{-1} \tag{1.6}$$

This neutrino luminosity yields an estimate to the blackbody temperature obtained if $L_{\text{Edd},\nu}$ comes from a sphere of radius R_*:

$$T_{\mathrm{Edd},\nu} = \left(\frac{L_{\mathrm{Edd},\nu}}{4\pi R_*^2 \sigma_\nu}\right)^{1/4} \sim 45 \left(\frac{M}{M_\odot}\right)^{-1/4} \left(\frac{E_\nu}{50\ \mathrm{MeV}}\right)^{-1/2} \mathrm{MeV}$$
$$\sim 5 \times 10^{11} \left(\frac{M}{M_\odot}\right)^{-1/4} \left(\frac{E_\nu}{50\ \mathrm{MeV}}\right)^{-1/2} \mathrm{K} \tag{1.7}$$

Then for an accreting $1\ M_\odot$ BH we have $T \sim 5 \times 10^{11}$ K for neutrinos with $E_\nu = 50$ MeV. Although we only considered the neutrino pair creation case, the estimates will vary little when considering coherent scattering of neutrinos by nuclei and/or free nucleons. The main difference resides in the energy scaling ($\sigma_\nu \propto E_\nu$ on those cases). From here we can effectively say that for accretion rates able to produce luminosities $\sim 10^{53}$ ergs s^{-1}, the temperatures and densities must be sufficiently high ($\rho \simeq 10^{10}$ g cm$^{-3}, T \simeq 10^{11}$ K) for photons to be trapped and neutrinos to be abundantly emitted, becoming the main cooling source. Although this calculations were made assuming a spherically symmetric accretion flow, they give a good estimate of the characteristic densities and temperatures reached on accretion disks with similar accretion rates.

These simple calculations show why neutrinos are thought to be one of the main mechanisms responsible for powering Gamma-ray Bursts (GRBs), whose isotropic luminosities range between $10^{49} - 10^{52}$ erg s^{-1}, making them the most luminous events in the Universe. Along this chapter we'll point out the most important features of GRBs as well as the theory which explains them more accurately. Eventually we will focus on studying one of the most accepted "inner engines" in charge of providing the energy required to produce the GRB, namely the Collapsar model.

1.1 GRB's Main Features

GRBs are bright flashes of radiation with spectral energy distributions peaking at γ ray band (~ 100 keV, see figure 1.1) (Fishman & Meegan, 1995). The duration of such events goes generally from a fraction of a second up to several hundred seconds, although there have been events with durations of several thousand seconds (Levan et al., 2014). Their isotropic luminosity ranges from $10^{49} - 10^{52}$ erg/s, which makes GRBs the most luminous events in the Universe observed to date. However there is evidence showing that radiation from GRBs is highly beamed

in a jet with an opening angle of a few degrees ($\theta_o \lesssim 10^\circ$, Frail et al., 2001; Panaitescu & Kumar, 2001; Piran et al., 2001), which implies that the integrated energy liberated from such events is of the order of 10^{51} erg, comparable with the energy release in a Supernova (SN).

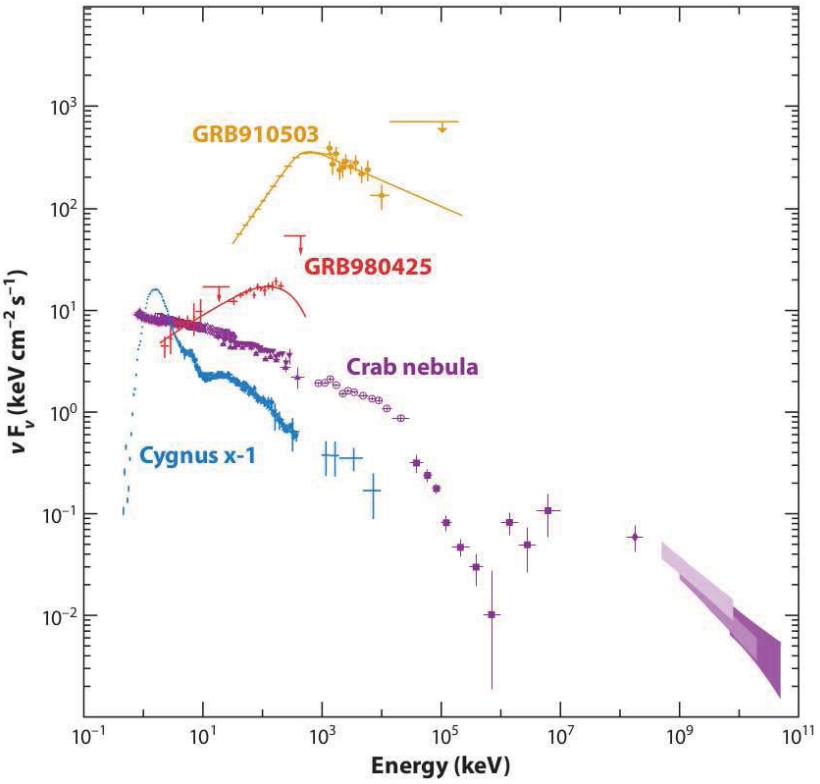

Figure 1.1: Spectral energy distribution (SED) of two GRBs from Kaneko et al. (2007, 2008) together with the Crab Nebula pulsar (Kuiper et al., 2001) and the galactic BH candidate Cygnus X-1 (McConnell et al., 2002). GRB's SEDs peak at higher energies than the other high energy events. Figure from Gehrels et al. (2009).

The high energies produced and the variability observed in time scales as short as milliseconds (see figure 1.2) suggest the presence of a compact object (such as a Neutron Star (NS), or a BH) in the production mechanism of such events. Up to date, despite the lack of direct evidence, it is widely accepted that GRBs are the result of intense events of hypercritical accretion onto compact objects as NSs or BHs, where a huge amount of energy is released, generating the electro-

magnetic radiation observed (see Piran, 2004; Nakar, 2007; Lee & Ramirez-Ruiz, 2007; Gehrels et al., 2009 for detailed reviews).

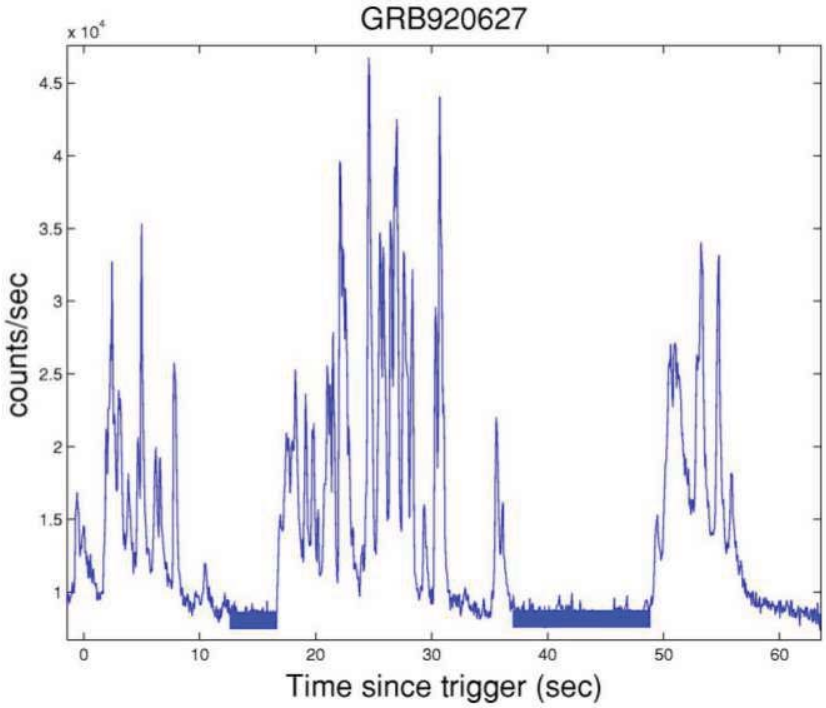

Figure 1.2: Light curve of GRB 920627. It is clear the presence of variability with time scales δt ranging from fractions of a second to several seconds. Image from Piran (2004). δt is determined by the width of the variations.

GRBs are generally followed by intense emissions with wavelength ranging from X rays to radio. It is because of this afterglow emission that absorption lines can be detected in GRB's spectra and thus, it is possible to determine the distance to the source (van Paradijs et al., 2000). It has been found that short duration GRBs (sGRB), lasting less than a second, are generally produced at $z \leq 1$, meanwhile long duration GRBs (lGRB) are produced at $z \simeq 1 - 5$ or higher, competing with quasars as the farthest observed objects (Berger, 2011; Levesque et al., 2014). It is also observed that short bursts generally have harder (more energetic) spectrum than long bursts (Kouveliotou, 1993). Both GRBs produce directed fluxes of relativistic matter with kinetic isotropic luminosities exceeding 10^{53} erg s^{-1}, making them the most luminous events known (Gehrels et al., 2009). Figure 1.3 shows the apparent isotropic energy from a sample of both long and short GRBs as a function of redshift (bottom axis) and duration in seconds (color bar). This energy is

calculated by assuming isotropic emission, and by the redshift measured from their afterglow. T_{90} accounts for the time during which the cumulative counts increase from 5% to 95% above background, thus encompassing 90% of the total GRB counts, and it is used for GRB classification as short or long (if $T_{90} \lesssim 2$ s then we have a short GRB, and vice versa, Kouveliotou, 1993).

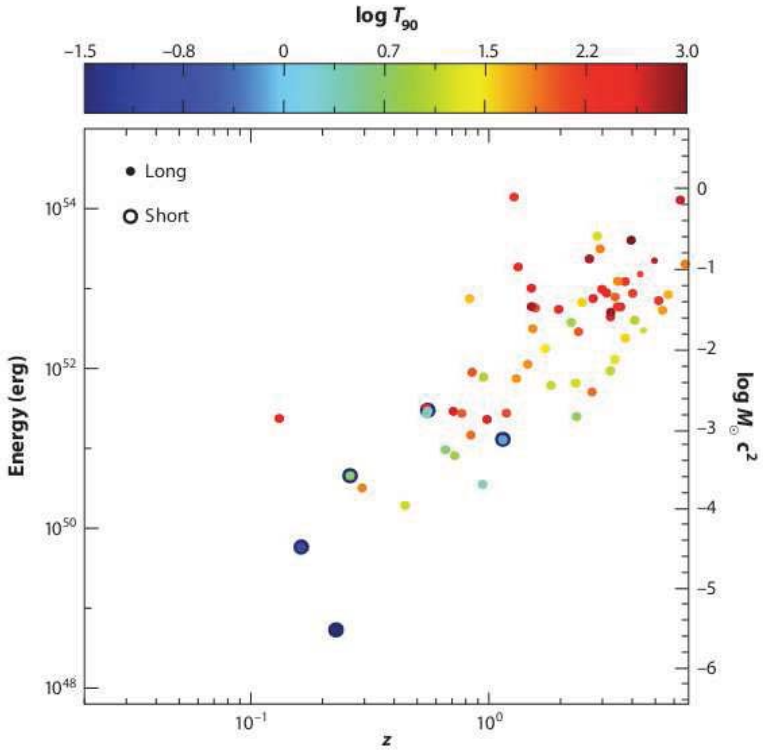

Figure 1.3: Apparent isotropic γ-ray energy as a function of redshift and observed duration. The energy is calculated assuming isotropic emission in a common comoving bandpass for a sample of short and long GRBs with measured redshifts. This spread in the inferred luminosities obtained under the assumption of isotropic emission may be reduced if most GRB outflows are jet-like. A beamed jet would alleviate the energy requirements, and some observational evidence does suggest the presence of a jet. From Gehrels et al. (2009).

On the whole, the hosts of sGRBs, and by extension the progenitors, are not drawn from the same parent population of lGRBs. The former appear to be more diffusely positioned around galaxies, and their associated hosts contain a generally older population of stars (Lee & Ramirez-Ruiz, 2006; Berger, 2011). Meanwhile lGRBs are generally associated to galaxies with intense star formation (generally

found at $z > 1$) and in occasions they can be associated to SN observations (with no H lines, i.e. type Ib or Ic) taking place at the same galaxy and detected a few days after the initial GRB, when the afterglow luminosity has decreased enough to stop masking the SN spectrum. The observation of GRB980425 (named after the year month and day of the event) in conjunction with the unusual SN1998bw (Galama et al., 1998), was the first of these associations between GRBs and SNe. The reviews by Woosley & Bloom (2006) and Hjorth & Bloom (2012) show the existing evidence supporting the link of long GRB at low redshift with type Ic SNe.

Although not all GRB's observational features can be explained with a single theoretical model, there is an agreement in that such events are produced due to the dissipation of the kinetic energy of a relativistic outflow (fireball model; Piran, 2004; Gehrels et al., 2009). In this scenario, the GRB is produced by internal dissipation (within the relativistic outflow), meanwhile the afterglow is produced by external shocks of the relativistic flux with circumburst material or interstellar medium surrounding the "inner engine". This fireball model is based on a list of minimum requirements or "ingredients" needed to produce a GRB, which we present below:

- Relativistic material: Practically all GRB models involve material moving at relativistic velocities with Lorentz factors $\Gamma > 100$. Besides theoretical arguments there is observational evidence to support this, such as the radio emission flickering (Goodman, 1997) and the low frequency self absorption (Katz & Piran, 1997), which provide an estimate of the expansion rate of the region where the afterglow is produced, explainable only by considering a relativistic expansion. A relativistic motion also implies that observed photons are less energetic in the rest frame in which they were emitted. Although all GRB models appeal on relativistically moving material, none of them convincingly explains how it is produced. There is also no consensus on whether it is a baryonic relativistic flux with high kinetic energy or if it is a magnetic dominated flux, or a combination of both (Nakar et al., 2003; Lazzati et al., 2004; Piran, 2004).

- Dissipation: The energy of such relativistic flow is dissipated in order to provide the energy to produce the GRB and the afterglow. Dissipation takes place through collisionless shocks[3] possibly by means of the plasma instability. There is a general agreement in that the afterglow is produced by

[3] Density is so low that collisions are very rare, instead interactions with the magnetic field and plasma waves act as collisionless shocks in which energy is dissipated.

external shocks with circumburst material. And there is convincing evidence (Fenimore et al., 1996; Sari & Piran, 1997; Ramirez-Ruiz & Fenimore, 2000; Nakar & Piran, 2002) that in most of the GRBs, energy dissipation during the γ ray emission peak takes place through internal shock within the relativistic flow.

- Synchrotron radiation: Once the dissipation of energy takes place, most of GRB models rely on synchrotron emission from relativistic electrons accelerated within the shocks to account for the radiation observed (both from the GRB and its afterglow). Another alternative is the self Compton synchrotron emission (Waxman, 1997; Ghisellini & Celotti, 1999) or the inverse Compton scattering of external light (Brainerd, 1994; Shemi, 1994; Shaviv & Dar, 1995; Lazzati et al., 2004).

- Relativistic collimated jets: The presence of monochromatic breaks in many afterglow light curves can be interpreted as a consequence of the decreasing velocity of the jet, which reduces Γ and the collimation of the radiation emitted by the relativistic material. Such decrease in the collimation reduces the amount of flux received by the observer after Γ becomes smaller than the inverse of the jet's opening angle θ_0. This is expected to happen during the evolution of a relativistic jet whose Lorentz factor Γ drops as the flow looses energy through dissipation. When $\Gamma < 1/\theta_0$ the jet can also expand to the sides and break out of the original jet, decreasing the observed flux (Panaitescu & Meszaros, 1999; Rhoads, 1999; Sari et al., 1999). Another interpretation is that GRB's jets share a universal structure and that different viewing angles account for the observed variations in energy which depends on the orientation (Lipunov et al., 1999; Zhang & Meszaros, 2002; Rossi et al., 2002). All these scenarios imply that GRB's integrated energies are smaller than the isotropic value and also, a higher occurrence rate for GRBs, given that not all of them are pointing towards our line of sight.

- A compact object: If we now take for granted that the GRB is produced due to a highly collimated relativistic jet, the total energy released in such events is $\sim 10^{51}$ erg (Frail et al., 2001; Panaitescu & Kumar, 2001). This energy is similar to the one produced by a SN, presumably related with the formation of a compact object (NS or BH). There is also no other known source of energy capable of producing such high amount of energy in such a short time. This requires the dissipation of the energy produced by $0.1M_{\odot}$ in the vicinity of the compact object in a relatively short time scale, which suggests a violent process that may point to the formation of the compact object itself. The shortest time scale variability showed on GRBs (around a few milliseconds)

provides another estimate of the region's size where the physical processes producing the variations occur ($\sim$ 300 km). And accretion of material onto a NS or a BH is certainly the most suitable candidate for explaining such variations due to their compactness. The last piece of "evidence" that a compact object may be involved in the production of a GRB is the observational association of a SN like spectra to the GRB afterglow after 10-15 days from the burst (Hjorth & Bloom, 2012). This indicates that at least some of the GRBs are related to the death of massive stars (Woosley & Bloom, 2006; Fruchter et al., 2006; Levesque et al., 2014), where NSs or BHs could be formed.

As shown above, for each one of these minimum requirements there are at least a couple of applicable theories. Nevertheless, up to date there is a reasonable amount of inner engine candidates that are able to provide the energies, time scales and variabilities observed in most GRBs. They are mainly separated into engines able to produce sGRBs (lasting less than a couple of seconds) and engines producing lGRBs (lasting from seconds to several hundreds of second). As for sGRBs, the current view is that they are produced by violent events occurring at the end of the evolution of a small fraction of stars. Namely, events such as the merger of double NS binaries (Goodman, 1986; Paczynski, 1986), a NS-BH merger (Lee & Kluzniak, 1995; Janka et al., 1999), a White Dwarf (WD) - BH merger (Fryer et al., 1999) or accretion induced collapse (AIC) of a NS (Vietri & Stella, 1999; MacFadyen et al., 2006). These and other possible candidates for sGRBs are discussed on the review by Lee & Ramirez-Ruiz (2007) and the one by Nakar (2007), along with the most important features for such kind of GRBs.

Meanwhile, given the association of lGRBs with the death of massive stars (which can only be confirmed for $\sim$ 10 events), the most accepted models are based on the violent collapse of a Pre-Supernova (PreSN) star. In such event the Fe core is compressed into a rapidly rotating and possibly with an intense magnetic field proto NS (pNS), which can become the central engine itself or further collapse into a BH that will accrete the infalling material, producing the immense amount of energy needed to produce a GRB. In case a rapidly spinning and highly magnetized pNS is formed, the presence of the magnetic field in the differentially rotating pNs induces the growth of the Magneto Rotational Instability (MRI) (Balbus & Hawley, 1998) which exponentially amplifies the seed magnetic field (from the preSN star) producing bipolar flows that could result in luminosities of $\sim 10^{52}$ erg and the explosion of the star or a GRB (Akiyama et al., 2003; Williams, 2005; Metzger et al., 2011). On the other hand, if the preSN core eventually collapses into a BH we end up with the Collapsar scenario proposed by Woosley (1993), where the recently

formed BH forms part of the energy producing mechanism to power the GRB. This can be done mainly in two ways, the first is the result of the BH's gravitational potential acting upon the infalling rotating material, which enables the formation of an extremely hot and dense accretion disk around it, able to emit a copious amount of neutrinos whose annihilation above the accretion disk is could be able to power the GRB (MacFadyen & Woosley, 1999). The second involves the rotational energy of the BH and its interaction with the accretion disk's magnetic field, know as the Blandford-Znajek mechanism (Blandford & Znajek, 1977), which can extract energy and angular momentum electromagnetically from both the magnetic field and the BH rotation.

The duration of such an event can be estimated by the dynamical time scale $t_{\rm dyn}$ it would take the PreSN star with mass M_* and radius R_* to collapse on itself:

$$t_{\rm dyn} \sim \sqrt{\frac{R_s^3}{2GM_s}} \sim 1100 \left(\frac{R_s}{R_\odot}\right)^3 \left(\frac{M}{M_\odot}\right)^{-1} \text{ s} \,. \tag{1.8}$$

Thus, if lGRBs are related to the death of massive stars, the duration of the burst will depend on the structure of the PreSN star at the time of collapse (mass, radius, angular momentum distribution, etc.), as well as any other physical process (such as neutrino cooling/heating or magnetic fields) able to alter the infall of material to the center of the dying star. Therefore, the progenitor properties could also determine whether the central engine is a a proto NS or a BH. A critical assessment of the outcome of collapsing cores has recently been given by Dessart et al. (2012) in their 1D general relativistic (GR) simulations. They found that most of the lGRB progenitor stars obtained by Woosley & Heger (2006) failed to form a BH directly from the collapse of the iron core, and resulted instead in rapidly rotating proto-neutron stars which could experience magneto-rotational instability (MRI) prior BH formation. Nevertheless, there are other 2D GR simulations (Mizuno et al., 2004a,b; Sekiguchi & Shibata, 2007, 2011), where direct formation of a BH is readily obtained from different collapsing cores. The equation of state (EoS), and microphysics (neutrino transport included) used in every one of these works, seem to be of importance in determining the fate of the collapsing core, but the greatest uncertainty remains in the properties of the preSN star, such as rotation rate, mass and radius, which can only be addressed by improving stellar evolution models. In the next section we will focus on describing the Collapsar model, giving the most important physical processes and requirements needed to produce a GRB from such a scenario.

1.2 Accretion and GRBs. The Collapsar Model

The collapsar model (Woosley, 1993) consists on a PreSN star, whose Fe core collapses almost directly into a BH after the shutdown of nuclear reactions. The infall of the outer stellar envelopes should form an accretion disk around the BH that will power the GRB. Two main variants on this model may occur. In the first, the Fe core is massive enough to induce a direct collapse of the core into a BH, while in the second an intermediate stage produces a proto-neutron star, which later collapses after enough matter has been accreted onto its surface (typically this would take a few seconds). Once a centrifugally supported disk forms around the BH, the temperature will be high enough that neutrino emission becomes the main cooling mechanism, as pointed out in the context of supernovae by Chevalier (1989) and Houck & Chevalier (1991), allowing accretion to proceed at extremely high rates with the attending energy release. In principle the burst itself may be powered by a combination of neutrinos themselves, or magnetic mechanisms that tap the rotation in the disk and/or the BH (Blandfor-Znajek mechanism).

Two key ingredients, presumably associated to the progenitor, make this a relatively rare occurrence (as they must, considering that the rate of core-collapse SNe far exceeds the observed GRB rate): rotation, and the lack of a hydrogen envelope. The first is necessary in order to ensure that a large fraction of the available energy is released in a disk close to the black hole through accretion, rather than simply be swallowed whole by the BH (in something akin to Bondi accretion). Evolutionary models for rapidly rotating stars (Woosley & Heger, 2006) show that the core is able to retain enough angular momentum to make this a possibility depending on the mass loss history and the presence (or lack) of magnetic fields coupling the envelope to the inner regions. The second is required in order for the relativistic jet that is launched at the center of the star to perforate it, break out, and eventually lead to high energy emission far from the stellar surface, which we observe as a GRB. This condition also supports observations of SN counterparts to GRBs that show no H lines.

1.2.1 Physics of the Collapsar and its Progenitors

The hydrogen envelope of a lGRB progenitor may either have been lost through interaction with a binary companion, or with models that include rotation (even though they are not in 3D) which induces almost complete mixing on the star and therefore an almost homogeneous solution. This helps avoiding the Red-giant

phase and produces He stars at the end of the MS that could serve as lGRB progenitors (Yoon & Langer, 2005; Woosley & Heger, 2006). Wolf Rayet (WR) stars could represent viable progenitors for GRBs given they have lost their H envelope due to strong winds. Such winds can also become a problem because expelled material could take away angular momentum from the rest of the star and may prevent further disk formation around the BH. Nevertheless, considering empiric wind models used on stellar evolution, WR stars with low metallicity would loss fewer mass, and therefore angular momentum, than a WR star with solar metallicity. This makes more likely that the collapsar model for GRBs works at regions of low metallicity, i.e. at cosmological distances.

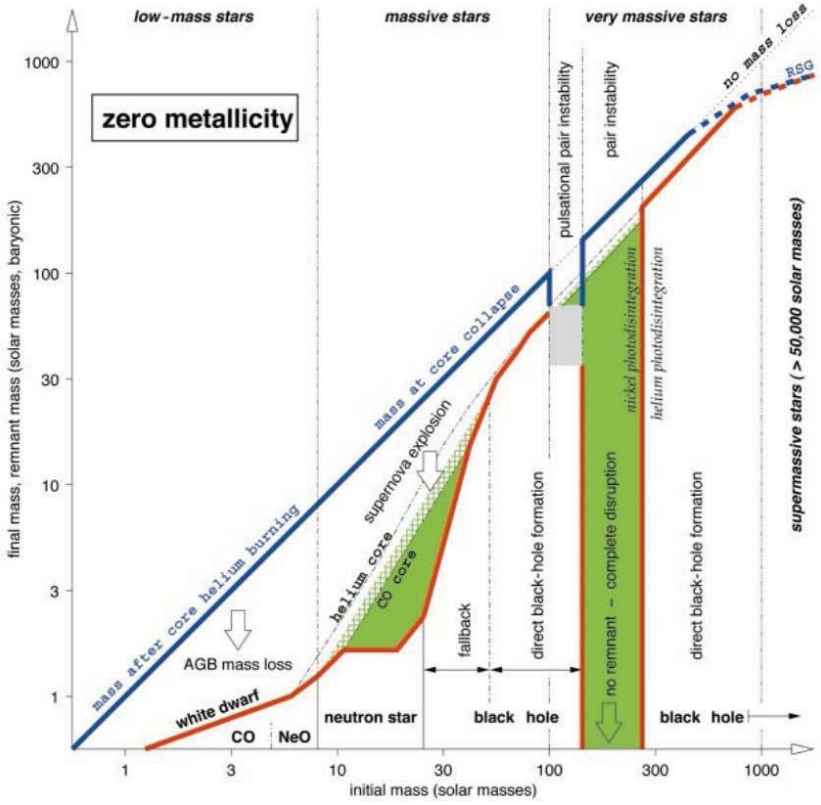

Figure 1.4: Final mass of the star and its remnant against its initial mass for zero metallicity. The blue line indicates the mass of the star after core helium burning. The red line shows the remnant mass of the Fe core (for massive stars with $\gtrsim 8\ M_\odot$) that can become a neutron star (NS) or a BH depending on its mass before collapse. Dark green shows regions with heavy-element synthesis, and cross-hatched green shows regions of partial He burning to C and O. Depending on the initial mass, the remnant can turn out to be a white dwarf (WD) (for low mass stars $M \lesssim 8\ M_\odot$), a NS (for stars with masses $10\ M_\odot \lesssim M \lesssim 25\ M_\odot$) or a BH (if $M \gtrsim 30\ M_\odot$). Figure from Woosley et al. (2002).

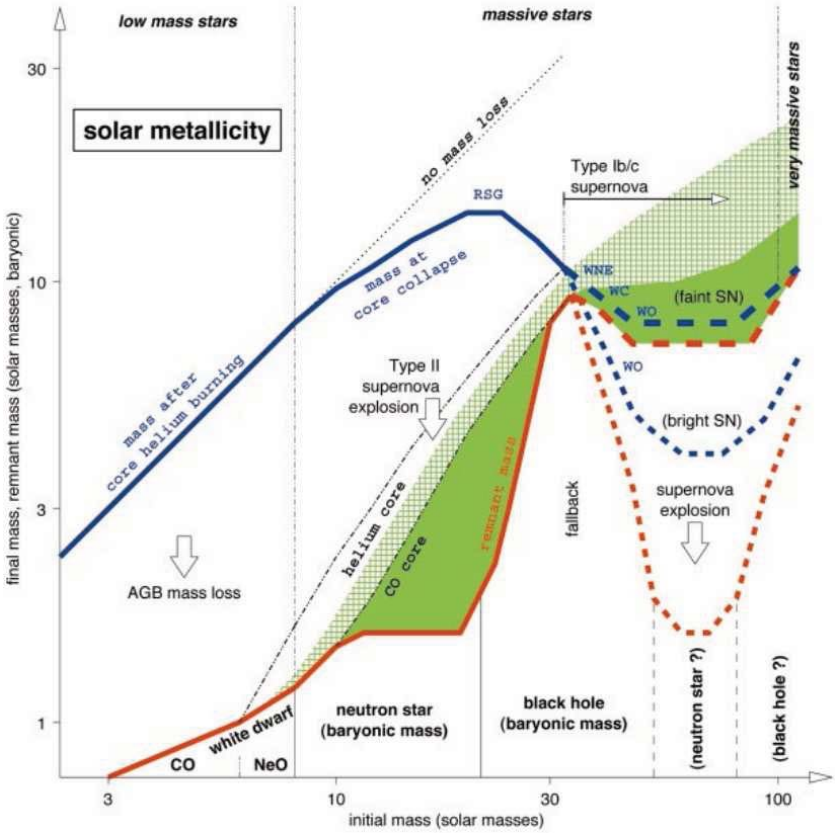

Figure 1.5: Final mass of the star and its remnant against its initial mass for solar metallicity. The blue line indicates the mass of the star after core helium burning and with increasing metallicity, the mass loss of the star through winds increases. The red line shows the remnant mass of the Fe core (for massive stars with $\gtrsim 8\ M_\odot$) that can become a neutron star (NS) or a BH depending on its mass before collapse. Dark green shows regions with heavy-element synthesis, and cross-hatched green shows regions of partial He burning to C and O. Depending on the initial mass, the remnant can turn out to be a white dwarf (WD) (for low mass stars $M \lesssim 8\ M_\odot$), a NS (for stars with masses $10\ M_\odot \lesssim M \lesssim 25\ M_\odot$) or a BH (if $M \gtrsim 30\ M_\odot$). Figure from (Woosley et al., 2002).

Thus, for this model to work, the evolutionary paths of lGRB progenitor stars must be such that they loose its H envelope, retain its rapid rotation and still have the required characteristics needed to form a BH from the collapse of its core. For that to happen, first of all, the star must be massive enough to exhaust all its nuclear fuel developing a Fe core at the end of its evolution. This implies a lower mass limit $M_{\rm min}$ (at Zero Age Main Sequence (ZAMS)) for the star to build up a Fe core, and such limit could increase when considering mass loss. Figures 1.2.1 and 1.5 (from Woosley et al., 2002) show results from stellar evolution models for stars with zero

and solar metallicity with initial masses between $1 \lesssim M/M_{\odot} \lesssim 300$. The y-axis shows the final mass for different massive components of the star. The blue line indicates the mass of the whole star after He burning, which decreases for massive stars with solar metallicity. This decrease is due to mass loss through stellar winds, whose modeling depends strongly on the presence of heavy materials such as Fe, whose large amount of available electron states are believed to help capturing an important amount of momentum from the stellar radiation. The red line shows the mass of the remnant (compact object) formed at the end of the stellar evolution, and the area below the line is separated into zones indicating whether the remnant is a WD, NS or BH. From this work, the minimum mass needed to obtain a BH is $M_{\text{min}} \gtrsim 25\ M_{\odot}$. The outcome mainly depends on the star's initial mass, its mass loss (winds, AGB mass loss, supernova explosion) and any other physical process able to modify the amount of mass that can collapse onto the stellar core, such as the Equation of State (EoS) of the material, cooling processes (like radiation or neutrinos), nuclear processes (photo-disintegration, neutronization), instabilities (pair instability (Fowler & Hoyle, 1964), Standing Accretion Shock Instability (SASI) (Blondin et al., 2003), Magneto-rotational Instability (MRI) (Balbus & Hawley, 1998)) and so on. All of them make the prediction of the remnant mass a truly complicated task.

More recently, Ugliano et al. (2012) used the 1D hydrodynamic code PROMETHEUS to study neutrino driven SN explosions on the solar metallicity stellar models from Woosley et al. (2002) obtaining that for stars with $M > 15\ M_{\odot}$ it is possible to have either a NS or a BH (shown on figure 1.6). The work by Ugliano showed that besides the stellar mass (either at ZAMS or just before collapse), the pre-collapse stellar structure was of great importance in determining the final fate of the remnant. And apparently, the large structural variations in the stellar models obtained by Woosley et al. (2002) for very similar ZAMS masses, could be responsible for the strong variability observed in the type of remnant as a function of the ZAMS mass. As stated at the end of the previous section, much work has been done in exploring the feasibility of the direct formation of a BH through the collapse of a stellar core (Dessart et al., 2012; Mizuno et al., 2004a,b; Sekiguchi & Shibata, 2007, 2011), and the structure of the collapsing core seems to be an important parameter in determining whether a NS or a BH is formed. Therefore, better stellar evolution models are needed in order to determine the specific properties of lGRB progenitors and to obtain conclusive information about the inner engine (if it is either a NS or a BH).

Based on the results by Ugliano et al. (2012), if we have a star that has lost most of his H envelope and is still massive enough ($M \gtrsim 15\ M_{\odot}$) to produce a BH from the collapse of its core, we still have to worry about its rotation rate. The PreSN

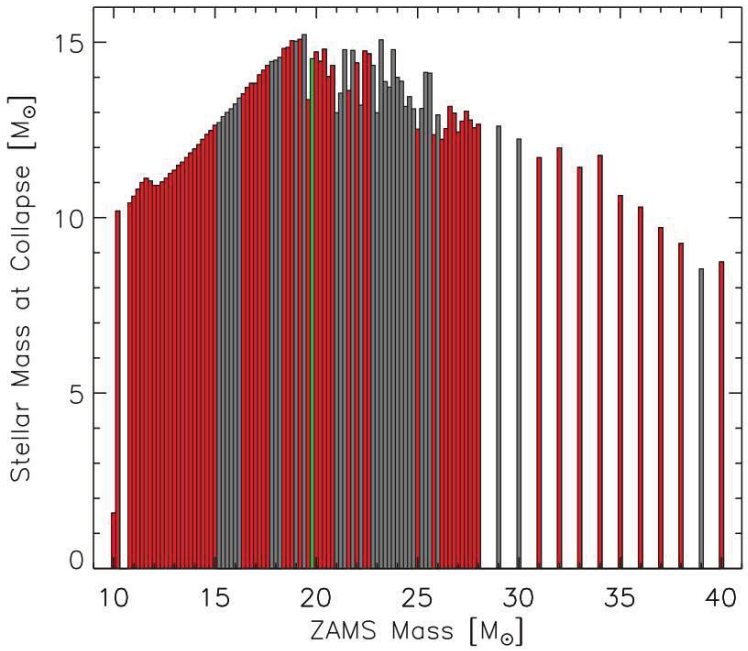

Figure 1.6: Stellar mass at collapse versus their initial mass (at ZAMS) from the work by Ugliano et al. (2012) based on stellar models from Woosley et al. (2002). Red bars indicate models whose remnant after a neutrino driven SN is a NS, gray bars indicate a BH and the green bar corresponds to the calibration with SN1987A. Figure from (Ugliano et al., 2012).

star must have enough angular momentum to enable the formation of an accretion disk around the BH. The minimum angular momentum needed $J_{\rm min} = r_{\rm isco} c$ is set by the innermost stable circular orbit (ISCO) at $r_{\rm isco} = 3\ r_g = 6GM_{\rm BH}/c^2$ from the BH:

$$J_{\rm min} = \frac{6GM_{\rm BH}}{c} = 2.6575 \times 10^{16} \left(\frac{M_{\rm BH}}{M_\odot}\right)\ {\rm cm}^2\ {\rm s}^{-1} \tag{1.9}$$

The amount of angular momentum in the star is crucial for GRB production in the collapsar scenario (Lee & Ramirez-Ruiz, 2006). Too much of it results in an accretion disk that forms far from the black hole. The temperatures and densities are then not high enough for efficient cooling through neutrinos, and hypercritical accretion cannot proceed. Too little of it leads to quasi-spherical accretion, where the mass accretion rate can be extremely large but with near zero efficiency for the conversion of gravitational binding energy into thermal energy through shocks (and subsequently radiation).

Once a progenitor star has been chosen we have to consider the most important physical processes known determining GRB formation in the collapsar model.

First we have to assume an EOS for the infalling gas, some treatment for the accretion onto the BH, as well as for its gravitational potential, and the cooling/heating processes that will take place at such temperatures and densities. When the collapse of the Fe core starts, density reaches values over 10^{10}g cm^{-3}. This condition favors electron capture on nuclei which reduces the contribution to the pressure due to electrons. This neutronization together with photo-dissociation due to γ rays produced at $T \gtrsim 10^9$ K induce further collapse of the Fe core into a BH. At this temperatures neutrino production via pair annihilation, becomes really important and is the main cooling process taking place.

With the BH formed, outer material keeps falling close to the BH and reaches densities and temperatures almost as high as the collapsing Fe core had. Nevertheless infalling gas can be treated as an ideal gas of free nucleons and α particles in nuclear statistical equilibrium (NSE). But given the high temperatures, relativistic electrons and positrons with arbitrary degeneracy $P_{e^\pm}$ are present due to pair creations. There is also a contribution to the pressure from blackbody radiation due to photons, which are completely trapped. We can obtain an approximation of the expected internal energy under such conditions, considering that the relativistic electron-positron pairs are hot and fully non-degenerate. Thus, besides the ideal gas ($u_{\rm gas} = 3/2\ kT\rho/(\mu m_p)$), photons and pairs will contribute together a radiation energy density $u_{\rm rad+pair} = (11/4)\ aT^4$. Therefore, the full internal energy of the gas (per unit volume) can be written as:

$$u = \frac{3}{2}\frac{kT\rho}{\mu m_p} + \frac{11}{4}aT^4, \tag{1.10}$$

and given that photons are trapped, neutrinos will become the main source of energy loss for the system. A first approximation to the neutrino luminosity can be obtained from the work by Narayan et al. (2001), where they study different accretion flow scenarios onto a compact object (BH) in the context of GRB production. For a given temperature T, and density ρ, the cooling rate per unit volume due to neutrinos is given by (Narayan et al., 2001):

$$q_\nu \simeq \left(5 \times 10^{33} T_{11}^9 + 9.0 \times 10^{23} \rho T_{11}^6\right)\ \text{ergs cm}^{-3}\ \text{s}^{-1}, \tag{1.11}$$

where the first term on the right hand side comes from pair annihilation and the second term from pair capture onto free nucleons (estimated for a fully photodesintegrated gas where the mass fraction of free nucleons is $X_{\rm nuc} = 1$). Both terms depend sensitively on temperature, $T_{11} = T/10^{11}$ K, so high temperatures, $T \gtrsim 10^{10}$ K, are required for this to become relevant. Neutrinos produced on cooling processes are the ones that would provide the energy to power the GRB. Obtained

neutrino luminosities L_ν from the collapsar, could be used to produce a relativistic jet by calculating the energy produced by neutrino annihilation.

Besides the EoS and energy exchange processes taking place, we have to account for some of the relativistic effects the BH may have on the disk. The infalling gas should reproduce the position of the innermost stable circular orbit (ISCO) at $r_{\rm isco}$. If material gets closer to the BH it would fall onto the BH no matter its rotation velocity. On this work we use the simplest approximation for the potential of a non-rotating (un-charged) BH, the Paczynski-Wiita (PW) potential (Paczynski & Wiita, 1980) given by:

$$\Phi_{\rm BH}(r) = \frac{GM_{\rm BH}}{r - r_g}, \tag{1.12}$$

which reproduces exactly the position of the ISCO and also gives a better approximation than Newtonian, to the distribution of angular momentum $J(r)$, that an orbiting point mass should have around a Schwarzschild BH (this will be discussed in the next chapter).

1.2.2 Production of GRBs from a Collapsar

MacFadyen & Woosley (1999) carried out a the first detailed numerical study of the collapsar, and further explored jet production, propagation and breakout from the star for a variety of configurations (MacFadyen et al., 2001; Zhang et al., 2003). They obtained energies from neutrino annihilation ranging between $1 - 14 \times 10^{51}$ ergs and lasting between 10 and 20 seconds, that could be enough to produce a directed relativistic jet with the same energy as a GRB. One possibility is that the explosion eventually does launch the stellar envelope outward and produces an extremely energetic event, leading to the observed hypernovae.

Much effort has been applied to explore the behavior of collapsars in two dimensions, assuming azimuthal symmetry. Some of them are GR-magneto hydrodynamical (MHD) simulations with simple (e.g. Sekiguchi & Shibata, 2007; Mizuno et al., 2004a,b) or detailed (Shibata et al., 2007; Sekiguchi & Shibata, 2011) EoS and microphysics, and a number of authors have addressed the problem using Newtonian or pseudo-Newtonian approximations in MHD or hydrodynamical simulations with approximate or realistic equations of state and neutrino cooling effects (Proga et al., 2003; Fujimoto et al., 2006; Nagataki et al., 2007; Nagataki, 2009; Lopez-Camara et al., 2009, 2010). However, relatively little work has been done in three dimensions, thus neglecting the potentially important role of the self–gravity of the infalling gas, and generic instabilities in 3D. The first study we are

aware of was that carried out by Rockefeller et al. (2006), and based on a 60 $M_{\odot}$ rotating Pop III star. They observed the formation of instabilities within the disk, mainly as spiral waves, which contribute to angular momentum transport. More recently, Taylor et al. (2011), considered a very rapidly rotating progenitor, formed from the merger of two He stars. They also saw the development of instabilities in the disk and based on the observed energy release concluded that some of their models are indeed capable of producing a GRB. We note that all of these models consider that the black hole is motionless at the origin of coordinates, which is a good approximation if the disk mass is negligible (which may not be the case) or if the infalling layers do not show strong asymmetries in their mass distribution. A recent analysis by Korobkin (2011) explores the evolution of self gravitating relativistic disks with a simple equation of state and no cooling, around a non–rotating BH with disk to BH mass ratio of 0.24, 0.17 and 0.11. Their work focused on the effects of the initial disk configuration and perturbations in the formation of non-axisymmetric instabilities at the disk.

In this work we focus on the dynamical effects in three dimensions, coming essentially from the self-gravity of the infalling gas and cooling, which occur during the initial stages of the collapse of a rotating polytropic envelope onto a central black hole in the context of the Collapsar model. Rather than make use of a very complex equation of state, we consider generic solutions with simplified cooling (assumed to be through neutrinos). In particular, we pay special attention to the comparison between the cooling and dynamical time scales in order to gauge their effect on the formation of structure and the evolution of the mass accretion and energy losses. The next chapter will treat the details of the physics included in the code GADGET-2 (Springel 2005, Springel, Yoshida & White 2001), that will be used for our simulations. Chapter 3 will include some test made to the code in order to insure that everything worked properly, and chapters 4 and 5 will show the main results of our work and their discussion and conclusions respectively.

Chapter 2

GADGET-2: Details, Modifications and Tests

The purpose of this chapter is to provide the most relevant details about how GADGET-2 works, as well as some tests made to the code in order to make sure it fitted our needs. By looking in detail the code's routines in charge of computing the most important physical processes concerning our study, we will be able to make the necessary modifications on the code, needed for a complete Collapsar model. Such physical processes include the gravity force calculation, the accretion of gas into a BH and the cooling of gas particles. We will also dedicate a section of this chapter to explain how the hydrodynamical part of the code works.

GADGET-2 (Springel et al., 2001; Springel, 2005) is a parallelized code, mainly used for performing cosmological simulations. It is capable of following a collisionless fluid with the N-Body method, but it is also able to solve the hydrodynamics of an ideal gas by means of Smoothed Particle Hydrodynamics (SPH). In our work we will make use of both of these functions. The first is used in order to calculate the gravitational force between the fluid elements (SPH particles) and the black hole (BH), meanwhile the second is used to follow the hydrodynamics of the gas. The main reason for using GADGET-2 for our project is that it contains a fully parallelized 3D SPH code, which we planned to modify in order to include the rest of the physical processes we needed for our work.

2.1 Gravity in GADGET-2

These part of the code is mainly used to follow the dynamics of non-interacting particles, such as dark matter, stars (bulge, disk) and boundary particles (black holes), but it also follows the gravitational dynamics of gas particles, all of them described by the collisionless Boltzmann equation, coupled to the Poisson equation in an expanding background Universe. This last feature can be turned off for simulations were Universe expansion is not relevant (as is our case). The dynamics of these particles is described by the Hamiltonian:

$$H = \sum_i \frac{\boldsymbol{p}_i^2}{2m_i a(t)^2} + \frac{1}{2}\sum_{i,j} \frac{m_i m_j \varphi(\boldsymbol{r}_i - \boldsymbol{r}_j)}{a(t)}, \tag{2.1}$$

where $\boldsymbol{r_i}$ and $\boldsymbol{p}_i$ are the co-moving coordinate vectors, and the corresponding canonical momenta of the particles respectively. φ is the interaction potential obtained from solving the Poisson equation for the particle distribution. The explicit time dependence of the Hamiltonian arises from the evolution of the scale factor $a(t)$ which in a Newtonian space (as is our case) is constant ($a(t) = 1$). The dynamics of the particles is followed by solving the N-body problem described by the total number of particles N.

For the particle dynamics to remain collisionless, the close encounters between them must be very rare or non existent. This translates in a motion of particles dictated solely by their interaction with the overall gravitational potential generated by the complete distribution of particles. Nevertheless, depending on the distribution and number of particles, the number of gravitational close encounters can become non negligible. Such collisions can introduce large numerical errors into the integration of the equations of motion if a constant or a minimum time step is used for the simulation[1]. Therefore a softened gravitational force is used to avoid non realistic accelerations due to those "poorly integrated" close encounters. Such gravitational softening is characterized by a softening length ε which modifies the gravitational force between two particles when the distance between them is too small ($r_{ij} \leq \varepsilon$). The use of gravitational softening implies the assumption that the mass density is smooth on all scales by replacing the corresponding δ function of each particle for an extended mass distribution (Dehnen, 2001)[2].

[1] The use of a minimum time step $\Delta t_{\min}$ is required to avoid increasingly smaller time steps that result in a prohibitively large CPU time for the integration of the equations of motion.

[2] As particles are represented by point masses, each one of them has an associated δ function to determine its mass distribution in space.

Thus, the gravitational potential at any given point $\boldsymbol{r}$ can be expressed as the potential due to the N particles located at $\boldsymbol{r}_i$ (Dehnen, 2001):

$$\Phi(\boldsymbol{r}) = -G\sum_{i=1}^{N} m_i\, \phi(|\boldsymbol{r} - \boldsymbol{r}_i|, \varepsilon), \tag{2.2}$$

where, we have defined the softening kernel function $\phi(|\boldsymbol{r} - \boldsymbol{r}_i|, \varepsilon)$, which determines the shape of the potential as a function of the softening length ε. When considering this gravitational softening length ε as constant in time and space, the force estimate for the potential in (2.2) is:

$$\mathbf{F}(\mathbf{r}) = -\nabla\Phi = -G\sum_{i}^{N} m_i \phi'(|\mathbf{r} - \mathbf{r}_i|, \varepsilon)\frac{\mathbf{r} - \mathbf{r}_i}{|\mathbf{r} - \mathbf{r}_i|}, \tag{2.3}$$

where $\phi' = \partial\phi/\partial r_i$. From the definition in (2.2) we can obtain the mass distribution following Poisson's equation $\nabla^2\Phi = 4\pi G\rho$:

$$\rho(\mathbf{r}) = \sum_{i}^{N} m_i W(|\mathbf{r} - \mathbf{r}_i|, \varepsilon), \tag{2.4}$$

where the density kernel $W(r, h)$ is related to the softening kernel by:

$$W(r, \varepsilon) = -\frac{1}{4\pi\varepsilon^3 r^2}\frac{\partial}{\partial r}\left(r^2\frac{\partial\phi}{\partial r}\right). \tag{2.5}$$

Therefore, once a density kernel $W(r, \varepsilon)$ is given (equation 2.5) can be solved to obtain $\phi(r, \varepsilon)$. This relation between the softening and the density kernel is very important in SPH codes, which are based on the construction of a smooth mass distribution from a discrete sample of gas particles. Thus, after defining the density kernel in SPH one can obtain the softening kernel needed for the calculation of gravity forces and potential. In the next section we'll introduce the density kernel $W(r, \varepsilon)$ used in GADGET-2 as well as the details on how SPH works. For the moment, let us keep in mind that once $W(r, \varepsilon)$ is set, the gravitational potential due to the particle distribution can be written as:

$$\Phi(\mathbf{x}) = \begin{cases} -G\sum m_i\, \phi(r, \varepsilon), & 0 \leq r \leq \varepsilon, \\ -G\sum \dfrac{m_i}{r}, & \varepsilon < r. \end{cases} \tag{2.6}$$

For $r > \varepsilon$ we have the exact Newtonian potential, and only close encounter interactions are softened to avoid poorly integration. From $\Phi(\boldsymbol{x})$ we can obtain

the gravitational force on each particle and solve the equations of motion for each one of them. The work by Dehnen (2001) shows how to make a good choice of the softening length parameter ε for several softening and density kernels (including the spline density kernel used in GADGET-2). The optimal softening length depends on the distribution of particles, therefore, it should vary in time as the particles move. Nevertheless, our version of GADGET-2 uses a fixed gravitational softening, so in order to make sure that the value selected for ε was not over softening the gravitational forces, we made several tests to observe the size of the smallest self gravitating structures formed in our simulations L_{min}. If $\varepsilon > L_{\text{min}}$ self gravitating structures smaller than L_{min} could not be properly resolved given that gravitational forces within that region would be always softened, making the structure less binded than it should and preventing it to further collapse on itself.

2.1.1 N-body Gravity Calculations in GADGET-2

Besides the need to include a softening kernel to account for the noise induced by having a discrete mass distribution, one needs to take into account that when the number of particles N included in a N-body simulation becomes significantly large, the number of operations needed to calculate the gravitational force acting on each of the particles is of order $\mathcal{O}(N^2)$ and the computational cost becomes too large. Therefore, in order to reduce the computational cost we must use a method that considerably reduces the number of operations needed and that yields an accurate approximation to the gravity forces.

To understand how GADGET-2 calculates the gravitational force on a particle let's start with an example. Suppose that we want to evaluate the gravity force on the particle lying on the bottom left blue cell from Figure 2.1 due to the rest of the particles. The exact force (disregarding any numerical error) will be given by the direct summation of the force exerted by each particle. In order to obtain the gravity force for all particles using this method, we require to repeat this operation N times, therefore, we need $\mathcal{O}(N^2)$ operations (including the summation) to obtain the force.

Nevertheless, we can calculate an approximation for the exact gravitational force based on the fact that the gravitational potential at $\boldsymbol{r}$ due to a mass distribution, can be fairly approximated by its multipole expansion (to a certain finite order) as long as r is significantly greater than the size of the mass distribution L. This can be seen by writing down the potential at $\boldsymbol{r}$ due to a mass distribution in space:

$$\Phi(\boldsymbol{r}) = -G \int \frac{\rho(\boldsymbol{r}')}{|\boldsymbol{r} - \boldsymbol{r}'|} dV', \tag{2.7}$$

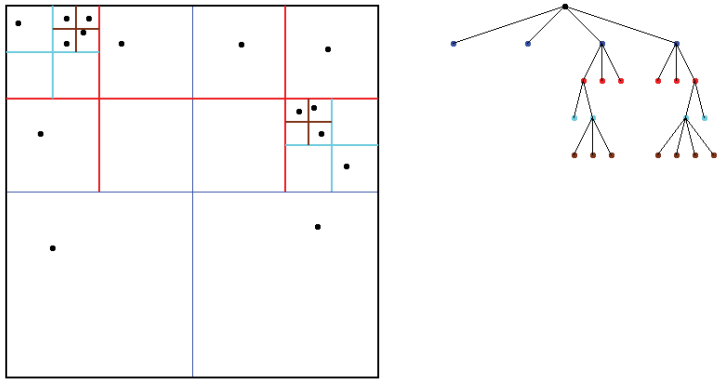

Figure 2.1: On the left, the space containing the point masses is successively divided into squares (or cubes in 3D), as shown in the figure, until there is only one particle at the square. Squares containing only one particle are not further divided. On the right, the Quad-tree diagram in 2D, the colored dots indicate on which square (node) we are at. The first level is the black square containing all the particles and its daughter nodes. The tree is "walked" along each node until the deepest level is reached (when only one particle is present).

where $\mathbf{r}'$ is determined by the mass distribution. If such mass distribution lies far from where we want to calculate the potential then $r \gg r'$, therefore, we can use a Taylor expansion to approximate the term $1/|\hat{\mathbf{r}} - (\mathbf{r}'/r)|$ for $(r'/r) \ll 1$. Considering that $|\mathbf{r} - \mathbf{r}'| = \sqrt{r^2 - 2(\mathbf{r}\cdot\mathbf{r}') + r'^2}$, and defining $\hat{\mathbf{r}} = \mathbf{r}/r$ as the unitary vector in the direction of $\mathbf{r}$, we can write the gravitational potential at $\mathbf{r}$ as:

$$\begin{aligned}\Phi(\mathbf{r}) &= \Phi_{\rm mon} + \Phi_{\rm dip} + \Phi_{\rm quad} + \mathcal{O}\left(\frac{r'}{r}\right)^3 \\ &= -\frac{G}{r}\int \rho(\mathbf{r}')dV' - \frac{G}{r^2}\int \rho(\mathbf{r}')\left(\hat{\mathbf{r}}\cdot\mathbf{r}'\right)dV' \\ &- \frac{G}{2r^3}\int \rho(\mathbf{r}')\left[3\left(\hat{\mathbf{r}}\cdot\mathbf{r}'\right)^2 - r'^2\right]dV' + \mathcal{O}\left(\frac{r'}{r}\right)^3\end{aligned} \tag{2.8}$$

The first term (the monopole) accounts for the contribution to the potential of the mass distribution as if it was located at a single point located at distance r, and the integral can be readily solved to give the total mass M of the distribution. The second (dipole), third (quadrupole) and higher order terms, contain the rest of the information of how the mass is distributed in space. After a little algebra, it can be shown that every term of this expansion, can be written in terms of a product of coefficients dependent only on the distribution of mass relative to the origin

(i.e. $\mathbf{r}'$), and a function dependent on the position vector $\mathbf{r}$ where the potential is to be calculated. Therefore, given a particle mass distribution it is possible to evaluate their multipole moments coefficients (depending only on $\mathbf{r}'$) and obtain the potential at any point $\mathbf{r}$ outside the mass distribution. Then, an approximation of the gravitational force can be obtained from (2.8):

$$\begin{aligned} F(r) &= -\nabla_r \Phi(\mathbf{r}) \\ &\simeq -\nabla_r \left(\Phi_{\mathrm{mon}} + \Phi_{\mathrm{dip}} + \Phi_{\mathrm{quad}}\right). \end{aligned} \tag{2.9}$$

The more terms are used in the multipole force approximation, the more accurate it will be. Thus, truncating the multipole expansion is equivalent to neglecting the detailed distribution of particles within a region, to a certain level of accuracy. Nevertheless, due to the intrinsic numerical errors present from truncation, round off and discreteness effects, there is a limit on the maximum accuracy one can get on the gravitational force calculations, even when calculating the exact force from each particle on a simulation. This way, one can obtain an approximated value of the force exerted on a particle located at $\mathbf{r}_j$ by a set of N_i particles lying far enough from $\mathbf{r}_j$, without calculating directly the N_i interactions.

The gravitational forces for particles on GADGET-2 are calculated using the Barnes-Hut algorithm (Barnes & Hut, 1986) consisting on a hierarchical subdivision of space into regular cubic cells. Such an algorithm was first implemented in SPH calculations by Hernquist & Katz (1989) in their TREESPH code. To explain how it works let us assume that the problem we are addressing is one in 2D, therefore instead of subdividing the space into cubes we will subdivide it into regular squared cells. As a first step, we can draw a square containing all of the SPH particles, then, the Barnes-Hut algorithm consists in subdividing such square in 4 equal sized squares (as shown in the left panel from Figure 2.1) and to continue the process until only one particle is contained within a squared cell. Whenever there is a cell (or square) containing one or less particles, that cell will not be further divided into more cells. This way we can construct a tree in the sense that from its root (the initial square containing all particles), the tree subdivides in four branches, each of them can be further subdivided in another four branches in a process that continues as long as a branch (or node) contains more than one particle. The last level (node) containing only one particle is called a leaf. The tree scheme is shown in the right panel of Figure 2.1, where we can notice the different levels of the tree (i.e. the squared cells) represented by the color dots, which develop deeper levels (branches) whenever there is more than one particle on that node.

Such hierarchical organization of particles into nodes will allow us to obtain an approximation of the force due to the particles lying within a cell by obtaining

the multipole expansion of such mass distribution. Thus, whenever we want to evaluate the gravitational force exerted on particle j by the rest of them, we can approximate the exact force by the sum of forces exerted by each node on the particle j. To make it more clear let us evaluate the force on the particle lying on the left bottom blue node on Figure 2.1.

If we consider a multipole approximation up to a quadratic term (quadrupole), then, a first approximation to the exact gravitational force could be given by considering the force due to each one of the remaining blue nodes. This means that we have to calculate the multipole terms due to the distribution of particles inside each of these nodes. If we "walk" deeper into the tree to the next nodes (the red ones), we would be calculating a more accurate force given that the multipole approximation would be made on smaller particle distributions, both in size L and mass (number of particles). This will provide more detailed information on how the particles are arranged. Therefore, for a given multipole approximation, calculating the gravitational forces up to the red nodes is more accurate than calculating it at the blue node level. Whenever one reaches the deepest level containing only one particle (a leaf) the force evaluated is the exact force between 2 particles. Thus, an important part of the Barnes-Hut algorithm, consists in the criterion used to decide whether we continue to explore further into the next level of nodes or if the depth level we're using is accurate enough for calculating the force. By using this hierarchical criterion, the operations needed to calculate gravitational forces for N particles are of order $\mathcal{O}(N \log N)$, considerably fewer than $\mathcal{O}(N^2)$, when $N \gg 1$.

Therefore, to obtain the force on a given particle we have to walk the tree beginning at the first level (containing all particles) and at each level a comparison between the size of the current cell L and the relative distance r between the particle and the center of mass of the node is made. Whenever:

$$\frac{L}{r} \leq \alpha, \tag{2.10}$$

where α is a fixed tolerance parameter, the gravitational influence of all particles within the cell is computed with the multipole approximation. If such criteria is not met by a node of that level, then that node is further explored until the criteria is met. Nevertheless, in GADGET-2 a more accurate criteria is used to open nodes, a node of mass M_n and length L at a distance r is used for force calculation if

$$\frac{GM_n}{r^2}\left(\frac{L}{r}\right)^2 \leq \alpha|\boldsymbol{a}|, \tag{2.11}$$

where, $\boldsymbol{a}$ is the total acceleration obtained in the last time step and α is the tolerance parameter. This criterion tries to limit the absolute force error in each particle-node

interaction by comparing a rough estimate of the truncation error with the size of the total expected force (Springel, 2005). This criterion is combined with a second one to protect against the situation where a particle satisfies (2.11) but it also resides inside a node

$$|\mathbf{r}_j - \mathbf{c}_k| \leq 0.6L. \tag{2.12}$$

Here, $\mathbf{c}_k$ and $\mathbf{r}_j$ are the geometrical center of the node and the particle position respectively. This protects against large force errors while maintaining a low average cost of the tree walk. The important parameter in this criteria is the tolerance parameter α which determines how deep into the tree we want to walk for computing the force. A smaller α will result in a more accurate force but also in a slow tree walk.

In GADGET-2, only monopole moments are calculated due to some advantages it presents over expansions to higher order. Their construction is more efficient in terms of memory. Less data stored in each node translates into an increased performance on processor level and communication processes, and it allows simple dynamical tree updates consistent with the time integrations scheme used in the code (Springel, 2005). The time and memory saved from only considering the monopole term, can be exchanged to use a smaller tolerance parameter α which will render more accurate forces.

2.1.2 BH Gravitational Potential and Gas Accretion in GADGET-2

Given that this work's goal is to study the formation and evolution of an accretion disk around a BH in a collapsar scenario, we need to account for the effects on the gas due to general relativity (GR). The best approach would be to solve the evolution of Einstein equations and fluid dynamics equations in a coupled manner. This can be extremely CPU- costly when considering a "long" time evolution and a large range in space. Therefore, instead of solving the GR problem we adopted an approximated solution to mimic the GR dynamical effects that the BH should have in the accretion disk. We adopted a pseudo-Newtonian potential, namely the Paczinski-Wiita (PW) potential (Paczynski & Wiita, 1980, see equation 2.13), which has the ability to reproduce exactly the location of the marginally stable orbit $r_{\rm mb} = 2\,r_g$ and the innermost stable circular orbit (ISCO) $r_{\rm isco} = 3\,r_g$ for a Schwarzschild BH, i.e. the radius $r_{\rm isco} = 3\,r_g = 6\,GM_{\rm BH}/c^2$. The PW potential also reproduces quite accurately the form of the angular momentum distribution $L(r) = \left(r^3 d\phi/dr\right)^{1/2}$ obtained for a test particle orbiting a Schwarzschild BH (See figure 2.2).

$$\Phi_{\rm PW} = -\frac{GM_{\rm BH}}{r - r_g}. \tag{2.13}$$

The PW potential also resembles the Newtonian one when $r \gg r_g$. Such characteristics make the PW potential very suitable to study the motion of matter around a non rotating BH without solving the full GR problem. Also, as the PW potential depends on $M_{\rm BH}$ and $r_g = 2\,GM_{\rm BH}/c^2$, its value will change in time as $M_{\rm BH}$ increases. The intensity of the BH potential will grow with its mass, as well as the ISCO $r_{\rm isco}$. Therefore, by considering the innermost stable circular orbit position $r_{\rm isco}$ as the accretion radius $r_{\rm acc} = 3\,r_g$ for the BH, we will avoid that any orbiting material reaches velocities superior to the speed of light c and also that the gravitational accelerations due to the BH diverge when $r \to r_g$. The later will act as a gravitational softening length, which will help to avoid large integration errors from such short range interactions.

When accretion of a gas particle occurs (at $r \leq r_{\rm acc}$), the mass will be removed from the gas and transferred to the BH. This changes the BH properties after an integration time dt on which the BH mass will have accreted a mass $M_{\rm acc}$ at a rate $M_{\rm acc}/dt$. This modifies r_g and therefore, the accretion radius $r_{\rm acc}$ and the PW potential at r. We carried out a series of tests of simple models of accretion, to ensure that the PW potential worked properly, such tests will be shown later on this chapter.

In order to implement the PW potential into GADGET-2, we needed to modify the function in charge of computing the gravitational forces and the potential acting on the gas particles. In the original version, a Newtonian gravitational force and potential is used for all kinds of particles (gas, boundary, halo, disk, bulge & stars), thus, in order to change the force and potential acting on a gas particle due to the BH (boundary particle) we had to include a criterion to distinguish between gas particles and boundary particles when doing the gravity force calculation.

In order to use the same oct-tree constructed for calculating the gravitational force on each particle, we had to include a node selection criteria (which we named `MassOpenNodeCriteria` throughout the code) to help us distinguish when a node contains a BH (boundary particle). We also had to make sure that when computing the force on a gas particle, every node containing the BH is walked until the deepest level, i.e. the leaf containing the BH. The later will ensure that only the BH's mass exerts a PW potential to the gas particles. The criteria consists in comparing the node's mass with a fixed mass parameter Ω_M. If the mass contained in the node M_n is greater than Ω_M, then the node is further explored to obtain a

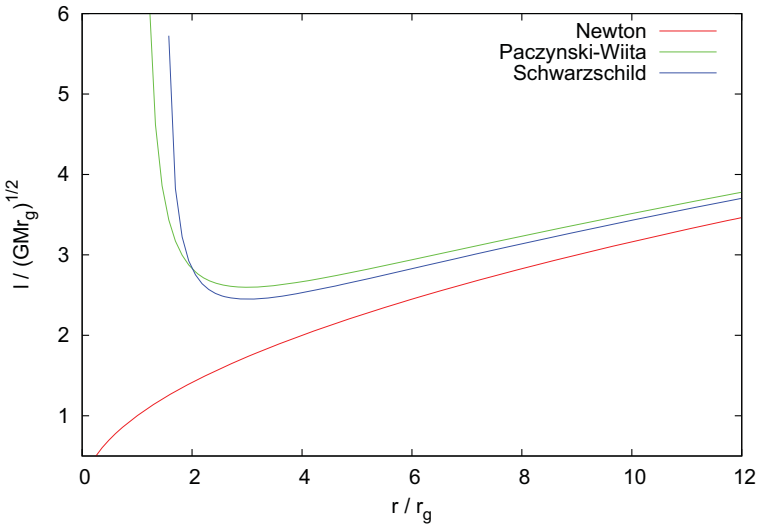

Figure 2.2: Keplerian angular momentum distribution for a test particle in a circular orbit in a Newtonian (red line), a Paczynski-Wiita (green line) and a Schwarzschild BH potential (blue line).

more accurate force calculation. When $\Omega_M \leq M_{\rm BH}$ this criteria also ensures that any node containing the BH (which is the most massive particle) will be further explored until reaching the deepest level (leaf) containing only the BH. And as with the tolerance parameter α, a smaller Ω_M results in a more accurate force calculation, and in a slower tree walk. We found over several tests, that simulations showing strong asymmetries require smaller values of Ω_M and/or α (up to two orders of magnitude) in order to reach convergence in the results, compared to simulations with no visible asymmetries.

We will now turn to the hydrodynamical part of GADGET-2 where we will describe the most important features in SPH. In order to keep the SPH section as clear and short as possible we obviated many details in the calculations, but there will be references to other works when needed.

2.2 SPH in GADGET-2

GADGET-2 solves the hydrodynamics of an ideal gas by means of Smoothed Particle Hydrodynamics (SPH). First introduced by Gingold & Monaghan (1977) and Lucy (1977) in an effort to simulate nonaxisymetric phenomena in astrophysics,

SPH is a Lagrangian method for studying the evolution of moving fluid elements. By comparison, in an Eulerian method derivatives are calculated at fixed points in space while in a Lagrangian one they are evaluated in a coordinate system attached to a moving fluid element, which in SPH, is represented by a particle at $\boldsymbol{r}_i$ containing all the relevant hydrodynamical information $(\rho_i, u_i, s_i, P_i, \boldsymbol{v}_i, \boldsymbol{a}_i)$. The SPH particles (fluid elements) will be subject to thermal and viscous pressures, gravitational forces and magnetic forces that will determine its thermodynamical properties and dynamics, i.e. the evolution of the flow.

As a first step let us define how to obtain the density ρ_i at the position of a SPH particle $\boldsymbol{r}_i$. Each of these N_{SPH} particles represents a moving fluid element, whose "shape" and size will be determined by the whole distribution of particles, and whose evolution in space and time will determine the hydrodynamical properties of the system.

2.2.1 Density in SPH

The idea used for obtaining the density in SPH is the same as the one used for obtaining the gravitational potential from a discrete distribution of point masses. As we saw in the gravity section, in order to obtain an accurate estimate of the gravitational potential due to a discrete set of point masses, we need to introduce a softening kernel in order to reduce the noise caused by collisions between particles. This softening kernel acts as an interpolation function which softens the discrete potential in order to obtain a smooth and continuous gravitational potential. In SPH, instead of worrying in defining an accurate gravitational softening kernel $\phi(r, \varepsilon)$ for the gravity force calculations, one has to worry about defining a density kernel $W(r, h)$ which depends on the relative distance to the particles $r = |\boldsymbol{r} - \boldsymbol{r}_i|$ and the SPH softening length h still to be defined, that gives the most accurate and efficient density interpolation for the discrete particle distribution. Once the density kernel $W(r, h)$ is chosen, the gravitational softening kernel ϕ is set.

As we're interested in following the evolution of the fluid elements (the SPH particles), we will calculate the thermodynamical properties at the position of the particles $\boldsymbol{r}_i$. Nevertheless, the thermodynamical properties can be obtained at any position in space $\boldsymbol{r}$ by following the same procedure. To obtain the best interpolation for the density, one should consider how the whole distribution of SPH particles contributes to the density ρ_i, but for $N_{\text{SPH}} \gg 1$ that implies a lot of operations. Thus, in most of the SPH implementations, the density ρ_i is obtained by considering a limited number of neighboring particles $N_{\text{Ngb}} \ll N_{\text{SPH}}$, replacing $\mathcal{O}(N_{\text{SPH}}^2)$ with $\mathcal{O}(N_{\text{SPH}} N_{\text{Ngb}})$ operations when computing the density of all SPH

particles. Thus, given a kernel $W_{ij} = W(r_{ij}, h_i)$, the density ρ_i and the smoothing length h_i at the position $\boldsymbol{r}_i$ of a SPH particle are defined as

$$\rho_i = \rho(\boldsymbol{r}_i) = \sum_{j=1}^{N_{\text{Ngb}}} m_j W_{ij}(r_{ij}, h_i); \qquad h_i = h(\boldsymbol{r}_i) = \eta \left(\frac{m_i}{\rho_i}\right)^{1/d}, \tag{2.14}$$

where r_{ij} is the distance between the particles i and j, m_j is the mass of the particle j, η is a parameter specifying the smoothing length h in terms of the mean particle spacing $(m/\rho)^{1/d}$, d is the dimensionality of the problem (3 in 3D) and W_{ij} (with dimensions of inverse volume) is the density kernel, depending on the distance between the particles i and j and on the SPH softening length h_i. The softening length h_i determines the kernel's rate of fall-off, and as we can see from equation (2.14), to consistently obtain ρ_i and h_i we must solve both equations simultaneously.

The density kernel W must satisfy the normalization condition within the volume containing the SPH particles ($\int W dV = 1$) to insure mass conservation. It should decrease monotonically with r_{ij} in order to give priority to the density contributions due to particles lying close to $\boldsymbol{r}_i$ ($r_{ij} \lesssim h_i$). And in order to have a zero contribution to the density from distant particles, SPH formulations usually choose a density kernel W_{ij} with compact support, i.e. that vanishes for particles lying at a distance $r_{ij} > \epsilon h_i$, where ϵ is known as the compact support radius, determined by the kernel W_{ij}. Many density kernels have been proposed (Gingold & Monaghan, 1982) but one of the most commonly used (also used by GADGET-2) is the cubic spline kernel, which is based on spline functions (Monaghan & Lattanzio, 1985) and is given by:

$$W(q) = \sigma \begin{cases} \frac{1}{4}(2-q)^3 - (1-q)^3, & 0 \le q < 1; \\ \frac{1}{4}(2-q)^3, & 1 \le q < 2; \\ 0 & q \ge 2 \end{cases} \tag{2.15}$$

where ($\sigma = [2/3, 10/(7\pi), 1/\pi]$) in 1D, 2D and 3D respectively and $q = r/h$. This cubic spline has a compact support radius $\epsilon = 2$, i.e. for $r > \epsilon h = 2h$ the cubic kernel and its derivatives are equal to zero. This kernel comes from the B-spline functions obtained by Schoenberg (1946), which give progressively better approximations to the Gaussian kernel with increasing order n, both by increasing the radius of compact support ϵ and by increasing smoothness, since each function M_n is continuous up to the $(n-2)$th derivatives (Price, 2012).

By choosing a kernel with compact support, one neglects contributions to the density from particles lying at large distances ($r > \epsilon h$), resulting in a diminished number of contributing particles, namely N_{Ngb} neighboring particles. By choosing a kernel with a larger compact support radius ϵ one usually obtains better density interpolations and considers a larger N_{Ngb} when obtaining ρ. This implies a relation between the number of neighbors N_{Ngb} and the compact support radius ϵ, that can be explicitly obtained for equal mass particles, given that enforcing the relation in (2.14) is equivalent to keep the mass inside the sphere of radius ϵh constant:

$$M_{\text{tot},j} = \int_{V_j} \rho dV \simeq \frac{4}{3}\pi\rho_j(\epsilon h)^3 = \frac{4}{3}\pi(\epsilon h)^3 \left(\frac{\eta}{h}\right)^3 m = \frac{4}{3}\pi(\epsilon\eta)^3 m. \quad (2.16)$$

And since $M_{\text{tot},j} = N_{\text{Ngb}} m$ for equal mass particles, solving simultaneously (2.14) is equivalent to keep N_{Ngb} almost constant ($N_{\text{Ngb}} \simeq (4/3)\pi(\epsilon\eta)^3$). In GADGET-2, instead of defining the parameter η, the user defines the number of neighbors N_{Ngb}. By choosing the cubic spline kernel (with compact support radius $\epsilon = 2$) and a value for N_{Ngb}, the parameter η is defined and ρ and h can be obtained. Nevertheless it is not a good idea to keep N_{Ngb} as a free parameter. Price (2012) discusses in detail how increasing N_{Ngb} does not necessarily results in a better density interpolation. For the cubic spline used in GADGET-2 there is an optimal value for the number of neighbors at $N_{\text{Ngb}} = 57.9$ which results in good estimates from W and it's gradients, and increasing N_{Ngb} to more than 100 particles, can result in the appearance of the pairing instability. This instability arises due to the shape of the kernel gradient which has a minimum around $r/h \sim 2/3$ and tends to zero at the origin. This means that the mutual repulsive force between particles (due to the pressure and the kernel gradient) tends to zero for neighbouring particles within the minimum. Thus as a result, two particles lying closer than the gradient's minimum will form a pair, eventually falling on top of each other (Price, 2012). Therefore, increasing N_{Ngb} will increase the parameter η and h will be stretched, moving the minimum to a larger distance $r \sim (2/3)h$ and allowing more particles to develop the pairing instability. Throughout our simulations, we used $N_{\text{Ngb}} = 60$ which is close to the optimal value for the cubic spline and safely below the ~ 100 particles needed to develop the pairing instability.

2.2.2 Interpolation Theory in SPH

Given the definition of density in equation (2.14), it is straightforward to think of SPH as an interpolating theory, in which the integral interpolant of any function $A(\boldsymbol{r})$ is defined as:

$$A_I(\boldsymbol{r}) = \int A(\boldsymbol{r}')\delta(\boldsymbol{r} - \boldsymbol{r}')d\boldsymbol{r}', \quad (2.17)$$

where the integration is performed over the entire space and δ is the Dirac delta function. This integral is approximated by replacing the delta function with a smoothing kernel W with finite width h i.e.

$$A_I(\boldsymbol{r}) = \int A(\boldsymbol{r}')W(\boldsymbol{r}-\boldsymbol{r}',h)d\boldsymbol{r}' + \mathcal{O}(h^2). \tag{2.18}$$

Where W approaches δ as $h \to 0$,

$$\lim_{h\to 0} W(\boldsymbol{r}-\boldsymbol{r}',h) = \delta(\boldsymbol{r}-\boldsymbol{r}') \tag{2.19}$$

and both W and δ satisfy the normalization condition. Furthermore, in SPH, the integral interpolant in equation (2.18) is discretized onto a finite set of interpolating points (SPH particles) by replacing the integral by a summation and ρdV by the particle's masses,

$$\begin{aligned} A_I(\boldsymbol{r}) &= \int \frac{A(\boldsymbol{r}')}{\rho(\boldsymbol{r}')}W(\boldsymbol{r}-\boldsymbol{r}',h)\rho(\boldsymbol{r}')d\boldsymbol{r}' \\ &\simeq \sum_{j=1}^{N_{\mathrm{Ngb}}} m_j \frac{A_j}{\rho_j} W(\boldsymbol{r}-\boldsymbol{r}_j,h). \end{aligned} \tag{2.20}$$

Equation (2.20) represents the basis of the SPH formalism, by choosing $A = \rho$ we'll obtain the definition of density given in (2.14). From the summation interpolant (2.20) we can obtain the interpolating value of any physical quantity at any point in space, for example, the pressure would be given by:

$$P(\boldsymbol{r}) = \sum_{j=1}^{N_{\mathrm{Ngb}}} m_j \frac{P_j}{\rho_j} W(\boldsymbol{r}-\boldsymbol{r}_j,h), \tag{2.21}$$

which will depend only on quantities defined at the position of the SPH particles. This interpolating theory allows us to compute gradients of such physical quantities at any position $\boldsymbol{r}$

$$\begin{aligned} \nabla A(\boldsymbol{r}) &= \int \frac{A(\boldsymbol{r}')}{\rho(\boldsymbol{r}')}W(\boldsymbol{r}-\boldsymbol{r}',h)\rho(\boldsymbol{r}')d\boldsymbol{r}' \\ &\simeq \nabla\left(\sum_{j=1}^{N_{\mathrm{Ngb}}} m_j \frac{A_j}{\rho_j} W(\boldsymbol{r}-\boldsymbol{r}_j,h)\right) \\ &\simeq \sum_{j=1}^{N_{\mathrm{Ngb}}} m_j \frac{A_j}{\rho_j} \nabla W(\boldsymbol{r}-\boldsymbol{r}_j,h), \end{aligned} \tag{2.22}$$

which depend on the physical quantities at the position of the SPH particles (m_j, ρ_j, P_j) and on the gradient of the density kernel ∇W with respect to $\boldsymbol{r}$. The same procedure applies for vector functions $\boldsymbol{A}(\boldsymbol{r})$ and its derivatives

$$\begin{aligned} \boldsymbol{A}(\boldsymbol{r}) &= \sum_j m_j \frac{\boldsymbol{A}_j}{\rho_j} W(\boldsymbol{r} - \boldsymbol{r}_j, h) \\ \nabla \cdot \boldsymbol{A}(\boldsymbol{r}) &= \sum_j m_j \frac{\boldsymbol{A}_j}{\rho_j} \cdot \nabla W(\boldsymbol{r} - \boldsymbol{r}_j, h) \\ \nabla \times \boldsymbol{A}(\boldsymbol{r}) &= -\sum_j m_j \frac{\boldsymbol{A}_j}{\rho_j} \times \nabla W(\boldsymbol{r} - \boldsymbol{r}_j, h) \\ \nabla^k A^i(\boldsymbol{r}) &= \sum_{j=1}^{N} m_j \frac{A_j^i}{\rho_j} \nabla^k W(\boldsymbol{r} - \boldsymbol{r}_j, h). \end{aligned} \tag{2.23}$$

These expressions should not be used as they are in an SPH implementation, since they generally lead to poor gradient estimates. A proper SPH implementation should consider errors due to higher order terms ($\mathcal{O}(h^2)$), but this equations will give us the main idea of how gradients are computed in SPH.

2.2.3 Evolution of Thermodynamical Properties in SPH

So far we have only seen how to determine the density from the distribution of SPH particles, and to compute the value of vectorial and scalar functions and its gradients at any point in space by means of the interpolating theory. As we saw from the summation interpolation, the value of a thermodynamical quantity A_i at the position of the i-th SPH particle can be expressed in terms of the quantity A_j, the mass m_j and density ρ_j at the position of the N_{Ngb} neighboring particles. Each SPH particle will contain information about the rest of the thermodynamical quantities, such as the pressure P_i, internal energy u_i, entropy s_i and temperature T_i. The relation between these quantities is given by the Equation of State (EoS), which in GADGET-2 is given by

$$u = \frac{A(s)}{\gamma - 1} \rho^{\gamma - 1}, \tag{2.24}$$

where γ is the adiabatic index defined by the ratio of specific heats and $A(s)$ is an entropic function which relates to the pressure and density as

$$P = \rho^2 \left(\frac{\partial u}{\partial \rho} \right)_s = A(s) \rho^{\gamma}. \tag{2.25}$$

Thus, once the density ρ_i is defined, we only need the internal energy u_i to determine the entropic function $A_i(s)$ and the pressure P_i at the position of a particle. SPH particles in GADGET-2, require three initial properties given by the user, internal energy u_i, mass m_i and position $\boldsymbol{r}_i$, with which the density ρ_i can be obtained.

In SPH, the evolution of the density at the position of a particle ρ_i is not done by solving a differential equation, but by calculating at each time step, the distribution of the closest N_{Ngb} particles contributing to the density. The density $\rho_i(r_{ij}, h_i)$ will change accordingly to the change in r_{ij} and h_i also determined by the neighboring particles. This can be seen by taking the time derivative of ρ_i

$$\begin{aligned}
\frac{d\rho_i}{dt} &= \frac{d}{dt}\left(\sum_{j=1}^{N_{\text{Ngb}}} m_j W_{ij}(r_{ij}, h_i)\right) \\
&= \sum_{j=1}^{N_{\text{Ngb}}} m_j \frac{d}{dt}\left(W_{ij}(r_{ij}, h_i)\right) \\
&= \sum_{j=1}^{N_{\text{Ngb}}} m_j \left(\frac{\partial W_{ij}}{\partial r}\frac{dr_{ij}}{dt} + \frac{\partial W_{ij}}{\partial h_i}\frac{dh_i}{dt}\right) \\
&= \sum_{j=1}^{N_{\text{Ngb}}} m_j \left(\boldsymbol{v}_{ij}\cdot\nabla_i W_{ij}(h_i) + \frac{\partial W_{ij}}{\partial h_i}\frac{d}{dt}\left[\eta\left(\frac{m_i}{\rho_i}\right)^{1/3}\right]\right) \\
&= \sum_{j=1}^{N_{\text{Ngb}}} m_j \left(\boldsymbol{v}_{ij}\cdot\nabla_i W_{ij}(h_i) + \frac{\partial W_{ij}}{\partial h_i}\left[-\frac{h_i}{3\rho_i}\frac{d\rho_i}{dt}\right]\right) \\
&= \frac{1}{\Omega_i}\sum_{j}^{N_{\text{Ngb}}} m_j \boldsymbol{v}_{ij}\cdot\nabla_i W_{ij},
\end{aligned} \tag{2.26}$$

where $\boldsymbol{v}_{ij} = \boldsymbol{v}_i - \boldsymbol{v}_j$ and

$$\Omega_i \equiv \left(1 + \frac{h_i}{3\rho_i}\frac{\partial W_{ij}}{\partial h_i}\right). \tag{2.27}$$

Here we have made use of some properties of the spherically symmetric kernel $W_{ij}(r_{ij})$ and spherically symmetric functions which can be found in Price (2012) and Rooswog (2009). Equation (2.27) shows that the change in density $\delta\rho$ is proportional to the change in position due to the term $\boldsymbol{v}_{ij}\delta t$. Thus, we need to obtain the equations of motion for the SPH particles in order to get the accelerations $\boldsymbol{a}_i = d\boldsymbol{v}_i/dt$, velocities $\boldsymbol{v}_i$ and positions $\boldsymbol{r}_i$ of the particles.

SPH particle's Equations of Motion

In order to obtain the equations of motion of the SPH particles, we start by writing down the Lagrangian of a discrete set of point masses composed by the kinetic and the potential energies (T and V respectively):

$$L = T - V = \sum_k m_k \left[\frac{1}{2} v_k^2 - (u_k + \Phi_k) \right], \tag{2.28}$$

where $v_k = |d\mathbf{r}_k/dt|$ is the velocity of each SPH particle, $u_k(\rho, s)$ is its internal energy (depending on density and entropy) and Φ_k is its gravitational potential (both per unit mass). We should keep in mind that when obtaining the equations of motion for each particle there could be extra terms due to magnetic forces or any other term included in the potential energy V. Thus, from (2.28) we can construct the Hamiltonian $H = \boldsymbol{p} \cdot \dot{\boldsymbol{q}} - L$ and obtain the equations of motion for the i-th particle through the principle of minimum action:

$$\frac{d}{dt} \left(\frac{\partial L}{\partial \boldsymbol{v}_i} \right) - \frac{\partial L}{\partial \boldsymbol{r}_i} = 0, \tag{2.29}$$

where $\boldsymbol{v}_i$ and $\boldsymbol{r}_i$ are the velocity and position of the particle i at time t. Up to this point we haven't considered any approximation, which makes this an exact solution that will conserve energy and linear and angular momentum. Any error will come from the time integration scheme. Moreover, as we're assuming L is differentiable we exclude the possibility of any discontinuous solution to the equations of motion. Therefore, any discontinuity present in the system (like a shock) requires an appropriate treatment to account for it, and such discontinuities must be softened in a scale $\gtrsim h$ in order to treat them as continuous.

The equations of motion are obtained by calculating the partial derivatives in (2.29):

$$\begin{aligned} \frac{\partial L}{\partial \boldsymbol{v}_i} &= m_i \boldsymbol{v}_i; \\ \frac{\partial L}{\partial \boldsymbol{r}_i} &= -\sum_j m_j \left(\left. \frac{\partial u_j}{\partial \rho_j} \right|_s \frac{\partial \rho_j}{\partial \boldsymbol{r}_i} + \frac{\partial \Phi_j}{\partial \boldsymbol{r}_i} \right), \end{aligned} \tag{2.30}$$

For obtaining $\partial L/\partial \boldsymbol{r}_i$ we have to make use of the EoS (2.24) and some properties of the kernel W_{ij} that can be found in Price (2012) and Rooswog (2009), which

results in

$$\frac{\partial L}{\partial \boldsymbol{r}_i} = -\sum_j m_j \left[\frac{P_j}{\Omega_j \rho_j^2} \sum_k m_k \frac{\partial W_{jk}(h_j)}{\partial \boldsymbol{r}_i} (\delta_{ji} - \delta_{ki}) + \frac{\partial \Phi_j}{\partial \boldsymbol{r}_i} \right], \tag{2.31}$$

where δ_{ki} is the Kronecker delta for the indexes k and i. After some algebra on this result and substituting in (2.29) we can express the equation of motion for particle i as:

$$\begin{aligned} \frac{d\boldsymbol{v_i}}{dt} &= -\sum_j m_j \left[\frac{P_i}{\Omega_i \rho_i^2} \frac{\partial W_{ij}(h_i)}{\partial \boldsymbol{r}_i} + \frac{P_j}{\Omega_j \rho_j^2} \frac{\partial W_{ij}(h_j)}{\partial \boldsymbol{r}_i} + \frac{\partial \Phi_j}{\partial \boldsymbol{r}_i} \right] \\ &= -\sum_j m_j \left[\frac{P_i}{\Omega_i \rho_i^2} \nabla_i W_{ij}(h_i) + \frac{P_j}{\Omega_j \rho_j^2} \nabla_i W_{ij}(h_j) + \nabla_i \Phi_j \right] \end{aligned} \tag{2.32}$$

Any other term due to magnetic fields or another physical interaction between particles should be introduced as an additional term to the Lagrangian (2.28) and therefore, it will translate in extra terms on (2.32). From this equation of motion it can be proved that linear and angular momentum are exactly conserved in this SPH formulation and errors imprinted on such quantities will come only from numerical integration of the problem and/or CPU round up errors[3]. Equation (2.32) fully defines reversible fluid dynamics in SPH, i.e. the entropy A_i of each particle will remain constant.

In order to account for the presence of shocks and discontinuities in the equations of motion of SPH particles, we must include a term which accounts for the entropy (heat) generated by the viscous interaction of the particles. This is done by means of including an artificial viscosity which in GADGET-2 translates into a viscous force

$$\left. \frac{d\boldsymbol{v}_i}{dt} \right|_{\text{visc}} = -\sum_{j=1}^{N} m_j \Pi_{ij} \nabla_i \bar{W}_{ij}, \tag{2.33}$$

where Π_{ij} is non-zero and positive only when particles approach each other in physical space and $\bar{W}_{ij} = \frac{1}{2}(W_{ij} + W_{ji}) = \frac{1}{2}[W(r_{ij}, h_i) + W(r_{ji}, h_j)]$. Π_{ij} denotes the Monaghan-Balsara form of the artificial viscosity (Monaghan & Gingold, 1983; Balsara, 1995) given by

$$\Pi_{ij} = \begin{cases} (-\alpha c_{ij} \mu_{ij} + \beta \mu_{ij}^2)/\rho_{ij} & \text{if } \boldsymbol{v}_{ij} \cdot \boldsymbol{r}_{ij} < 0 \\ 0 & \text{otherwise} \end{cases}, \tag{2.34}$$

[3]Numerical integration errors will appear due to approximations made in the integration scheme or to not small enough time steps, meanwhile round up errors will intrinsically appear when only a finite number of digits is available for every real number.

with

$$\mu_{ij} = \frac{h_{ij}\boldsymbol{v}_{ij}\cdot\boldsymbol{r}_{ij}}{r_{ij}^2}. \tag{2.35}$$

Where c_{ij}, h_{ij} and ρ_{ij} denote the arithmetic means of the sound speed, smoothing length and density involving particles i and j. The strength of the viscosity is regulated by the parameters α and β, with typical values of $\alpha \simeq 0.5 - 1.0$ and $\beta = 2\alpha$. From this definition, Monaghan (1997) derived a slightly modified parametrization of the viscosity, which is used by default in GADGET-2

$$\Pi_{ij} = -\frac{\alpha}{2} w_{ij} \frac{v_{ij}^{\rm sig}}{\rho_{ij}}, \tag{2.36}$$

where $v_{ij}^{\rm sig} = c_i + c_j - 3w_{ij}$ represents the signal velocity between two particles (based on an analogy with the Riemann problem) and $w_{ij} = \boldsymbol{v}_{ij}\cdot\boldsymbol{r}_{ij}/r_{ij}$ is the relative velocity projected on to the separation vector defined only when particles are approaching each other, i.e. for $\boldsymbol{v}_{ij}\cdot\boldsymbol{r}_{ij} < 0$, otherwise $w_{ij} = 0$. This results in a viscosity of the form:

$$\Pi_{ij} = -\frac{\alpha}{2} \frac{(c_i + c_j - 3w_{ij})w_{ij}}{\rho_{ij}}, \tag{2.37}$$

which reduces to equation (2.34) when $\beta = (3/2)\alpha$ and w_{ij} is replaced with μ_{ij}. The main difference in this definition for the artificial viscosity lies in the additional factor h_{ij}/r_{ij} that μ_{ij} carries with respect to w_{ij}. This factor weights the viscous force making it more intense for particle pairs with small separations. Springel (2005) found that the modified viscosity (2.37) gives equivalent or improved results in their tests compared with the standard formulation of equation (2.34), this has the advantage that in simulations with dissipation, the occurrence of very large viscous acceleration is reduced, resulting in a more efficient and stable time integration.

Now we need to evolve another of the thermodynamical properties in order to get a complete characterization of the fluid's properties. Thus, in order to evolve the thermodynamical properties of the SPH particles given by (2.24) and (2.25), we must evolve in time the internal energy u_i or the entropic function $A_i(s)$ of the particles. Evolving the density and either u or A will determine completely the evolution of the SPH's thermodynamic quantities. In GADGET-2, the evolution of the thermodynamic quantities is followed by formulating SPH in terms of dynamical equations for the entropic function $A(s)$ rather than the internal energy. Springel & Hernquist (2002) presented the formulation used in GADGET-2 (Springel, 2005) on which the specific entropy s of a fluid element is characterized in terms of the entropic function $A(s)$ defined in (2.25). In this approach the temperature can be obtained from the EoS in equation (2.24).

By taking the time derivative of $A(s)$ and considering an adiabatic flow where $A(s)$ is conserved and there are no sources of heat ($du/dt = 0$), we must include a viscosity term in order to account for entropy generation from the heat produced in viscous interactions. Thus, the change in the entropic function proposed by Springel & Hernquist (2002) is given by:

$$\frac{dA_i}{dt} = \frac{\gamma - 1}{\rho_i^{\gamma}} \frac{du}{dt} + \frac{1}{2} \frac{\gamma - 1}{\rho_i^{\gamma - 1}} \sum_{j=1}^{N} m_j \Pi_{ij} \boldsymbol{v}_{ij} \cdot \nabla_i \bar{W}_{ij}. \tag{2.38}$$

Equation (2.38) states that entropy is generated only by the artificial viscosity in shocks, and by external sources of heat (when $du/dt \neq 0$). In the absence of sink and source terms ($du/dt = 0$) only the second term in equation (2.38) remains. This term transforms kinetic energy irreversibly into heat. This approach provides tight control on sources of entropy and it is possible to guarantee that the specific entropy of a SPH particle can only grow in time (assuming negligible contributions from external sinks or sources of entropy). Evolving equation (2.38) is equivalent to solving the gas dynamics by means of the internal energy in the continuum limit ($N >> 1$). However in practice, as SPH estimates are approximated by a finite number of neighbors, the two formulations exhibit some differences. Hernquist (1993) showed that while integrating the internal energy equation results in a good energy conservation, the entropy of the system is not conserved even for purely adiabatic flows. On the other hand if the entropy is integrated, the total energy is not necessarily conserved, while the entropy is.

2.3 Time Integration

The signal velocity approach for the viscosity given in (2.37) naturally leads to an hydrodynamical time step very similar to the Courant time step used in Eulerian simulations

$$\Delta t_i^{\text{hyd}} = \frac{C_{\text{courant}} h_i}{\max(c_i + c_j - 3w_{ij})}. \tag{2.39}$$

The parameter C_{courant} must be set on every SPH simulation in GADGET-2[4], and the maximum in (2.39) is determined with respect to all neighbors j of particle i.

In order to reduce spurious angular momentum transport in the presence of shear flows, GADGET-2 includes an additional viscosity limiter (Balsara, 1995;

[4]Trough all of our simulations the Courant parameter was set to a value $C_{\text{courant}} = 0.2$ which is close to the value of 0.15 suggested in the users manual of the code GADGET-2.

Steinmetz, 1996). The limiter consists in multiplying the viscous tensor with $(f_i + f_j)/2$, where

$$f_i = \frac{|\nabla \times \boldsymbol{v}|_i}{|\nabla \cdot v| - i + |\nabla \times \boldsymbol{v}|_i} \tag{2.40}$$

is a measure of the relative amount of shear in the flow around particle i based on standard SPH estimates for divergence and curl (Monaghan, 1992).

Besides the hydrodynamical time step $\Delta t_i^{(\mathrm{hyd})}$, the gravitational interactions of the particles require an appropriate gravitational time step Δt_{grav} that might not have the same value as the hydrodynamical one. In GAGDET-2 the time step for collisionless particles is

$$\Delta t_{\mathrm{grav}} = \min \left[\Delta t_{\mathrm{max}}, \left(\frac{2\eta\epsilon}{|\boldsymbol{a}|} \right)^{1/2} \right] \tag{2.41}$$

where η is an accuracy parameter, ϵ is the gravitational softening, $\boldsymbol{a}$ is the acceleration of the particle and Δt_{max} is the maximum allowed time step, which must be set to a small fraction of the dynamical time of the system at issue. For SPH particles, the minimum between Δt_{grav} and Δt_{hyd} is used for evolving their equations of motion.

Due to the Hamiltonian nature of the system, it makes sense to use a symplectic integrator to solve the evolution of the equations of motion. The symplectic integrators are by definition, canonical transformations, which preserve the Hamiltonian structure of the system. This integrators are widely used to study long term chaotic Hamiltonian systems like the N-body problem. GADGET-2 uses a second order leapfrog integrator (i.e. the error is $\mathcal{O}(\Delta t^3)$), that conserves exactly angular momentum and is symplectic, which means that it possesses global stability and the energy is conserved. The leapfrog integrator solves the equations of motion of the i-th particle by means of one of the following algorithms:

$$\begin{aligned} \boldsymbol{v}^i_{n+1/2} &= \boldsymbol{v}^i_n + \frac{1}{2}\Delta t \boldsymbol{f}^i(\boldsymbol{x}^i_n) \\ \boldsymbol{x}^i_{n+1} &= \boldsymbol{x}^i_n + \Delta t \boldsymbol{v}^i_{n+1/2} \qquad \text{Drift-Kick-Drift (DKD) leapfrog} \\ \boldsymbol{v}^i_{n+1} &= \boldsymbol{v}^i_{n+1/2} + \frac{1}{2}\Delta t \boldsymbol{f}^i(\boldsymbol{x}^i_{n+1}), \end{aligned} \tag{2.42}$$

or

$$\begin{aligned} \boldsymbol{x}^i_{n+1/2} &= \boldsymbol{x}^i_n + \frac{1}{2}\Delta t \boldsymbol{v}_n \\ \boldsymbol{v}^i_{n+1} &= \boldsymbol{v}^i_n + \Delta t \boldsymbol{f}^i(\boldsymbol{x}^i_{n+1/2}) \qquad \text{Kick-Drift-Kick (KDK) leapfrog} \\ \boldsymbol{x}^i_{n+1} &= \boldsymbol{x}^i_{n+1/2} + \frac{1}{2}\Delta t \boldsymbol{v}_{n+1} \end{aligned} \tag{2.43}$$

where $\boldsymbol{x}_n^i, \boldsymbol{v}_n^i$ and $\boldsymbol{f}^i(\boldsymbol{x}_n^i)$ are the position, velocity and acceleration of the i-th particle at the time t_n (with $n = 0, 1, 2, ...$ and $t_n < t_{n+1}$). The acceleration $\boldsymbol{f}^i(\boldsymbol{x}_n^i)$ is the acceleration due to the forces acting on the particle i with position $\boldsymbol{x}_n^i$ at the time t_n. These algorithms show the leapfrogging nature of the integrators, in the KDK scheme, the first step is to advance the position to its new value at $t_{n+1/2}$ (kick), then the velocity is updated to its value at a time t_{n+1} (drift), leapfrogging the position which remains at an earlier time $t_{n+1/2}$. At the end, both quantities catch up by updating the position to t_{n+1} (kick). The DKD scheme consists on doing first a Drift (update the velocity one half time step), then a kick (update the position one time step) and then another drift (update the velocity another half time step). GADGET-2 uses the KDK leapfrog integrator given that it shows smaller energy errors in some test problems like the 2 body problem.

The integration in GADGET-2 is done by discretizing the time steps in a power of two hierarchy, where all time steps are a power of two subdivision of a global time step determined by the initial and final time of the simulation. This is done in order to synchronize the evolution of the particles and to perform the kicks and drifts at half the time step during the leapfrog integration.

2.4 Stability Tests for GADGET-2

In order to test the general stability of GADGET-2 and if the modifications previously noted worked properly, we ran some tests to check how accurately could GADGET-2 solve the problem of hydrostatic equilibrium of a non-rotating polytropic star with EoS

$$P = K\rho^{\gamma} \qquad \text{with } \gamma = 1 + 1/n = 5/3. \tag{2.44}$$

The polytropic star shouldn't present increasingly large instabilities breaking the expected spherical symmetry, and all of the important quantities should be conserved (energy linear and angular momentum). We obtained the structure of $2\ M_{\odot}$ polytropic stars by solving the hydrostatic equilibrium equation (Lane-Emden equation (2.45)) for a polytrope with polytropic index n given by:

$$\begin{aligned} &\frac{1}{\xi^2}\frac{d}{d\xi}\left(\xi^2\frac{d\theta}{d\xi}\right) + \theta^n = 0 \\ &\text{where,} \qquad \xi = rA = r\left(\frac{4\pi G\rho_c^2}{(n+1)P_c}\right)^{1/2} = r\left(\frac{4\pi G}{(n+1)K\rho_c^{1/n-1}}\right)^{1/2} \\ &\text{and} \qquad \rho = \rho_c\theta^n. \end{aligned} \tag{2.45}$$

Here P_c and ρ_c represent the central values (at $r = 0$) for the pressure and density of the star. Thus, in order to solve equation (2.45) with polytropic index $n = 3/2$ and obtain $\theta(\xi)$, we must impose the right boundary conditions at the center and the surface of the star, the central density ρ_c, and the parameter K or the central pressure P_c of the star. This will determine the value of the parameter A which will be used to get the right units from ξ. The boundary conditions must satisfy that $\rho(r = 0) = \rho_c$, therefore at $\xi = rA = 0$, $\theta(0) = 1$. We can also obtain the value of $d\theta/d\xi = \theta'$ at $\xi = 0$ by noticing that the mass near the center of the star is $m(r) \simeq 4\pi\rho_c r^3/3$, which combined with the hydrostatic equilibrium equation $dP/dt = -Gm(r)\rho/r^2$, and the fact that $(dP/dr)_{r=0} = d\rho/dr$ for our polytropic star, results in $\theta'(0) = 0$. The outer boundary conditions require that the pressure and density outside the star's surface ($R = \xi_*/A$) is zero $P(\xi_*/A) = \rho(\xi_*/A) = 0$ $\Rightarrow \theta(\xi_*) = 0$.

Equation (2.45) can be solved numerically (and analytically for some n values) to obtain $\theta(\xi)$ and $\theta'(\xi)$ for $0 \leq \xi \leq \xi_*$ (both quantities are dimensionless), just using the boundary conditions stated above and a value for n, but without giving values to the parameters ρ_c, K. Figure 2.3 shows the solution θ^n as a function of ξ for $n = 3/2$. This solution can be scaled by ρ_c and $A(\rho_c, K)$ to give $\rho(r)$ and thus $P(r)$ or $u(r)$.

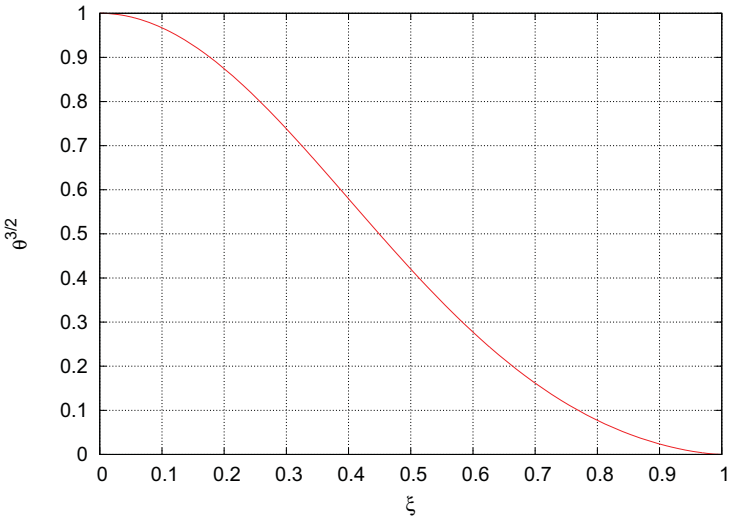

Figure 2.3: Solution to the Lane-Emden equation (2.45) for θ^n as a function of ξ. At this point only the boundary conditions and the value $n = 3/2$ have been used. From this curve it is possible to obtain $\rho(r)$, $P(r)$ and $u(r)$ by choosing the parameters ρ_c and K or M.

To scale the solution and obtain ρ and r in the proper units, we must define the

value of K and ρ_c. But instead of defining K we can use a relation between the mass M of the star and the parameter A, obtained by calculating the mass of the star with radius $R = \xi_*/A$:

$$\begin{aligned} M &= 4\pi \int_0^R r^2 \rho(r) dr \\ &= 4\pi \rho_c A^{-3} \int_0^{\xi_*} \xi^2 \theta^n d\xi \\ &= -4\pi \rho_c A^{-3} \int_0^{\xi_*} \frac{d}{d\xi}\left(\xi^2 \frac{d\theta}{d\xi}\right) d\xi \\ &= 4\pi \rho_c A^{-3} \xi_*^2 \left.\frac{d\theta}{d\xi}\right|_{\xi_*} \end{aligned} \tag{2.46}$$

As we can see from the latest equation, the mass M is defined by A and by the solutions ξ_* and $\theta'(\xi_*)$, which are obtained from solving equation (2.45). Thus, we can use this relation to obtain the parameter K as a function of the mass M and central density ρ_c we would like our polytropic star to have.

$$K = \frac{4\pi G}{(n+1)} \left(\frac{M \rho_c^{(n-3)/2n}}{4\pi\ \xi_*^2\ \theta'(\xi_*)} \right)^{2/3} . \tag{2.47}$$

From the EoS $P = K\rho^\gamma$ we can obtain the pressure $P(r)$ and internal energy $u(r)$ radial profiles, and we will have a complete solution for the hydrodynamical equilibrium of a non rotating polytropic star of mass M and central density ρ_c.

To emulate conditions similar to the ones expected in a Collapsar, we used the central density $\rho_c \simeq 2.5 \times 10^9$ g cm^{-3} from the PreSN model HE16A from Woosley & Heger (2006), and constructed a polytropic star with 2 $M_\odot$. Once the 1D radial profiles for the density, pressure and internal energy were obtained, we mapped them into a 3D particle distribution of $N_{\rm SPH}$ particles that followed the original mass distribution. We did so by means of a MonteCarlo accept/reject procedure, which introduced a random initial perturbation to the system due to the randomness of the sample, which produced a slightly asymmetrical distribution of SPH particles. The intensity of these perturbations can be reduced by increasing the number of particles, but they will always be present. We used 3 different resolutions, $N_{\rm SPH} = 50000, 500000$ and 1000000 particles but most of the results come from simulations with $N_{\rm SPH} = 500000$ particles which showed no difference with the higher resolution simulations.

Once the 3D polytropic stars in hydrostatic equilibrium were mapped by SPH particles following the $\rho(r)$ and $u(r)$ profiles, we studied their evolution during

several dynamical timescales (at least 10), in order to look for any important growth of an instability that could alter the equilibrium of the system. For our simulations we used natural units, which consists in considering $G = 1$ and scaling all units with the mass $M_p = 2M_\odot = 3.98 \times 10^{33}$ g, length $R_p = 1.3099 \times 10^8$ cm and dynamical time scale $t_{dyn} = (R_p^3/GM_p)^{1/2} = 0.092$ s, of the system.

2.4.1 Gravitational Force Tests

We made 3 simulations with the same initial conditions, but with different values for the parameter Ω_M, which increases the accuracy of the gravitational force calculation for smaller values. The values employed where $\Omega_M = 0.5\ M_p, 0.05\ M_p$ and $0.005\ M_p$, accounting for $50\%, 5\%$ and 0.5% of the polytropic star mass respectively. In the problem we are dealing with, the first level nodes will consist on dividing the cube containing the polytropic star into 8 equally sized cubes containing roughly the same amount of mass. Thus, considering that the polytropic star will remain in hydrostatic equilibrium, the mass contained in each one of these nodes will never be significantly higher than $\sim M_p/8$. Therefore, at all times, the mass contained in the nodes will always be smaller than Ω_M, and the simulation with $\Omega_M = 0.5\ M_p$ will behave like a simulation where the mass opening node criteria is not used.

Shown in the left panels of figure 2.4 are the density profiles $\rho(r)$ at times $t = 0$ (top) and $t = 21\, t_{\rm dyn}$ (bottom) for the 1D Lane-Emden solution (black line), and the 3D SPH particle distribution generated (red line), together with the SPH densities ρ_i calculated for each of the $N_{\rm SPH}$ particles (blue dots). They correspond to the simulation with $\Omega_M = 0.5\ M_p$. As can be seen, at $t = 0$ the 3D SPH particle distribution generated has a density profile $\rho(r)$ (red line) that goes almost exactly like the one expected for the 1D Lane-Emden solution (black line), even when the SPH particles's densities ρ_i are scattered around these lines. This scattering is due to the fact that the number of particles $N_{\rm SPH}$ is not big enough to prevent clustering or voids obtained when generating the 3D particle distribution from a discrete set of "random" point masses following the 1D mass distribution. Thus, given that ρ_i is calculated from the local distribution of $N_{\rm Ngb}$ particles, any local clustering or void of particles will result in slightly higher or lower SPH densities $\rho_i(r)$ than expected from the 1D mass distribution $\rho(r)$. This effect can also be appreciated in the column density map along the Z axis (in CGS) shown in the top right panel from figure 2.4, which is seen as noise in the map that reduces the smoothness in the color transition.

The bottom panels of figure 2.4 show the density profile of the polytropic star (bottom left) and the column density map along the Z axis at $t = 21\, t_{\rm dyn}$. There,

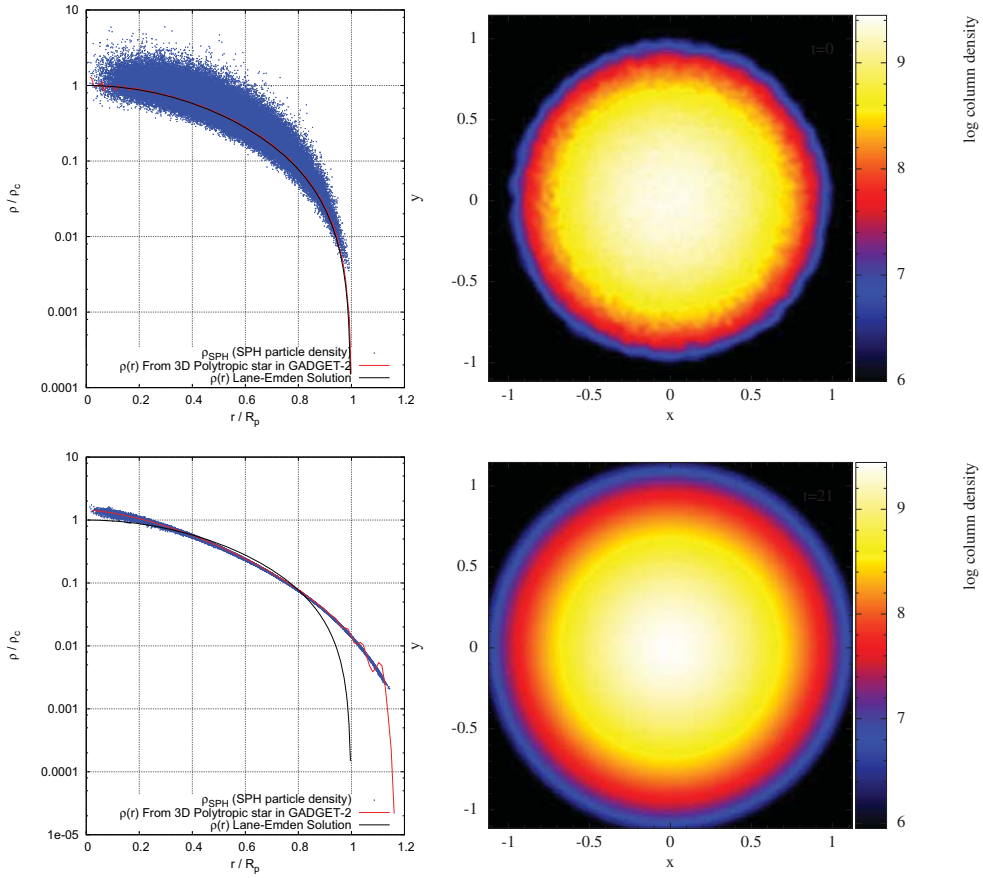

Figure 2.4: 3D polytropic star density profiles $\rho(r)$ at $t = 0$ (top left) and 21 $t_{\rm dyn}$ (bottom left), and their corresponding column density maps (in CGS) along the Z axis (right panels). The black line on the left panels shows $\rho(r)$ for the 1D Lane-Emden solution of our 2 $M_{\odot}$ polytropic stars meanwhile the red line shows $\rho(r)$ obtained from the 3D SPH particle distribution and the blue points represent the SPH density at the position of each of the SPH particles. The density profiles are scaled by the central density ρ_c and the initial radius of the star R_p.

SPH's Hamiltonian nature can be fully appreciated. The particles "naturally" arrange into a more stable configuration, trying to correct the small inhomogeneities from the original particle distribution. This translates in a density profile $\rho(r)$ that differs from the 1D Lane-Emden solution. The particle distribution is also affected by the 3D nature of the problem which allows any departure from spherical symmetry to give rise to forces not contemplated in the simple 1D Lane-Emden equation for hydrostatic equilibrium. An important feature to notice is that there is

no visible symmetry breaking in the system, except from a small shift of the star's center from the origin. This might be due to the initially non uniform distribution of particles obtained from the Monte Carlo 3D mapping of the density profile. All simulations had very similar behavior showing no sign of symmetry breaking and presenting a small expansion of the polytropic star.

In figure 2.5, we show the evolution of the normalized total energy deviation $(E_{\text{tot,init}} - E_{\text{tot}})/E_{\text{tot,init}}$ (top panel) and the total angular momentum (bottom panel) for our 3 simulations of non rotating polytropic stars. The difference between simulations is the value of the parameter Ω_M. The red line corresponds to $\Omega_M \simeq 0.5 M_p$, the green and blue lines correspond to simulations with $\Omega_M = 0.05\ M_p$ and $0.005\ M_p$ respectively, which ensures that nodes with mass $M_n \geq \Omega_M$ are further explored to obtain a more accurate force estimation. As shown in figure 2.5 the total energy shows variations as large as 0.6% in all three simulations, and the total angular momentum (initially zero) is also conserved with variations smaller than 0.00005. It is important to notice that the angular momentum conservation seems to be better when implementing a smaller Ω_M, and when dealing with accretion, such process is also affected by the selection of this parameter.

It is also possible to compare the gravitational force computation obtained by the Grav-Tree approach with the exact gravitational force computation obtained from N-body interactions. By compiling the `forcetest` option in the **Makefile**, a routine in GADGET-2 selects randomly at each time step, a percentage of the particles in the simulation (defined by the user as a parameter) and calculates their gravitational force by their direct interaction with all the particles. This of course increases the computational time required but can be used for estimating the error for only a small part of the simulation. The output of this test is a file containing the exact and the Grav-Tree forces of the N_{test} particles selected at each time step, from which we can obtain the average deviation of the Grav-Tree force with respect to the exact force at each time step.

We used this routine to estimate the deviation from the exact gravitational force for different values of the opening node parameter Ω_M. Figure 2.6 shows the evolution of the average normalized error on the gravitational force defined by

$$\frac{\Delta F}{F_{\text{Nb}}} = \frac{F_{\text{Nb}} - F_{\text{Tree}}}{F_{\text{Nb}}}, \tag{2.48}$$

for the three different values of $\Omega_M = 0.5\ M_p$, $0.05\ M_p$ and $0.005\ M_p$. Here ΔF is the difference between the exact force F_{Nb} and the Grav-Tree force F_{Tree}. As we see from figure 2.6 the error for $\Omega_M = 0.5\ M_p$ and 0.05 oscillates around 0.2%

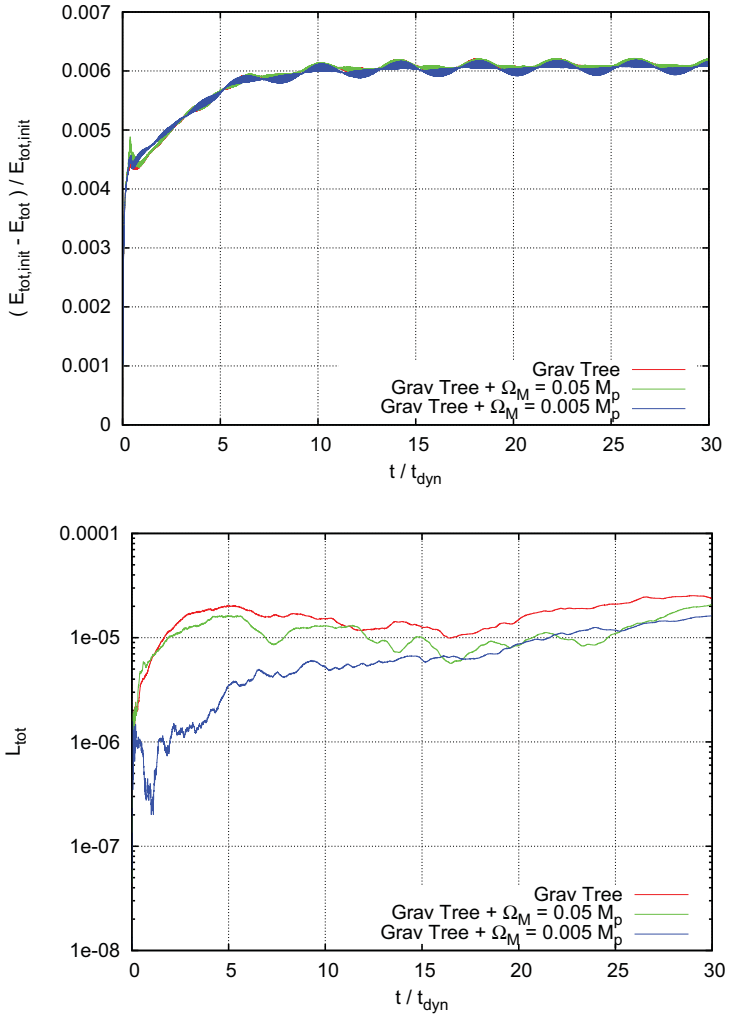

Figure 2.5: On the top panel the total energy deviation ($E_{\rm tot,init} - E_{\rm tot}$) normalized to the initial total energy (left), showing variations up to $0.006\ E_{\rm tot,init}$. On the bottom panel the total angular momentum L_{tot} showing variations up to 3×10^{-5} with respect to $L_{\rm tot,init} = 0$.

and for Ω_M it is reduced to $\sim 0.01\%$. Bottom panel from figure 2.6 shows what is the fraction of particles that have force error $\Delta F/F_{\rm Nb}$ larger than shown in the x axis. The black lines correspond to 50%, 90% and 99% of the particles (from top to bottom). This figure shows that $N_{\rm SPH} \times 10^{-5}$ particles have force errors smaller than 1%, which represents 99.999% of the SPH particles.

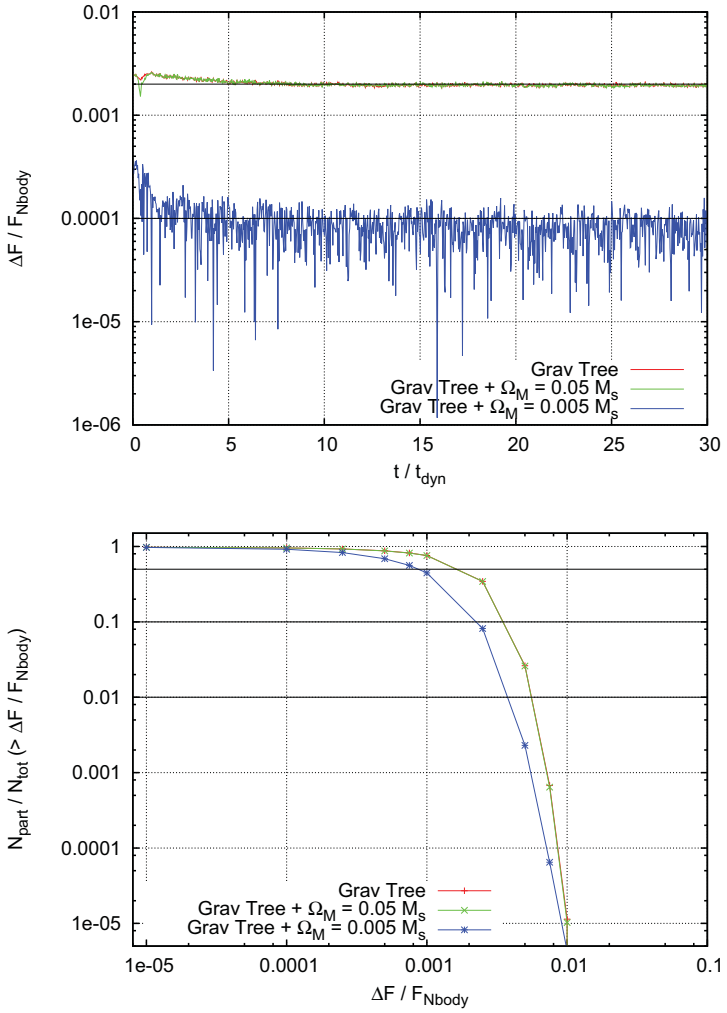

Figure 2.6: On top, the evolution of the average normalized error on the gravitational force $\Delta F/F_{\rm Nb} = (F_{\rm Nb} - F_{\rm Tree})/F_{\rm Nb}$ for the three models with different Ω_M. Black lines of constant $\Delta F/F$ are only shown as reference. On the bottom panel, the fraction of particles showing force errors greater than the corresponding $\Delta F/F_{\rm Nb}$ on the x axis. The crossing points of the black and colored lines show the top limit error for 50%, 90% and 99% of the particles (from top to bottom). Less than 0.00001% of the particles show force errors larger than 1% on all simulations.

From figure 2.6 we see that it is a good idea to lower the value of Ω_M up to $\sim 0.005 M_p$ when an accurate gravitational force computation is needed. We should keep in mind that the distribution of SPH particles used in these simulations is fairly

spherically symmetric, and we don't expect to have excessively large errors on the gravitational force computations. Nevertheless, in a highly asymmetric distribution of particles, force errors could become larger and a smaller value of the parameter Ω_M could be needed. The rest of our simulations employed $\Omega_M = 0.005\, M_p$ which gives better estimates to the gravitational force and still only doubles the CPU time required for the simulations.

2.5 Collapse and Accretion of Rotating Polytropic Envelopes

Working towards a Collapsar model we proceeded to study the collapse of such polytropic stars by removing half the internal energy $E_{\rm st}$ needed for a stable solution (i.e. decreasing the pressure). All models were also given a rigid body rotation along the Z axis by assigning a constant angular velocity Ω_0 to the star. Due to the diminished pressure (internal energy) of the star, it will collapse (contract) in order to reach equilibrium. An increasing rotation rate will induce a shallower collapse due to the presence of the centrifugal force.

Results from such simulations are shown in Figure 2.7 where the evolution of the potential and total energy for simulations with different rotation rates ($\Omega_0 = 2.0866, 1.5650, 1.0433, 0.52166$ and 0.13041 in code units) is shown. Increasing angular momentum translates into a shallower collapse shown in the potential energy, meanwhile the total energy remains almost constant at least for the first 10 dynamical times. The potential energy in figure 2.7 will help us to identify a limit on the maximum angular momentum Ω_0 that the envelope should have to experience a collapse (contraction). Apparently for $\Omega_0 \lesssim 1.5$ the envelope must still collapse to reach equilibrium, but for higher rotation rates the star will barely contract or even expand to larger radii.

The next step in building the initial conditions of a Collapsar scenario is to place a sink particle that acts as a blackhole (BH) and accretes any SPH particle at a radius $r \leq r_{\rm acc}$. GADGET-2 allows the use of sink or boundary particles (type$= 5$) which interact only by means of the gravitational force. Thus, we made use of such particles and modified a subroutine to handle the accretion of gas particles.

2.5.1 Accretion in GADGET-2

The routine **blackhole.c** is the one in charge of handling the accretion of gas particles onto the BH. This subroutine acts before the gravitational forces and the SPH

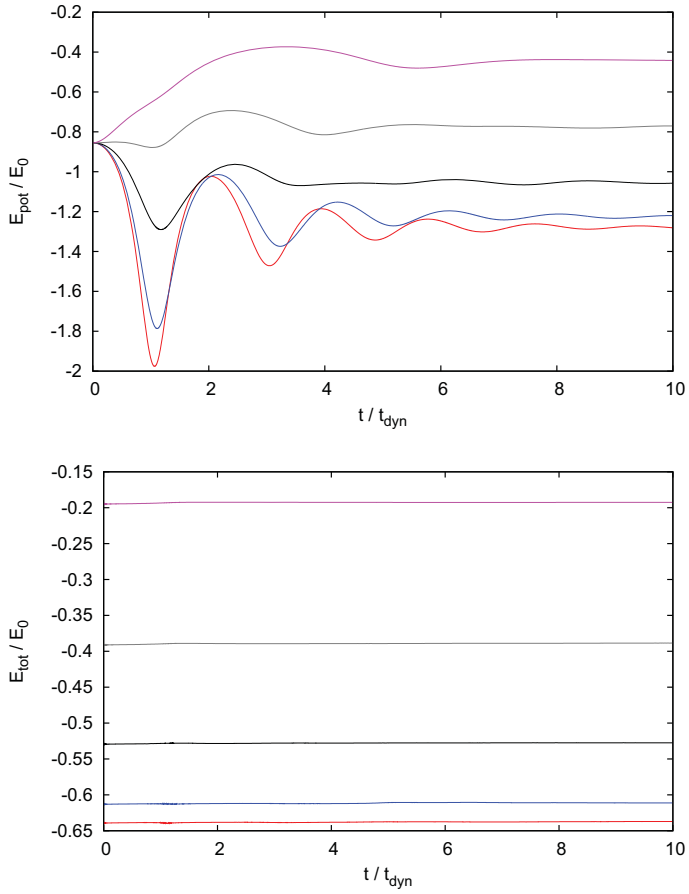

Figure 2.7: Potential and total energies (top and bottom respectively) for the collapse of $\gamma = 5/3$ polytropes with low internal energy (half the value needed for a stable solution $E_{\rm int} = E_{\rm st}/2$). Each curve represents different rotation rates (rigid body angular velocity); $\Omega_0 = 2.0866, 1.5650, 1.0433, 0.52166$ and 0.13041 (purple, gray, black, blue and red lines respectively).

properties are computed, to avoid that particles lying within the accretion radius $r_{\rm acc}$ are accounted in the gravity force and SPH calculations. During the accretion process, a search is performed through all SPH particles in the simulation. Any particle lying at a distance $r < r_{\rm acc}$ will be considered as accreted. The properties of the accreted SPH particles, such as mass, linear momentum and position of the center of mass are stored in the variables $M_{\rm acc}, \boldsymbol{p}_{\rm acc}$ and $\boldsymbol{X}_{\rm acc}$ and transfered to the

BH according to the following algorithm:

$$\begin{aligned} M_{\rm BH} &= M_{\rm BH} + M_{\rm acc} \\ \boldsymbol{v}_{\rm BH} &= \frac{\boldsymbol{p}_{\rm BH} + \boldsymbol{p}_{\rm acc}}{M_{\rm BH} + M_{\rm acc}} \\ \boldsymbol{X}_{\rm BH} &= \frac{M_{\rm BH}\boldsymbol{X}_{\rm BH} + M_{\rm acc}\boldsymbol{X}_{\rm acc}}{M_{\rm BH} + M_{\rm acc}} \end{aligned} \tag{2.49}$$

These expressions guarantee mass and linear momentum conservation and also that the center of mass of the system is not altered by the accretion process. From the accreted mass $M_{\rm acc}$ at the current time step of size δt we can obtain the accretion rate as $dM_{\rm acc}/dt = M_{\rm acc}/\delta t$. Both the BH mass and the total mass from SPH particles is stored at each time step in order to check if the mass is conserved during the simulation.

Accretion of Polytropic Envelopes

Our next step in constructing a Collapsar scenario was to produce spherical polytropic envelopes that will collapse onto a BH situated at the center of the distribution. We will make use of our 2 $M_\odot$ polytropic stars to approach such scenario by removing its innermost 1 $M_\odot$ and replacing it with a BH of the same mass located at the center of the original distribution. This can be easily made following the same procedure used for the construction of our 2 $M_\odot$ polytropic stars. Even though the BH should be more massive in a Collapsar ($M_{\rm BH} \gtrsim 2\ M_\odot$), this scenario will be of use to test the accretion routine.

Figure 2.8 shows the column density of such polytropic envelope (right panel), along with the pressure profile $P(r)$ of the 3D polytropic envelope and the original pressure profile from the Lane-Emden solution (left panel). The whitest (densest) region at $r \simeq 0.5R_s$ indicates the location of innermost part of the envelope, which surrounds the BH located at the center of the distribution. Due to the lack of pressure support caused by removing the innermost 1 $M_\odot$ and replacing it with the BH, the remaining envelope will collapse onto the BH where it could be accreted. If no rotation is included the envelope will collapse radially in a time scale $t_{\rm fall} \simeq t_{\rm dyn}/2$ given by:

$$t_{\rm fall} = \frac{1}{2}\sqrt{\frac{R_p^3}{GM_p}} \simeq 0.04s \tag{2.50}$$

where R_p and M_p are the radius and mass of the original 2 $M_\odot$ polytropic star. If a rigid body rotation is given to the polytropic envelope, material at the poles of the

rotation axis, will collapse radially meanwhile material at the equator will collapse at a lower pace due to the centrifugal support. A rotating envelope will be able to produce an accretion disk around the BH as expected on a Collapsar scenario.

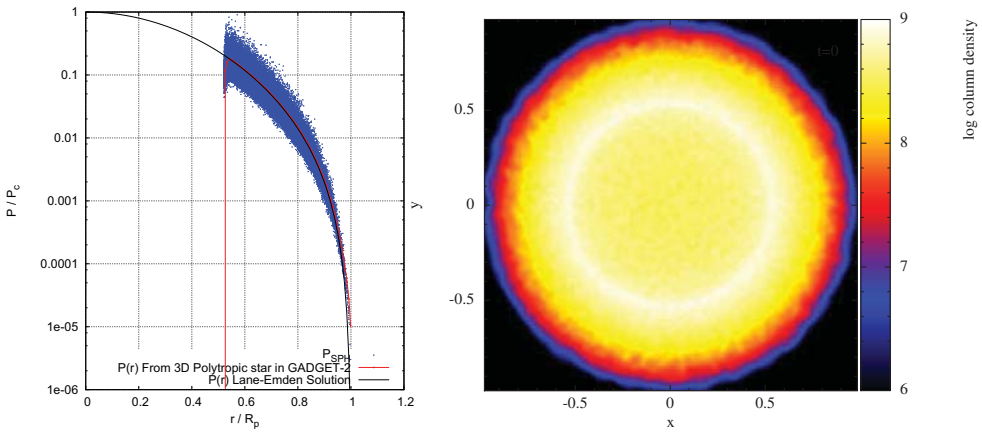

Figure 2.8: On the left, the pressure profile $P(r)$ for the polytropic envelope (red line) together with the SPH's particles pressure P_i (blue dots) and the original pressure profile from the 1D Lane-Emden solution. On the right, the column density of the spherical 1 $M_\odot$ polytropic envelope with a BH situated at the center of the distribution. The whitest regions show the innermost and densest part of the envelope. The lack of pressure in the central region and the gravitational pull from the BH will induce the collapse of the envelope.

In order to test the required resolution to properly follow the accretion of such polytropic envelopes, we performed tests with three different SPH resolutions; low resolution ($N_{\rm SPH} = 50000$), normal resolution ($N_{\rm SPH} = 500000$) and high resolution ($N_{\rm SPH} = 1000000$). As can be seen in Figure 2.9 the accretion rate determining the evolution of the BH's mass seems to converge for simulations with $N_{\rm SPH} \gtrsim 500000$ particles. Based on this tests we decided to run our simulations with $N_{\rm SPH} = 500000$ particles, which allowed us to increase the frequency between snapshots without significantly increasing the CPU-time and the hard drive's space used. This proved to be very useful when looking for structure formation events through the evolution of the accretion disk.

2.5.2 Testing the PW Potential

As we stated before, instead of a Newtonian gravitational potential $\Phi_N \propto M/r$ we will use the Paczinski-Wiita potential $\Phi_{\rm PW} \propto M/(r - r_g)$ defined in (2.13)

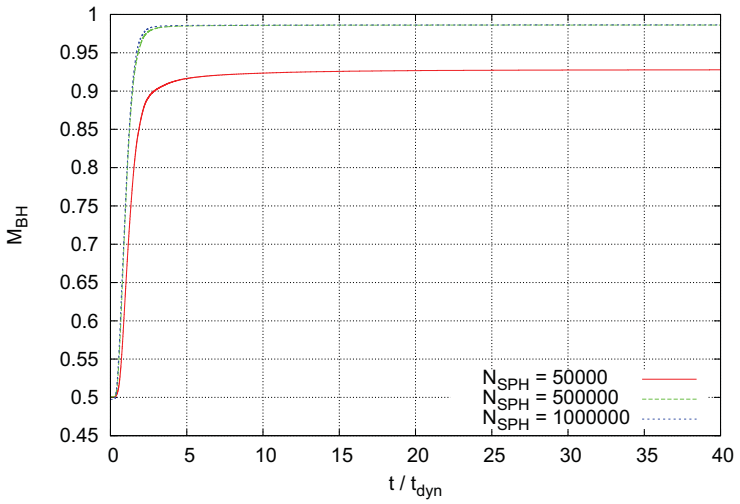

Figure 2.9: BH's mass evolution from the collapse and accretion of a 1 $M_\odot$ slowly rotating polytropic envelope (as shown in Figure 2.8), for three different SPH resolutions. Low resolution (red line with $N_{\rm SPH} = 50000$), normal resolution (green line with $N_{\rm SPH} = 500000$) and high resolution (blue line with $N_{\rm SPH} = 1000000$).

to account for some of the GR effects acting upon the gas particles. We made a series of tests in order to test that the PW potential was applied correctly to the gas particles. We used the 1 $M_\odot$ non-rotating polytropic envelopes with a 1 $M_\odot$ BH located at the center of the distribution. The polytropic envelope located between 683.3 km and 1309.3 km will fall onto the BH due to the lack of pressure support and to the BH's gravitational pull.

Two kinds of tests were made, the first had envelopes of reduced mass ($10^{-5} M_\odot$) and specific internal energy ($10^{-10} E_{\rm st}$), and the second one had an envelope with reduced internal energy ($10^{-10} E_{\rm st}$) and a mass of 1 $M_\odot$. The scaling of the envelope's mass was made in order to have a negligible contribution to gravity from the SPH particles. Meanwhile, the scaling of the internal energy was made in order to reduce the effect of the pressure in the total acceleration of the gas particles. Reducing the internal energy will allows us to see only the acceleration due to gravity, as long as the envelope is far from the BH ($r \gtrsim r_{\rm acc}$). Once the envelope approaches the BH near the accretion radius, its density, pressure and internal energy will increase rapidly due to the pressure exerted by the collapsing particles at larger radii, and in consequence, the accelerations due to hydrodynamical processes will also increase. This made difficult to test the PW potential against the

Newtonian one, due to the small difference between them at $r \gg r_g$ and to the fact that at $r \sim r_{\rm acc} = 3\,r_g$ the hydrodynamical processes start to have a non negligible contribution to the particle's accelerations.

Given that we were interested in testing if the SPH particles were subject to the modified potential instead of the Newtonian one, we used a variation of the PW potential, which differed in using $10\,r_g$ instead of r_g (the accretion radius was also scaled to $30\,r_{\rm acc}$ accordingly to the scaling of r_g). This guaranteed that this modified PW potential and the Newtonian one will be considerably different at larger radii where the gas has not collapsed to such a small region. In figure 2.10 we can see the acceleration of the gas particles (red dots) from the $10^{-5} M_\odot$ envelope, compared to the expected gravitational acceleration for a test particle in the $1\ M_\odot$ modified PW potential $a_{\rm PW} = GM_{\rm BH}/(r - 10r_g)^2$ (black line) and the expected Newtonian gravitational acceleration of a test particle due to a $1\ M_\odot$ "Newtonian BH" (blue line). It is clear that the gravitational acceleration acting on the particles is the one from the modified PW potential of the $1\ M_\odot$ BH.

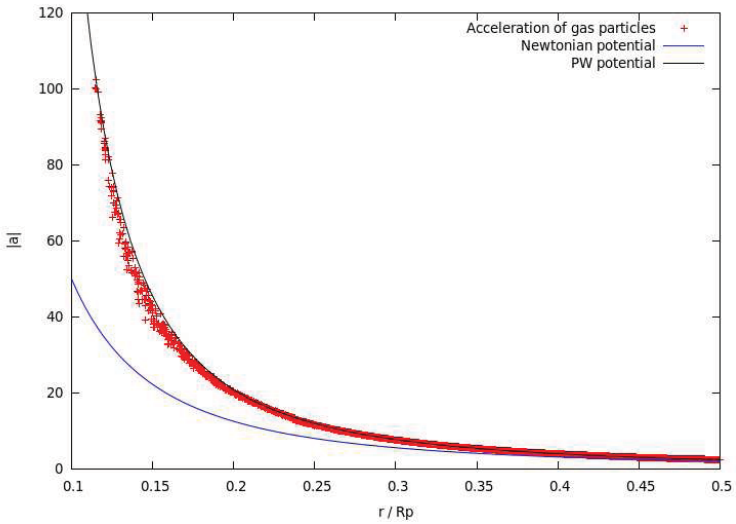

Figure 2.10: Modified PW potential test for a $10^{-5} M_\odot$ polytropic envelope with reduced internal energy. Gas particles (red dots) follow the modified PW potential instead of the Newtonian.

The second test involving a $1\ M_\odot$ envelope was made in order to check if the BH was in fact the only particle applying the modified PW potential. Because of the initial spherical symmetry of the envelope, which was preserved for some time due to the lack of rotation, we could easily account for the gravitational pull on a particle at radius r due to the SPH particles lying at $r_i < r$. Thus, from the particles

acceleration a_r obtained in the simulation, which includes the gravitational pull from the BH (modified PW potential) and the gas particles lying within r we can obtain the gravitational pull due only to the BH as follows:

$$\begin{aligned} a_{BH} &= a_r - a_{\rm gas} \\ &= a_r - \frac{GM_{\rm gas}(r)}{r^2} \\ &= a_r - \frac{4\pi G}{r^2}\int_0^r \rho(r')r'^2 dr'. \end{aligned} \tag{2.51}$$

Thus, by integrating the gas mass contained within r we can obtain the acceleration due to the modified PW potential and check for any deviation from it. In Figure 2.11 we can see the modified PW potential (black line), along with the Newtonian potential (blue line) and the gas particle's accelerations without the gas gravitational pull (cyan dots) and including the gas's gravitational pull (red dots). Clearly the envelope's mass is not negligible and the particle's accelerations are affected due to the inner gas mass. As expected, the gas acceleration due to the BH follows the modified PW potential almost exactly.

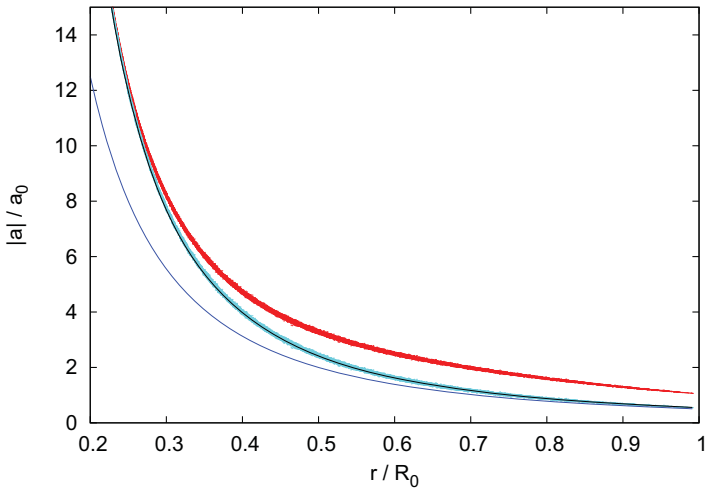

Figure 2.11: Modified PW potential test for a 1 $M_\odot$ polytropic envelope with reduced internal energy. The gas accelerations (red dots) include the gravitational pull due to both the gas (which is not negligible) and the BH, but if the gas gravitational pull is accounted for (cyan dots), the gas acceleration is the same as one produced by the modified PW potential (black line). The blue line represents the expected Newtonian acceleration for the inner mass distribution.

The tests shown in this chapter are the ones we considered the most relevant for starting our study on accretion of collapsing envelopes, nevertheless, we still need to include a cooling routine in order to account for neutrino energy losses in the Collapsar scenario. Rotation also plays a role in the accretion process, given that it will determine if an accretion disk forms around the BH and how far from it it is formed. The next chapter will describe the functioning of the cooling implementation and will show the tests made to study the accretion of rotating polytropic envelopes with different cooling efficiencies. This will help in the construction of a Collapsar scenario.

Chapter 3

Cooling and Instabilities in Rotating Collapsed Envelopes

In this chapter we present a study of the collapse and accretion of the same $1\ M_\odot$ polytropic envelopes onto a $1\ M_\odot$ BH located at the center of the spherical distribution, for the adiabatic, isothermal and finite cooling cases. The adiabatic case is basically the one observed in the previous section, where no cooling is implemented on the envelope. The isothermal case will account for a cooling mechanism that is efficient enough to provide an isothermal collapse of the envelope. Meanwhile, we will introduce a simplified cooling prescription that will be used throughout our work based on a cooling time scale that will determine the efficiency which with cooling is able to take energy from the infalling envelope.

The work presented in this chapter consists on a series of tests made in order to guarantee that the cooling routine worked properly and to have some information on the importance of cooling in the evolution of the accretion disk. All these tests were made using the same initial angular momentum distribution (rigid body rotation) with an initial angular velocity of $\Omega_0 \simeq 15.872\ \mathrm{s}^{-1}$. This rotation rate is considerably high, so we wanted to make sure that the star was not at the verge of breaking up due to its rapid rotation. Or that at least it guaranteed that a substantial part of the $1\ M_\odot$ envelope collapsed onto the BH and formed an accretion disk.

3.1 On the Initial Rotation of the Star

Though all tests were already made using this angular velocity, we wanted to make sure that a substantial part of the star was not rotating beyond the breakup rotation velocity $V_{c,b}$. This will ensure that an important amount of gas could collapse and form a disk around the BH, and this results will be applied to implement more realistic models. Therefore before showing the results obtained in the different cooling schemes, we will compare the rotational velocity of the star V_c with the breakup velocity $V_{c,b}$. To estimate the breakup velocity for the rotating star we need to consider the limiting case where the centrifugal and gravity forces are equal on a circular orbit around the center of the star. So considering a gas particle orbiting its interior mass $M(r)$ on a circular orbit at a radius r along the equator of the star, one obtains a breakup angular velocity:

$$\Omega_b = \sqrt{\frac{GM}{r^3}}. \tag{3.1}$$

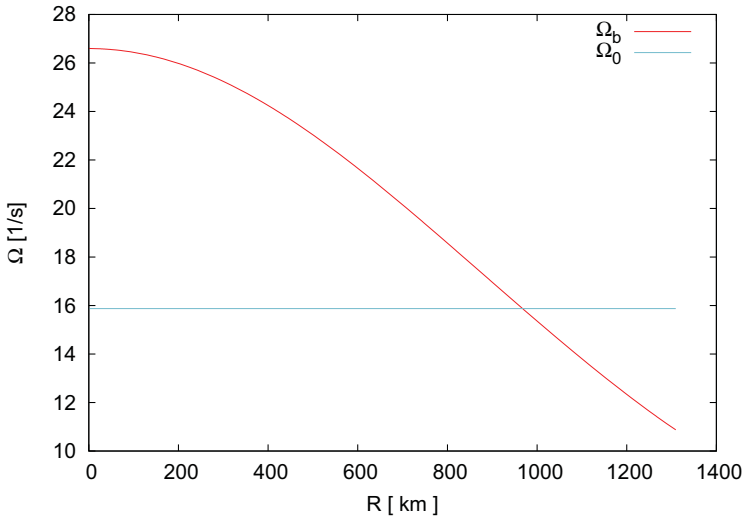

Figure 3.1: Breakup angular velocity for the 2 $M_\odot$ $\gamma = 5/3$ polytropic star (red line) and angular velocity assigned to the star for collapsing models. At radii $\gtrsim$ 967 km material at the equatorial plane is not gravitationally bound (blue line).

Thus, any material rotating with $\Omega > \Omega_b$ will not be gravitationally bound to the rest of the star and could break free from the inner material. We have to consider that (3.1) only provides an upper limit for the actual Ω_b, given that we are neglecting pressure gradients within the star, which would decrease Ω_b's value,

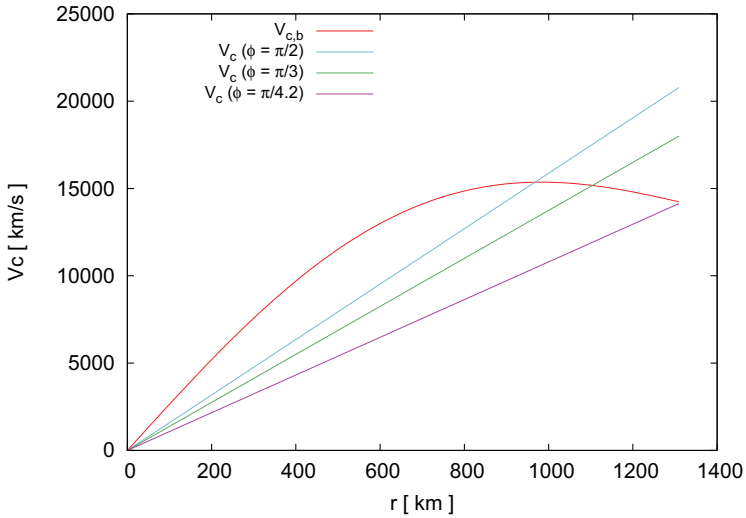

Figure 3.2: Breakup circular velocity for the polytrope as a function of the spherical radius r (red line), circular velocity for stellar material at the equatorial plane (green line) and circular velocity for stellar material on planes at angles $\phi = \pi/2, \pi/3,$ and $\pi/4.2$. From this figure we can ensure that all material at planes above $\phi_{\rm fall} \simeq \pi/4.2$ would be gravitationally bounded.

as well as the intrinsic change on the mass distribution $M(r, z)$ due to rotation. Nevertheless, this will give us a good estimate on the breakup velocity of the star. In figure 3.1 we show Ω_b versus r obtained for our polytropic star (red line), as well as the constant angular velocity assigned to the star for rigid body rotation ($\Omega_0 = 15.872\ \mathrm{s}^{-1}$). At radii $\lesssim 967$ km, where the blue line lies below the red one, material is gravitationally bound, otherwise it rotates fast enough to overcome the gravitational attraction from the rest of the star. This criterium only applies along the equatorial plane. Stellar material closer to the rotation axis would have slower rotation compared to the breakup velocity and would be gravitationally bound.

In order to estimate the amount of mass that won't be able to fall to the BH due to rapid rotation, we calculated the circular velocity $V_c = \Omega_0 R$ (where $R = r \sin\phi$, and ϕ is the angle between the position vector $\boldsymbol{r}$ and the Z axis) for gas lying on planes at different angles from the Z axis. Figure 3.2 shows the circular velocity of the envelope $V_c(r, \phi)$ as a function of R for $\phi = \pi/2, \pi/3$ and $\pi/4.2$ (blue, green and purple lines respectively), compared with the break up rotational velocity at the equator $V_{c,b} = \Omega_b r$ (red line). As we see from figure 3.2, when ϕ departs from $\pi/2$ (approaching the poles), material at larger r becomes bound (lies below $V_{c,b}$).

Each line $V_c(r, \phi)$ represents the rotation velocity of material at an angle ϕ

with the Z axis and at a distance r from the center of the mass distribution. Due to spherical symmetry, each of these lines will translate into a conic surface with opening angle ϕ with respect to the Z axis which will contain all material with circular velocity $V_c(r, \phi)$. As we decrease the cone's opening angle, the maximum circular velocity stellar material can reach decreases. Thus, we can define the angle $\phi_{\rm fall}$, for which all material lying within the cone with opening angle $\phi < \phi_{\rm fall}$ will have rotation velocities below breakup ($V_c < V_{c,b}$) at all radii, i.e., will be gravitationally bound. This ensures that material lying inside that cone could collapse to form a disk around the BH. Figure 3.2 shows that $\phi_{\rm fall} \simeq \pi/4.2$, an thus, all material lying inside cones with opening angles $\phi \lesssim \pi/4$, will have circular velocities below the breakup velocity at all radii. This cones will also be present on the lower parts of the sphere, with symmetry along the equator. This indicates that almost all the mass contained within the cones with opening angle $\phi = \pi/4$ will be gravitationally bound. This accounts for half of the polytropic envelope, therefore, at least $0.5\,M_\odot$ contained within this cones are gravitationally bound in our polytropic envelopes.

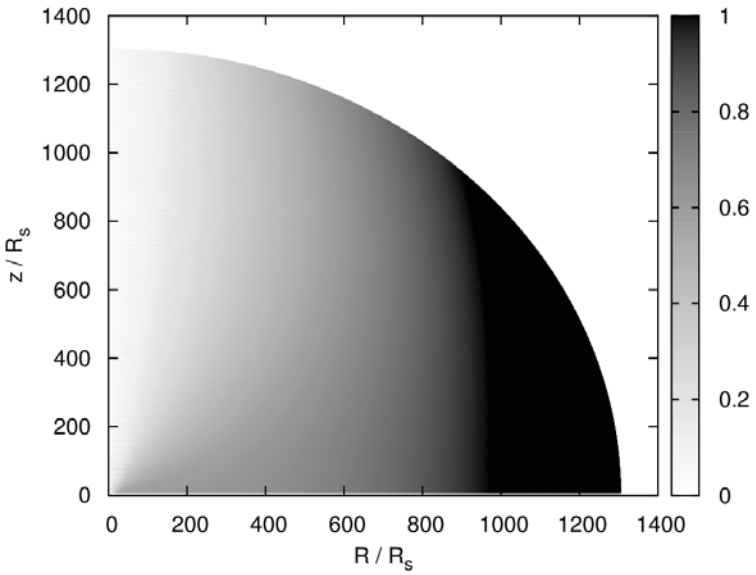

Figure 3.3: Meridional cut of the polytropic star showing the gravitationally bound region calculated from the ratio $V_c/V_{c,b}$. The black colored zones represent material with $V_c \geq V_{c,b}$, and thus are not gravitationally bound due to the rapid rotation, meanwhile the gray and white colored regions have $V_c < V_{c,b}$ and thus, are gravitationally bound.

Another way to obtain $\phi_{\rm fall}$ is to look at the ratio $V_c(r, \phi)/V_{c,b}(r)$ in a 2D

map. Figure 3.3 shows a meridional cut of the polytropic star with a color map of the ratio $V_c/V_{c,b}$. Black colored regions account for zones where material has $V_c > V_{c,b}$ and thus, are gravitationally unbound. The rest gray and white colored regions represent gravitationally bound material. It is clear from figure 3.3 that $\phi_{\rm fall} \lesssim \pi/4$ as stated before. And for obtaining a better estimate on the amount of gravitationally bound mass of our star we should calculate the amount of mass contained within this black colored region.

In order to do so, let us obtain the mass contained at the shell beyond 967 km (where all material is gravitationally unbound at the equator). As stated before, only mass outside the cones with opening angle $\phi = \pi/4$ is contained inside the black colored regions of gravitationally unbound matter. Thus, the mass inside this shell and outside the cones with $\phi = \pi/4$ will provide an upper limit on the gravitationally unbound mass, contained in the black colored region. The mass inside such region is $M(r > 967\,\text{km}, \phi > \pi/4) \simeq 0.15\,M_\odot$. Therefore, it is safe to say that $\gtrsim 85\%$ of the envelope's mass is gravitationally bound for rotation. This result will be shown later where clearly a huge amount of the envelope collapses to the BH and forms an accretion disk around it.

3.2 Collapse and Accretion onto a Fixed BH

Here we present our results on the collapse and accretion of $1\,M_\odot$ polytropic envelopes onto a $1M_\odot$ BH fixed at the center of the spherical distribution. All simulations shown were followed until ~ 0.5 s ($\sim 5\,t_{\rm dyn}$) and used $N_{\rm gas} = 5 \times 10^5$ SPH particles. The goal of these simulations is to study the importance of cooling in the evolution of the accretion flow in the context of the collapse and accretion of massive rotating envelopes. We intend to do this by using envelopes in different cooling scenarios. The first will be an adiabatic one, where no cooling mechanism is implemented. At the opposite extreme we will study the collapse and accretion of an isothermal envelope (with an adiabatic index $\Gamma \simeq 1$), which accounts as an envelope whose intrinsic cooling mechanism is so efficient that energy is radiated in order to maintain a constant temperature T throughout the envelope. Later on we will define a simplified cooling prescription whose cooling efficiency (chosen as a parameter in our simulations) will determine if the envelope behaves like an adiabatic or an isothermal one. By exploring different cooling efficiencies we will be able to determine the importance of cooling in the evolution of the accretion flow.

The formation of a BH with the innermost $1\,M_\odot$ of our $2\,M_\odot$ polytropic star will result in a vacuum formed between the polytropic envelope and the BH. This,

along with the gravitational pull from the BH, will induce the collapse of the $1\,M_\odot$ rotating envelope onto the BH. The envelope internal pressure will cause its expansion to the inner region which will accelerate the infall of material onto the BH. As we saw earlier in this chapter, rotation will also prevent some of the material from reaching the BH, thus, the time it will take to the envelope to fall onto the BH will be shorter than the free fall time scale t_{fall} that can be estimated from the dynamical time scale of the system t_{dyn} as follows:

$$t_{\text{fall}} \simeq \frac{1}{2} t_{\text{dyn}} = \frac{1}{2}\sqrt{\frac{R_s^3}{GM_s}} = 0.046 \text{ s}, \tag{3.2}$$

where $R_s = 1310$ km is the radius of the original polytropic star and $M_s = 2\,M_\odot$ the total mass of the system. Therefore, given that all envelopes have the same rotation rate, the cooling implementation will be the one parameter determining the time actual time t_{fall} it will take the envelope to fall onto the BH. The more efficient the cooling, both the internal energy and the pressure of the envelope will be smaller, and their contribution to the expansion of the material into the region containing the BH will be diminished. Thus, the isothermal envelope, which will immediately loose internal energy in order to maintain its temperature constant, should fall in a free fall time t_{fall} very similar to the one determined by equation (3.2), meanwhile envelopes with less efficient cooling, will take fewer time to collapse due to the higher internal energy and pressure of the envelope that contribute to the acceleration of material into the region containing the BH. Equation (3.2) neglects the fact that when material reaches its centrifugal barrier around the BH, it will be highly compressed and heated up, which will translate in the formation of an outgoing shock which could prevent some of the material to fall directly onto the BH, or at least delay it.

We will start by showing results from the adiabatic and isothermal envelopes, which have very different behavior in the evolution of the accretion flow. Then we'll define our simplified cooling prescription and explore different cooling efficiencies to study a transition between the adiabatic and the isothermal previously presented.

3.2.1 Adiabatic envelope

Given that the adiabatic envelope has no way of loosing energy when material is heated up when reaching its centrifugal barrier, the outgoing shock formed, will prevent the infall of a considerable amount of material after a time $t > t_{\text{fall}}$. This

will halt the accretion of low angular momentum material which will be obliged to form part of an accretion disk or torus before being accreted. Figure 3.4 shows precisely how after a time $t \sim 0.4$ s, accretion of material with low angular momentum (close to the the rotation axis) is diminished and the accretion rate (showed on the bottom panel from figure 3.4) starts decreasing almost monotonically. On the top panel of figure 3.4 we see the evolution of the BH mass which increases smoothly. This coincides with the rather smooth accretion rates obtained.

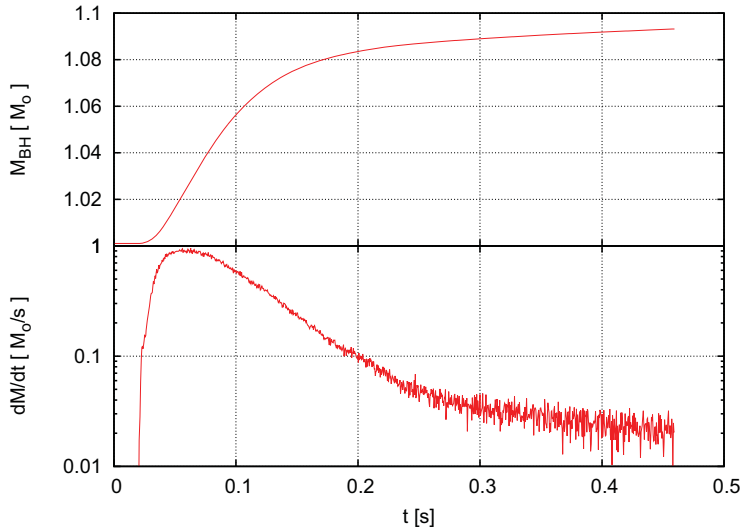

Figure 3.4: BH Mass (top panel) and accretion rate $\dot{M}$ for the adiabatic envelope (bottom panel). We see that accretion onto the BH is significant ($\sim 0.1\, M_\odot$ on half a second) even though there are not any cooling mechanisms. $\dot{M}$ has a maximum value of $\sim 0.9\, M_\odot$ s^{-1} and then decreases to $\sim 2 \times 10^{-2} M_\odot$ s^{-1}, it also shows two different slopes after the maximum, corresponding to $\dot{M} \propto 10^{-7.6\, t}$ (up to 0.25 s) and $\dot{M} \propto 10^{-1.5\, t}$ (after 0.25 s).

The maximum accretion rate at $t \simeq 0.05$ s $\simeq t_{\rm fall}$ is reached before the disk is completely formed. This can be seen in figure 3.5 where density plots at the XY (top six panels) and XZ (bottom six panels) planes are showed for times $t = 0, 0.064, 0.14, 0.23, 0.32$ and 0.41 s. All panels show material within the cubic region of size $2\, R_s = 2620$ km, which contained the initial configuration. Due to the rapid rotation, some material at the equator and at large radii break away from the original star. Bottom six panels from figure 3.5 show that the envelope is still collapsing at $t \simeq 0.14$ s, and only after $t = 0.23$ s it is clear that all low angular

momentum material from the poles has been already accreted by the BH or the accretion disk. When the disk is already established around the BH, most of the accretion already took place and the accretion rate decreases to $\dot{M} \lesssim 10^{-1} M_{\odot}$ s^{-1} from $t = 0.2$ s to $t = 0.45$ s.

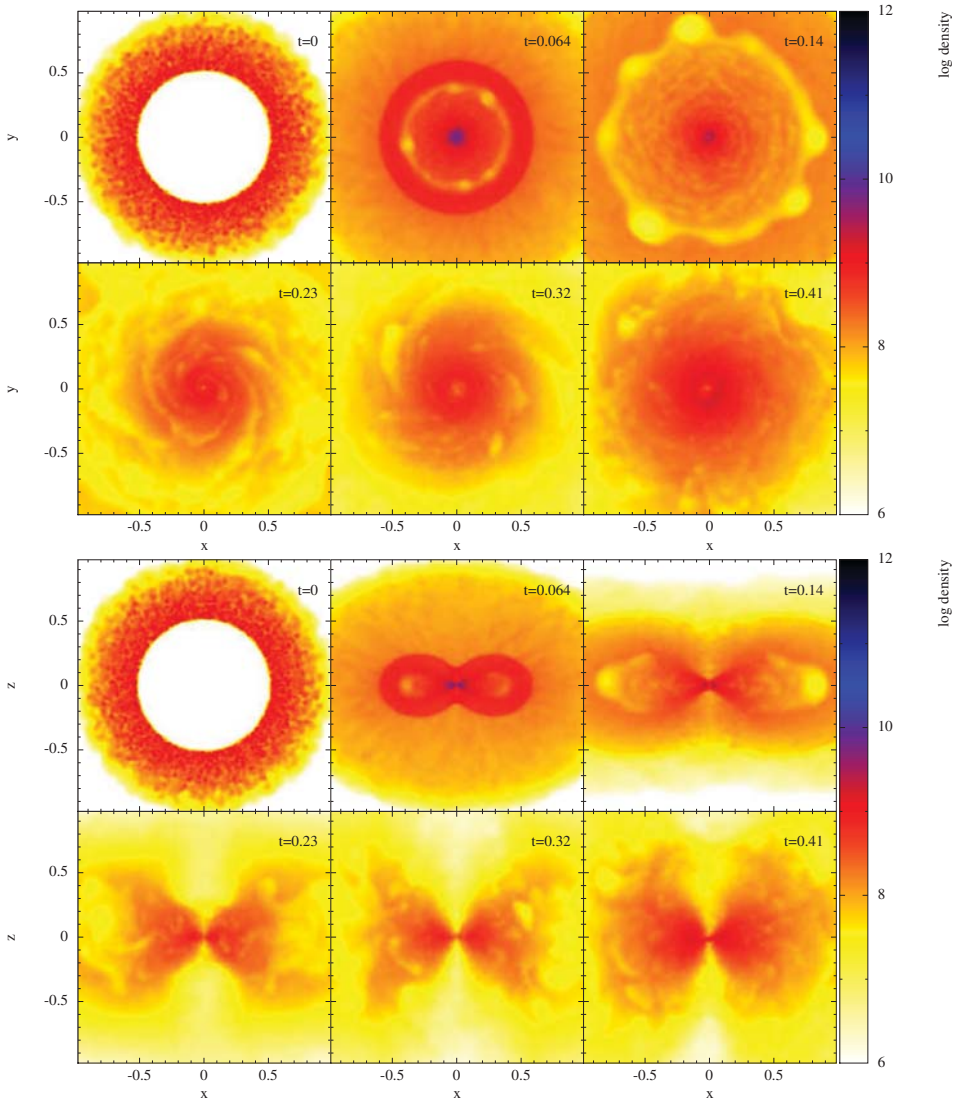

Figure 3.5: $\log \rho$ (in cgs) on the XY plane (top 6 panels) and the XZ (bottom 6 panels) for the collapse and accretion of the adiabatic $1\,M_\odot$ polytropic envelope onto the $1\,M_\odot$ BH fixed at the origin. Each panel corresponds to a different time in seconds. This simulation was followed until ~ 0.5 s ($\sim 5\,t_{\rm dyn}$). We can see the formation of instabilities on the disk such as spiral structures at the XY plane, as well as the existence of a thick disk around the BH from $t = 0.32$ s showed at the XZ plane.

At $t \simeq 0.064$ s, figure 3.5 shows the presence of the outgoing shock formed by material being compressed when reaching its centrifugal barrier. The yellow colored ring at $r \simeq 0.4\,R_s$ represents a low density region of shocked material that moves outwards as shown at $t = 0.14$ s. After $2.5\,t_{\text{dyn}}$ ($t = 0.23$ s) density along the rotation axis (Z) lowers at least one order of magnitude and a thick disk around the BH has formed. At this point it seems that the accretion rate will only diminish due to the slow exhaustion of material at the accretion disk.

3.2.2 Isothermal envelope

In this simulation, we used the same polytropic envelope but forced GADGET-2 to have an isothermal EOS by setting the adiabatic index as $\Gamma \simeq 1$. This accounts as postulating some physical process that cools the material and keeps T constant. The cooling of the envelope takes place immediately, thus, the internal energy and pressure of the envelope quickly decreases with the collapse. This delays the infall of material onto the BH as shown on figure 3.6 where the evolution of the accretion rate $\dot{M}$ (bottom panel) and BH's mass (top panel) of the isothermal and adiabatic envelopes are compared. The isothermal envelope takes almost twice the time to fall onto the BH and commence accretion compared to the adiabatic one. Also, the isothermal cooling implemented allows more material to reach the BH in the initial collapse. The outgoing shock formed when material reaches its centrifugal barrier is rapidly slowed down, due to the isothermal cooling which decreases the internal energy of the shock. This translates into an accretion rate of $\dot{M} \simeq 5\,M_\odot$ reached at $\gtrsim 0.7$ s, almost one order of magnitude higher than the one obtained in the adiabatic envelope.

The most important result from this simulation is the large amount of intense variations on $\dot{M}$ after the initial collapse and the following exhaustion of low angular momentum material. Such intense increases in the accretion rate were not observed in the adiabatic scenario. The most intense variation is reached at $t \simeq 0.29$ s when the accretion rate rises from $0.1\,M_\odot$ s^{-1} to $\simeq 80\,M_\odot$ s^{-1}. Figure 3.6 shows that the cooling mechanism could be extremely important in determining the evolution of the accretion flow.

By looking at density plots at the XY plane and at the XZ plane (top six and bottom six panels from figure 3.7 respectively), we can see that the morphology of the accretion disk in the isothermal scenario is also very different compared to the adiabatic one. At $t \simeq 0.14$ s, a thin accretion disk seems to be completely formed, and at such times there is also formation of highly dense structure (with $\rho \gtrsim 10^{12}$ g cm^{-3}) at the accretion disk, such as spiral arms and gas clumps. The

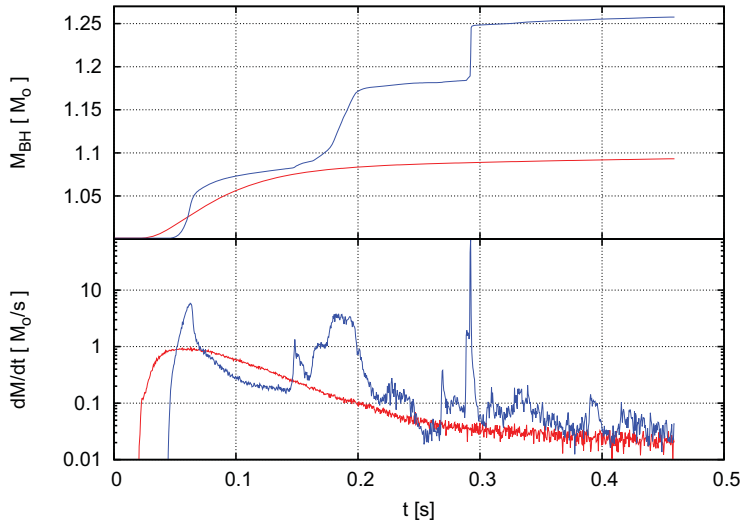

Figure 3.6: BH Mass (top panel) and accretion rate $\dot{M}$ (bottom panel) for the isothermal (blue lines) and adiabatic envelopes (red lines). Accretion at the isothermal envelope begins at later than at the adiabatic one. The isothermal envelope shows higher accretion rates and fluctuations up to ~ 3 orders of magnitude larger. This translates into a larger mass accreted by the BH.

densities reached in the disk are several orders of magnitude higher than in the adiabatic envelope. And apparently, the formation of structure such as clumps or spiral arms, seems to be related with the intense variations on $\dot{M}$. The big fluctuations on $\dot{M}$ are apparently caused by close encounters of gas clumps with the BH. This shows that cooling and formation of instabilities are of great importance for the accretion rates and the way material falls onto the BH, as well as for the properties of the disk.

3.2.3 Simple Cooling envelopes

In order to study envelopes with cooling efficiencies ranging between the adiabatic and isothermal ones, we introduce a simple cooling prescription to the $\gamma = 5/3$ polytropic envelope. It is based in considering a cooling process which depends on the current internal energy $u_{\rm int}$ and a cooling time $t_{\rm cool}$. We wanted to characterize cooling efficiency by the orbital time of the accretion disk formed around the BH $t_{\rm disk}$, so we can determine how many orbits it would take the disk to cool down. At first, $t_{\rm disk}$ will be given by the original angular velocity $\Omega_0 = 15.872\ {\rm s}^{-1}$ of the envelope, but once the disk forms around the BH, the angular velocity distribution

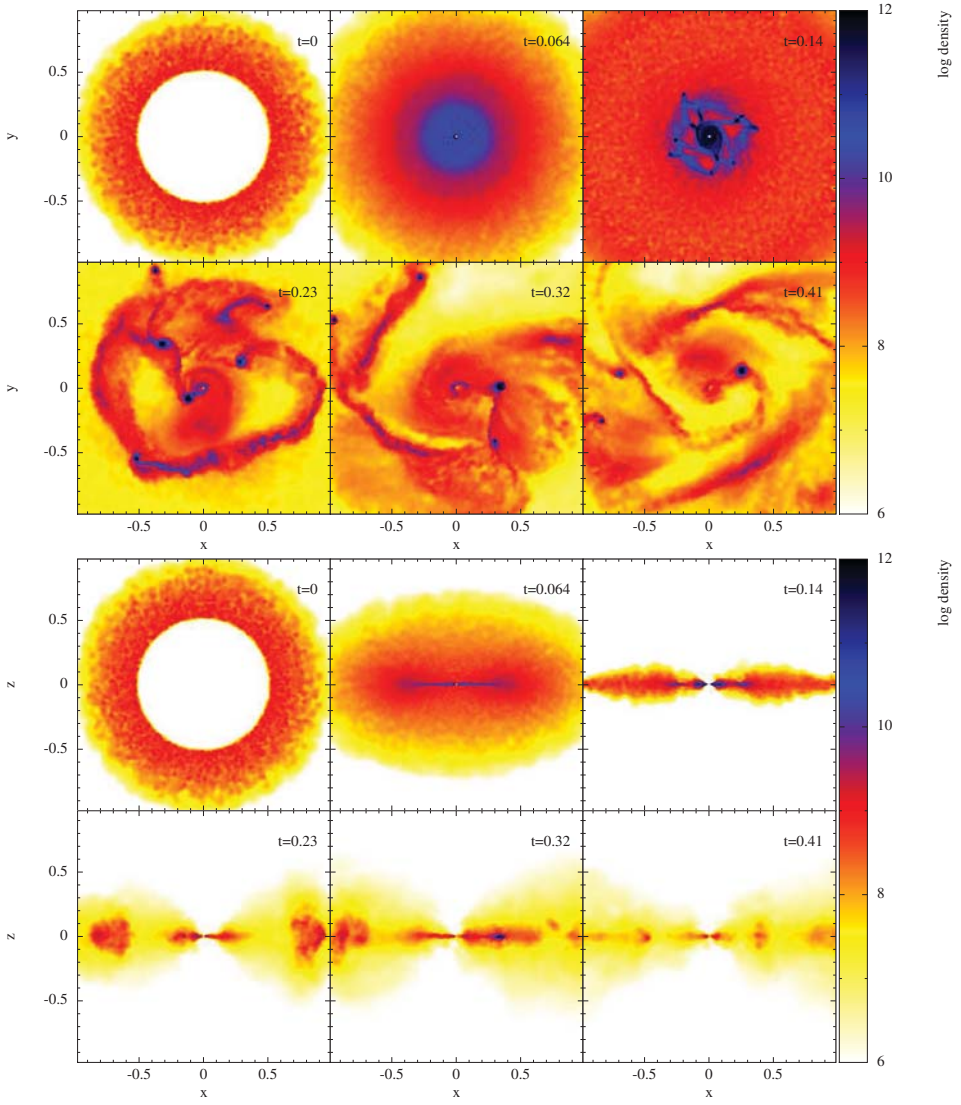

Figure 3.7: $\log \rho$ (in cgs) on the XY plane (top 6 panels) and the XZ (bottom 6 panels) for the collapse and accretion of the isothermal $1\,M_\odot$ polytropic envelope onto the $1\,M_\odot$ BH fixed at the origin. There is formation of instabilities on the disk such as spiral structures and also compact and dense gas clumps orbiting around the BH, which managed to change significantly the density on some parts of the disk. A thin disk can be appreciated even at $t = 0.14$ s. Disk density near the BH is close or above 10^9 g cm^{-3} at all times but due to gas clumps density can increase a few orders of magnitude within the disk.

$\Omega(r)$ will be close to a Keplerian one, determined by the PW potential. Nevertheless, considering $t_{\text{disk}} = \Omega_0^{-1}$ will give us an estimate of the angular velocity of the disk. Therefore, we define the cooling efficiency parameter β, which accounts for the number of times material will orbit the BH before being significantly cooled down, which translates in a cooling time t_{cool} defined as:

$$t_{\text{cool}} \equiv \beta t_{\text{disk}} \qquad \text{where} \qquad t_{\text{disk}} \simeq \Omega_0^{-1}. \tag{3.3}$$

And the cooling would be given by:

$$u_{\text{new}} = u_{\text{old}} - du \qquad \text{where} \qquad du = -\frac{u_{\text{old}}}{t_{\text{cool}}}\, dt = -\frac{u_{\text{old}}}{\beta t_{\text{disk}}}\, dt \tag{3.4}$$

Equation 3.4 can be easily integrated to obtain $u(t) = u_0 \exp(-t/t_{\text{cool}})$. This will represent the exact evolution of the internal energy u if the polytropic envelope didn't suffer any expansion or compression that would change its density and internal energy. Just considering its exponential decay, the internal energy would have decreased $1/e$ times after $t \sim t_{\text{cool}}$, but it would take $\sim 10 t_{\text{cool}}$ for the system to decrease by two orders of magnitude. Table 3.1 shows the cooling times used for our models named after its cooling efficiency parameter β.

Model	Cooling time t_{cool} [s]	Cooling efficiency β
β0.1	0.009	0.14
β1.4	0.092	1.46
β2.9	0.184	2.92
β8.7	0.552	8.76

Table 3.1: Cooling times and efficiencies used for the different simulations with the implemented simplified cooling prescription. Models are named after its cooling efficiency β.

This simple calculation gives us an estimate on the behavior of the internal energy u with our simple cooling process, but given that the envelope is collapsing, and not static, significant changes on density, pressure and temperature could raise from shocks and disk formation. All these could affect energy loss on the disk. In Figure 3.8 we plot the evolution of the BH's mass and mass accretion rates for all the models showed in Table 3.1 (including the adiabatic and isothermal ones). We can see from the bottom panel of figure 3.8 that increasing cooling efficiency, results in higher accretion rates after disk formation ($t \gtrsim 0.2$ s). And models

with cooling times $t_{\rm cool} \gtrsim 0.1$ s show an accretion flow evolution very similar to the adiabatic one. Only model $\beta 0.1$ has an accretion rate which resembles the isothermal one, showing intense variations after disk formation and significantly higher accretion rates than the adiabatic one ($\gtrsim 1\, M_\odot\ {\rm s}^{-1}$). This suggest that the density maps from model $\beta 0.1$ should resemble the most the ones obtained in the isothermal envelope.

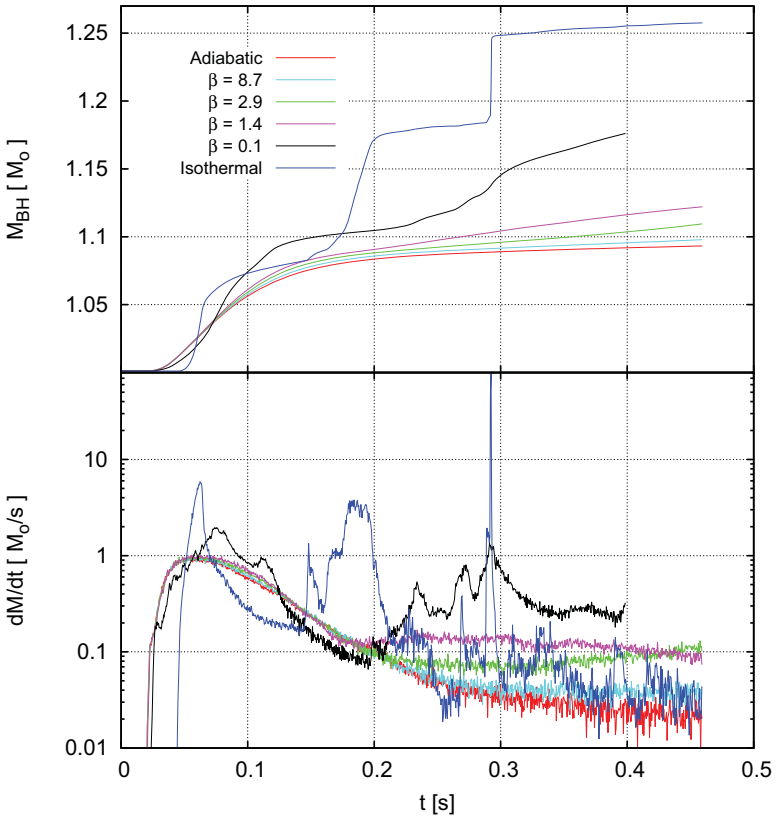

Figure 3.8: BH Mass (left) and accretion rate $\dot{M}$ (right on log scale) for the isothermal (blue), adiabatic (red) and cooled envelopes with cooling times $t_c = 0.009$ s (black), 0.09 s (cyan), 0.18 s (green) and, 0.55 s (orange). For the model with $t_c = 0.009$ s, accretion starts to resemble the isothermal case but accretion begins earlier as in the adiabatic envelope.

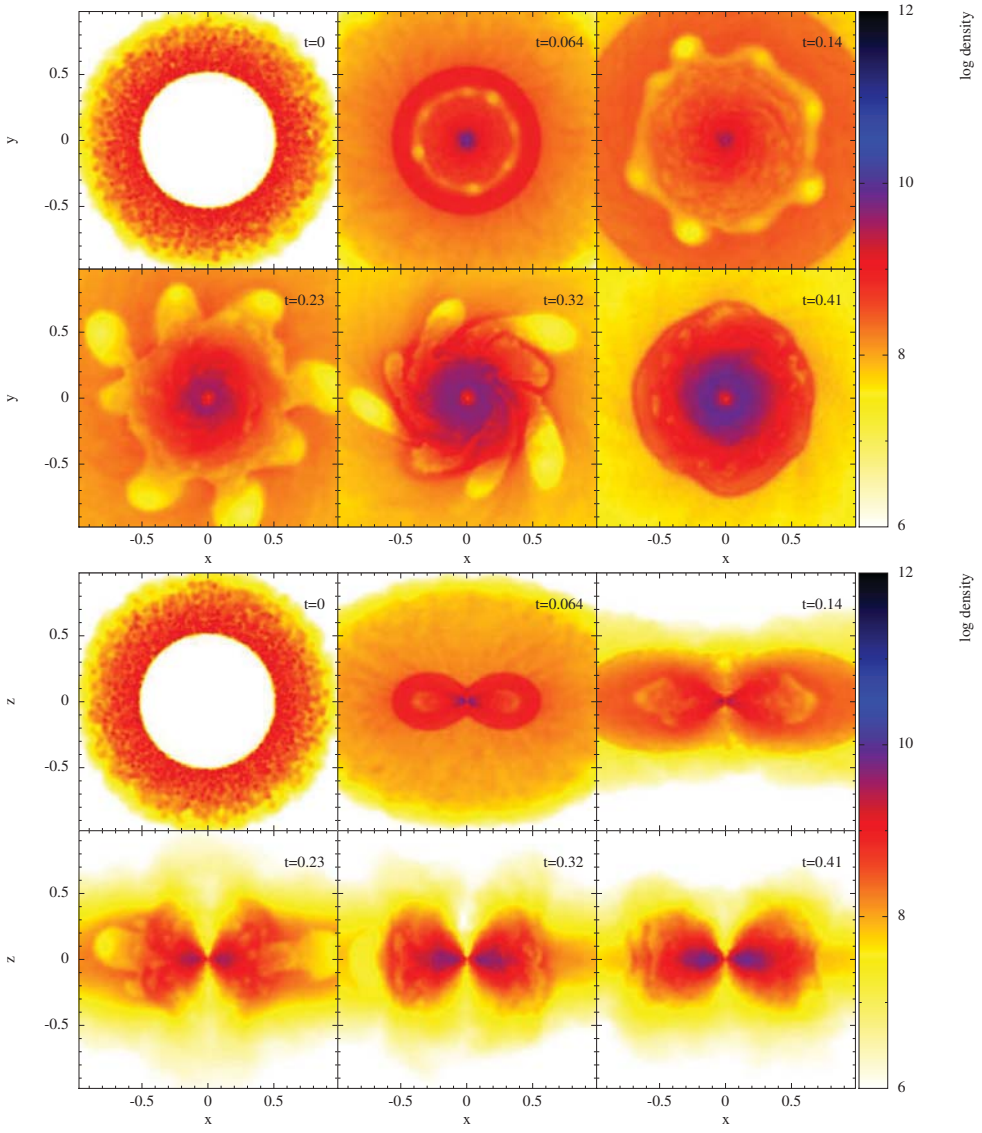

Figure 3.9: $\log \rho$ (in cgs) on the XY plane (top 6 panels) and the XZ (bottom 6 panels) for the collapse and accretion of $\beta 2.9$ model with $t_c = 0.18$ s. We can see the formation of instabilities on the disk such as spiral structures. The disk density is higher near the BH than the one at the adiabatic case for later times. A thinner disk than the one formed at the adiabatic envelope can be appreciated at $t = 0.23$ s.

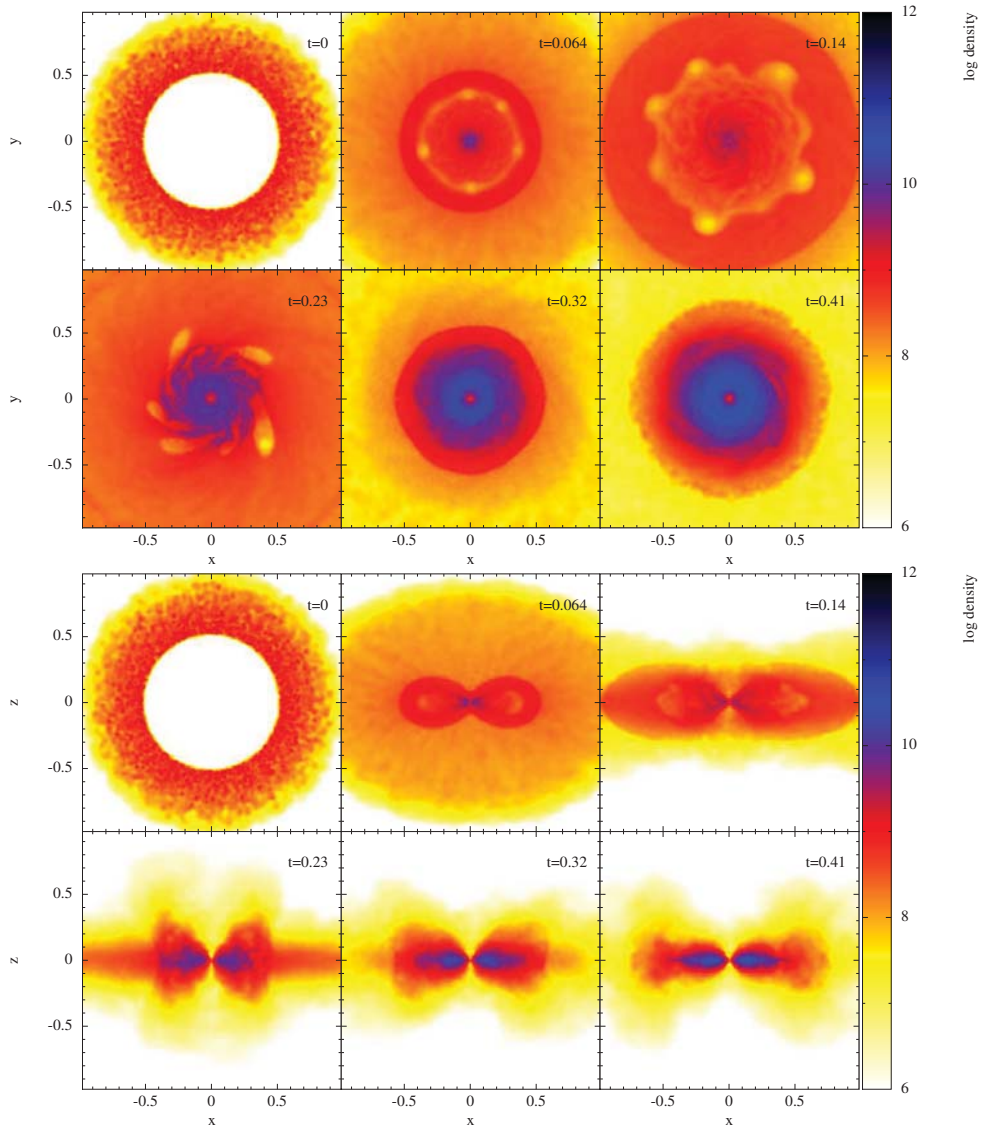

Figure 3.10: $\log \rho$ (in cgs) on the XY plane (top 6 panels) and the XZ (bottom 6 panels) for the collapse and accretion of $\beta 1.4$ model with $t_c = 0.09$ s. We can see the formation of instabilities on the disk such as spiral structures. The disk density is ~ 10 times higher than the one in the adiabatic case. A thinner disk than the one formed at the adiabatic envelope and the model with $t_c = 0.18$ s, can be appreciated at $t = 0.23$ s.

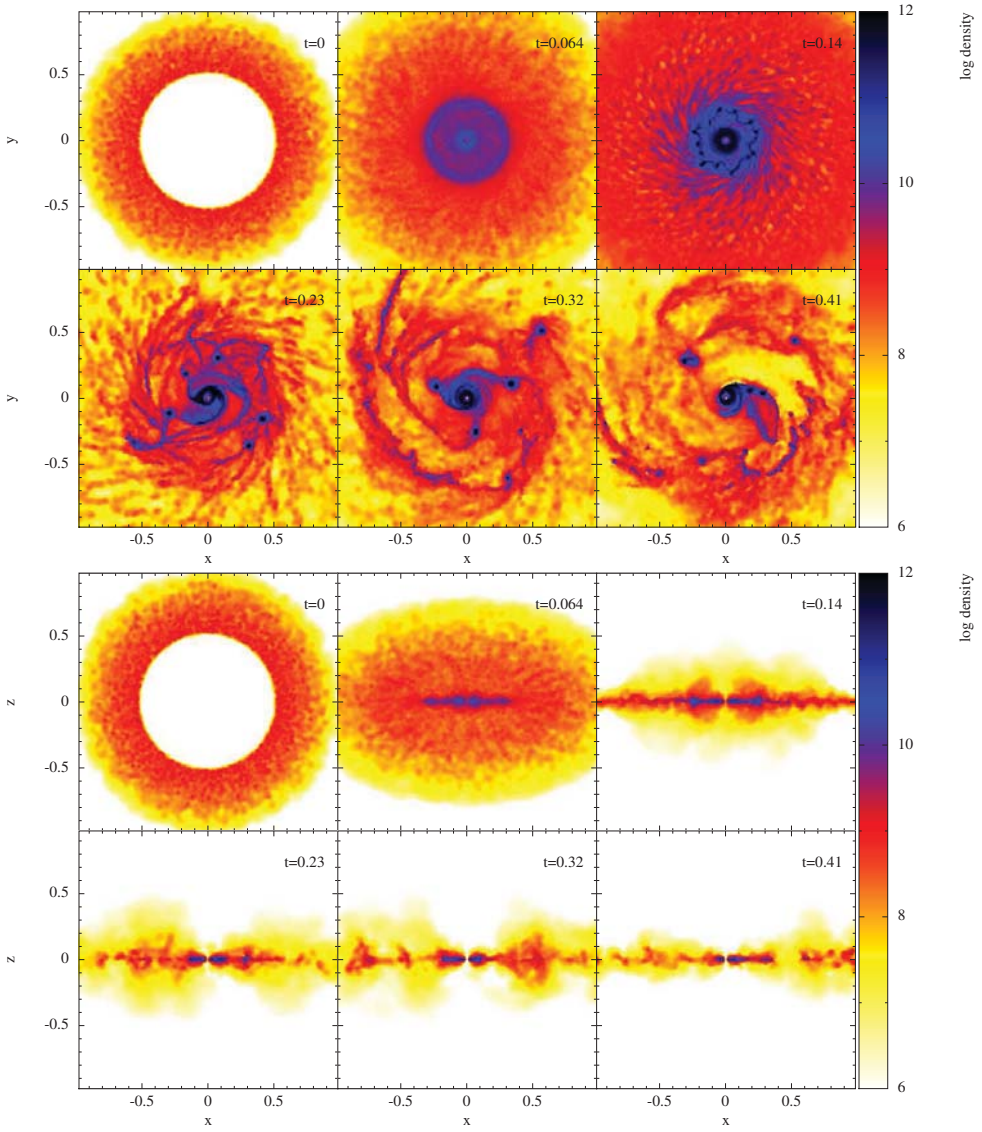

Figure 3.11: $\log \rho$ (in cgs) on the XY plane (top 6 panels) and the XZ (bottom 6 panels) for the collapse and accretion of $\beta 0.1$ model with $t_c = 0.009$ s. We can see the formation of instabilities on the disk such as spiral structures and also compact and dense gas clumps orbiting around the BH which managed to change significantly the density on some parts of the disk. A thin disk can be appreciated even at $t = 0.14$ s. Disk density near the BH is close or above 10^{11} g cm^{-3} at all times but due to gas clumps, density can increase a few orders of magnitude within the disk.

In figures 3.9, 3.10 and 3.11 we show density plots at the XY (upper six panels) and XZ planes (bottom 6 panels) for models $\beta 2.9$, $\beta 1.4$ and $\beta 0.1$ respectively ($\beta 8.7$ model looked very similar to the adiabatic case). It is clear that our cooling mechanism is working correctly given that decreasing t_c translates into a more effective cooling and therefore, into a thinner and more dense disk around the BH. As expected from figure 3.8, $\beta 0.1$ model (with $t_c = 0.009$ s) really resembles the isothermal case and shows formation of dense spiral arms and gas clumps that orbit the BH. The main difference with the isothermal model resides in the smaller accretion rates, which results in the presence of a dense disk ($\sim 10^{12}$ g cm^{-3}) formed around the BH that lingers more time in $\beta 0.1$ model than in the isothermal one. Material at this high densities will be highly compressed and its internal energy and temperature will be further increased, resulting in a larger energy loss rate $du/dt = u/t_{\rm cool}$.

Figures 3.9, 3.10 and 3.11 show that the cooling efficiency is important to determine the properties of the accretion disk, such as its density and temperature (or internal energy). Models $\beta 8.7$, $\beta 2.9$ and $\beta 1.4$ resemble the adiabatic one only prior to disk formation. Once the accretion disk has formed, the cooling mechanism determines the height and density of the accretion disk, which becomes increasingly dense with smaller β.

3.3 Summary From Collapse and Accretion onto a Fixed BH

These results show that there is an important dependence of the accretion rate $\dot{M}$ on the efficiency of the cooling mechanism present in the system. For slowly cooled envelopes (with $t_{\rm cool} \gtrsim 0.1$ s) a more efficient cooling translates into a deeper collapse and a thinner and denser disk around the BH. This affects the amount of mass that can reach the BH and therefore its accretion rate $\dot{M}$. As seen in the $\beta 0.1$ and isothermal models, strongly fluctuating accretion rates seem to be produced by the accretion of gas clumps and spiral structure formed at the disk. Therefore, the cooling mechanism which determines the structure formation at the disk, seems to determine the evolution of the accretion flow.

Even when models with small cooling efficiencies ($\beta \gtrsim 1.0$) did not show any important structure formation at the disk (such as clumps or spiral arms) there is a lot of previous work on studying the evolution of accretion disks with this simplified cooling prescription (Gammie 2001, Rice et al. 2003, Meru & Bate 2011, Lodato & Clarke 2011, Rice, Forgan & Armitage 2012). They are mostly

applied to the context of fragmentation on protoplanetary disks or star formation in galaxies.

These works explore the existence of a critical value for the cooling efficiency parameter β_{crit}, for which a self gravitating accretion disk with $\beta < \beta_{\text{crit}}$ shows fragmentation. First results by Gammie (2001) using local shearing box simulations on the code ZEUS obtained a value of $\beta_{\text{crit}} \simeq 3$, meanwhile global SPH simulations from Rice et al (2003) obtained $\beta_{\text{crit}} \geq 3$ depending on the disk's superficial density distribution $\Sigma(r)$. More recent works have pointed out that the exact value of β_{crit} may depend on the resolution of the simulations (Meru & Bate 2011, Lodato & Clarke 2011, Meru & Bate 2012) and the implementation of cooling in the SPH equations (Rice, Forgan & Armitage 2012). Our work isn't focused on exploring the value β_{crit}, but in exploring the possibility of structure formation in a Collapsar's accretion disk with cooling efficiencies according to the expected neutrino cooling time scale in such scenario. Nevertheless, these works provided important information for guaranteeing enough resolution in our simulations to properly solve fragmentation or structure formation at the Collapsar's accretion disk.

Up to this point we are not studying the energy losses on the envelope, but it is clear that disk's properties will determine the evolution of the total energy loss rate $L_c = \sum du_i/dt$ determined by the energy loss of all SPH particles. In the next subsection we will take a step forward on our simulations and study the evolution of the accretion flow considering cooling time scales, and envelope and BH masses expected on the Collapsar scenario. Hopefully this will give us some insight on what to expect from using a more realistic cooling implementation.

Chapter 4

Cooling-induced Structure Formation and Evolution in Collapsars

As we saw from the last chapter, cooling efficiency seems to be of great importance in determining the variation of the accretion flow. Its efficiency determines whether structure formation events occur or not (such as spiral arms or clumps). These instabilities can alter considerably how angular momentum is transported along the accretion disk and therefore, the mass accretion rate. Moreover, given that the cooling prescription depends upon the internal energy of the SPH particles u_i, structure formation events could induce variations in the energy loss rate. Therefore, in the following simulations, we will take into account the total energy loss rate $L = \sum_i (du_i/dt)$ at each time step, in order to obtain an estimate of the amount of energy lost by our cooling implementation.

We also intend to approach our initial setup to one that resembles more accurately the accretion flow in a Collapsar. Thus, we will have to determine the right cooling efficiency parameter β which results in energy loss rates matching the ones expected in a Collapsar. In order to do this, we will obtain an approximation to the neutrino cooling time scale expected on Collapsars, which will point out the values the parameter β should have. There will also be changes in the properties of the collapsing envelope and the accreting BH. For a more realistic setup, the BH was given an initial mass of $2\,M_\odot$, meanwhile the infalling envelope had an initial mass of $2.5\,M_\odot$.

Along this chapter we will show the most relevant results obtained in our work and we will leave most of the discussion and conclusions for the last chapter, where the implications of the results will be treated in detail.

4.1 Initial Conditions and Input Physics

In the context of the Collapsar model, we studied the collapse and accretion of $2.5\,M_\odot$ rotating polytropic envelopes with adiabatic index $\gamma = 5/3$ onto a $2\,M_\odot$ BH fixed at the center of the mass distribution. For constructing this setup we used the same procedure as the one in last chapter, but the mass of the polytropic star used was $4.5\,M_\odot$. We took special care that the selected rotation rate for the polytropic envelope guaranteed the formation of an accretion disk close to the BH with as much mass as possible. In this section we will present the relevant details of the initial conditions and physical processes taken into account in our simulations.

4.1.1 The Polytropic Envelope and its Characteristics

The polytropic envelope was constructed by solving the Lane-Emden equation for hydrostatic equilibrium (see Shapiro & Teukolsky, 1983), from which we obtained radial profiles for the density and internal energy of $4.5\,M_\odot$ polytropic stars with central density $\rho_c = 2.53 \times 10^9$ g cm^{-3} and $\gamma = 5/3$. From the density profile we mapped a 3D particle distribution with an accept/reject MonteCarlo procedure. To account for the BH, we removed the innermost $2\,M_\odot$ from this 3D polytropic star and concentrated it in a $2\,M_\odot$ sink particle placed at the center of the distribution, leaving the remaining mass unaffected, now with inner radius $r_{\rm int}$. In table 4.1 we show the total mass of the system M_s, as well as the initial outer and inner radii of the polytropic envelope (R_s and $r_{\rm int}$ respectively). From these quantities we can obtain a characteristic time scale $t_{\rm dyn} = \sqrt{R_s^3/GM_s}$ from which all physical units are scaled in the code.

For the distribution of angular momentum in the star, of great relevance for the Collapsar model, we have assumed rigid body rotation, and assigned a constant angular velocity Ω_0, defined in terms of the circularization radius r_c the infalling gas would have in a Keplerian orbit around the BH. This circularization radius is estimated assuming a Newtonian gravitational potential (a pseudo-Newtonian potential like Paczynski & Wiita's (Paczynski & Wiita, 1980) would result in a smaller r_c, but differing in less than $\sim 3\%$ from the Newtonian one at the values involved here), a negligible contribution from gas pressure, and conservation of

System parameter	value
M_s	$4.5\ M_\odot$
$M_{\rm env}$	$2.5\ M_\odot$
R_s	1715.7 km
$r_{\rm int}$	844.69 km
$t_{\rm dyn} = \sqrt{R^3/GM_s}$	0.0919 s

Table 4.1: Envelope and total system masses, along with the characteristic time scale t_{dyn} and the outer and inner radius of the envelope.

angular momentum for the envelope material at its initial radius $r_i = (R_i^2 + z^2)^{1/2}$, where R_i is the cylindrical radius. Thus r_c can be expressed as:

$$r_c = \Omega_0^2 R_i^4 / GM(r_i) \tag{4.1}$$

where $M(r_i)$ is the mass contained inside r_i. We have assumed spherical symmetry in the mass distribution, so the gravitational pull only depends on the radius r_i. The former consideration implies that r_c would be underestimated. Figure 4.1 shows r_c as a function of the initial cylindrical radius R_i for our $2.5\ M_\odot$ polytropic envelopes at the equatorial plane. Each color represents a different constant angular velocity, the dotted lines show the circularization radius r_c neglecting gravitational interaction with the rest of the envelope, whereas solid lines represent r_c considering both the BH and the envelope gravitational interaction (with spherical symmetry). In reality, given that rotation and gravitational collapse would induce a symmetry breakup on the envelope, r_c would take values somewhere in-between the dotted and solid lines for a given angular velocity Ω_0. For simplicity, from now on, we will only focus on the circularization radius r_c for the innermost envelope material at $r_{\rm int}$, and so r_c will give an approximate position for the inner edge of the disk with respect to the BH. Figure 4.2 shows the color-coded circularization radius in a meridional slice. Clearly material close to the equator has the greatest rotation rate and will circularize at a larger radius. Close to the rotation axis angular momentum goes to zero and matter will essentially free fall into the BH.

With the purpose of choosing an adequate value for Ω_0, we first obtained from the initial spherical profiles, an estimation of the breakup rotational velocity for such polytropic envelope. Then, assuming rigid body rotation, we compared the rotational velocities obtained for an angular velocity Ω_0 with the breakup rotational velocity for the polytrope. Figure 4.3 shows the calculated breakup rotational velocity for such a polytropic star (red line) and rotational velocities in the equatorial plane for different values of the circularization radius r_c ($r_c \propto \Omega_0^2$). Rotational

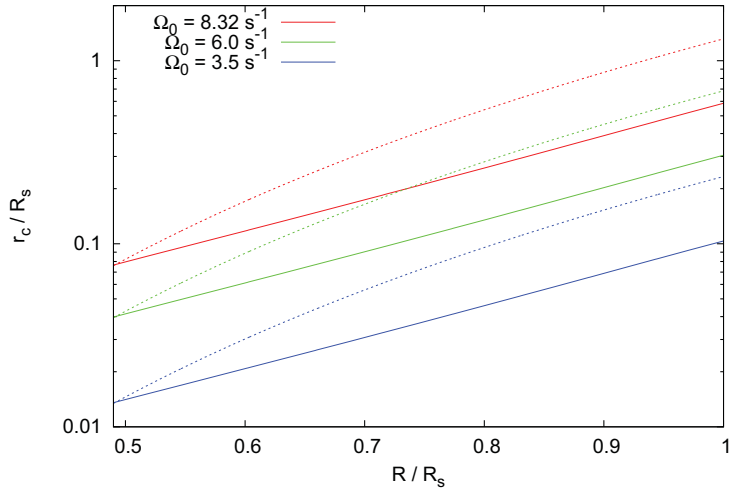

Figure 4.1: Circularization radius r_c in the equatorial plane for our 2.5 $M_\odot$ polytropic envelope as a function of the cylindrical distance R/R_s. Each color represents a different angular velocity Ω_0. Dotted lines only consider the BH mass, and solid lines consider the BH mass and an the spherical envelope mass contained at r_i.

velocities below the breakup velocity curve ensure formation of a disk around the BH at r_c (r_c for the innermost material). This estimation does not take into account asymmetric effects on the mass distribution due to rotation, given that the envelope should be rotating from the beginning and therefore, it could depart from spherical symmetry. Figure 4.3 shows that in order to obtain rotating velocities below breakup, we have to consider a circularization radius r_c smaller than $\simeq 12.8\, r_{\rm acc}$, where $r_{\rm acc}$ is the accretion radius (its value is given in the BH physics which follows). All simulations were made using $r_c = 7.49\, r_{\rm acc}$ and thus correspond to maximal disks, placing as much matter as possible in the disk while avoiding centrifugal mass loss. The estimates for energy release which we obtain should be considered accordingly. The previous setup ensures the formation of an accretion disk outside of the region of the innermost circular stable orbit around a Schwarzschild BH given by $r_{\rm isco} = 3\, r_g = 6GM_{BH}/c^2$. Gas orbiting the BH at $r < r_{\rm isco}$ would fall inevitably onto it, no matter its rotational velocity.

In order to have a handle on the accuracy of the simulations, we carried out convergence tests of the collapse and accretion of such rotating polytropic envelopes onto an accreting sink particle, using 50,000, 500,000 and 5,000,000 SPH particles of equal mass. After substantial testing, we have found no relevant difference in the accretion rates observed, or in the general properties of the accretion disk, when

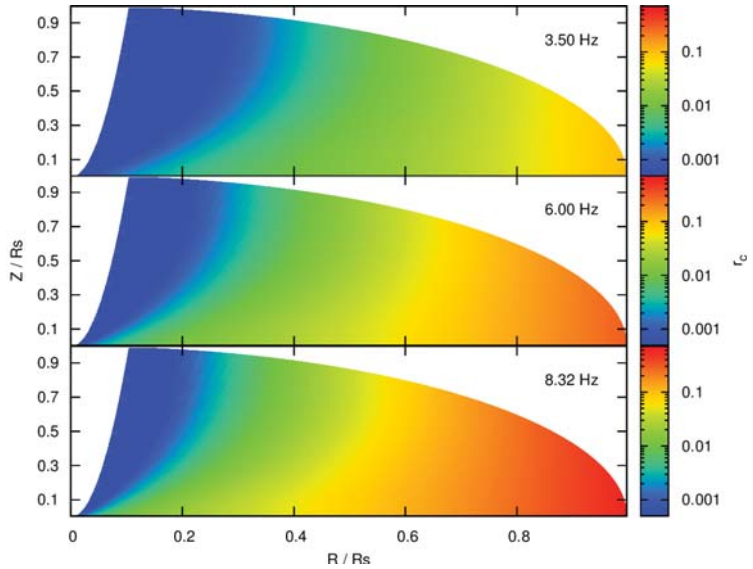

Figure 4.2: Circularization radius r_c for our $4.5\ M_\odot$ polytropic star as a function of the cylindrical distance R/R_s (X axis) and Z/R_s (Y axis) for three different angular velocities ($\Omega_0 = 8.32,\ 6.0,\ 3.5\ \mathrm{s}^{-1}$ from bottom to top). This map assumes a spherical mass distribution $M(r_i)$.

using more than 500,000 SPH particles, and so all runs described in this paper have this initial resolution. Moreover, given that the snapshots obtained for such resolution had a reasonable size ($\lesssim 30$ MB), we were able to achieve a very good time resolution between snapshots $\sim 1/20\, t_{\mathrm{dyn}}$ which proved to be helpful when looking for structure formation at the accretion disk.

Given the nature of our work, it is of great importance to ensure that the accretion disk has enough particle resolution to observe the formation of structures such as clumps or spiral arms. As shown by Bate & Burkert (1997), in order to properly represent fragmentation in an SPH simulation, the Jeans mass in the disk must be greater than the minimum resolvable mass M_{min} given by:

$$M_{\mathrm{min}} = 2M_{\mathrm{tot}}(N_{\mathrm{Ngb}}/N_{\mathrm{tot}}), \tag{4.2}$$

where M_{tot}, N_{tot} and N_{Ngb} are the total gas mass, the total number of particles and the SPH number of neighbors, respectively. For all of our simulations we found that, at all times, the Jean's mass M_J at radii $R < 0.9R_p$ was at least one order of magnitude above the resolution mass of the simulation. Meanwhile, for $R > 0.9R_p$ this condition was not always satisfied. It is therefore safe to say that for $R \lesssim 0.9R_p$, where more than 90% of the disk's mass is contained, the formation of structure is properly resolved.

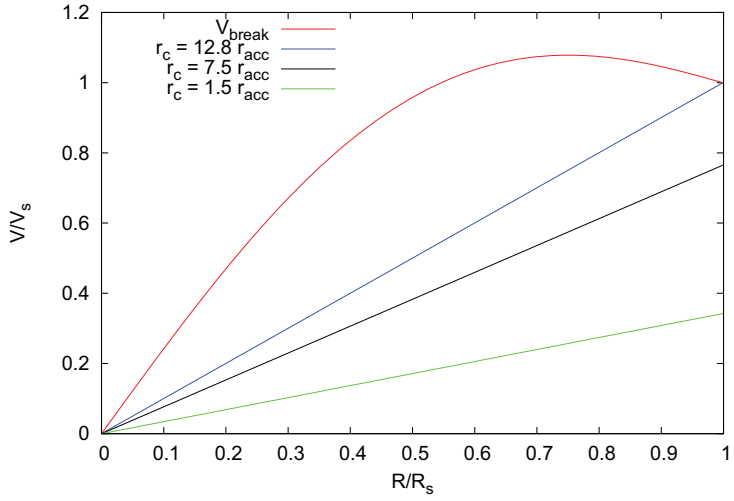

Figure 4.3: Normalized breakup velocity $V_{\rm break}$ as a function of radius for our $4.5\ M_\odot$ polytropic star (red line), and rotation velocities on the equatorial plane for rigid body rotation with circularization radius ($r_c \propto \Omega_0^2$) $12.8\ r_{\rm acc}$ (blue line), $7.5\ r_{\rm acc}$ (black line) and $1.5\ r_{\rm acc}$ (green line)).

4.1.2 Black Hole Physics

We consider the formation of a Schwarzschild BH at the center of the distribution from the innermost $2\ M_\odot$ of the initial $4.5\ M_\odot$ polytropic star. In general relativity (GR), the Schwarszchild solution for a non rotating, neutral spherical BH of mass $M_{\rm BH}$ implies the definition of the gravitational radius $r_g = 2GM_{\rm BH}/c^2$. This radius represents the event horizon, and therefore there cannot be static observers within $r < r_g$. When studying the motion of a test particle in the Schwarzschild metric, and considering a circular orbit at radius r around the BH, a relationship emerges between the orbital angular momentum L and the radius r, from which the innermost stable circular orbit can be obtained as $r_{\rm isco} = 3\,r_g$. At $r > 3\,r_g$ there can be stable circular orbits, and at $r < 3r_g$ they are all unstable. Given that at distances $r < r_{\rm isco}$ all circular orbits will fall inevitably onto the singularity, we will consider $r_{\rm isco}$ as our accretion radius ($r_{\rm acc} = 3\,r_g$), and all material at $r < r_{\rm acc}$ will be considered to enter the event horizon (at r_g), and all of its properties (such as mass, angular and linear momentum, etc...) will be transferred to the BH.

As our study is mainly focused on studying the effects of cooling and self-gravity in the formation of instabilities at the accretion disk, we will consider a pseudo-Newtonian potential to account for the most important general relativistic effects determining the motion of matter near a non-rotating BH. This together with

an adequate equation of state (EOS) and cooling mechanisms will give important information about the accretion flow without solving the problem in GR. Therefore, we will consider the BH as a $2\,M_{\odot}$ particle, artificially fixed at the origin (by canceling the forces acting on it). Nevertheless, all linear and angular momentum accreted from the gas is stored, and would be taken into account for future simulations where a freely moving BH will be considered.

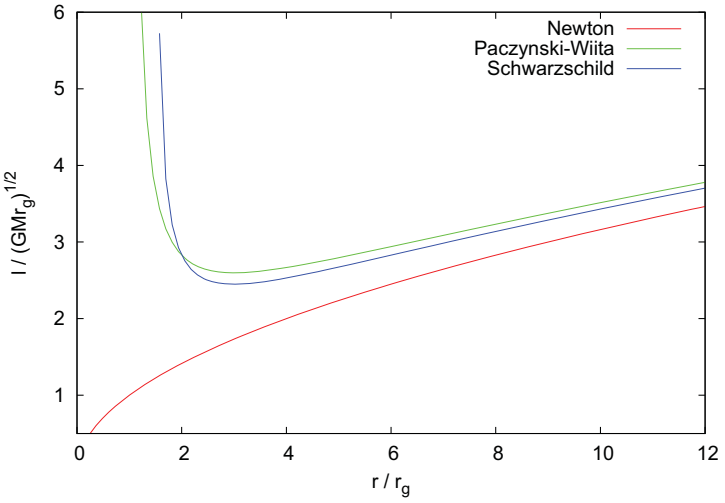

Figure 4.4: Keplerian angular momentum distribution for a test particle in a circular orbit in a Newtonian (red line), a Paczynski-Wiita (green line) and a Schwarzschild BH potential (blue line).

We considered a Paczynski-Wiita (PW) potential Φ_{PW} (Paczynski & Wiita, 1980), which reproduces exactly, the location of the marginally stable and the innermost stable circular orbit ($r_{mb} = 2\,r_g$ and $r_{\rm isco} = 3\,r_g$ respectively) for a Schwarzschild BH.

$$\Phi_{PW} = -\frac{GM_{BH}}{r - r_g} \tag{4.3}$$

This pseudo-Newtonian potential reproduces quite accurately the form of the Keplerian angular momentum distribution $L(r) = \left(r^3 d\phi/dr\right)^{1/2}$ obtained for a test particle orbiting a Schwarzschild BH (See Fig 4.4). The deviation from the Schwarzschild distribution translates into a slightly different accretion rate than the expected for GR, given that it would have a direct effect on the angular momentum transported, which in turn, would affect how material is transported at the disk. Nevertheless, considering a PW potential results in a more realistic agreement with GR than considering a Newtonian potential.

When accretion of a gas particle occurs, its mass is removed from the gas and

transferred to the BH. This changes the BH properties after an integration time dt on which the BH mass will have accreted a mass $M_{\rm acc}$ at a rate $M_{\rm acc}/dt$. This modifies r_g and therefore, the accretion radius $r_{\rm acc}$ and the PW potential at r. We carried out a series of tests of simple models of accretion, with and without rotation, and with and without hydrodynamical effects playing a role (by effectively reducing drastically the internal energy in the gas) to ensure that the modifications in the GADGET code accurately conserved mass, and linear and angular momentum during the accretion process.

4.1.3 Thermodynamics & Cooling

The code GADGET-2 (Springel, 2005) includes an ideal gas EOS, in terms of an entropic function $A(s) \equiv P/\rho^{\gamma}$. Where $\gamma = 5/3$ is the adiabatic index. Therefore, if we study the collapse of our $2.5\,M_{\odot}$ polytropic envelopes without the inclusion of any cooling mechanism on the code, the collapse would be an adiabatic one. The gas would only loose energy (internal, potential & kinetic) when it gets accreted by the BH. Although this scenario is not the one we expect in a Collapsar, given that there would be an important neutrino cooling at some regions of the disk (where T and ρ are high enough to achieve par creation & annihilation or neutronization), it is important to study it to determine the importance of cooling mechanisms in the accretion flow and the overall morphology of the accretion disk formed around the BH.

The adiabatic collapse will give us information about the collapse and formation of instabilities in an envelope whose cooling mechanisms are highly inefficient. On the other hand, an isothermal collapse accounts for an undetermined cooling process which "radiates" energy in order to maintain a constant temperature throughout the envelope as it collapses and orbits the BH. In the former scenario the energy loses are immediate, and the envelope would have already loss a great amount of energy prior disk formation. Therefore, the isothermal scheme accounts as a collapse with a highly efficient cooling mechanism. This isothermal collapse is obtained by setting $\gamma \simeq 1$ in the EOS.

In order to explore the implications of different efficiencies in the cooling mechanism, we explored the transition from an adiabatic collapse ($\gamma = 5/3$) without cooling, to an isothermal one ($\gamma \simeq 1$), in a $2.5\,M_{\odot}$ polytropic envelope with a fixed circularization radius $r_c = 7.5\,r_{\rm acc}$. For $\gamma = 5/3$, we adopted a simplified cooling prescription based on a fixed cooling time $t_{\rm cool}$ dependent of the dynamical time scale of the accretion disk (orbital period) $t_{\rm disk}$ formed around the BH.

$$t_{\rm cool} = \beta t_{\rm disk}\ , \qquad \frac{du_i}{dt} = -\frac{u_i}{t_{\rm cool}} \tag{4.4}$$

This cooling prescription is determined by the internal energy u_i and the efficiency parameter β, which determines how many times the gas must orbit the BH before it gets significantly cooled. If $\beta \gg 1$ then the gas goes around the BH many times before losing a significant fraction of its internal energy and the infall will resemble an adiabatic one. Meanwhile, if $\beta \ll 1$ then the envelope cools down before forming the disk and the cold gas would fall freely (except for rotation) onto the BH. Without compression or expansion of the envelope, the only change in the internal energy would be given by equation (4.4) and the cooling would be exponential.

The dynamical time scale for the disk can be estimated from the initial angular velocity $\Omega_0 = 8.33\ \mathrm{s}^{-1}$ obtained for a circularization radius $r_c = 7.5 r_{\mathrm{acc}}$, such that $t_{\mathrm{disk}} = 1/\Omega_0 = 0.12$ s. After disk formation, the accretion disk would have a nearly keplerian angular momentum distribution. Therefore, Ω_0 will not represent anymore the angular velocity of the whole disk, and this t_{disk} will not correspond to the local dynamical time at every radius. Nevertheless, it will still give us an estimate of the time it takes the innermost material to orbit around the BH.

Neutrino Cooling Time

In order to better understand and characterize the formation and evolution of instabilities within the disk with the presence of an effective cooling mechanism, such as neutrino emission, we explored the case where t_{cool} is close to the physical neutrino cooling time scale, t_ν. A first approximation to t_ν can be obtained from the work by Narayan, Piran & Kumar (2001), where they study different accretion flow scenarios onto a compact object (BH) in the context of GRB production. For a given temperature, T, and density, ρ, the cooling rate per unit volume due to neutrinos is given by (Narayan et al., 2001):

$$q_\nu \simeq 5 \times 10^{33} T_{11}^9 + 9.0 \times 10^{23} \rho T_{11}^6 \ \mathrm{ergs\ cm^{-3}\ s^{-1}}, \tag{4.5}$$

where the first term on the right hand side comes from pair annihilation and the second term from pair capture onto free nucleons (estimated for a fully photodesintegrated gas where the mass fraction of free nucleons is $X_{\mathrm{nuc}} = 1$). Both terms depend sensitively on temperature, $T_{11} = T/10^{11}$ K, so high temperatures, $T \gtrsim 10^{10}$ K, are required for this to become relevant.

We can estimate the temperature that the infalling gas would acquire upon arrival to the disk by calculating its free fall velocity v_{ff} at the centrifugal barrier ($r = r_c$), where material would be shocked and heated. Assuming that at the

shock ($r = r_c$) all kinetic energy is transformed into thermal energy, we can estimate an upper limit $T_{\rm up}$ to the temperature T the infalling gas would acquire as $T_{\rm up} = m v_{\rm ff}^2/3k$. To estimate $v_{\rm ff}$ we will assume the hydrogen gas has negligible pressure support and no rotation. This results in an overestimation of $v_{\rm ff}$ since the velocity won't be completely radial when rotation is included but is a fair approximation since the rotation rate is actually quite low. So, we may plot the temperature $T_{\rm up}$ acquired by the infalling gas at r_c as a function of its initial radius r_i (figure 4.5). For the circularization radius used in our simulations, $r_c = 7.5\, r_{\rm acc}$, $T_{\rm up}$ is $10^{10}\ {\rm K} \lesssim T \lesssim 10^{11}\ {\rm K}$. Therefore, assuming that the infalling gas will acquire temperatures between $10^{10}\ {\rm K} \lesssim T \lesssim 10^{11}\ {\rm K}$ at the innermost part of the disc is seen to be a good approximation.

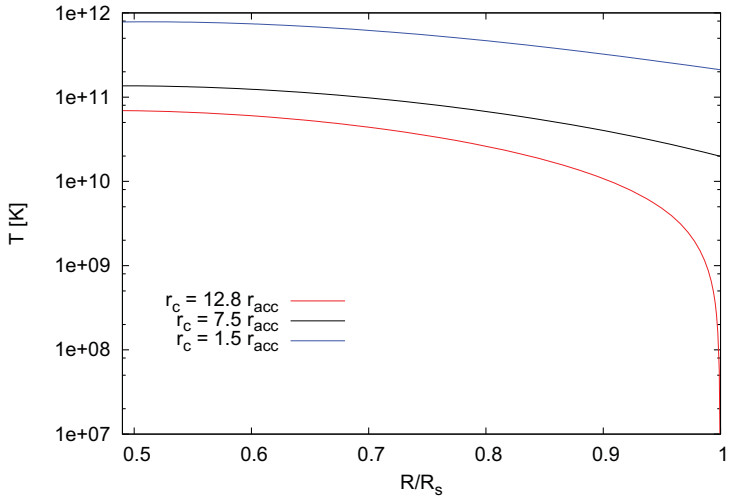

Figure 4.5: Estimated temperature T at the centrifugal barrier $r = r_c$ as function of the initial position of the envelope material. Each line corresponds to a different circularization radius r_c (or equivalently, angular velocity Ω_0).

On the other hand, the mean density of the pre-collapse polytropic envelope, $\bar{\rho}$, can be obtained from the data in Table 4.1, as $\bar{\rho} = 1.7 \times 10^9\ {\rm g\ cm^{-3}}$. This implies that after collapsing onto the BH, with a change in spatial scale of a factor of a few to 10 at the least, material will be further compressed in some regions and can easily reach densities from 10 to 1000 times larger, depending on the local pressure and the cooling mechanism implemented. Thus densities comparable to those considered by Narayan et al. (2001), $10^{10}\ {\rm g\ cm^{-3}} \lesssim \rho \lesssim 10^{12}\ {\rm g\ cm^{-3}}$ will also occur.

The internal energy of the gas will have three main contributions. Firstly, from

an ideal gas composed of α particles and free nucleons. Secondly, a contribution from radiation, which would be effectively trapped due to the high densities reached at neutrino cooling regions (the photon mean free path is many orders of magnitude smaller than the typical length scale of the problem). And finally, a relativistic electron-positron component, which can have arbitrary degeneracy. To obtain an approximation of the expected internal energy under such conditions, we will consider that the relativistic electron-positron pairs are hot and fully non-degenerate. Thus $u_{\rm gas} = 3/2\ kT\rho/(\mu m_p)$, and photons and pairs will contribute together a radiation energy density $u_{\rm rad+pair} = (11/4)\ aT^4$. Therefore the full internal energy of the gas (per unit volume) can be estimated by:

$$u = \frac{3}{2}\frac{kT\rho}{\mu m_p} + \frac{11}{4}aT^4 \tag{4.6}$$

From equations (4.5) and (4.6) and considering densities in the range $\rho \simeq 10^8 - 10^{12}$ g cm^{-3} and temperatures of the order $T \simeq 10^9 - 10^{11}$ K, we can estimate a neutrino cooling time scale $t_\nu = u/q_\nu$ as shown in figure 4.6. We limited the plot to 10^{-4} s $\leq t_\nu \leq 10$ s, which contains the cooling times explored here. t_ν depends strongly on the temperature of the system when reaching $T \sim 10^{11}$ K, when neutrinos from pair annihilation dominate q_ν. Table 4.2 shows the efficiency parameter β used in our simulations, and the corresponding cooling time, $t_{\rm cool}$. Our models will be labeled after their $t_{\rm cool}/t_{\rm dyn}$ ratio, as shown in Table4.2.

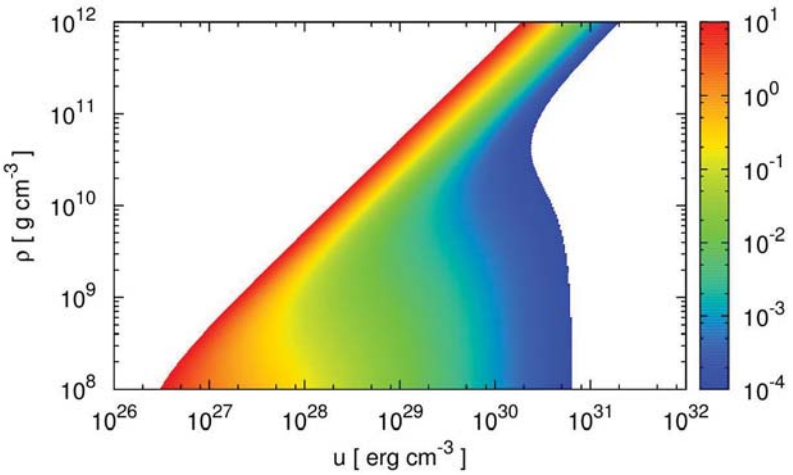

Figure 4.6: Neutrino cooling time scale t_ν estimated for an ideal gas ($\mu = 1/2$) with thermal relativistic electron-positron pairs and radiation pressure contributions. White regions on the left account for $t_\nu > 10$ s and white regions on the right for $t_\nu < 10^{-4}$ s.

Model	Cooling efficiency β	$t_{\rm cool}$	$t_{\rm cool}/t_{\rm dyn}$
βAd	Adiabatic	–	–
β13.4	10.27	1.2319 s	13.4
β2.68	2.054	0.24639 s	2.68
β1.34	1.027	0.12319 s	1.34
β0.67	0.513	0.061595 s	0.67
β0.134	0.1027	0.012319 s	0.134
β0.067	0.0513	0.0061595 s	0.067
βIso	Isothermal	–	–

Table 4.2: Cooling times $t_{\rm cool}$ and efficiency parameters β used in our simulations. All times range within the neutrino cooling time, t_ν previously estimated.

4.2 Results

We will first discuss the general features of the accretion process, such as the BH mass accretion rate $\dot{M} = dM/dt$, the evolution of the BH mass $M_{\rm BH}$, and the energy loss rate L_c, defined by the cooling times from Table4.2. These quantities will give us information on the general changes in the behavior of the system when implementing different cooling schemes. Then we will study in detail some specific models, in order to look for a relation between these quantities's behavior and the disk's specific properties, or the cooling time scale itself.

4.2.1 Accretion Rates and BH Mass

Given that the polytropic envelope is intrinsically located at a distance $\sim R_s/2$ from the BH at $t = 0$, the accretion will not begin until the innermost material reaches the center of the distribution. The time the envelope takes to reach the BH is affected by the gas pressure which, in the case of being negligible, would translate into a free-fall time of the envelope $t_{\rm fall} \sim t_{\rm dyn}/2$. In reality, gas pressure will make the envelope reach the BH at a slightly earlier time, $t_{\rm fall} \lesssim t_{\rm dyn}/2$.

Figure 4.7 shows the accreted mass as a function of time for all different models. In every case, accretion begins at a time $0.02\ {\rm s} \lesssim t \lesssim 0.05\ {\rm s}$ depending on the cooling scheme. The more efficient the cooling, the more $t_{\rm fall}$ and the accreted mass increase. At the bottom panel of figure 4.7 we can see the slowly cooled envelopes (β13.4, β2.68 & β1.34) which resemble the adiabatic one (red line) the most. All these models show a smooth increase in the accreted mass for at least

the first ~ 0.9 seconds. Models $\beta 2.68$ and $\beta 1.34$ have an abrupt increase in the accreted mass after ~ 1.9 and ~ 0.9 s respectively. In the top panel, we can see the cooled envelopes with higher cooling efficiency ($\beta 0.67$, $\beta 0.134$ & $\beta 0.067$) which resemble the isothermal envelope (red line) the most. Efficiently cooled models show abrupt changes in the accreted mass and considerably higher accreted mass than the slowly cooled ones. Models with high cooling efficiency (as well as the isothermal one) are terminated at earlier times because of the computational demands imposed by an increasingly shorter time step in the final stages. Special care was taken in order to keep the gas from cooling below $u = 0$, by imposing a threshold in the cooling subroutine so that the energy was lost only for gas with $T > 1000$ K.

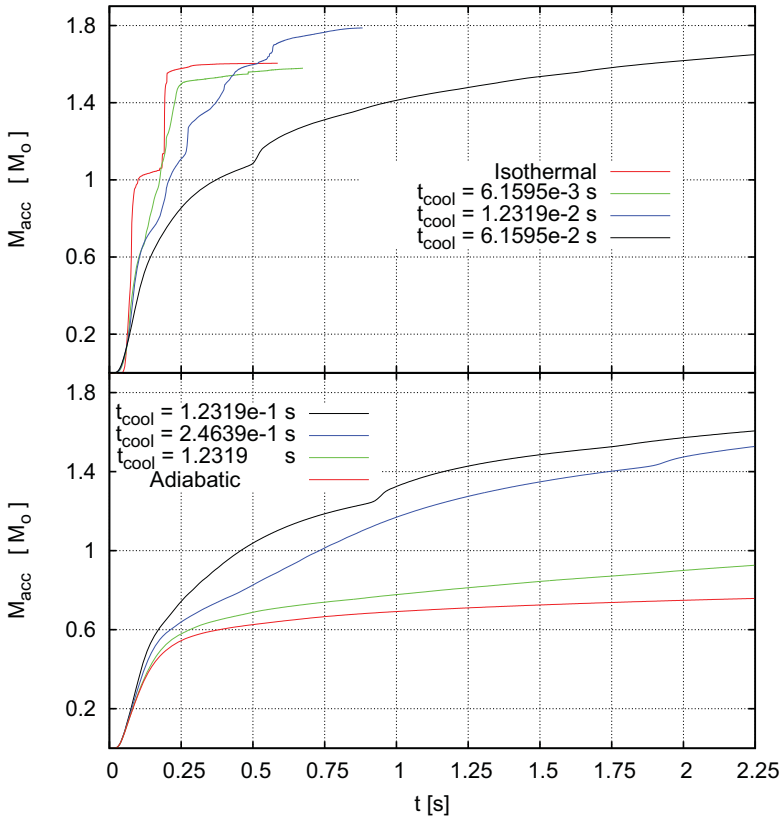

Figure 4.7: Accreted mass (solar masses) as function of time (seconds) for all different cooling rates used. In the top panel we show the models $\beta 0.067$ (green line), $\beta 0.134$ (blue line) and $\beta 0.67$ (black line) with the shorter cooling time scale $t_{\rm cool}$ which resemble the isothermal envelope (red line) the most. The bottom panel shows models $\beta 13.4$ (green line), $\beta 2.68$ (blue line) and $\beta 1.34$ (black line) which cool slowly and resemble the adiabatic case (red line).

Figure 4.8 shows the evolution of the accretion mass rate for all models, whose first peak at $t \lesssim 0.1$ s is due to the accretion of infalling material with low angular momentum. As material reaches the BH, a shock is formed and propagates outwards. If no cooling is enabled, the evolution is adiabatic, which will slow down the infalling material and prevent some of it from being accreted. Meanwhile, with finite cooling, the shocked material is able to lose energy, and the shock is slowed down faster than in the adiabatic envelope. This translates into a higher accretion rate shown as a peak at $t \sim 0.1$ s in figure 4.8 (more distinguishable in the bottom panel).

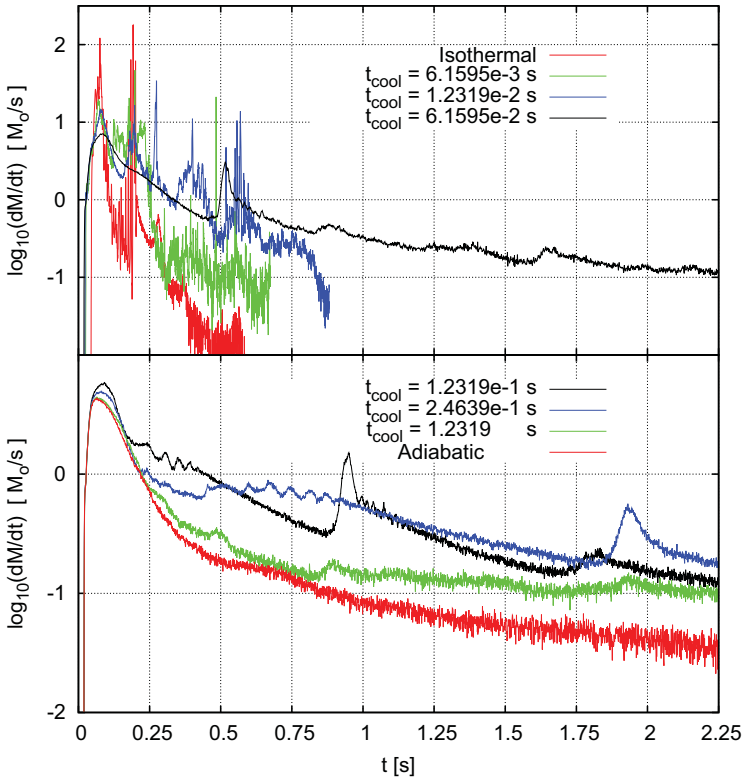

Figure 4.8: Logarithm of the BH mass accretion rate $\dot{M}$ in solar masses per second. In the top panel we show models $\beta 0.067$ (green line), $\beta 0.134$ (blue line) and $\beta 0.67$ (black line) which resemble the isothermal envelope (red line) the most, while the bottom panel shows models $\beta 13.4$ (green line), $\beta 2.68$ (blue line) and $\beta 1.34$ (black line), akin to the adiabatic case (red line).

If the shock is strong enough to slow down the infalling material, the accretion rate will be diminished considerably. This, together with the exhaustion of low angular momentum material, translates into a decrease in the accretion rate, shown

at times $0.1 \text{ s} \lesssim t \lesssim 0.25 \text{ s}$ in figure 4.8. This does not seem to hold for models $\beta 0.134$, $\beta 0.067$ and βIso which show strong variations in dM/dt after $t \simeq 0.1$ s. Once the shock has passed through the whole envelope, material will settle around the BH and form an accretion disk, whose thickness decreases with increasing cooling efficiency, as expected. From this point on, material from the disk will be able to fall onto the BH if angular momentum transport occurs. This can be seen in the bottom panel of figure 4.8 around $t = 0.3$ s, when the accretion rate has decreased by nearly one order of magnitude with respect to the initial peak.

As we can see from figure 4.8, the slowly cooled models show smaller variations in the accretion rate $\dot{M}$ than the more efficiently cooled ones. Such variations must be due to a change in the way material is transported within the disk. Particularly, model $\beta 0.134$ (blue line in the top panel of figure 4.8) shows several peaks in $\dot{M}$ at times $t \sim 0.2, 0.3,$ and 0.4 s. Some quasi-periodic pattern may be present in the accretion rate of model $\beta 0.134$, and it will be studied carefully below.

4.2.2 Cooling Efficiency and Heat Losses

Models implemented with our cooling prescription will be loosing energy each time step at a rate $du_i/dt = -u_i/t_{\rm cool}$. This cooling rate depends on the internal energy u_i, at the position (R, ϕ, z). Therefore, energy losses won't be uniform throughout time and/or space. Considering the contribution from each SPH particle, we can obtain the total energy loss rate $L_c = \sum_j (-du_i/dt)_j$ at a given time t. Note that L_c is defined to be positive, this allows us to associate the energy loss rate with the neutrino luminosity L_ν expected in an accretion disk with a characteristic neutrino time scale t_ν.

Energy loss rates L_c (i.e., neutrino luminosities) for different cooling efficiencies are showed in the bottom panel of figure 4.9. The maximum L_c is obtained for the model with higher cooling efficiency, reaching up to $L_c \sim 10^{54}$ erg s^{-1} = 1000 foe s^{-1} [1]. The total energy lost $u_{\rm lost} = \int L_c \, dt$ is shown in the top panel of figure 4.9, with a maximum value $u_{\rm lost} \sim 10^{53}$ erg that is also reached by the most efficiently cooled model, in only $t \lesssim 0.7$ s.

As the cooling efficiency increases, the changes in the energy loss rates L_c become more drastic. By comparing figures 4.8 and 4.9, we see that such abrupt changes coincide in time with intense increases in the accretion rates. Given that a rapid increase in the energy loss rate L_c is only possible if there is an increase in the internal energy ($du/dt \propto u/t_{\rm cool}$), some mechanism must be causing the increase

[1] 1 foe $= 10^{51}$ erg, stands for the energy's order of magnitude "fifty one ergs".

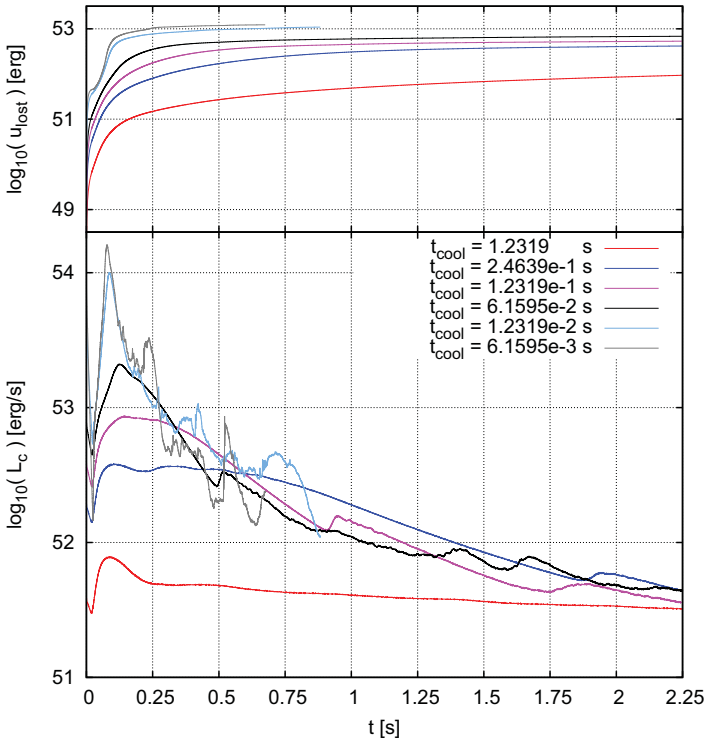

Figure 4.9: Logarithm of the energy loss rate L_c (bottom panel) in erg/s for models $\beta 13.4$ (red line), $\beta 2.68$ (blue line), $\beta 1.34$ (pink line), $\beta 0.67$ (black line), $\beta 0.134$ (light blue line) and $\beta 0.067$ (gray line). In the top panel we show the integrated energy lost by all SPH particles, $u_{\rm lost}$, as a function of time.

in the local internal energy u. As these intense variations on both $\dot{M}$ and L_c appear as the cooling efficiency is improved, it seems logical to assume that the formation of structure within the accretion disk is triggering these variations. Therefore, we study in detail the formation of structures, such as spiral arms, in order to look for a coincidence of structure formation events with the intense increases in both the accretion rate and the energy loss rate.

Based on the obtained energy loss rates L_c from our different models, and the assumption that the neutrino cooling would have a cooling time scale t_ν ranging within the cooling times t_{cool} explored here, we can expect to obtain neutrino luminosities L_ν ranging between $1 \lesssim L_c \lesssim 2000$ foe s^{-1} (depending on the local temperature and density conditions) when a realistic neutrino prescription is used. An efficient neutrino cooling will be restricted to regions with really high temperatures ($T \gtrsim 10^{11}$ K) and densities ($\rho \gtrsim 10^{10}$ g cm^{-3}), and this cooling mechanism

won't be efficient during the initial collapse of the envelope, when the bulk of the gas has not yet reached the BH. This may affect the energy loss rates significantly at earlier times. Moreover, here we do not consider the possibility of energy deposition from the cooling mechanism itself, which will be important for neutrino cooling at regions of high density ($\rho \gtrsim 10^{12}$ g cm^{-3}) when the opacity due to neutrons and α particles becomes important (Shapiro & Teukolsky, 1983). This may diminish the neutrino luminosity and could also prevent the material from cooling down so efficiently.

4.2.3 Characteristic Time Scales in the Disk

In order to look for characteristic time scales for the gas in the accretion disk, we performed Fourier transforms of the time series for $\dot{M}$, L_c and the cylindrical radial component of the momentum P_r. Any characteristic time scale occurring in them will appear as a peak in the Fourier transform amplitude $|F(\nu)|^2$. Figures 4.10 and 4.11 show the Fourier transforms for L_c (red line), $\dot{M}$ (blue line) and P_r (black line) for all models (except L_c for the adiabatic and isothermal models) as a function of inverse frequency $t = 1/\nu$ (in seconds). Figure 4.10 shows that there is a transition in the peaks in $|F(\nu)|^2$ for $\dot{M}$ appearing at $t \simeq 0.2$ and 0.05 s when the cooling efficiency β increases. These two peaks in $\dot{M}$ also appear in L_c for models $\beta 13.4$ and $\beta 2.68$, but the peak at $t \simeq 0.05$ s is not that clear for model $\beta 1.34$. The transform for L_c also shows less intense peaks at time scales shorter than 0.02 s and longer than 0.001 s.

There are more characteristic time scales appearing on the cylindrical radial component of the momentum P_r, and they become clearer on models with more efficient cooling than $\beta 2.68$, with characteristic time scales ranging from $t \simeq 0.02$ to 0.2 s. This range partly coincides with that associated to the epicyclic frequency due to the BH, which varies approximately from 0.001 to 0.1 seconds along the disk. There also seems to be an intense radial oscillation in the disk, seen in the transform for model $\beta 0.67$ (on figure 4.11), with period $T \simeq 0.08$ s, as well as another oscillation of smaller intensity with period $T \simeq 0.01$ s. Models with higher cooling efficiency also show the presence of a characteristic period in the range $0.007 \lesssim t \lesssim 0.015$ s.

Comparing figures 4.10 and 4.11 we can see that increasing the cooling efficiency increases the number of peaks appearing at higher frequencies (smaller characteristic time scales) in the Fourier transforms. This coincides with the increase of variations in $\dot{M}$ and L_c seen when increasing the cooling efficiency. We note that only the more efficiently cooled models show significant variations on

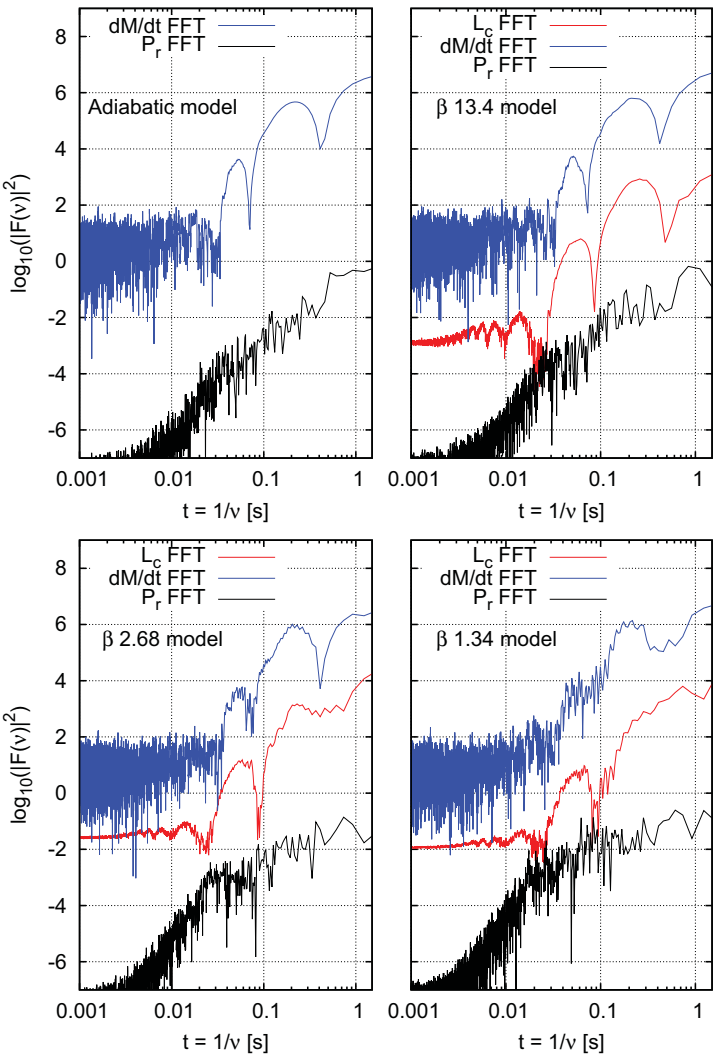

Figure 4.10: Logarithm of the renormalized Fourier's transform power $|F(\nu)|^2$ of the mass accretion rate $\dot{M}$ (blue line), the energy loss rate L_c (red line) and the cylindrical radial component of momentum P_r (black line) versus inverse frequency $1/\nu$ (time), for the adiabatic case, and models $\beta 13.4$, $\beta 2.68$ and $\beta 1.34$ (we only show the transform of L_c for cooled models). The spectrum of the mass accretion rate $\dot{M}$ shows power at intrinsic time scales of $t \simeq 0.2$ and 0.05 s that also appear in the spectrum of L_c. Increasing the cooling efficiency alters the position and intensity of the peaks time scales and in model $\beta 1.34$ an additional peak is present at $t \simeq 0.02$ s.

time scales shorter than 10 milliseconds, and as stated in the previous sections, these variations seem to be produced by the formation of instabilities in the disk.

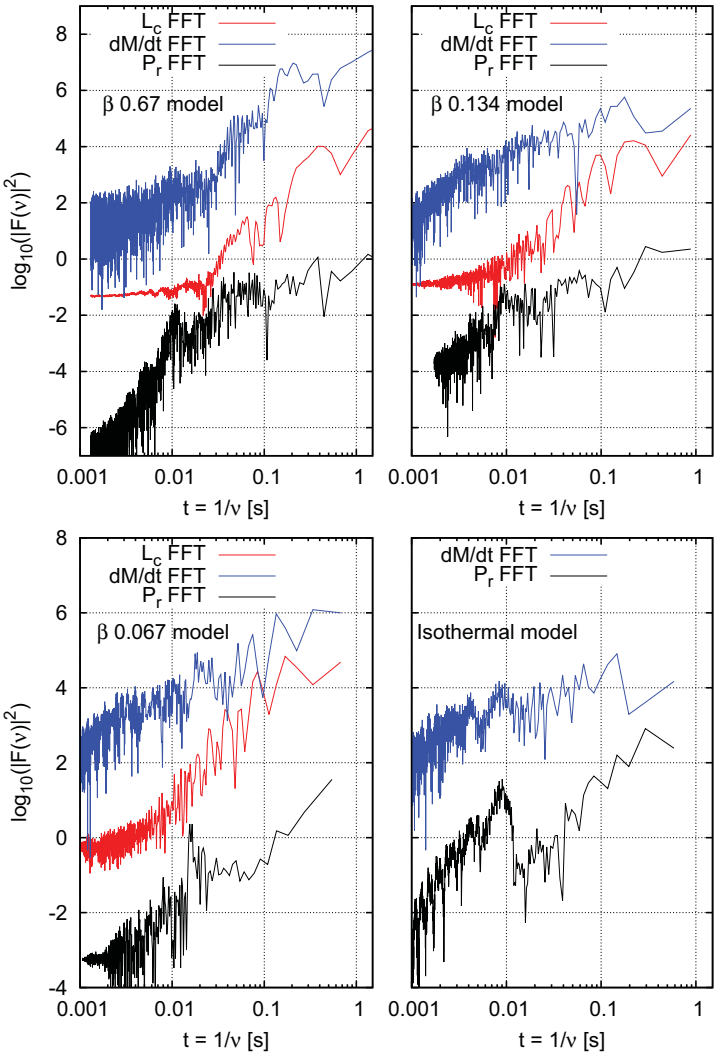

Figure 4.11: Logarithm of the renormalized Fourier's transform power $|F(\nu)|^2$ of the mass accretion rate $\dot{M}$ (blue line), the energy loss rate L_c (red line) and the cylindrical radial component of momentum P_r (black line) versus $1/\nu$ (time), for models $\beta 0.67$, $\beta 0.134$, $\beta 0.067$ and the isothermal case. More efficient cooling seems to increase the number of intense peaks appearing also at shorter time scales (higher frequencies).

4.2.4 Morphological Features

If the formation of patterns in the disk is responsible for the rapid variations in both $\dot{M}$ and L_c, we must start by looking for instabilities that may give rise to the formation of such structures. This can be done by looking for regions where local gravitational instability arises because of the high density and/or low pressure (internal energy). This may be observable in density and/or internal energy maps in the disk plane. Moreover, the appearance of any asymmetric structures in the disk could alter the angular momentum distribution and transport. Spiral arms and high-density gas clumps can alter the gravitational interaction between the disk and the black hole and lead to the transport of angular momentum across the disk, independently of the presence of any viscous mechanism (such as the magneto-rotational instability; Balbus & Hawley, 1991).

In order to characterize non-axisymmetric instabilities, we performed a one-dimensional Fourier transform of the azimuthal distribution of mass Φ_M, as in the work of Zurek & Benz (1986), defining the amplitude of the m-th mode by:

$$\begin{aligned} C_m &= \frac{1}{2\pi}\int_0^{2\pi} e^{im\phi}\Phi_M d\phi, \qquad \text{where} \\ \Phi_M &= \int \left[\int \rho(\phi, r, z)dz\right] r\, dr. \end{aligned} \tag{4.7}$$

The power in each mode, $|C_m|^2$, will give us information about the presence of over-dense structures with $2\pi/m$ azimuthal symmetry in the disk. Therefore, the relative power $|c_m|^2 = |C_m|^2/|C_0|^2$ will give us information on the intensity of m spiral arms compared to the integrated disk mass C_0, at time t. By plotting the evolution in time of such relative powers $|c_m|^2$ we can study the evolution of the disk and look for the formation and disruption of spiral arms forming at the disk.

Such spiral structures should also be observable in density maps at the $z = 0$ plane or, more appropriately, in the surface density, $\Sigma(r, \phi) = \int \rho(r, \phi, z)dz$, maps as over-dense regions. Nevertheless, in order to obtain quantitative information about the formation of structure in our simulations, we have found it more useful to study the evolution of the Toomre parameter in the disk (Toomre 1964), which provides insight on the conditions under which the accretion disk around the BH becomes unstable. The Toomre parameter is given by:

$$Q_T = \frac{\kappa c_s}{\pi G \Sigma}, \tag{4.8}$$

where, $\kappa = (\partial W/\partial r)^{1/2}$ is the epicyclic frequency of motion for material in the disk, obtained from first order perturbations and subject to the effective potential $W(r) = \phi(r) + l^2/2r^2$, $\Sigma(r,\phi)$ is the surface density of the disk, and c_s is the local sound speed[2]. By evaluating the Toomre parameter Q_T throughout the disk, we should be able to notice the formation of any spiral structures, as a region with Q_T lower than the average value, given the higher surface density caused by its collapse. Considering that we are only using Q_T as a parameter to visualize collapsing regions with significantly higher density and/or lower temperature, we will consider an approximation to the epicyclic frequency which neglects the contribution of the disk to the gravitational potential. The epicyclic frequency of a gas particle orbiting a BH with a PW potential is given by:

$$\kappa = \left(\frac{\partial W}{\partial r}\right)^{1/2} = \left(\frac{GM_{BH}(r-3r_g)}{r(r-r_g)^3}\right)^{1/2}. \tag{4.9}$$

This approximation will translate in values for κ that are 1.5 to 3.5 times smaller than those obtained directly from the simulation data, because of the self-gravity of the disk, but it will be significantly simpler to evaluate them uniformly thus. In the next section section we will study the morphology of some models individually, in order to obtain information on the importance of structure formation for the variability in the mass accretion and energy loss rates. We will focus on the models with $t_{\rm cool} \lesssim 0.2$ s, which show the most significant variability.

$\beta 2.6$ **Model**

This model with cooling time $t_{\rm cool} = 0.246$ s has the less efficient cooling showing at least one intense variation in $\dot{M}$ and L_c after the initial collapse and formation of the accretion disk. Its accretion rate and energy loss rate show an abrupt change at $t \simeq 1.9$ s (figure 4.12), which suggests the presence of a structure formation event, which induces compression and heating of material in the accretion disk. The evidence of such structure formation event can be observed in figure 4.13 where the evolution of the relative power $|c_m|^2$ for the modes $m = 1, 2, 3,$ and 4 is plotted on the top panels (red lines). At $t \simeq 1.75$ s there is an intense increase on mode $m = 2$ which reaches a peak at $t \simeq 1.9$ s becoming the most intense mode of all. This increase in mode $m = 2$ is followed by the increase in the rest of the modes which have peaks also close to $t \simeq 1.9$ s. From the Fourier modes we expect to see the formation of two spiral arms at the disk at $t \simeq 1.75$ s, and these spiral arms seem to be producing the increases on both $\dot{M}$ and L_c at $t \simeq 1.9$ s.

[2]The epicyclic frequency is the harmonic oscillator frequency obtained from a first order analysis of a linear perturbation to the disk's potential.

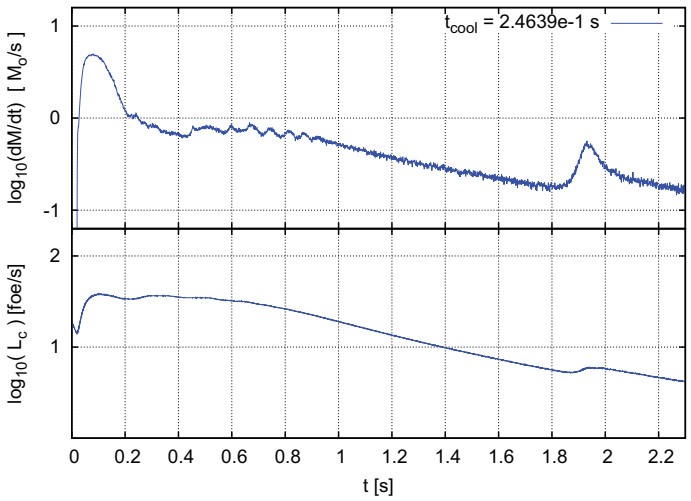

Figure 4.12: Mass accretion and energy loss rates for $\beta 2.6$ model (top and bottom panel respectively). There is an intense increase on both L_c and $\dot{M}$ at $t \simeq 1.9$ s, when the mode $m = 2$ reaches a maximum.

In figures 4.14, 4.15 and 4.16 we plot a series of Toomre parameter maps as far as $r = 0.8\,R_s$ where most of the disks mass is contained and where we expect to see the most intense structure formation events. Each group of six panels shows a color map of Q whose evolution is followed from 1.74 s $\lesssim t \lesssim 2.14$ s. The initial and final times of each plot are indicated on the top left panel and the right bottom panel respectively, and the evolution of time goes from top to bottom and from left to right. A blue color indicates the lowest Q value on the color map (showed on the log scaled color bar at the right side of the panel), and Q increases as the color turns to red. In order to easily explore the transition between $Q > 1$ and $Q < 1$ we set a limit on the highest Q value the map would plot. White color regions inside $r = 0.8\,R_s$ indicate that Q has a higher value than the top limit. As we see from figure 4.14 at $t \simeq 1.75$ s there are no discernible spiral structures present in the disk, but at $t \simeq 1.86$ s it is clear that two spiral arms have formed, becoming more collapsed (decreasing Q) as time evolves. These spiral arms remain strong for at least ~ 0.15 seconds until they are dissipated and broken into more structure (shown on figures 4.15 and 4.16). The remaining structure is shown as noise on all modes $|c_m|^2$ on figure 4.13.

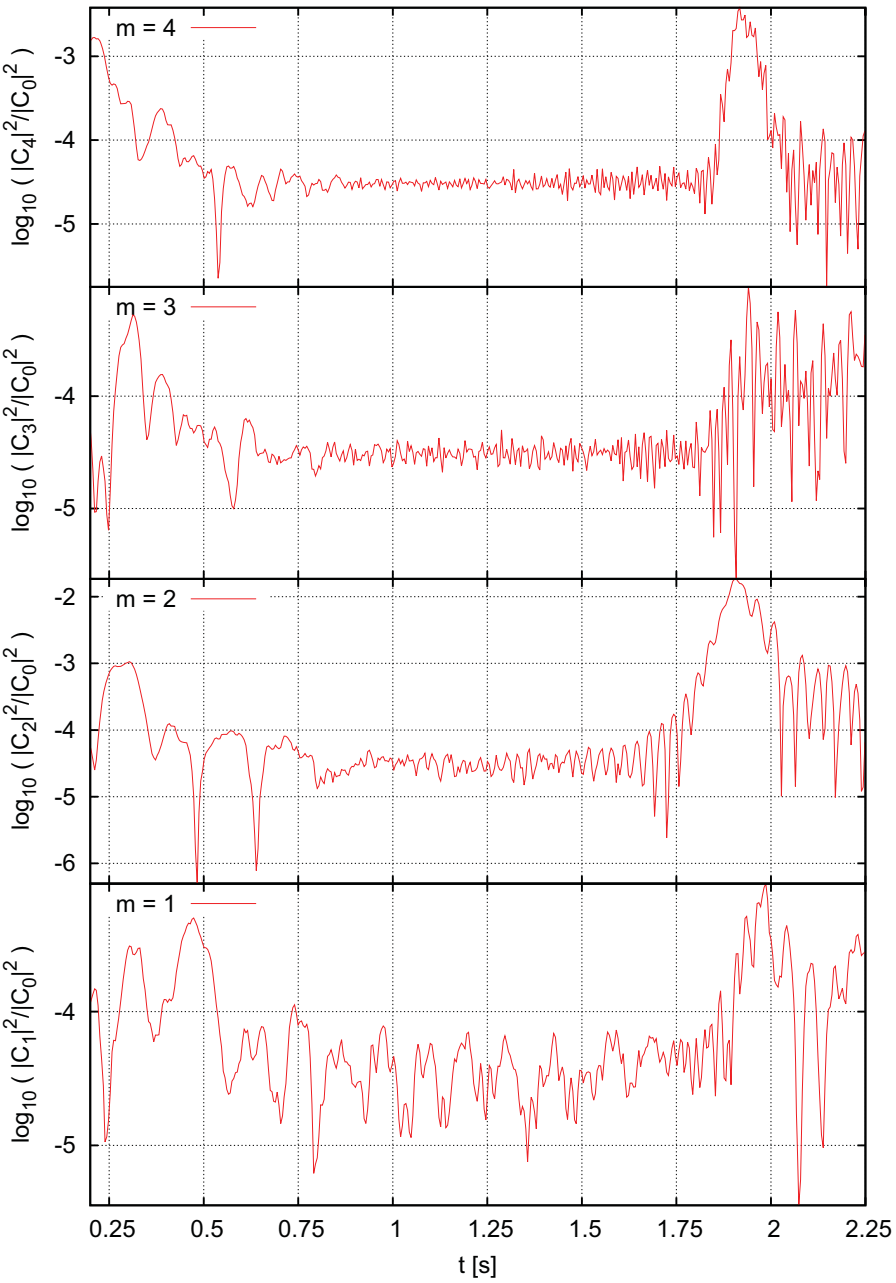

Figure 4.13: Evolution of the relative power $|c_m|^2 = |C_m|^2/|C_0|^2$ ($m = 1, 2, 3, 4$) for the azimuthal mass distribution Φ_M Fourier transform of $\beta 2.6$ model. At $t \simeq 1.75$ s mode $m = 2$ starts an ongoing increase which reaches a maximum at $t \simeq 1.9$ s.

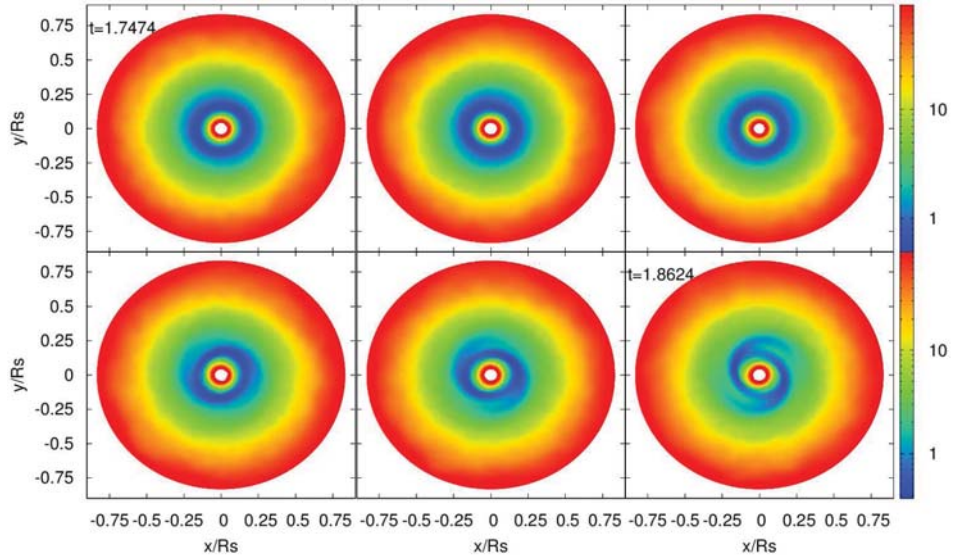

Figure 4.14: Evolution of the Toomre parameter Q for the $\beta 2.6$ model at times $1.74\text{ s} \lesssim t \lesssim 1.87\text{ s}$. The initial and final times are indicated on the top left panel and the right bottom panel respectively, and the evolution of time goes from left to right and top to bottom. The last two panels show the appearance of two spiral arms as expected from the relative power $|c_2|^2$.

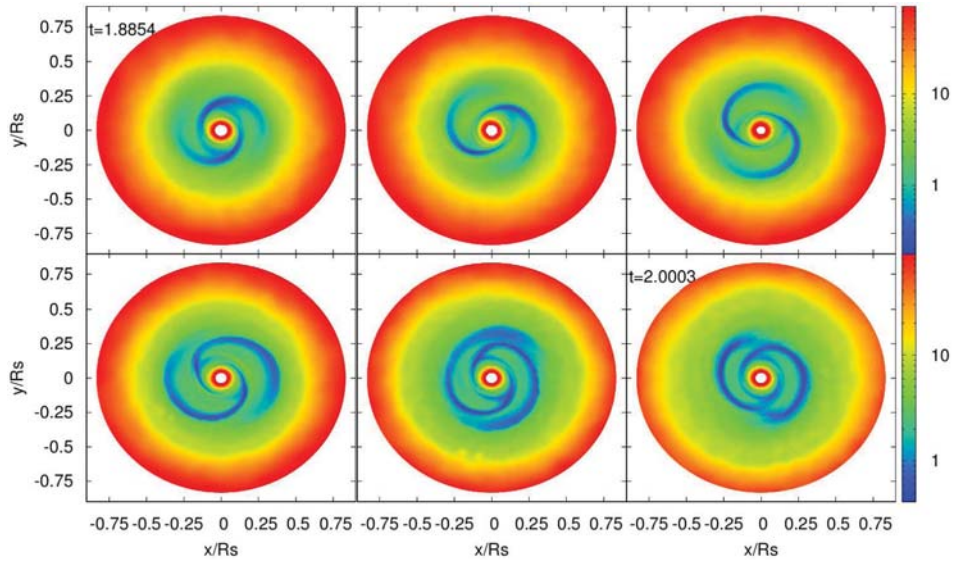

Figure 4.15: Evolution of the Toomre parameter Q for the $\beta 2.6$ model at times$1.88\text{ s} \lesssim t \lesssim 2.0\text{ s}$. The two spiral arms shown by the relative power $|c_2|^2$ are clearly visible.

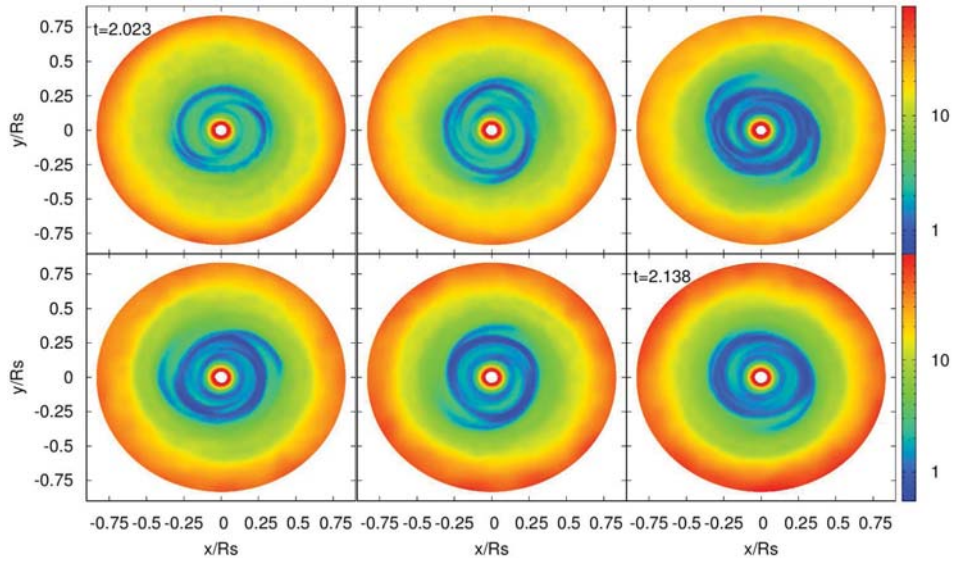

Figure 4.16: Evolution of the Toomre parameter Q for the $\beta 2.6$ model at times2.02 s $\lesssim t \lesssim 2.1$ s. The two spiral arms have broken into more structure.

$\beta 1.34$ Model

As with model $\beta 2.68$, this model, with $t_{\rm cool} = 0.12319$ s, shows an abrupt change in both the accretion rate and the energy loss rate, but at an earlier time, $t \simeq 0.9$ s (figure 4.17). Therefore, it also suggests there should be a structure formation event producing such variations. In figure 4.18 we see the evolution in time of the relative power $|c_m|^2$ for the modes $m = 1, 2, 3$ and 4, and there is an intense structure formation event starting at $t \simeq 0.8$ s, shown in every Fourier mode in figure 4.18. Nevertheless, the $m = 2$ mode seems to be the most intense of all, and therefore, we expect to observe two spiral arms on the Toomre parameter plots at $t \simeq 0.9$ s when it reaches its maximum.

Figures 4.19, 4.20 and 4.21 show the evolution in time of the Toomre parameter Q for times 0.78 s $\lesssim t \lesssim 1.2$ s where the mode $m = 2$ reaches its maximum. The last panel from figure 4.19 shows the appearance of two spiral arms at $t \simeq 0.9$ s. These spiral arms are disrupted at $t \simeq 1$ s (Fig. 4.20), but they are followed by the appearance of another two spiral arms on the following Toomre parameter maps (figures 4.20 and 4.21). This is also visible in the Fourier mode $m = 2$ showing strong variations at such times. Figure 4.22 shows the Toomre parameter Q at times 1.74 s $\lesssim t \lesssim 1.86$ s s, where an increase on both $\dot{M}$ and L_c can be seen

in figure 4.17. This increase is also shown in the Fourier modes in Figure 4.18 as strong variations in modes $m = 2, 3$.

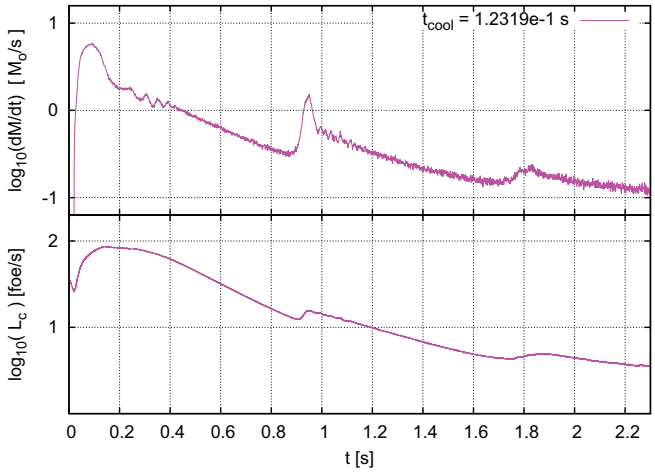

Figure 4.17: Mass accretion and energy loss rates for model $\beta 1.34$ (top and bottom panel respectively). There is an intense increase in both L_c and $\dot{M}$ at $t \simeq 0.9$ s .

There seems to be a relationship between the time of the first structure formation event and the cooling time, but the formation of structures should also depend on the amount of mass contained in the disk. As increasing the cooling efficiency allows more material to be accreted during the initial collapse, the disk's mass can be considerably reduced and therefore, the first structure formation event could be delayed due to the fact that the disk does not have enough material to become unstable until enough cooling has taken place.

As in Korobkin (2011), we calculated the phase ϕ and velocity $d\phi/dt$ of the Fourier mode $m = 2$ according to Woodward et al. (1994) (based on the work by Williams & Tohline, 1987) at a time $t \simeq 0.09$ s, when two spiral arms are clearly visible in density maps. Then, in order to obtain the corotation radius we calculated the time derivative of the mode's phase $d\phi/dt$ as a function of the radius r. Thus, by comparing $(d\phi/dt)(r)$ and the disk's integrated angular velocity distribution $\Omega(r)$ it was straightforward to obtain the corotation radius of both components. We found that at times where the spiral structure is clearly visible in density maps, the phase, and intensity of such modes coincide very well with the overdense regions (see figure 4.23). For radii where there is no visible spiral structure in the density map, the phase of the mode becomes quite noisy, and there are large phase jumps until the Fourier approximation finds a structure identifiable with a $2\pi/m$ mode.

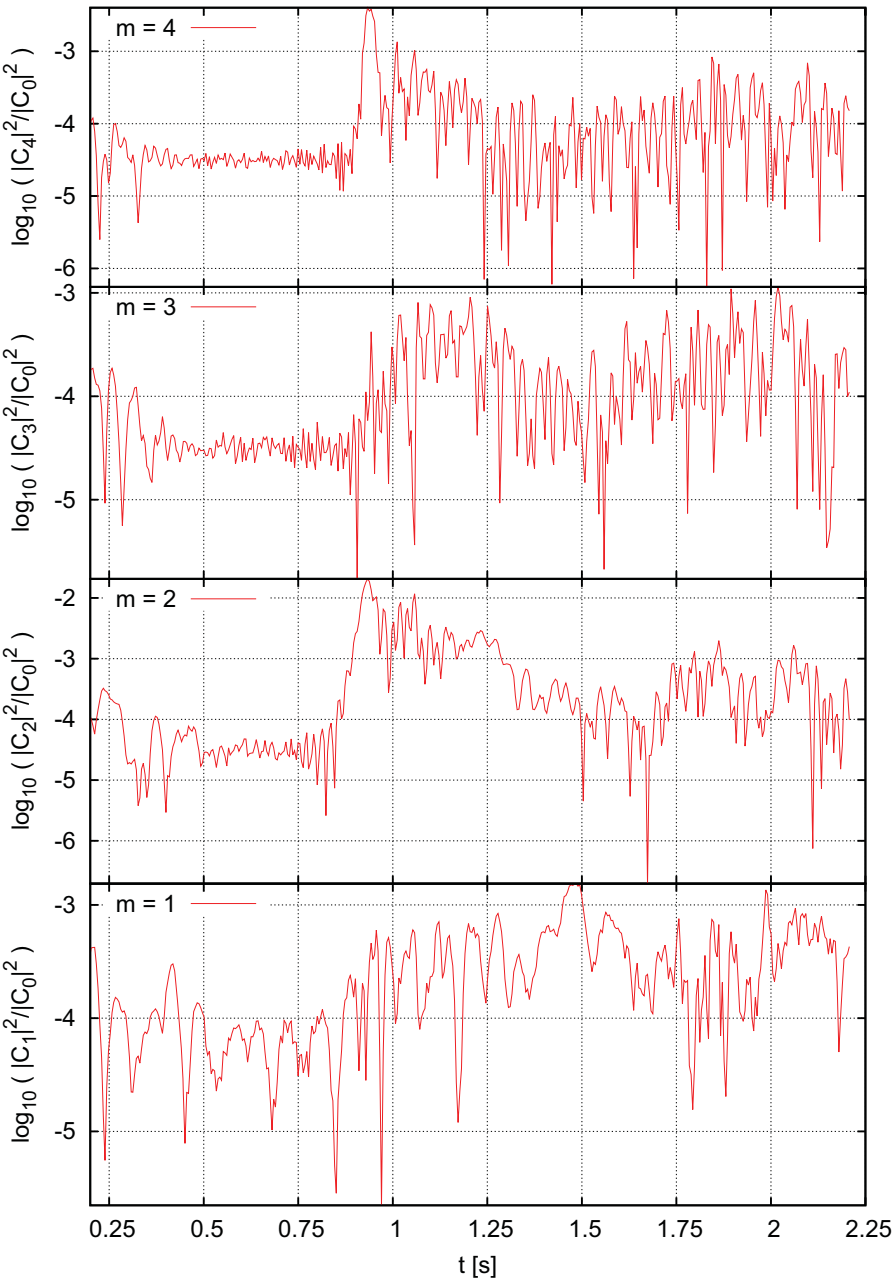

Figure 4.18: Evolution of the relative power $|c_m|^2 = |C_m|^2/|C_0|^2$ ($m = 1, 2, 3, 4$) for the azimuthal mass distribution Φ_M Fourier transform in model $\beta 1.34$. At $t \gtrsim 0.75$ s mode $m = 2$, begins to rise, and peaks at ~ 0.9 s.

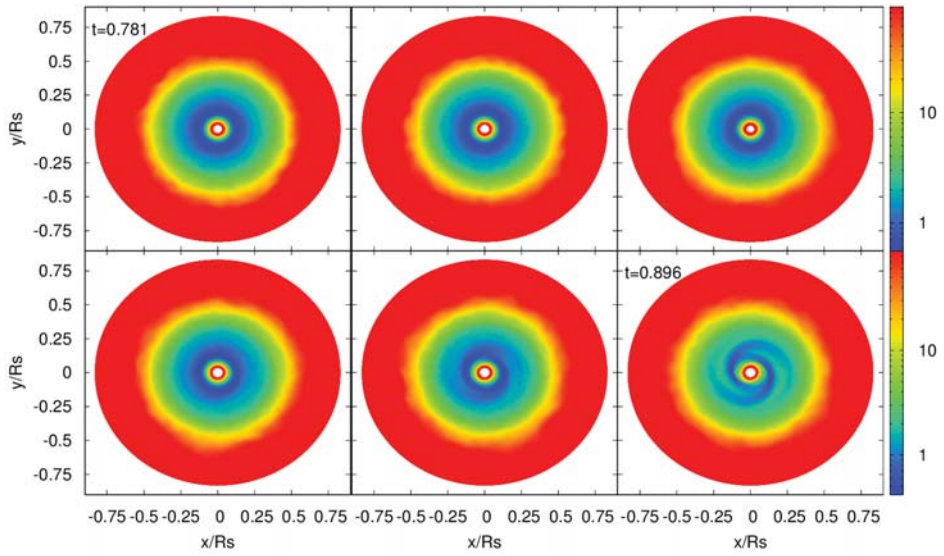

Figure 4.19: Evolution of the Toomre parameter Q for model $\beta 1.34$ at times $0.78\ \mathrm{s} \lesssim t \lesssim 0.89\ \mathrm{s}$. The initial and final times are indicated on the top left panel and the right bottom panel respectively, and the evolution of time goes from top to bottom and from left to right. The last panels show the formation of two spiral arms at $t \simeq 0.89$ s.

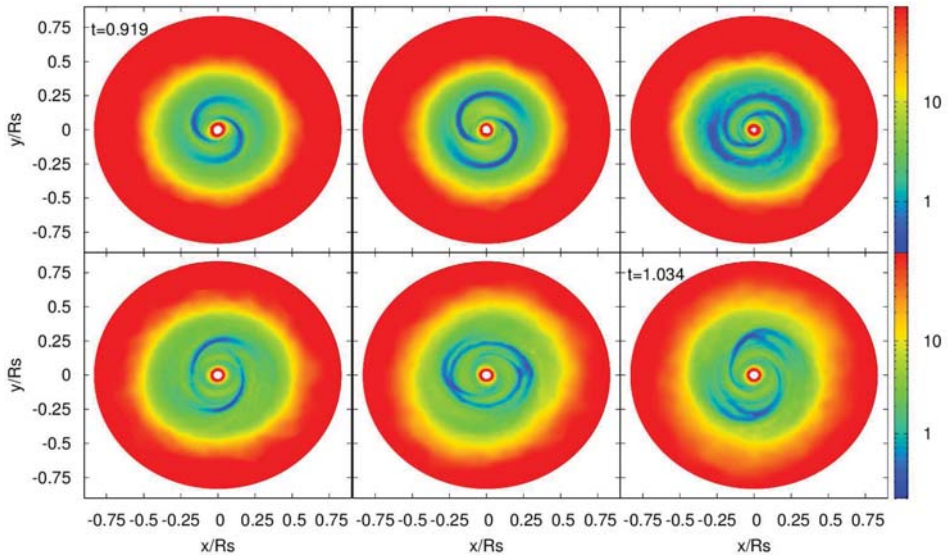

Figure 4.20: Evolution of the Toomre parameter Q for model $\beta 1.34$ at times $0.91\ \mathrm{s} \lesssim t \lesssim 1.03\ \mathrm{s}$. The spiral arms remain intense for ~ 0.1 s and break into several structures on the last panel.

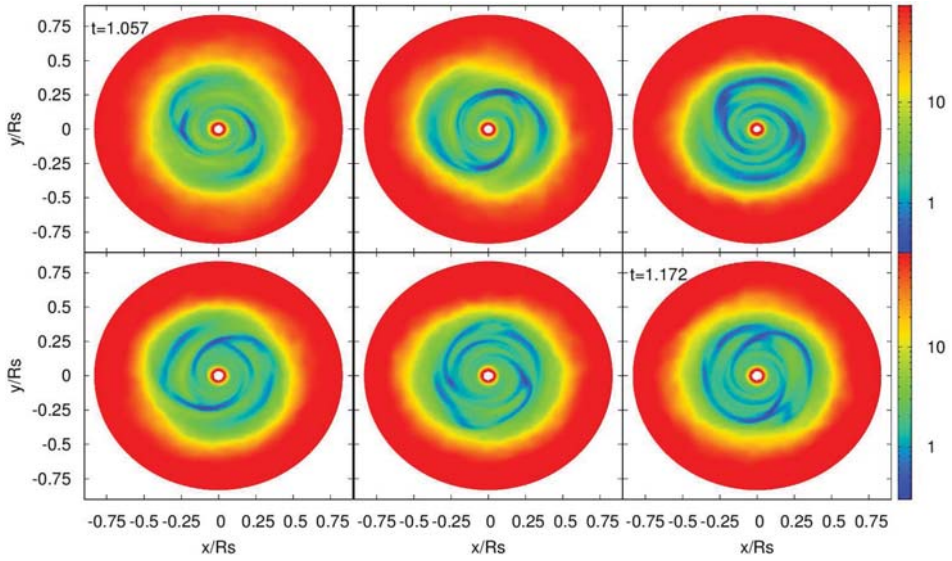

Figure 4.21: Evolution of the Toomre parameter Q for model $\beta 1.34$ at times $1.05\text{ s} \lesssim t \lesssim 1.17\text{ s}$. The two spiral arms are now barely noticeable.

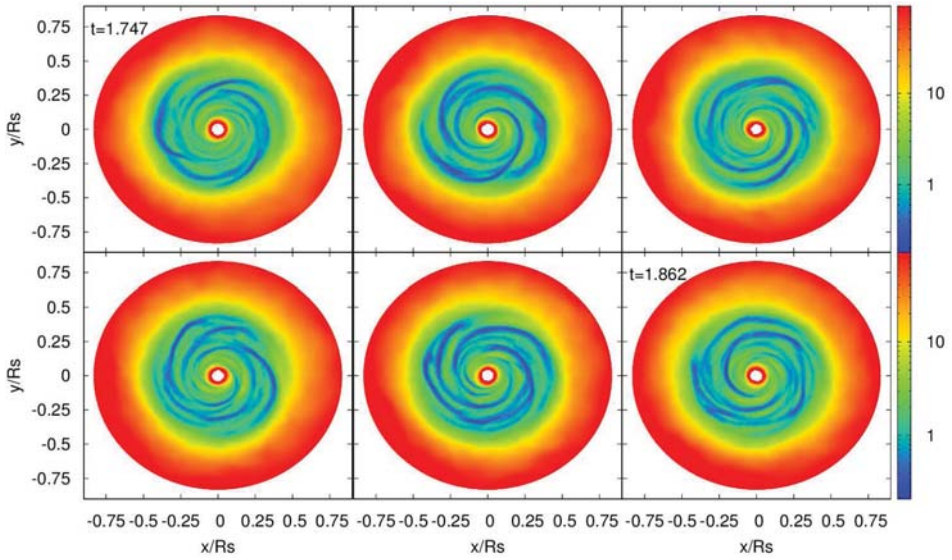

Figure 4.22: Evolution of the Toomre parameter Q for model $\beta 1.34$ at times $1.74\text{ s} \lesssim t \lesssim 1.86\text{ s}$. There are several spiral structures at the disk which are shown as intense variations in modes $m = 2, 3$.

The spiral instabilities found in models $\beta 2.68$ and $\beta 1.34$ resemble one of the specific eigenmodes found by Woodward et al. (1994) in simulations where the accreting body is able to move freely, and where the disk's mass is comparable to the mass of the accreting body. They named such eigenmode as the A-mode for its similarity with the modes encountered by Adams et al., 1989 (ARS). Such ARS modes develop when density waves reflect at the outer Lindblad resonance and the outer edge of the disk, while being forced to be unstable by the gravitational potential disturbance caused by the motion of the accreting body. Instead of developing a $m = 1$ A-mode, like in Woodward et al. (1994), our simulations developed a $m = 2$ mode in most of the simulations, this might be due to the fact that the accreting body was attached at its original position at all times. The main characteristic of the A-mode is that the spiral pattern is trailing through more than 2π radians covering a considerable part of the disk (as in our simulations). Such spiral structures do not seem to have any important change at the corotation radius r_c, unlike the rest of the modes encountered by Woodward et al (1994).

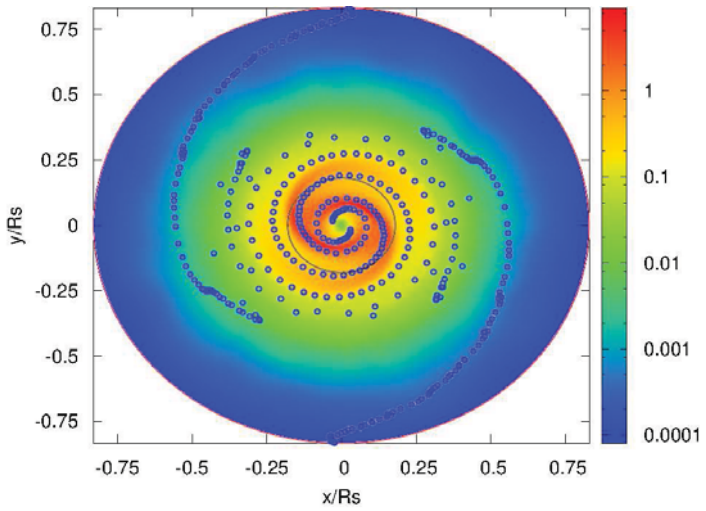

Figure 4.23: Normalized density map ρ/ρ_0 ($\rho_0 = 1.77 \times 10^9$ g/cm^3) in the orbital plane and the phase $\phi_2(r)$ of the $m = 2$ Fourier mode (blue points). The corotation radius is shown as a black line at $r \simeq 0.18 R_s$. Past the yellow zone, from where the spiral arms become less prominent, the phase shows several significant jumps until another $2\pi/2$ structure is found.

$\beta 0.67$ Model

As can be seen in figure 4.24, this model, with $t_{\rm cool} = 0.0616$ s shows at least two events where both $\dot{M}$ and L_c have intense and rapid increases. Comparing with

figure 4.25 where we plot the evolution in time of the relative power $|c_m|^2$ for the modes $m = 1, 2, 3$ and 4, we see that the first event can be related to an increase in all Fourier modes beginning at $t \simeq 0.45$ s. At that time, all Fourier modes seem to have comparable power, but modes $m = 1$ and 2, peaking at $t \simeq 0.5$ s reach the highest values and have the longest duration. We therefore expect to see a prominent presence of one or two spiral arms, that will remain strong for a time $\lesssim 0.05$ s. Comparing models $\beta 1.34$ and $\beta 0.67$ we see that changing the cooling efficiency, alters the width of the peaks in the Fourier power, which seems to be smaller (i.e., more sharply defined in time) with increasing cooling efficiency.

Figures 4.26, 4.27 and 4.28 show the evolution in time of the Toomre parameter Q in the range $0.45 \text{ s} \lesssim t \lesssim 0.98$ s. We see in figure 4.26 that at about $t = 0.5$ s one and two spiral arms are formed and disrupted in less than 0.1 s. Remarkably, these spiral structures then break up into small and dense gas clumps, noticeable in figure 4.28. These then interact with the rest of the spiral pattern, disrupting it and further breaking it up.

As shown in figure 4.24, there is another important variation in $\dot{M}$ and L_c at a times $1.6 \text{ s} \lesssim t \lesssim 1.8$ s, when all modes reach at some point values $|c_m|^2 \gtrsim 10^{-3}$. In this event all peaks are extremely narrow, because the pattern is rapidly broken up, possibly due to presence of gas clumps formed at earlier times. Figure 4.29 shows the evolution of Q for $1.58 \text{ s} \lesssim t \lesssim 1.70$ s, also showing clumps and spiral patterns in the disk.

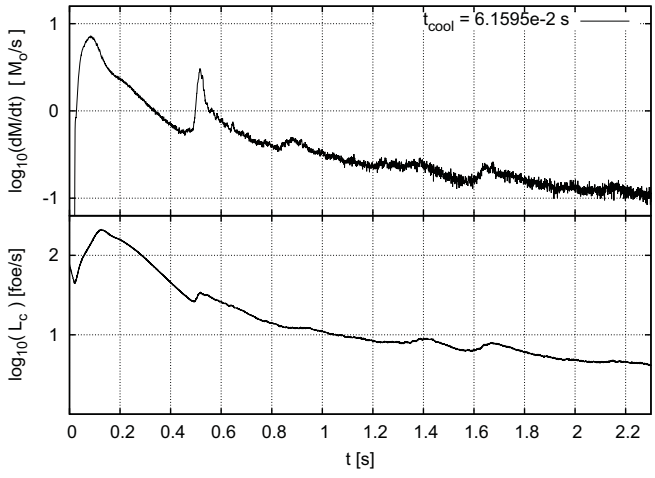

Figure 4.24: Mass accretion and energy loss rates for model $\beta 0.67$ (top and bottom panel respectively). There are intense variations in both L_c and $\dot{M}$ at times $t \simeq 0.5$ and 1.6 s.

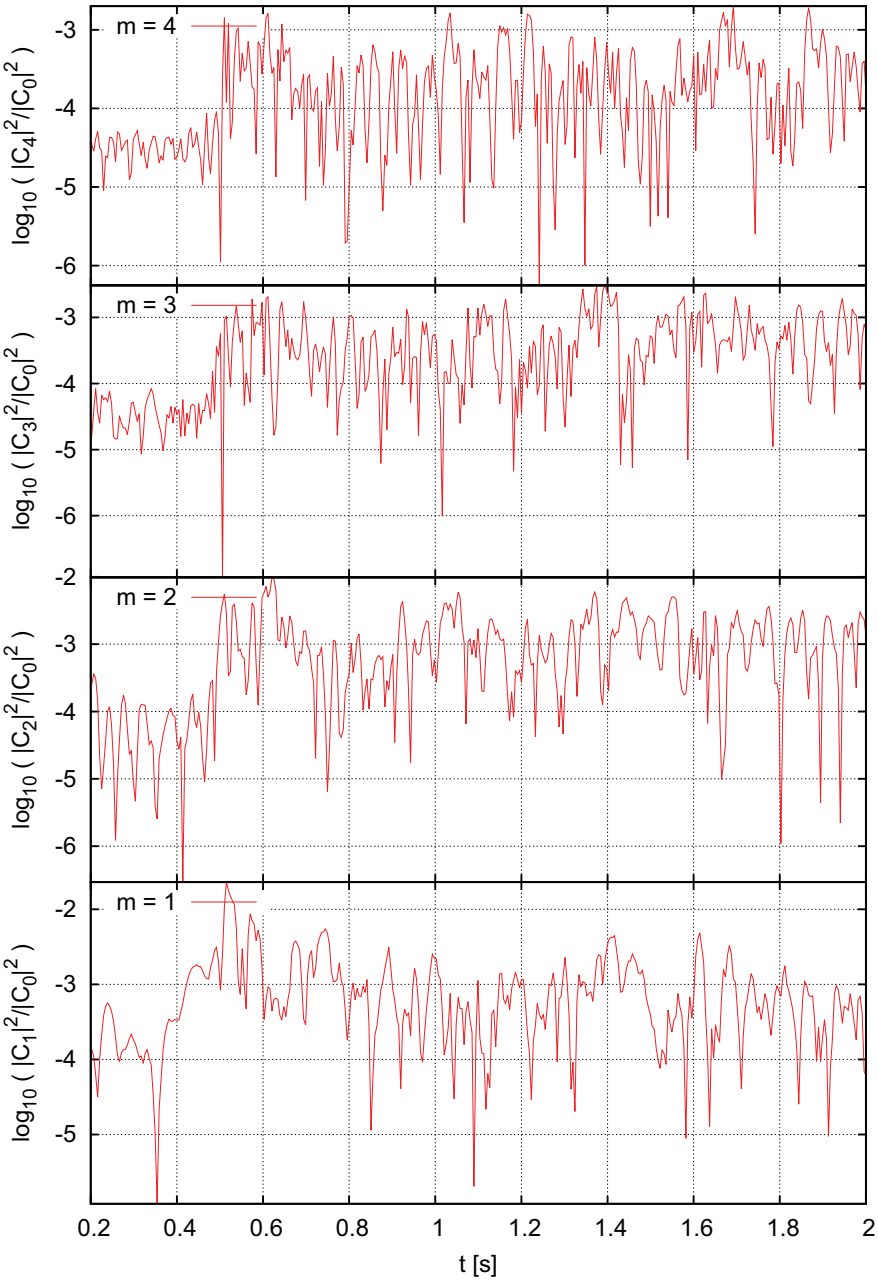

Figure 4.25: Relative power $|c_m|^2 = |C_m|^2/|C_0|^2$ ($m = 1, 2, 3, 4$) for the azimuthal mass distribution Φ_M Fourier transform of model $\beta 0.67$. All modes show an important increase at $t \simeq 0.5$ s. Modes $m = 2, 1$ reach the highest values at times $0.55 \text{ s} \lesssim t \lesssim 0.7$ s.

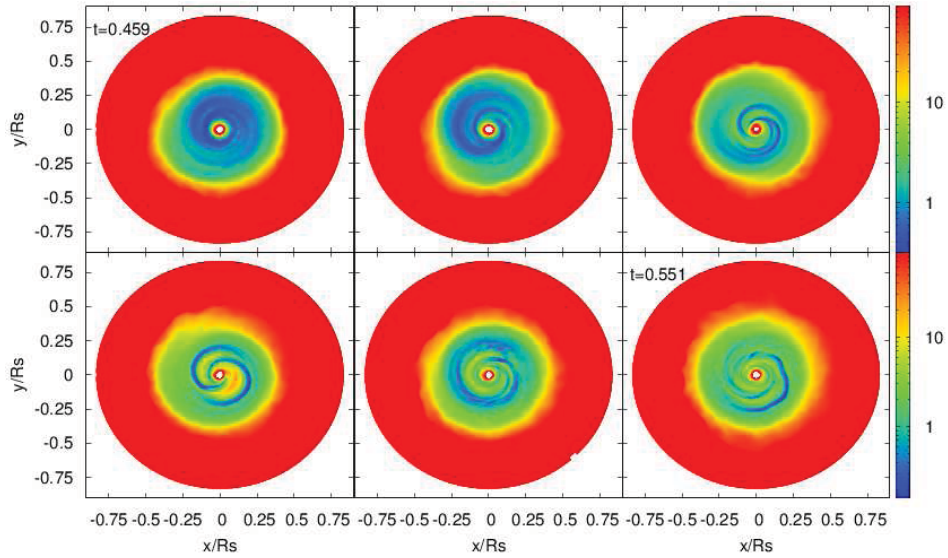

Figure 4.26: Evolution of the Toomre parameter Q for model $\beta 0.67$ at times $0.45\ \mathrm{s} \lesssim t \lesssim 0.55\ \mathrm{s}$. Formation of structure is triggered at early times but does not survive for long. Transient spiral arms corresponding to Fourier modes $m = 1, 2$ rapidly form and disappear.

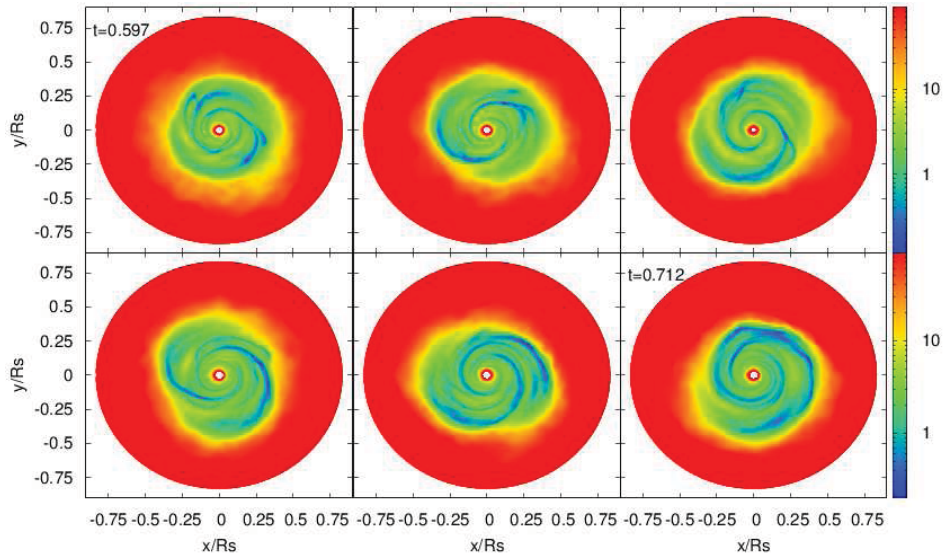

Figure 4.27: Evolution of the Toomre parameter Q for model $\beta 0.67$ at times $0.59\ \mathrm{s} \lesssim t \lesssim 0.712\ \mathrm{s}$. Spiral arms break down into smaller and more collapsed structures ($Q \lesssim 0.1$) such as clumps.

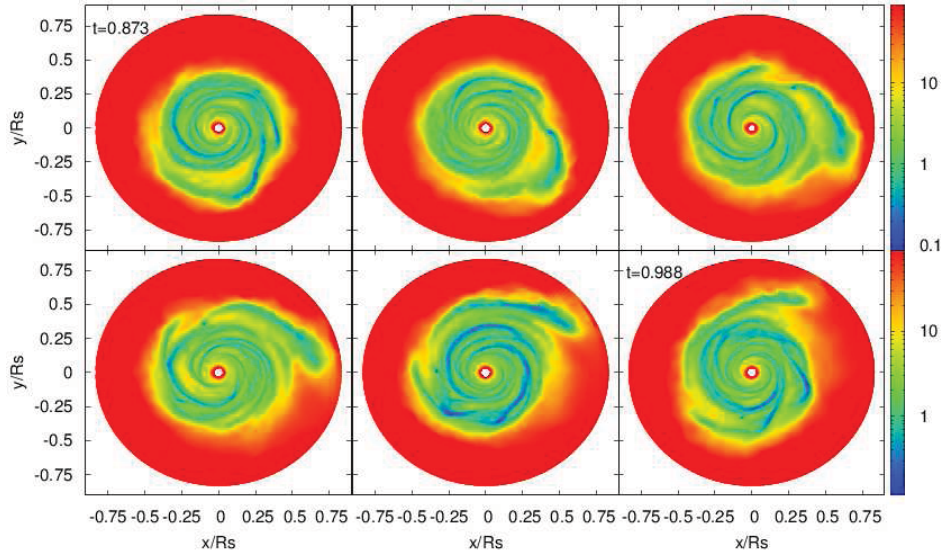

Figure 4.28: Evolution of the Toomre parameter Q for model $\beta 0.67$ at times $0.87\text{ s} \lesssim t \lesssim 0.98\text{ s}$. There are noticeable spiral arms and clumps with $Q \lesssim 0.01$.

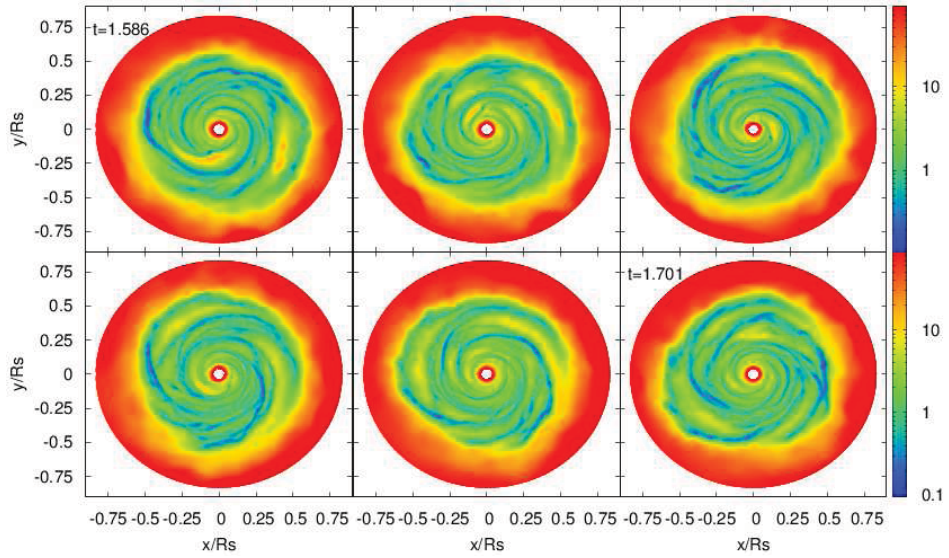

Figure 4.29: Evolution of the Toomre parameter Q for model $\beta 0.67$ at times $1.58\text{ s} \lesssim t \lesssim 1.70\text{ s}$. At this time we observe an increase in both L_c and $\dot{M}$ and there is intense spiral structure and some gas clumps with $Q \lesssim 0.1$.

$\beta 0.134$ Model

The cooling time used in this model was so short that the envelope was significantly cooled before $t \simeq t_{dyn}$. By looking at the Fourier modes amplitude $|c_m|^2$ in figure 4.32, we can see that modes $m = 1, 2$ are quite intense ($|c_m|^2 > 10^{-2}$) before $t \simeq 0.2$ s when the accretion disk has just been formed. This suggests that we should see spiral structure at times as early as 0.15 s. This can be seen in figure 4.31 where the Toomre parameter Q evolution is plotted for times $0.13 \text{ s} \lesssim t \lesssim 0.25$ s, where we can observe the presence of spiral arms that form and rapidly dissipate. Before $t \simeq 0.2$ s there is an increase in all Fourier modes which seems to be related to the intense variation seen in figure 4.30 in both $\dot{M}$ and L_c at those times.

It is difficult to associate the intense and rapid increase shown in $\dot{M}$ and L_c at $t \simeq 0.28$ s in figure 4.30 with the spiral structure formation event seen in figure 4.32 given that all modes oscillate between $10^{-3} \lesssim |c_m|^2 \lesssim 10^{-2}$ right before $t \simeq 0.3$ s. The same happens with the increase shown in figure 4.30 at $t \simeq 0.35$ s, and which lasts for ~ 0.1 s. Nevertheless, the increase shown on figure 4.30 at $t \gtrsim 0.5$ s can be associated with an intense increase on all Fourier modes at the same time from figure 4.32. At $t \simeq 0.525$ s all Fourier modes reach a maximum value $\gtrsim 10^{-1}$, which is not attained by less efficiently cooled models. This means that the mass ratio between the spiral structures and the disk's mass is greater than in previous models, which can be due to the fact that the BH has accreted a significantly greater amount of mass from the disk (more than twice the mass accreted with respect to less efficiently cooled models).

Figure 4.33 shows the evolution of the Toomre parameter Q at times $0.27 \text{ s} \lesssim t \lesssim 0.38$ s (top six panels), and $0.50 \text{ s} \lesssim t \lesssim 0.61$ s (bottom six panels). As can be seen from the figure, Q reaches higher values within the disk, probably because the surface density is considerably lower after the rapid BH mass accretion. Nevertheless, all regions ranging from green to blue have $Q \lesssim 1$ and it is clear that there are intense spiral structures and clumps forming in the disk. These clumps can be observed as early as $t \simeq 0.2$ s. In order to better appreciate the presence of instabilities in the disk (regions with $Q \lesssim 1$), we fixed a lower limit on the Toomre parameter at 0.02 so that all regions with $Q \lesssim 1$ will have a color between blue and green (Q reaches values as low as ~ 0.002).

This is the model with one of the highest cooling efficiencies that we have applied to our simplified system, and its results should be taken with care when relating them to an actual Collapsar model due to the fact that the envelope was significantly cooled down before reaching the BH. Nevertheless, the intense structure formation observed is something we would expect to see in the innermost

part of the disk of a Collapsar, given that the neutrino cooling efficiency is a very steep function of temperature. The same reasoning applies to model $\beta 0.067$ shown below.

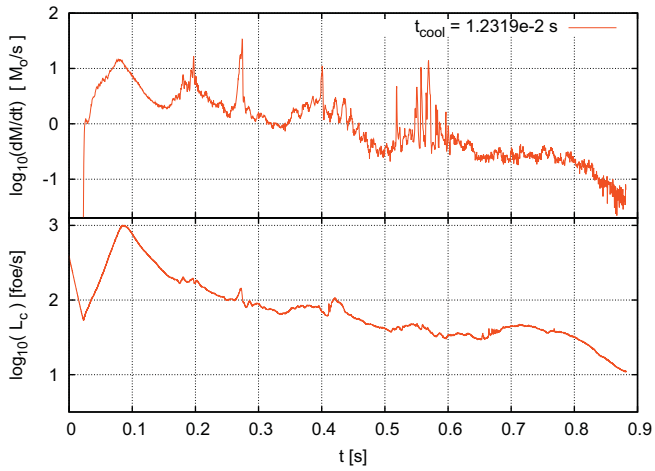

Figure 4.30: Mass accretion and energy loss rates for model $\beta 0.134$ (top and bottom panels respectively). There are several intense changes in both L_c and $\dot{M}$ starting at $t \simeq 0.15$ s. We note that some of the intense variations in $\dot{M}$ are barely visible in L_c.

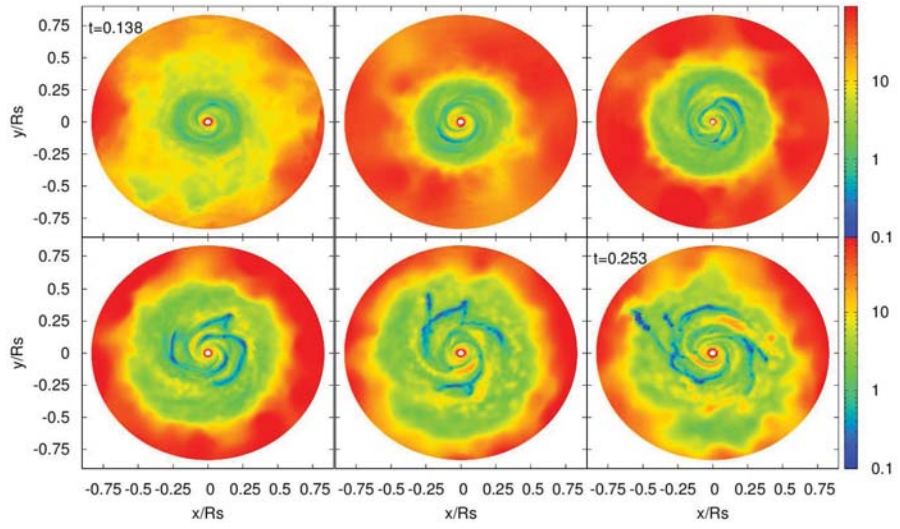

Figure 4.31: Evolution of the Toomre parameter Q for model $\beta 0.134$ at times $0.13 \text{ s} \lesssim t \lesssim 0.25 \text{ s}$. The spiral structures formed at very early times are quickly disrupted into clumps.

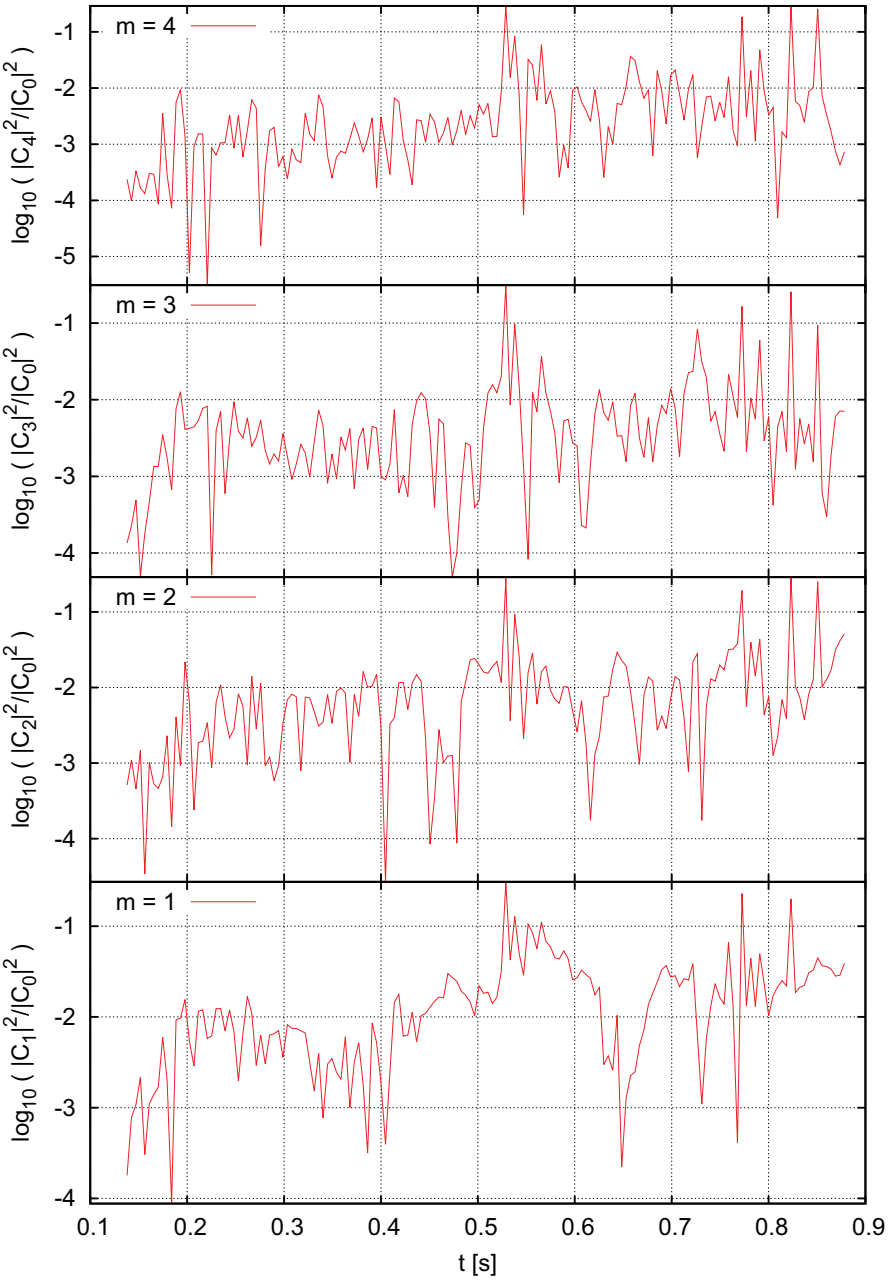

Figure 4.32: Relative power $|c_m|^2 = |C_m|^2/|C_0|^2$ ($m = 1, 2, 3, 4$) for the azimuthal mass distribution Φ_M Fourier transform of model $\beta 0.134$. Mode $m = 1$ is the strongest at times $0.2 \lesssim t \lesssim 0.3$ s, where an strong variation is shown in figure 28. A structure formation event occurs at $t \simeq 0.52$ s, when all modes reach $|c_m|^2 \gtrsim 0.1$.

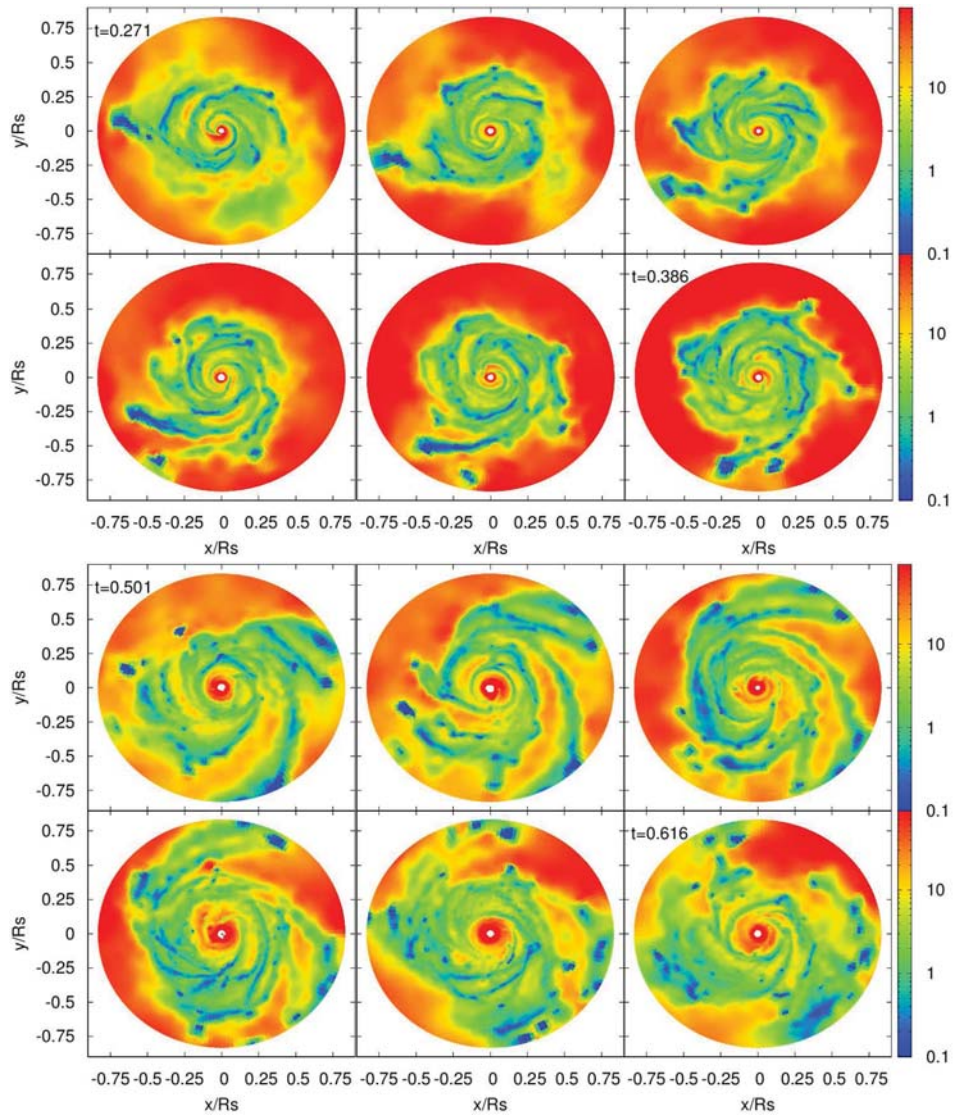

Figure 4.33: Evolution of the Toomre parameter Q for model $\beta 0.134$ at times $0.27\text{ s} \lesssim t \lesssim 0.38\text{ s}$ (top six panels) and $0.50\text{ s} \lesssim t \lesssim 0.61\text{ s}$ (bottom six panels). A large number of clumps with low Q values are seen orbiting at various distances from the BH. All gas with $Q \leq 10^{-1}$ is plotted as the darkest blue color, even thought it can reach values as low as $Q \sim 10^{-3}$.

$\beta 0.067$ Model

Figure 4.34 shows the evolution of the mass accretion rate $\dot{M}$ and the energy loss rate L_c. As in model $\beta 0.013$, there are some rapid increases (more easily visible in $\dot{M}$) which are not seen previously. Some of these episodes can be related to structure formation events observed in the Fourier modes $|c_m|^2$, shown in figure 4.35. The strong increase in $\dot{M}$ at $t \simeq 0.48$ s seems to be correlated with the changes in the Fourier modes (figure 35) at $t \simeq 0.49$ s, and are followed by a huge increase in L_c at $t \simeq 0.52$ s. This particular event seems to be related to the close encounter of the BH with one of the gas clumps, which is partially disrupted.

The disruption of a gas clump can be appreciated in figure 4.37, where a small gas clump approaches the BH at 0.43 s $\lesssim t \lesssim 0.55$ s. Its disruption and accretion is related to the associated rises in $\dot{M}$, L_c and in the Fourier modes $|c_m|^2$ at $t \simeq 0.5$ s. The intense accretion at early times has decreased considerably the amount of mass in the accretion disk, which translates in lower accretion rates that only increase when one of these clumps gets disrupted.

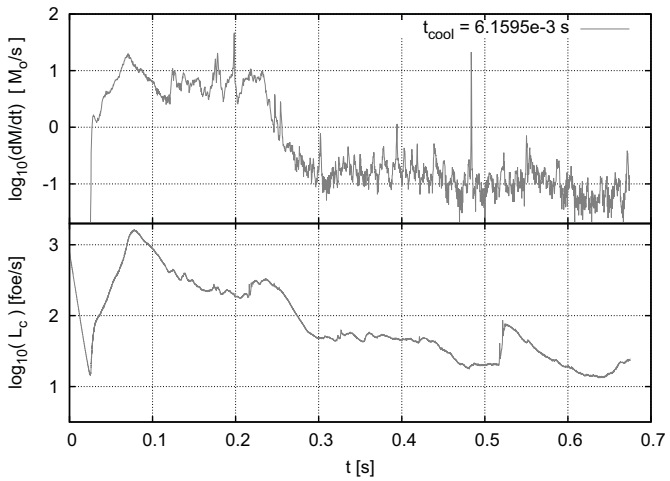

Figure 4.34: Mass accretion and energy loss rates for model $\beta 0.067$ (top and bottom panel respectively). There are several intense increases on both L_c and $\dot{M}$ starting at $t \simeq 0.12$ s, and the number of variations is considerablyt larger that in previous models, as seen in the Fourier transform from figure 11.

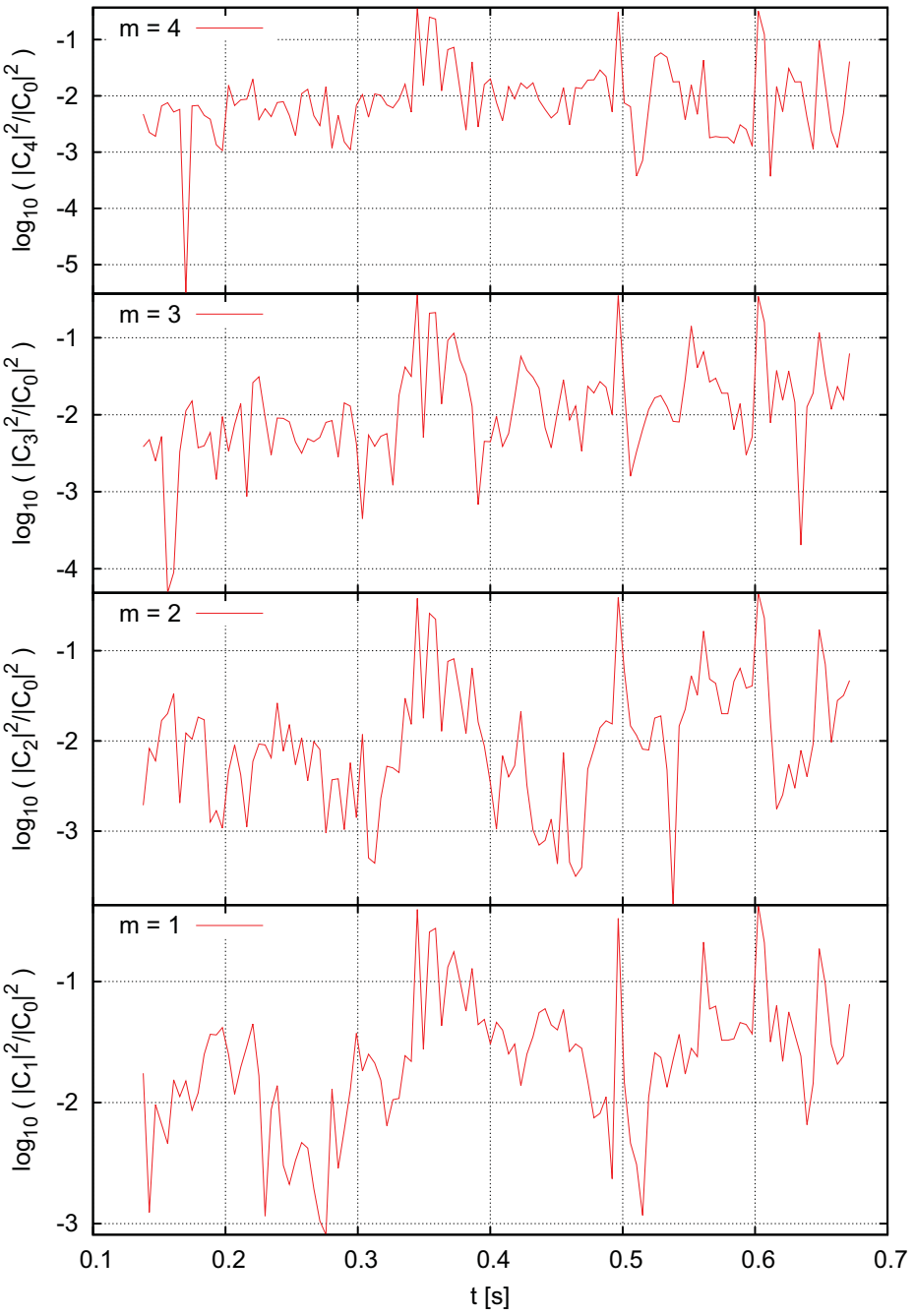

Figure 4.35: Fourier modes C_m (for $m = 1, 2, 3, 4$) for the integrated angular mass distribution ρ_ϕ of model $\beta 0.067$. All modes show an increase in amplitude at $t \simeq 0.35, 0.5$ and 0.6 s.

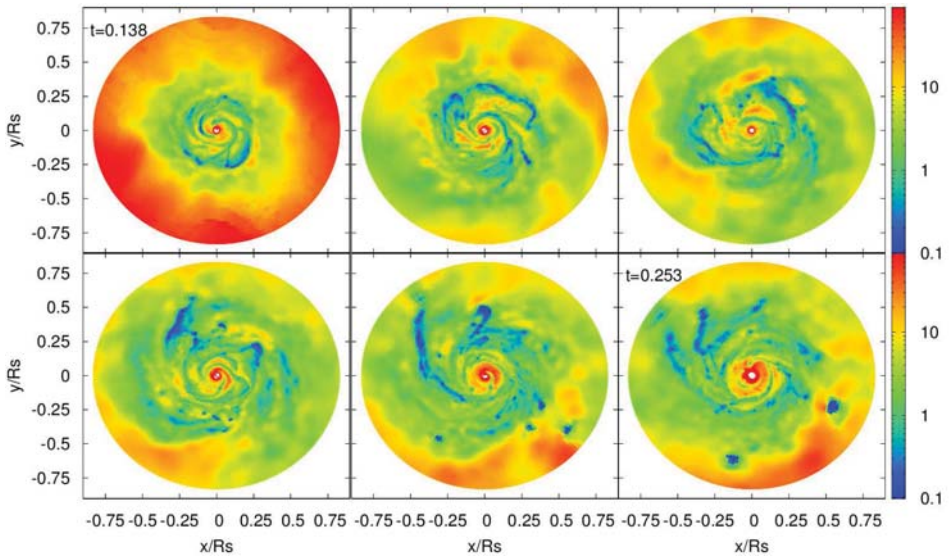

Figure 4.36: Evolution of the Toomre parameter Q for model $\beta 0.067$ at times $0.13\ \mathrm{s} \lesssim t \lesssim 0.25\ \mathrm{s}$, when gas clumps are already forming.

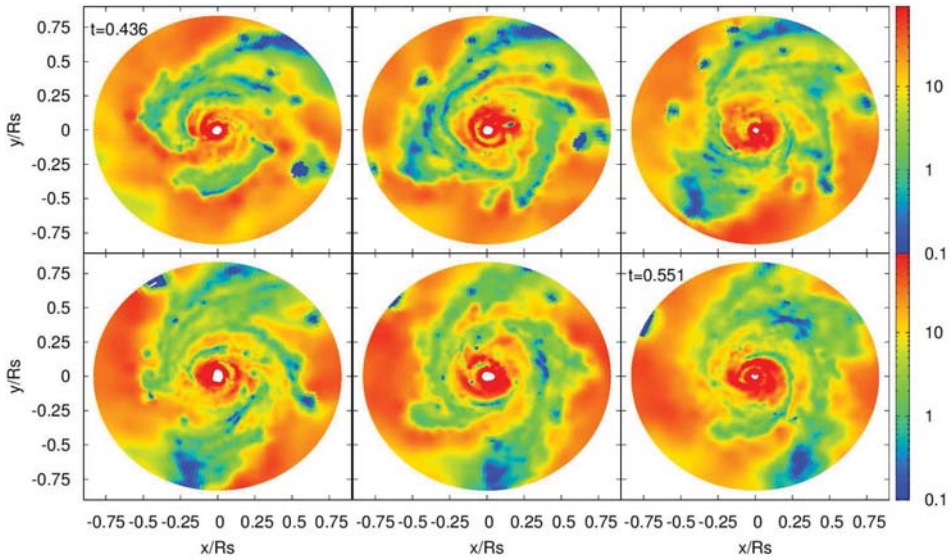

Figure 4.37: Evolution of the Toomre parameter Q for model $\beta 0.067$ at times $0.43\ \mathrm{s} \lesssim t \lesssim 0.55\ \mathrm{s}$. A clump passes close to the BH and is disrupted, triggering intense variations in $\dot{M}$, L_c and the formation of spiral structure.

4.3 Discussion

From the results obtained in section 4.2 it is clear that increasing the cooling efficiency induces more profuse and intense structure formation which in turn produces strong variations both in the mass accretion rate and the energy losses. In this section we will summarize our main results:

• Structures with a Toomre parameter $Q \ll 1$ and high relative power $|c_m|^2$ contain considerable amounts of gas within compact regions, and can therefore be accreted quickly, leading to large variations in $\dot{M}$ and L_c. The frequency of these variations (and structure formation) increases with rising cooling efficiency, as observed in the Fourier power spectra of $\dot{M}$ and L_c's on figures 4.10 and 4.11. The duration and intensity of the structure induced variations on $\dot{M}$ and L_c is related with the intensity and lifetime of the collapsed structures, whether they are spiral arms or clumps. The change in duration of such events can be seen by comparing the width of the peak on the mode $m = 2$ from models $\beta 2.68$ or $\beta 1.34$ with the width of the peaks from more efficiently cooled models.

• The spiral structures that form are clearly transient in nature, forming and disappearing within a few orbital periods. Their relative power is particularly strong in the lowest azimuthal modes, $m = 1, 2$ at modest cooling, when $t_{\rm cool} \simeq t_{\rm disk}$ and rapidly spreads to higher modes, $m = 3, 4$ for increasing cooling efficiency, when $t_{\rm cool} \ll t_{\rm disk}$. The development of such instabilities is due to the inhomogeneities obtained when generating the 3D SPH particle distribution from our spherically symmetric polytropic stars, done by a MonteCarlo sampling on the density profile $\rho(r)$. Therefore, other than changing the number of SPH particles, or the random number generator, we exert no control over the intensity and direction of the initial perturbation given to the system. Having said that, all models have the same initial perturbation, yet they can develop different non-axisymmetric modes (spiral structure) for different cooling time scales. Therefore, given an initial random perturbation on the particle distribution, the main driver of structure formation in our system is the cooling efficiency given that it determines which mode will develop to be the strongest and the time it will take to become important. We follow the evolution of the instabilities through their power in the corresponding Fourier modes both in radius and in angle, and show that they are associated with episodes of enhanced mass accretion.

• The spiral structure and gas clumps in the disk not only induce intense variations (with different durations) in both $\dot{M}$ and L_c, but are also significant enough to break the symmetry in gravitational interaction between the disk and the black hole. This can be seen in figures 4.10 and 4.11 where the Fourier transforms of the

radial momentum component P_r of the disk are shown. As cooling becomes more efficient, greater power is seen at higher frequencies (shorter time scales) in P_r. Such characteristic frequencies are easily noticeable just by looking the time series of the components of momentum P_x and P_y separately, where one can identify a "periodic" oscillation of the accretion disk. By forcing the BH to remain fixed at the origin during the simulations, we cannot here give a full account of this effect, but clearly these oscillations could have important consequences for the overall dynamics of the flow and are further discussed below.

• The integrated energy losses obtained range from 1 to 2000 foe (10^{51} to 10^{54} erg) for adiabatic to isothermal models. Now, this is only what would count as "neutrino" energy release. The integrated accretion energy $E_{\rm acc} = \int \dot{M} c^2 dt$ ranges from 10^{54} to 3×10^{54} erg. Both of these indicate that as expected, the available power to drive a GRB is present in the system. How it eventually manages to do so is a different matter, but, more to the point here, it is clear that the time variations imprinted on the outflow are dependent on the initial mechanism driving it. This is in way akin to the argument presented in Carballido & Lee (2011), where temporal variability in local shearing box simulations for different neutrino cooling prescriptions, when integrated over the entire disk on a large scale, produces a different and characteristic power spectrum which is the underlying shape upon which further processes are superimposed, each adding its typical signature layer of behavior.

• By obtaining the cooling efficiency $L_c/L_{\rm acc}$ as a function of the mass accretion rates, we are able to compare our results with previous work. The cooling efficiency obtained in our simulations is consistent with the ones found by Chen & Beloborodov (2007) and Di Matteo et al. (2002) for stationary accretion disks. As our configuration is not stationary, the accretion rate is not the only factor determining the cooling efficiency. As shown in figure 4.38, there are intense increases in dM/dt shown as a loop where a maximum accretion rate and a minimum cooling efficiency are reached, followed by an increase in the energy loss rate due to material heating from approaching the BH and a decrease in the accretion rate. All models show a loop due to the initial collapse of the envelope, and models showing structure formation events exhibit similar events further on. This plot clearly shows the strong transient behavior at early times, followed by a near stabilization of the flow, with intermittent episodes of intense accretion when structure forms (red and blue lines). As our approach does not consider neutrino transport and scattering, not negligible within the regions of highest density ($\rho \gtrsim 10^{11}$ g cm^{-3}), the cooling efficiency could reach smaller values in principle. This indicates that in some cases, our assumption of a totally transparent fluid (to

neutrinos) may need revising when including a more detailed equation of state and neutrino emission formalism.

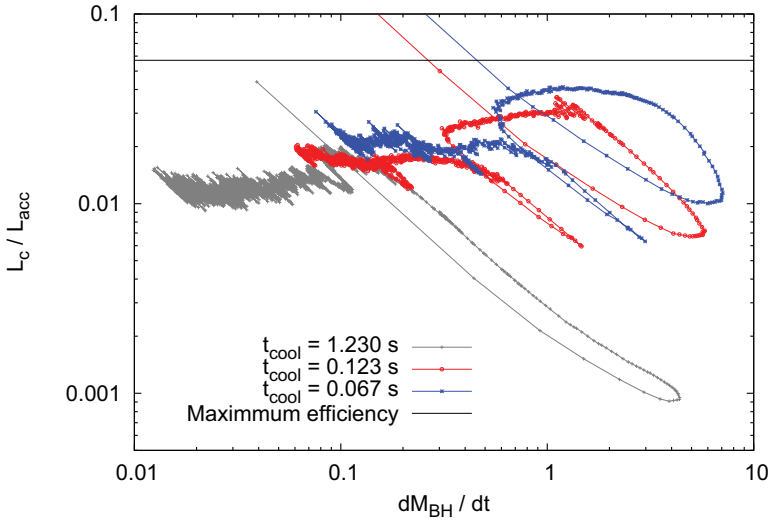

Figure 4.38: Cooling efficiency $L_c/L_{\rm acc}$ as a function of dM/dt for models $\beta 13.4$ (gray line), $\beta 1.34$ (red line) and $\beta 0.67$ (blue line). The lines start from the points located at the highest cooling efficiency when the accretion rate starts to drastically grow due to the initial collapse of the envelope. The evolution in time then goes to the bottom right, where the accretion rate becomes the highest when the low angular momentum material is reaching the BH. The maximum radiative efficiency is determined by the binding energy at the last stable orbit (0.057 for a Schwarszchild BH).

• The formation and destruction of accretion structures, in particular arms and clumps, is not only transient, but recurrent in an orderly fashion. Inspection of figures 4.8 and 4.9, where the mass accretion rates and energy release are plotted, shows that for greater efficiency, the interval between enhancements in $\dot{M}$ and L_c is smaller. The disk is draining of matter in the process as well, of course, and so each subsequent episode is of lesser intensity. But the trend appears to be clear: as structure forms, the disruption of azimuthal symmetry allows for a degree of angular momentum transport through the dense spiral arms (or even clumps), leading to an accretion episode. Having suppressed this structure, a second cooling interval must elapse before new condensations form and allow the process to repeat, indicating a correlation between the time elapsed between accretion (or luminosity) spikes and the cooling time itself. For decreasing cooling times the disk is being depleted even faster and so the trend becomes increasingly difficult to see (note the accretion rate and luminosity are plotted in a logarithmic scale).

• Given our cooling implementation, Eq. (4.4), the internal energy per unit mass of the accretion disk $u_M = U/M_{\rm disk}$ is directly related to the energy loss rate L_c by:

$$u_M = \frac{U}{M_{\rm disk}} = \frac{1}{M_{\rm disk}} \left(\sum_j u_{i,j} \right) = \frac{t_{\rm cool} L_c}{M_{\rm disk}}, \tag{4.10}$$

where $u_{i,j}$ is the internal energy of the particle j and $M_{\rm disk}$ is the mass of the accretion disk at time t. Thus, u_M contains information on both the energy loss rate and the accretion rate (determining the disk's remaining mass). The evolution of u_M as a function of the normalized time $t/t_{\rm cool}$, shows some intrinsic properties of this particular cooling scenario.

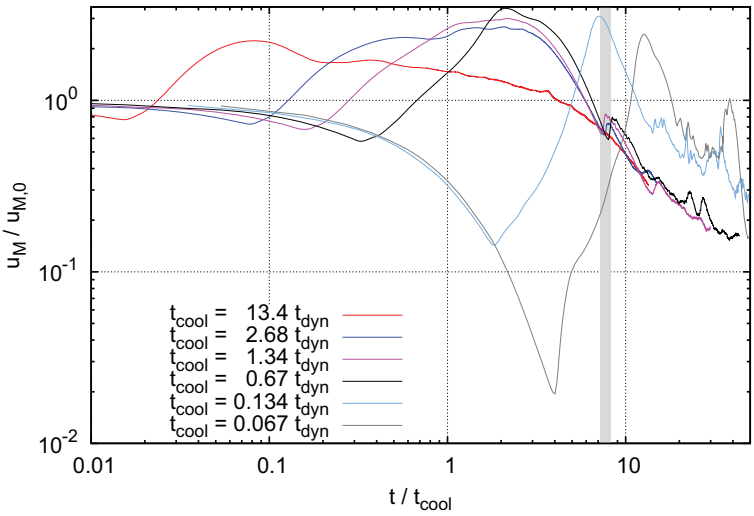

Figure 4.39: Internal energy per unit mass u_M as a function of $t/t_{\rm cool}$. The grey shaded region from $7.2 \leq t/t_{\rm cool} \leq 8.2$ shows the times at which models with $t_{\rm cool} \gtrsim t_{\rm dyn}$ show the first structure formation event represented as an increase in u_M (except for model $\beta 13.4$).

Figure 4.39 shows the normalized internal energy per unit mass $u_M/u_{M,0}$ ($u_{M,0} = u_M(t = 0)$) as a function of $t/t_{\rm cool}$ for all simulations with our cooling prescription, Eq. 4.4. All models show the initial decrease in u_M due to the cooling and collapse of the envelope, followed by an intense increase from the outward shock produced by the heated material reaching its centrifugal barrier near the black hole. Both of these events take place at times $t \lesssim t_{\rm dyn}$ and therefore, models with $t_{\rm cool} \gtrsim t_{\rm dyn}$ will start accreting and will have formed an accretion

disk at times $t \lesssim t_{\rm cool}$. Meanwhile models with $t_{\rm cool} \ll t_{\rm dyn}$ will form an accretion disk only after several cooling times have elapsed. Models displaying such scenarios are intrinsically different, and hence we do not expect to observe similar behavior when comparing them. Models with $t_{\rm cool} \gtrsim t_{\rm dyn}$ display an increase in u_M at a time $7.2 > t/t_{\rm cool} > 8.2$, which corresponds to the structure formation event previously noted in models $\beta 2.68$, $\beta 1.34$ and $\beta 0.67$. The exception to this trend is model $\beta 13.4$, which shows no significant increase in u_M and no structure formation event at such times.

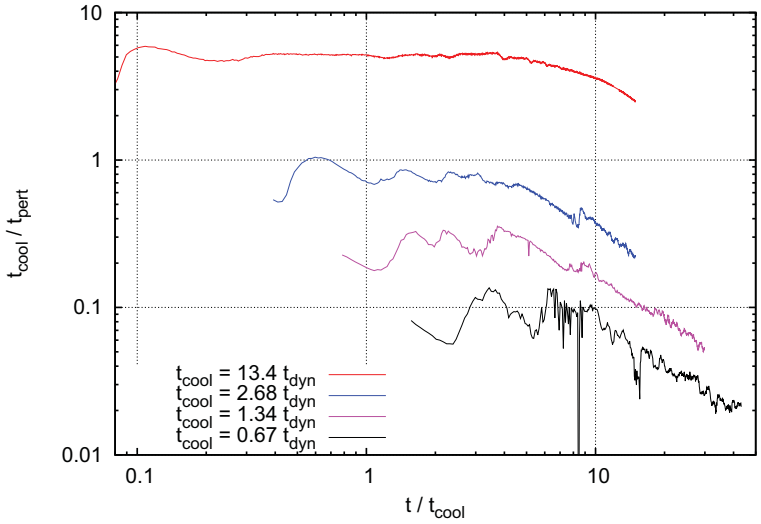

Figure 4.40: Time evolution of the ratio between $t_{\rm cool}$ and $t_{\rm pert}$ for models $\beta 13.4$, $\beta 2.68$, $\beta 1.34$ and $\beta 0.67$. Models with efficient cooling have ratios $\lesssim 1$ and are therefore, able to have structure formation events.

The exception can be explained by considering the minimum azimuthally averaged sound speed in the disk $c_{\rm s,min} = \min\left[c_s(R), (0.05 < R/R_s < 1)\right]$, from which we can estimate an upper limit for the time, $t_{\rm pert} = R_s/c_{\rm s,min}$, it would take a pressure perturbation to transfer its information throughout a disk of size R_s. In particular, this perturbation could be induced precisely by cooling. Thus, if the cooling time scale is smaller than this perturbation time scale $t_{\rm pert}$, there is a region within the disk where any significant drop in pressure (brought about by a reduction in the internal energy), could not be immediately compensated by hydrodynamical processes and it could experience a collapse if the pressure drop is strong enough. On the other hand, if the cooling time scale is significantly higher than $t_{\rm pert}$, any drop in pressure will be quickly accounted for, and softened, by

hydrodynamical processes before the gas gets cool enough to undergo collapse. This is the case in model $\beta 13.4$ which, at all times, satisfies $t_{\rm cool} > 2\,t_{\rm pert}$, as seen on figure 4.40 where the evolution of $t_{\rm cool}/t_{\rm pert}$ vs $t/t_{\rm cool}$ is plotted. Hence, we do not expect to see any structure formation event from this model as long as the condition $t_{\rm cool}/t_{\rm pert} \lesssim 1$ is not satisfied.

Even when our simulations are still far from representing an accurate Collapsar, the results obtained so far in these simple models cast light on the importance of self gravity and cooling in such a scenario. The implications of our results in the Collapsar scenario and the production of GRBs, as well as some more discussion about the improvements that could be done to our work, will be given in the final chapter along with the main conclusions.

Chapter 5

Summary and Conclusions

We have presented a thorough 3D numerical study of the accretion of infalling envelopes onto black holes, using an simplified equation of state for the gas, considering that the ideal gas contribution from free nuclei dominates over radiation and a hot $e^{\pm}$ gas. We have further included a simplified prescription for cooling based on realistic emission rates expected at the given densities and temperatures within a collapsar, with which we can study scenarios ranging from adiabatic to isothermal, with the aim of identifying and characterizing the morphology and the variations in structure induced within the disk as a result of the energy losses to neutrinos. With these caveats, which we discuss further below, we find global features which are likely to be present in real collapsing stellar cores and are relevant for the dynamics and energy release leading to the production of cosmological GRBs from massive stars.

Here we summarize our main results:

• The most important parameter governing the energy release in the collapse of a stellar core in the context of a collapsar is the rotation rate. If it is too low, the gas will flow essentially in radial fashion, and accrete onto the central black hole releasing very little of its energy (akin to Bondi flow). If it is too high, the disk will form at a radius that may be too large for efficient cooling to kick in (recall the sensitive dependence on neutrino emissivity on temperature), and the accretion efficiency may be too low to provide sufficient energy. It is the combination of placing shocked matter in centrifugal support as close to the BH as possible (and hence deep in the potential well), but not allowing it to fall in, that is critical for a successful event. In 2D, this has been characterized before (Lee & Ramirez-Ruiz,

2006; Lopez-Camara et al., 2009, 2010), and it is plainly important in 3D as well. In this sense, modeling the black hole through the pseudo Newtonian potential of Paczynski & Wiita (1980) is the most important ingredient as far as gravitational effects are concerned, which is why we have adopted it in the present work. Of course, considering a rotating BH may change the quantitative results somewhat, but not the qualitative nature of this conclusion.

• Increasing the cooling efficiency induces more profuse and intense structure formation which in turn produces strong variations both in the mass accretion rate and the energy losses. The duration and intensity of these variations is related with the intensity and lifetime of the collapsed structures, whether they are spiral arms or clumps. Structures with a Toomre parameter $Q \ll 1$ and high relative power $|c_m|^2$ contain considerable amounts of gas within compact regions, and can therefore be accreted quickly, leading to large variations in $\dot{M}$ and L_c. The frequency of these variations (and structure formation) increases with rising cooling efficiency, as observed in the Fourier power spectra of $\dot{M}$ and L_c.

• The spiral structures that form are clearly transient in nature, forming and disappearing within a few orbital periods. Their relative power is particularly strong in the lowest azimuthal modes, $m = 1, 2$ at modest cooling, when $t_{\rm cool} \simeq t_{\rm disk}$ and rapidly spreads to higher modes, $m = 3, 4$ for increasing cooling efficiency, when $t_{\rm cool} \ll t_{\rm disk}$. All models have the same initial perturbation, yet they can develop different non-axisymmetric modes (spiral structure) for different cooling time scales. Therefore, given an initial random perturbation on the particle distribution, the main driver of structure formation in our system is the cooling efficiency and it determines which mode will develop to be the strongest and the time it will take to become important. By following the evolution of the instabilities through their power in the corresponding Fourier modes we showed that they are associated with episodes of enhanced mass accretion and energy loss.

• The intense structures (spiral arms and gas clumps) formed in the disk are significant enough to break the symmetry in gravitational interaction between the disk and the black hole. This can be seen in the Fourier transforms of the radial momentum component P_r of the disk for efficiently cooled models. As cooling becomes more efficient, greater power is seen at higher frequencies (shorter time scales) in P_r. By forcing the BH to remain fixed at the origin during the simulations, we cannot here give a full account of this effect, but clearly these oscillations could have important consequences for the overall dynamics of the flow and are further discussed below.

• The integrated energy losses obtained (10^{51} to 10^{54} erg) account only for what would count as "neutrino" energy release. This energy is comparable with

the integrated accretion energy $E_{\rm acc} = \int \dot{M} c^2 dt$ (ranging from 10^{54} to 3×10^{54} erg). Both of these indicate that as expected, the available power to drive a GRB is present in the system. How it eventually manages to do so is a different matter, but, more to the point here, it is clear that the time variations imprinted on the outflow are dependent on the initial mechanism driving it. The intense characteristic time scales obtained in the Fourier transforms of L_c and $\dot{M}$ allow for structure formation events, to account for variations on time scales of a fraction of a second to tens of milliseconds.

Clearly there is also room for improvement in what we have presented here, we detail some of these issues here:

• First, a more detailed implementation of neutrino cooling is likely to lead to more realistic results. Particularly, this refers to the fact that we have assumed a uniform cooling efficiency throughout the flow, β. As the temperature dependence of cooling is significant, the outer regions will not emit as copiously as the inner disk, leading to different behavior. We believe this is one of the two most important points which would require addressing.

• The gravitational interaction between the disk and the black hole does not always allow one to assume that the latter is always lying at the origin. Rather, it will oscillate with the disk, as in a binary. This has two important consequences: first, the accretion rate will be modified somewhat, as clumps and spiral arms will not be disrupted/accreted in the same way, and second, the site of accretion, and potential jet driving through the envelope, will be in continuous motion within the disk and stellar envelope. A quantitative analysis of this is effect is clearly necessary, and it may have far-reaching consequences, as the common assumption has been that the energy deposition driving a relativistic outflow leading to breakout sits motionless at the center of the star.

We have already some preliminary work that shows that a BH able to move freely, will experience considerable oscillations in its position due to the spiral structure formation events. Figure 5.1 shows the evolution of the distance from the BH to the center of mass (CM) of the system $r_{\rm XY}$ in the plane where the accretion disk lies. The structure formation events at $t \simeq 0.9$ s (red line) and $t \simeq 0.5$ s (blue line) induce a stronger oscillation of the BH around the CM.

It is also probable that allowing the BH to move will change somehow the characteristic time scales shown in the Fourier transforms of P_r. Figure 5.2 shows a comparison between the characteristic frequencies of the distance $r_{\rm XY}$ between the BH and the CM (top panel) and the characteristic frequencies obtained for the radial component of the disk's linear momentum P_r in the plane of the disk for a

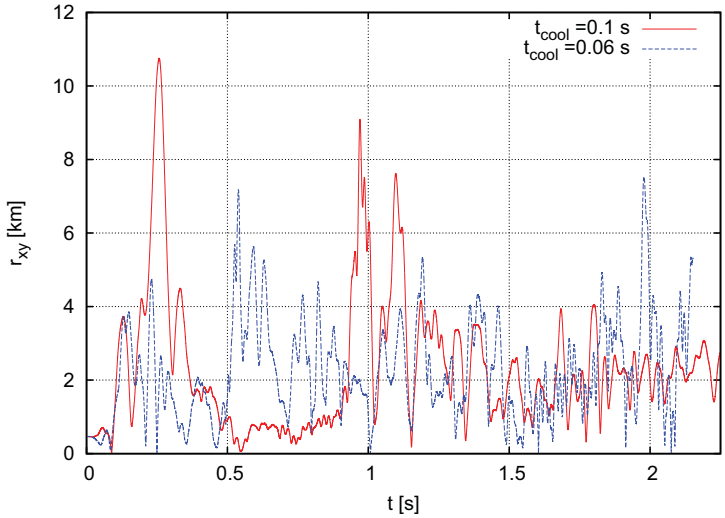

Figure 5.1: Distance from the BH to the center of mass (CM) of the system $r_{\rm XY}$ in the plane where the accretion disk lies. The structure formation events at $t \simeq 0.9$ s (red line) and $t \simeq 0.5$ s (blue line) induce a stronger oscillation of the BH around the CM.

fixed BH (blue line) and an free BH (red line). Clearly by letting the BH to move freely, the radial oscillations of the disk will develop in a different manner.

The main difficulty with these simulations lies in the accuracy with which the gravitational forces are calculated in the code. Firstly, the force between the BH and the SPH particles must be symmetric, i.e., the SPH particles must also exert a Paczynksi-Wiita gravitational potential on the BH, accordingly to the one the BH exerts on the SPH particles. Secondly, when intense structure such as gas clumps forms, the dynamical evolution of the system can become extremely chaotic, therefore, any change in the accuracy of the gravitational force will translate in different a evolution of the accretion flow, determined by short range interactions between the gas clumps and the BH. This is clearly one of the most important features that should be explored in future work in order to determine if the effect of such gravitational interactions could alter significantly the deposition of energy to form a GRB within the collapsing star.

• Although the PW pseudo Newtonian potential, as mentioned above, captures the most essential features of General Relativity for accretion purposes, a full relativistic treatment of the problem is desirable. In particular, not only the effects of a spinning (Kerr) black hole, but of the field produced by the flow itself, which, as we have seen, can in some cases produce a significant pull on the central object.

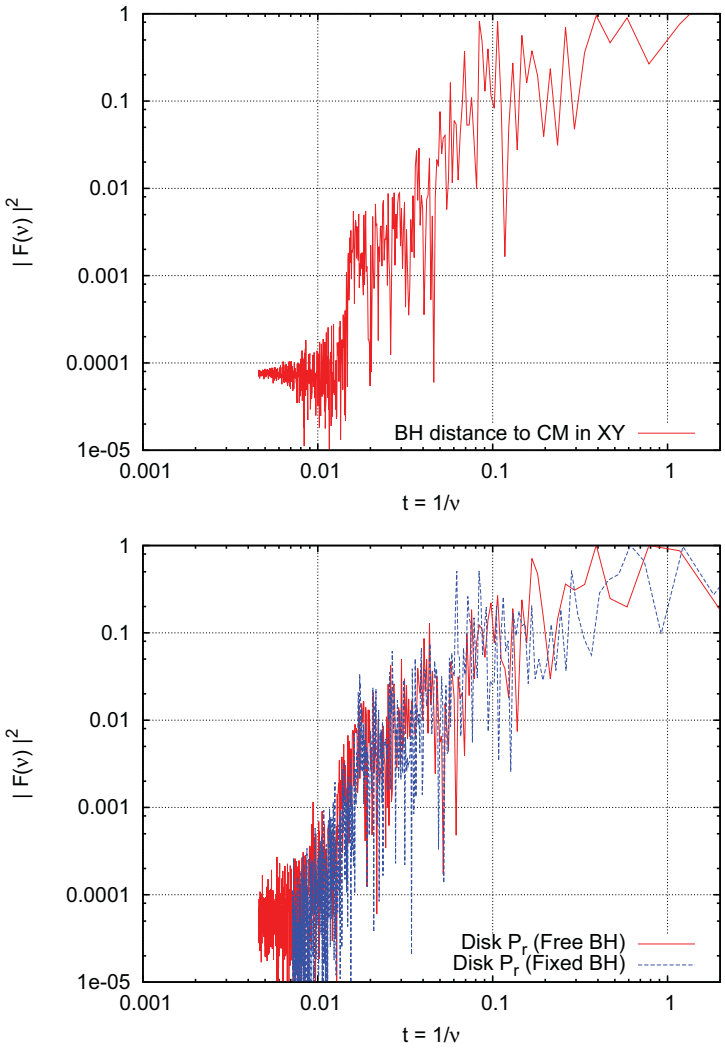

Figure 5.2: Fourier transform of the evolution of the position of the BH $r_{\rm XY}$ (top panel) and of the radial component of the disk's linear momentum P_r in the plane of the disk for a fixed BH (blue line) and an free BH (red line).

• Finally, a proper treatment of neutrinos should consider the effects of neutrino transport and energy deposition. Since the emitted neutrinos could be able to deposit a significant amount of energy in the gas at high density regions ($\rho \gtrsim 10^{11}$ g cm^{-3}) due to inelastic scattering off free nucleons and α particles, and because of neutrino opacity effects even in the elastic scattering regime, some of the structure formation we see may be inhibited, or limited, preventing the formation

of the densest features.

The rich behavior seen here, and characterized for the first time in 3D, clearly shows that using only 2D studies of the collapse of stellar cores is insufficient to explain all of the behavior and variability, even qualitatively, that is likely to occur in such systems. As we already know that only a small fraction of collapsing massive stars will produce a GRB, it is relevant in the sense of identifying precisely which conditions will lead to one in the evolution of the star. Preliminary work on the first two topics, in particular the disk-BH interaction, leads us to believe that these may be significant for the behavior and evolution of Collapsar disks, and they will be the subject of future work.

Bibliography

Akiyama S., Wheeler C. , Meier D. & Lichtenstadt I., *The Magnetorotational Instability in CCSN explosions*. ApJ, 584:954–970, 2003.

Adams F., Ruden S. & Shu F., *Eccentric gravitational instabilities in nearly Keplerian disks*. ApJ Part 1, Vol. 347, 959-976, 1989.

Balsara D., *von Neumann Stability Analysis of Smooth Particle Hydrodynamics: Suggestions for Optimal Algorithms*. Journal of Computational Physics, Vol. 121, no. 2, pp.357-372, 1995.

Balbus S. & Hawley J., *A Powerful Local Shear Instability in Weakly Magnetized Disks. I - Linear Analysis*. ApJ vol. 376, July 20, 1991, p. 214-222, 1991.

Balbus S. & Hawley J., *Instability, turbulence, and enhanced transport in accretion disks*. Reviews of Modern Physics, Vol. 70, No. 1, 1998.

Barnes J. & Hut P., *A hierarchical O(N log N) force-calculation algorithm*. Nature (ISSN 0028-0836), vol. 324, 446-449, 1986.

Bate M. & Burkert A., *Resolution requirements for smoothed particle hydrodynamics calculations with self-gravity*. MNRAS, Volume 288, Issue 4, pp. 1060-1072, 1997.

Berger E., *The environments of sGRB and implications for their progenitors*. New Astronomy Reviews, Volume 55, Issue 1-2, p. 1-22, 2011.

Blandford R. D. & Znajek R. L., *Electromagnetic extraction of energy from Kerr BHs*. MNRAS 179, 433-456, 1977.

Blondin J., Mezzacapa A. & DeMarino C., *Stability of Standing Accretion Shocks, with an eye toward CCSNe*. ApJ 584, 971-980, 2003.

Brainerd J., *Producing the universal spectrum of cosmological gamma-ray bursts with the Klein-Nishina cross section*. ApJ 428, 21-27, 1994.

Carballido A. & Lee W.H. *Characterizing the time variability in magnetized neutrino-cooled accretion disks: signatures of the gamma-ray burst central engine*. ApJL, 727, L41, 2011

Chen W.X. & Beloborodov A.M. *Neutrino-cooled Accretion Disks around Spinning Black Holes*. ApJ, 657, Issue 1, 383-399, 2007

Chevalier R., *Neutron Star accretion in a supernova*. ApJ, 346, 847-859, 1989.

Dehnen W., *Towards optimal softening in three-dimensional N-body codes - I. Minimizing the force error*. MNRAS, 324, 273-291 2001.

de Mink S., Langer N., Izzard G., Sana H. & de Koter A., *The Rotation Rates of Massive Stars: The Role of Binary Interaction through Tides, Mass Transfer, and Mergers*. ApJ, 764, Issue 2, 166, 17 pp. 2013

Dessart L., O'Connor E. & Ott C., *The arduous journey to BH formation in potential GRB progenitors*. ApJ, 754: 76 (10pp), 2012

Di Matteo T., Perna R. & Narayan R., *Neutrino Trapping and Accretion Models for Gamma-Ray Bursts*. ApJ, Vol. 579 Issue 2, 706-715, 2002

Fenimore E., Madras C. & Nayakshin S., *Expanding Relativistic Shells and Gamma-Ray Burst Temporal Structure*. ApJ, Vol. 473, p.998, 1996

Fishman G. & Meegan C., *Gamma Ray Bursts*. Annu. Rev. Astron. Astrophys. 1995, 33:415-458, 1995

Fowler W. & Hoyle F., *Neutrino processes and pair formation in Massive Stars and Supernovae*. ApJ Supplement, Vol. 9, p.201, 1964

Fujimoto S., Kotake K., Yamada S., Hashimoto M. & Sato K., *Magnetohydrodynamic Simulations of a Rotating Massive Star Collapsing to a Black Hole*. ApJ, Vol. 644, Issue 2, pp. 1040-1055, 2006

Frail et al., *Beaming in GRBs: Evidence for a Standard energy reservoir*. ApJ, Vol. 562 L55-L58, 2001.

Fruchter et al., *Long GRBs and CCSNe have different environments*. Nature, Volume 441, Issue 7092, pp. 463-468, 2006.

Fryer C., Woosley S., Herant M. & Davies M., *Merging White Dwarf/Black Hole Binaries and Gamma-Ray Bursts*. ApJ, Vol. 520, Issue 2, pp. 650-660

Galama et al., *An unusual SN in the error box of the GRB980425*. Nature, Volume 395, Issue 6703, pp. 670-672, 1998

Gammie C., *Nonlinear Outcome of Gravitational Instability in Cooling, Gaseous Disks*. ApJ, Vol. 553, Issue 1, pp. 174-183, 2001

Gehrels N., Ramirez-Ruiz E. & Fox D., *GRBs in the Swift era*. Annu. Rev. Astron. Astrophys. 47:567–617, 2009

Ghisellini G. & Celotti A., *Quasithermal comptonization and GRBs*. Astronomy and Astrophysics Supplement, v.138, p.527-528, 1999

Gingold R. & Monaghan J., *Smoothed particle hydrodynamics - Theory and application to non-spherical stars*. Mon. Not. R. Astron. Soc., 181, p. 375-389, 1977

Gingold R. & Monaghan J., *Kernel estimates as a basis for general particle methods in hydrodynamics*. Journal of Computational Physics, vol. 46, p. 429-453, 1982

Goodman J., *Are GRBs Optically thick?*. ApJ, 308, L47, L50, 1986

Goodman, *Radio scintillation of GRBs afterglows*. New Astronomy, Volume 2, Issue 5, p. 449-460, 1997

Hawley J. & Balbus S., *A Powerful Local Shear Instability in Weakly Magnetized Disks. II. Nonlinear Evolution*. ApJ, Vol. 376, p.223, 1991.

Houck J. & Chevalier R., *Gamma-Ray Bursts*. Cambridge Astrophysics Series 51, eds. C. Kouveliotou, R. A. M. J. Wijers and S. Woosley, Cambridge University Press (Cambridge), p. 169-190

Houck J. & Chevalier R., *Steady Spherical Hypercritical accretion onto Neutron Stars*. ApJ, 376, 234-244, 1991

Hernquist L. & Katz N., *TreeSPH: A Unification of SPH with the hierarchical tree method*. ApJ Supplement Series, 70, 419-446, 1989

Hernquist L., *Some cautionary remarks about SPH*. ApJ, 404: 717-722, 1993

Janka T., Eberl T., Ruffert M. & Fryer C., *BH NS mergers as central engines of GRBs*. ApJ 527, L39, L42, 1999

Kaneko et al., *Prompt and Afterglow Emission Properties of Gamma-Ray Bursts with Spectroscopically Identified Supernovae*. ApJ, Vol. 654, Issue 1, pp. 385-402, 2007.

Kaneko et al., *Broadband Spectral Properties of Bright High-Energy Gamma-Ray Bursts Observed with BATSE and EGRET*. ApJ, Vol. 677, Issue 2, pp. 1168-1183, 2008.

Katz J. & Piran T., *Persistent counterparts to GRBs*. ApJ, Vol. 490, p.772, 1997.

Kouveliotou C. et al., *Identification of two classes of GRBs*. ApJ, Vol. 413, L101-L104, 1993.

Korobkin O. et al., *Stability of general-relativistic accretion disks*. Phys. Rev. D, Vol. 83, 043007, 2011.

Kuiper et al., *The Crab pulsar in the* $0.7 - 30$ *MeV range as seen by CGRO COMPTEL*. A&A, Vol. 378, pp. 918-935, 2001.

Lazzati D., Rossi E., Ghisellini G. & Rees M., *Compton drag as a mechanism for very high linear polarization in gamma-ray bursts*. MNRAS, Volume 347, Issue 1, pp. L1-L5, 2004

Lee W.H. & Kluzniak W., *Merger of a Neutron Star with a Newtonian Black Hole*. Acta Astronomica Vol 45. 705-723, 1995

Lee W.H., Ramirez-Ruiz E. & Page D., *Dynamical Evolution of Neutrino-cooled Accretion Disks: Detailed Microphysics, Lepton-driven Convection, and Global Energetics*. ApJ, Vol. 632, Issue 1, pp. 421-437, 2005

Lee W.H. & Ramirez-Ruiz E., *Accretion Modes in Collapsars: Prospects for Gamma-Ray Burst Production*. ApJ, Vol. 641, Issue 2, pp. 961-971, 2006

Lee W.H. & Ramirez-Ruiz E., *The progenitors of short GRBs*. New J. Phys. 9, 17, 2007

Levan A.J. et al., *A New Population of Ultra-long Duration Gamma-Ray Bursts*. ApJ, Vol. 781, Issue 1, 13, 22 pp., 2014

Levesque E., *The host galaxies of LGRB*. Publications of the Astronomical Society of the Pacific, Volume 126, issue 935, pp.1-14, 2014

Lipunov V., Postnov K. & Prokhorov M., *Gamma-Ray Bursts as Standard-Energy Explosions*. Astronomy Reports, Vol. 45, Issue 3, pp.236-240, 2001

Lodato G. & Clarke C., 2011, *Resolution requirements for smoothed particle hydrodynamics simulations of self-gravitating accretion discs*. MNRAS 413, 2735–2740, 2011

Lopez-Camara D., Lee W.H. & Ramirez-Ruiz E., *GRB Production and SN signatures in slowly rotating Collapsars*. ApJ, 692, 804-815, 2009

Lopez-Camara D., Lee W.H. & Ramirez-Ruiz E., *Critical Angular momentum distributions in Collapsars, Quiescent Periods from accretion state transitions in lGRB*. ApJ, 716, 1308-1314, 2010

Lucy L.B., *A numerical approach to the testing of the fission hypothesis*. ApJ ,Vol 82, Number 12, 1013 - 1024, 1977

MacFadyen A. & Woosley S., *Collapsars: GRBs and explosions in Failed SNe*. ApJ, Vol. 524, 262-289, 1999

MacFadyen A., Woosley S. & Heger A., *SNe, Jets and Collapsars*. ApJ, Vol. 550, Issue 1, pp. 410-425, 2001

MacFadyen A., Ramirez-Ruiz E. & Zhang W., *Late flares from GRBs: Clues about the Central Engine*. AIP Conf. Proc. 836, 48, 2006

McConnell et al., *The Soft Gamma-Ray Spectral Variability of Cygnus X-1*. ApJ, Vol. 572, Issue 2, pp. 984-995, 2002

Meru F. & Bate M., *On the fragmentation criteria of self-gravitating protoplanetary discs*. MNRAS, 410, 559–572, 2011.

Meru F. & Bate M., *On the convergence of the critical cooling time-scale for the fragmentation of self-gravitating discs*. MNRAS, 427, Issue 3, pp. 2022-2046, 2012.

Metzger B. et al., *The protomagnetar model for gamma-ray bursts*. MNRAS, Vol. 413, Issue 3, pp. 2031-2056, 2011

Mizuno Y., Yamada S., Koide S. & Shibata K., *General Relativistic Magnetohydrodynamic Simulations of Collapsars*. ApJ, Vol. 606, Issue 1, pp. 395-412, 2004

Mizuno Y., Yamada S., Koide S. & Shibata K., *General Relativistic Magnetohydrodynamic Simulations of Collapsars: Rotating BH cases*. ApJ, Vol. 615, Issue 1, pp. 389-401, 2004

Monaghan J. & Gingold R., *Shock simulation by the particle method SPH*. Journal of Computational Physics Vol. 52, Issue 2, Pages 374–389, 1983

Monaghan J. & Lattanzio J., *A refined particle method for astrophysical problems*. Astron. and Astrophys., Vol. 149, no. 1, p. 135-143, 1985

Monaghan J.J., *Smoothed Particle Hydrodynamics*. Annu. Rev. Astron. Astrophys., 30: 543-574, 1992

Monaghan J.J., *SPH and Riemann Solvers*. Journal of Computational Physics, Vol. 136, Issue 2, Pages 298–307, 1997

Nagataki S., Takahashi R., Mizuta A. & Takiwaki T., *Numerical Study of Gamma-Ray Burst Jet Formation in Collapsars*. ApJ, Vol. 659, Issue 1, pp. 512-529, 2007

Nagataki S., *Development of a General Relativistic Magnetohydrodynamic Code and Its Application to the Central Engine of Long Gamma-Ray Bursts*. ApJ, Vol. 704, Issue 2, pp. 937-950, 2009

Nakar E., *Short-hard gamma-ray bursts*. Physics Reports Volume 442, Issues 1–6, Pages 166–236, 2007

Nakar E. & Piran T., *Gamma-Ray Burst Light Curves-Another Clue on the Inner Engine*. ApJ, Vol. 572, Issue 2, pp. L139-L142, 2002

Nakar E., Piran T. & Waxman E., *Implications of gamma-ray polarization of GRB 021206*. Journal of Cosmology and Astroparticle Physics, Issue 10, id. 005, 2003

Narayan R., Piran T. & Kumar P., *Accretion models of GRBs*. ApJ, 557, 949-957, 2001

Paczynski B. & Wiita P., *Thick accretion disks and supercritical luminosities*. Astronomy and Astrophysics, vol. 88, no. 1-2, p. 23-31, 1980

Paczynski B., *GRBs at cosmological distances*. ApJ, Vol. 308, L43, L46, 1986

Panaitescu A. & Meszaros P., *Dynamical Evolution, Light Curves, and Spectra of Spherical and Collimated Gamma-Ray Burst Remnants*. ApJ, Vol. 526, Issue 2, pp. 707-715, 1999

Panaitescu A. & Kumar P., *Fundamental physical parameters of collimated GRBs Afterglows*. ApJ, Vol 560, L49-L53, 2001

Piran T., Kumar P., Panaitescu A. & Piro L., *The Energy of Long-Duration Gamma-Ray Bursts*. ApJ, Vol. 560, Issue 2, pp. L167-L169, 2001

Piran T., *The physics of GRBs*. Reviews of modern physics Vol. 76, 2004

Price D., *SPLASH: An Interactive Visualisation Tool for Smoothed Particle Hydrodynamics Simulations*. Publ. Astron. Soc. Aust. 24, 159-173. (2007)

Price D., *Smoothed particle hydrodynamics and magnetohydrodynamics*. Journal of Computational Physics 231, 759–794, 2012

Proga D., MacFadyen A., Armitage P. & Begelman M., *Axisymmetric MHD simulations of the Collapsar Model for GRBs*. ApJ, Vol. 599, Issue 1, pp. L5-L8, 2003

Ramirez-Ruiz E. & Fenimore E., *Pulse Width Evolution in Gamma-Ray Bursts: Evidence for Internal Shocks*. ApJ, Vol. 539, Issue 2, pp. 712-717, 2000

Rhoads J.E., *The Dynamics and Light Curves of Beamed Gamma-Ray Burst Afterglows*. ApJ, Vol. 525, Issue 2, pp. 737-749

Rice W., Armitage P., Bate M. & Bonnell I., *The effect of cooling on the global stability of self-gravitating protoplanetary discs*. MNRAS, 339, 1025–1030 , 2003

Rice W., Forgan D. & Armitage P., *Convergence of smoothed particle hydrodynamics simulations of self-gravitating accretion discs: sensitivity to the implementation of radiative cooling*. MNRAS, 420, 1640–1647, 2012

Rockefeller G., Fryer C. & Li H., *Collapsars in Three Dimensions*. eprint arXiv:astro-ph/0608028, 2006

Rossi E., Lazzati D. & Rees M., *Afterglow light curves, viewing angle and the jet structure of Gamma ray bursts*. MNRAS, Vol. 332, Issue 4, pp. 945-950, 2002

Rosswog S., *Astrophysical smooth particle hydrodynamics*. New Astronomy Reviews, 53, 78–104, 2009

Sari R. & Piran T., *Variability in GRBs*. ApJ. Vol.485, p.270-273, 1997

Sari R., Piran T. & Halpern J., *Jets in GRBs*. ApJ, 519, L17-L20 1999

Schoenberg I.J., *Contributions to the problem of approximation of equidistant data by analytic functions. Part A: On the problem of smoothing of graduation. A first class of analytic approximation formulae*. Quart. Appl Math., 4, pp. 45–99, 1946

Sekiguchi Y. & Shibata M., *A Formation Mechanism of Collapsar Black Hole*. Progress of Theoretical Physics, Vol. 117, No. 6, 2007

Sekiguchi Y. & Shibata M., *Formation of Black Hole and Accretion Disk in a Massive High-entropy Stellar Core Collapse*. ApJ, Vol. 737, Issue 1, article id. 6, 28 pp., 2011

Shapiro S. & Teukolsky S., *Black Holes, White Dwarfs and NSs; The physics of compact objects*. Wiley 1983

Shaviv N. & Dar A., *Gamma-Ray Bursts from Minijets*. ApJ, Vol. 447, p.863, 1995

Shemi A., *Gamma-Ray Bursts from Interaction of Relativistic Flows with Radiation Fields* . MNRAS, Vol. 269, 4, pp.1112, 1994

Shibata M., Sekiguchi Y. & Takahashi R., *Magnetohydrodynamics of Neutrino-Cooled Accretion Tori around a Rotating Black Hole in General Relativity*. Progress of Theoretical Physics, Vol. 118, No. 2, 2007

Springel V., *The cosmological simulation code GADGET-2*. MNRAS, 364, 1105-1134, 2005

Springel V, Yoshida N. & White S., *GADGET: a code for collisionless and gas-dynamical cosmological simulations*. New Astronomy, Volume 6, Issue 2, p. 79-117, 2001

Springel V. & Hernquist L., *Cosmological smoothed particle hydrodynamics simulations: the entropy equation*. MNRAS, Vol. 333, 649-664, 2002

Steinmetz M., *GRAPESPH: cosmological smoothed particle hydrodynamics simulations with the special-purpose hardware GRAPE*. MNRAS, Vol. 278, Issue 4, pp. 1005-1017, 1996

Schwarzschild K., *On the Gravitational Field of a Mass Point According to Einstein's Theory*. Sitzungsberichte der Königlich Preussischen Akademie der Wissenschaften zu Berlin, Phys.-Math. Klasse, 189-196, 1916

Taylor P., Miller J. & Podsiadlowski P., *Long-duration gamma-ray bursts: hydrodynamic instabilities in collapsar discs*. MNRAS, Vol. 410, Issue 4, pp. 2385-2413, 2011

Toomre A., *On the gravitational stability of a disk of stars* ApJ, Vol. 139, p. 1217-1238, 1964

Ugliano M., Janka T., Marek A. & Arcones A., *Progenitor-Explosion connection and remnant birth masses for neutrino driven supernovae of Iron-Core Progenitors*. ApJ, Vol. 757, 69, 2012

van Paradijs J., Kouveliotou C. & Wijers M., *GRB Afterglows*. Annu. Rev. Astron. Astrophys. 38:379–425, 2000

Vietri M. & Stella L., *Supranova Events from Spun-up Neutron Stars: an Explosion in Search of an Observation*. ApJ, Vol. 527, Issue 1, pp. L43-L46, 1999

Waxman E., *GRB Afterglow:Supporting the cosmological fireball model, constraining parameters and making predictions*. ApJ, Vol 485, L5-L8, 1997

Williams H. & Tohline J., *Linear and nonlinear dynamic instability of rotating polytropes*. ApJ, 315: 594-601, 1987

Williams P., *Three routes to jet collimation by the Balbus-Hawley MRI*. MNRAS, 361, 345-356, 2005

Woodward J., Tohline J. & Hachisu I., *The stability of thick, self gravitating disks in protostellar systems*. ApJ, 420, 247-267, 1994

Woosley S., *GRBs from stellar mass accretion disks around BHs*. ApJ, Vol. 405, 273-277, 1993

Woosley S., Heger A. & Weaver T., *The evolution and explosion of massive stars*. Reviews of Modern Physics, vol. 74, Issue 4, pp. 1015-1071, 2002

Woosley S. & Heger A., *The progenitors of GRBs*. ApJ, Vol. 637:914–921, 2006

Woosley S. & Bloom J., *The SN-GRB connection*. Annu. Rev. Astron. Astrophys. 2006. 44:507–56

Yoon S. & Langer N., *Evolution of rapidly rotating metal-poor massive stars towards gamma-ray bursts*. A&A 443, 643–648, 2005

Zurek W. & Benz W., *Redistribution of angular momentum by nonaxisymmetric instabilities in a thick accretion disk*. ApJ, 308: 123-133, 1986

Zhang B., Woosley S. & MacFadyen A., *Relativistic Jets in Collapsars*. ApJ, Vol. 586, Issue 1, pp. 356-371, 2003

Zhang B. & Meszaros P., *Gamma-Ray Burst Beaming: A Universal Configuration with a Standard Energy Reservoir?*. ApJ, Vol. 571, Issue 2, pp. 876-879, 2002